TECHNISCHE UNIVERSITÄT MÜNCHEN
Lehrstuhl für Aerodynamik und Strömungsmechanik

Unsteady Vehicle Aerodynamics in Gusty Crosswind

Pascal Theissen

Vollständiger Abdruck der von der Fakultät für Maschinenwesen
der Technischen Universität München zur Erlangung des akademischen Grades eines

Doktor-Ingenieurs

genehmigten Dissertation

Vorsitzender:		Univ.-Prof. Dr.-Ing. Markus Lienkamp
Prüfer der Dissertation:	1.	Univ.-Prof. Dr.-Ing. habil Nikolaus A. Adams
	2.	Univ.-Prof. Dr.-Ing. Thomas Roesgen Eidgenössische Technische Hochschule Zürich, Schweiz

Die Dissertation wurde am 19. Januar 2012 bei der Technischen Universität eingereicht und durch die Fakultät für Maschinenwesen am 12. Juli 2012 angenommen.

Abstract

Unsteady vehicle aerodynamics in gusty crosswind are investigated using both numerical simulation and wind tunnel experiments with the aim of providing an understanding of the unsteady aerodynamic behavior. For a realistic but generic sinusoidal gust event, significant unsteady effects are identified for the aerodynamic side force, roll and yaw moment. Unsteady side force and roll moment exhibit smaller amplitudes compared to steady-state measurements. The unsteady yaw moment, however, shows a significant increase in amplitude compared to the corresponding steady-state values. Furthermore, positive time delays are identified for the side force and the roll moment, while the yaw moment exhibits a negative time delay compared to the quasi-steady approximation. With the help of numerical simulations, an unsteady mechanism is derived where a delayed reaction of the wake flow causes a time delay and an increase of the load contributions of the rear end which eventually lead to the differences between the unsteady and quasi-steady aerodynamic loads. In this context, a characteristic wake topology is identified consisting of fluid entering into the wake region from the leeward side flanked by two counter-rotating vortices above and below, which is at the core of the proposed unsteady mechanism. Following the identification and characterization of the above described unsteady phenomena, their main features are verified experimentally. For this purpose, a complex experimental setup is applied that provides time-dependent flow conditions at realistic Reynolds and Strouhal numbers by rotating a 50% scale model around its vertical axis.

Afterwards, the sensitivity of the identified unsteady effects to a variation of the gust parameters number of oscillations, gust frequency, vehicle speed, gust amplitude and initial yaw angle is investigated numerically using multiple-peak gust simulations. The unsteady phenomena are shown to strongly depend on the Strouhal number featuring a maximum intensity at $St \approx 0.2$. On the other hand, for the investigated vehicle speeds of 70 km/h to 220 km/h, the influence of the Reynolds number is small. Furthermore, the impact of the unsteady effects is significantly reduced for unrealistically large gust amplitudes as they occur for example at crosswind testing facilities. Similarly, it is shown that for the absence of a zero-crossing in the variation of the yaw angle, the unsteady effects disappear almost completely. Finally, the influence of different vehicle rear end types and of geometrical variations is investigated. Again using the gust simulation, unsteady effects are identified for all three investigated rear end types notchback, fastback and fullback. Furthermore, variations of the vehicle length and of the shape of the rear end of a sedan vehicle show that the unsteady aerodynamic loads differ significantly from the corresponding quasi-steady loads and that very often even the trends are inversed.

Preface

This thesis concludes the research work on unsteady vehicle aerodynamics that I conducted within a joint project of the BMW Group and the Institute of Aerodynamics and Fluid Dynamics at the Technische Universität München.

I would like to thank my doctoral advisor Prof. Dr.-Ing. Nikolaus Adams for his critical advice and continuous support regardless of arising challenges. Furthermore, I want to thank Prof. Dr.-Ing. Thomas Rösgen and Prof. Dr.-Ing. Markus Lienkamp for their effort during the examination process.

In particular, I thank my supervisors Holger Winkelmann and Hans Kerschbaum as well as my advisor Dr.-Ing. Rainer Demuth and Dr.-Ing. Thomas Indinger for their dedication to the joint research project reassuring everyone of its relevance. Seemingly endless meetings on complex unsteady mechanisms will not be forgotten.

The enormous effort of the model building and wind tunnel staff at BMW is greatly acknowledged - in particular numerous last-minute fixes.

I also appreciate the contribution of EXA Corporation supporting the complex numerical investigation and countless unsteady simulations.

I especially thank Marie-Charline Gilson, Kirstin Heuler, Maxime Mancosu, Andreas Puff and Bastian Schnepf for their valuable help during their internships.

A very special thank you goes to my colleague and close friend Johannes Wojciak. Three memorable years of challenging discussions, experimental preparations, code programming, set-backs and final success as well as night shifts that often ended in downtown bars inevitably resulted in a very special friendship.

Finally, I want to express my deep gratitude for the tremendous support and sympathy of my wife Anja and my parents.

Thank you very much!

Pascal

Contents

Nomenclature

β	Yaw angle
γ	Adiabatic index
δ_{ij}	Kronecker delta; $i = j : \delta_{ij} = 1, i \neq j : \delta_{ij} = 0$
ϵ	Dissipation rate
λ	Thermal conductivity
ν	Kinematic viscosity
ν_t	Eddy-viscosity
μ	Dynamic viscosity
ω	Molecular collision frequency
ρ	Density
σ_{ij}	Viscous stress tensor
τ_W	Wall shear stress
$\boldsymbol{\xi}, \xi, \xi_i$	Particle velocity
$\boldsymbol{\xi}_i$	Discrete patricle velocity
X_i	Aerodynamic admittance of load component C_i

a	Speed of sound
c	Thermal velocity
c_S	Molecular velocity
c_f	Skin friction coefficient
e	Internal energy
f	(Gust) frequency
$f(\boldsymbol{r}, \boldsymbol{\xi}, t)$	Velocity distribution function
k	Turbulent kinetic energy
l_f	Mean free path without collision
m	Mass
p	Static pressure
p_∞	Reference pressure
q, q_i	Heat flux
t	Time
Δt	Time delay
u_τ	Friction velocity in the boundary layer
u^+	Non-dimensional velocity in the boundary layer
$\boldsymbol{v}, v, v_i$	Velocity
y^+	Non-dimensional wall-normal distance in the boundary layer

A	Cross section
A_C	Collision cross section
E	Total energy
F	Maxwell-Boltzmann equilibrium distribution function
F_x, C_x	Drag force and drag coefficient
F_y, C_y	Side force and side force coefficient
F_z, C_z	Lift force and lift force coefficient
M_x, C_{Mx}	Roll moment and roll moment coefficient
M_y, C_{My}	Pitching moment and pitching moment coefficient
M_z, C_{Mz}	Yaw moment and yaw moment coefficient
C_p	Pressure coefficient
L	Characteristic length scale (vehicle length)
L_{WB}	Length of wheelbase
R	Ideal gas constant
$S_\beta(f)$	Frequency spectrum of the yaw angle β
$S_{C_i}(f)$	Frequency spectrum of the aerodynamic load component C_i
S_{ij}	Strain tensor
T	Temperature
T	Time period
U	Characteristic velocity (vehicle speed)
Kn	Knudsen number
Ma	Mach number
Re	Reynolds number
St	Strouhal number
QS	Quasi-steady
US	Unsteady

Chapter 1

Introduction

Today, crosswind stability of cars is mainly relevant for passenger comfort. Only in extreme weather conditions it is considered a real safety issue. However, crosswind stability certainly influences the driver's perception of vehicle safety in particular at highway speeds of 140kph and above. A vehicle, which is sensitive to crosswind, generally requires more steering action by the driver and thus may raise concern about the general stability and safety of the vehicle although from an objective point of view the vehicle is not critical. From a marketing standpoint it is clear that crosswind stability is not a unique selling point, but in particular for medium and large size vehicles it is considered a pre-requisite. Hence, it is unlikely that a customer will select a car because of its superb crosswind stability, but a customer will certainly not buy a car if he does not feel safe driving it.

The term crosswind stability describes the behavior of a vehicle under flow conditions with lateral velocity components. These flow conditions can be caused by atmospheric winds as well as other vehicles, for example during passing maneuvers, and are strongly dependent on road-side obstacles or the preceeding vehicle. Crosswind sensitivity is often confounded with general directional stability under windless conditions. In the first case, lateral incoming flow conditions cause an asymmetric flow around the car, which results in aerodynamic loads that alter the motion of the vehicle. In the second case, path deviations are generally caused by road imperfections and can be mainly influenced by suspension and wheel parameters or, in particular at high speed, by reducing the aerodynamic lift. Self-induced fluctuations of aerodynamic loads due to flow separation have not yet been reported to have a relevant impact on directional stability.

Recently, research regarding crosswind stability has seen a rise of interest. Given the increasing focus on the sustainability of cars, OEMs are investigating a variety of means for reducing car CO2 emissions. In this context, vehicle aerodynamic improvements and weight reduction are expected to significantly contribute to lowering fuel consumption. However, more streamlined vehicle geometries, that produce less drag, are likely to increase the aerodynamic side force and yaw moment in crosswind. Additionally, a reduction in vehicle weight further increases the ratio of aerodynamic loads to the inertia of the vehicle. Hence, a shift towards more streamlined and lighter cars is likely to have a negative effect on driving stability and consequentially the safety and comfort perceived by the driver. In addition to the focus on sustainability, a consumer trend towards taller vehicles like SUVs or city cars can be observed. This also has a negative influence on crosswind stability as the aerodynamic loads generally increase due to the larger lateral cross-section. At the same time the center of gravity is raised, diminishing vehicle dynamics even further.

Therefore, a reliable prediction of crosswind sensitivity early in the development process is required in order to avoid costly modifications shortly before start of production or even recalls, which can affect the image of a brand over years. However, today's development tools like crosswind testing facilities or constant yaw wind tunnel tests do not fully replicate real-world conditions and thus, do not capture all relevant phenomena. Furthermore, crosswind stability is the result of complex unsteady interactions between aerodynamics, vehicle dynamics and the driver. The causal connection between wind excitation and the resulting driver's perception of the vehicle sensitivity are not fully understood, in particular occurring unsteady phenomena. Hence, in order to provide development tools that reliably predict crosswind stability, first the unsteady behavior of the sub-systems and finally the complete system aerodynamics - vehicle dynamics - driver need to be analyzed and understood. This work focuses on vehicle aerodynamics and aims at providing insight into the unsteady aerodynamic behavior of vehicles under time-dependent flow conditions.

Chapter 2

Definitions and State of Knowledge

After the definition of specific terms and conventions in Chap. 2.1, a detailed overview of the research and state of knowledge on crosswind stability is given in Chap. 2.2.

2.1 Definitions

2.1.1 Coordinate System

The vehicle coordinate system is defined as shown in Fig. 2.1, with the x-axis pointing towards the rear, the y-axis towards the passenger side and the z-axis towards the roof of the vehicle. The corresponding moments, roll, pitch and yaw, are defined according to the right-hand rule. The aerodynamic reference point is set at mid wheel base in x-direction, on the vehicle symmetry plane in y-direction and at ground level in z-direction. The yaw angle β is defined according to the definition often used in wind tunnels where turning the car around the z-axis according to the right-hand rule defines a positive yaw angle. Therefore, crosswind from the passenger side corresponds to a positive rotation of the car and hence a positive yaw angle, compare Fig. 2.1.

2.1.2 Dimensionless Parameters

When modeling real-world flow conditions, Reynolds and Strouhal similarity need to be considered to ensure the validity of the results. In order to compare results from investigations under different testing conditions, the results are non-dimensionalized as defined below.

Reynolds Number. The Reynolds number is defined as the ratio of inertial to viscous forces:

$$Re = \frac{\rho U L}{\mu} = \frac{U L}{\nu}, \tag{2.1}$$

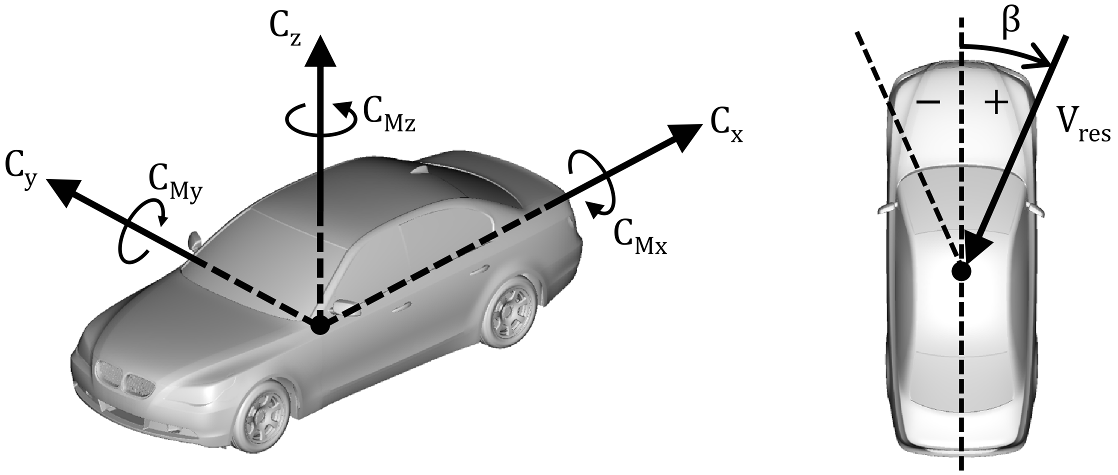

Figure 2.1: Definition of coordinate system.

where ρ is the density, μ the dynamic viscosity and ν the kinematic viscosity. U is a characteristic velocity and L a characteristic length scale. In the following, the free stream velocity in x-direction is used, which is defined in the vehicle coordinate system for the numerical investigations and in the wind tunnel coordinate system for the experimental analysis. The vehicle length is used as characteristic length scale.

Strouhal Number. The Strouhal number is defined as the frequency f non-dimensionalized by the characteristic length scale L and the characteristic velocity U as used for the Reynolds number:

$$Sr = \frac{fL}{U} \tag{2.2}$$

Hence, the Strouhal number is the ratio of the time scale of flow oscillations at a frequency f to the time scale that is required for the flow to travel one vehicle length L/U. The frequency f can be the flow excitation due to crosswind gusts as well as for example flow oscillations in the wake of the vehicle. Often, the reduced frequency f_n is used instead of the Strouhal number.

$$f_n = \frac{\pi f L}{U} \tag{2.3}$$

Mach Number. The Mach number is defined as the ratio of velocity v over speed of sound a.

$$Ma = \frac{v}{a} \tag{2.4}$$

The speed of sound is calculated as $a = \sqrt{\gamma R T}$, where γ is the adiabatic index, R the ideal gas constant and T the temperature. The Mach number needs to be considered when effects of compressibility are of relevance. For vehicle aerodynamics, where the

Mach number is generally small $Ma < 0.3$, effects of compressibility are of minor importance.

Load Coefficients. Aerodynamic forces are non-dimensionalized using the dynamic pressure $\frac{1}{2}\rho U^2$ and the cross section in x-direction A. For normalizing aerodynamic moments, additionally a characteristic length scale is required. Due to the importance of aerodynamic moments for vehicle dynamics, the wheelbase L_{WB} is commonly used for non-dimensionalization.

$$C_i = \frac{F_i}{\frac{1}{2}\rho U^2 A} \tag{2.5a}$$

$$C_{Mi} = \frac{M_i}{\frac{1}{2}\rho U^2 A L_{WB}} \tag{2.5b}$$

Pressure Coefficient. Dimensionless pressure coefficients are defined as the ratio of the difference between static and reference pressure $p - p_\infty$ over dynamic pressure $\frac{1}{2}\rho U^2$.

$$C_p = \frac{p - p_\infty}{\frac{1}{2}\rho U^2}. \tag{2.6}$$

2.1.3 Unsteady and Quasi-Steady Comparison

Quasi-Steady. In the context of this work, quasi-steady means that although a time-dependent event is investigated, it is assumed that at each time step all parameters reach steady-state. Hence, quasi-steady approximation is an estimate of the resulting time-dependent signals irrespective of possible unsteady phenomena.

In order to compare unsteady (index US) and quasi-steady (index QS) aerodynamic loads, the parameters magnification factor and time shift are used in this work. In many references aerodynamic admittance is used instead of a magnification factor.

Magnification Factor. The magnification factor is simply the ratio of unsteady peak value or amplitude to its quasi-steady equivalent. Usually the magnification factor is used when investigating an excitation with a singular, fixed frequency, as it is the case in this work.

Aerodynamic Admittance. In comparison, aerodynamic admittance is generally used when analyzing an excitation containing a frequency spectrum instead of a singular frequency. Aerodynamic admittance was introduced by Davenport (1961) and is calculated as the ratio of the frequency spectrum of unsteady to quasi-steady aerodynamic loads. The frequency spectrum of quasi-steady loads is derived from the frequency spectrum of the yaw angle $S_\beta(f)$ and the variation of the steady-state aerodynamic load over the yaw angle dc_i/d_β. Simply put, aerodynamic admittance is a frequency-dependent magnification factor. From Equation 2.7 it can be seen that the term $X_i^2(f)(dc_i/d\beta)^2$ is the transfer function between wind excitation and the unsteady aerodynamic response.

$$X_i{}^2(f) = \frac{S_{c_i}(f)}{\left(\frac{dc_i}{d\beta}\right)^2 S_\beta(f)}. \tag{2.7}$$

Admittance was initially used by Davenport (1961) to describe the wind loads on buildings. Indicating the ratio of unsteady over steady loads admittance should theoretically tend towards 1 for frequencies approaching zero as flow conditions converge towards steady state. For large frequencies admittance tends towards 0 as the length scales of wind excitation become small relative to the size of the investigated object and therefore their impact diminishes. This behavior was confirmed by Bearman (1971) for flat plates normal to turbulent flow. If the function of admittance over frequency is known, the unsteady loads can be calculated from its steady values. The use of admittance instead of the magnification factor can be observed in investigations that use spectral analysis which is often the case for experimental studies.

Time Shift. Time shift is defined as the delay Δt between two signals $f_1(t)$ and $f_2(t)$ with $f_2(t) = f_1(t - \Delta t)$. In this case $f_2(t)$ lags $f_1(t)$ by Δt. In this work, time shifts of unsteady signals are always given relative to the quasi-steady signal. Hence, a positive time shift means that the unsteady signal lags behind the quasi-steady signal.

2.1.4 Visualization of Vortices

In this work, vortices are visualized using isosurfaces of vorticity and the so-called λ_2-criterion. Vorticity is simply defined as the curl of the velocity field.

$$\boldsymbol{\omega} = \boldsymbol{\nabla} \times \boldsymbol{v} \tag{2.8}$$

The λ_2-criterion was proposed by Jeong and Hussain (1995) extending the typical pressure-minimum criterion which shows deficiencies in unsteady irrotational and viscous straining. λ_2 is the second largest eigenvalue of the symmetric tensor $\boldsymbol{S}^2 + \boldsymbol{\Omega}^2$. $\boldsymbol{S}$ is the symmetric strain-rate tensor and $\boldsymbol{\Omega}$ the anti-symmetric spin tensor.

$$\boldsymbol{S} = \frac{1}{2}\left(\frac{\partial v_i}{x_j} + \frac{\partial v_j}{x_i}\right) \qquad \boldsymbol{\Omega} = \frac{1}{2}\left(\frac{\partial v_i}{x_j} - \frac{\partial v_j}{x_i}\right) \tag{2.9}$$

2.2 State of Knowledge

2.2.1 Overview Vehicle Crosswind Stability

Assessing Crosswind Stability. Vehicle crosswind stability is influenced by the four factors wind excitation, aerodynamics, vehicle dynamics and driver as sketched in Fig. 2.2. As pointed out by for example Wallentowitz (1981), Schaible (1998) or Wagner (2003), the whole system including the driver has to be considered in order to assess the crosswind stability of a vehicle. Wallentowitz (1981) proposed to analyze vehicle crosswind stability by measuring the wind excitation and the resulting vehicle yaw rate during tests on public roads. Thus, the transfer function of vehicle reaction in yaw due to the wind excitation can be calculated. A vehicle that exhibits larger values of yaw rate over wind excitation, in particular close to the vehicle eigen frequencies, is considered to be more sensitive to crosswind.

Wagner (2003) extended the approach of Wallentowitz (1981) relying on the parameters intensity of vehicle yaw reaction, efficiency of driver influence, steering effort and steering rate in order to determine a combined sensitivity index.

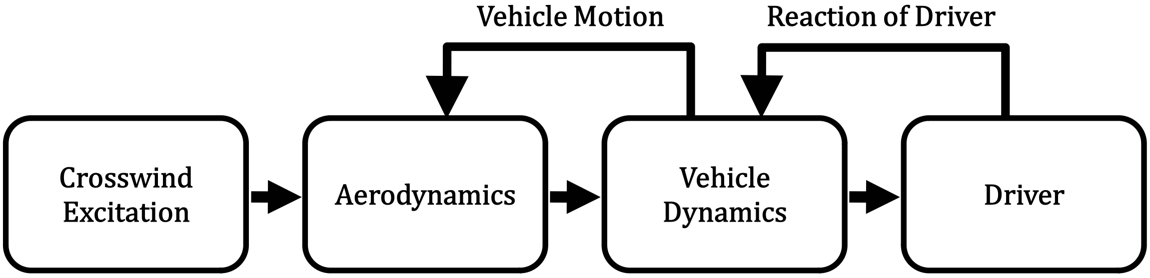

Figure 2.2: Schematic view of complete system crosswind stability.

Influence of Driver. Building on the approach of Wallentowitz (1981), Schaible (1998) used the measured steering angle and a simple single-track model to calculate the vehicle motion induced by the driver. By subtracting this vehicle motion caused by the reaction of the driver from the measured total vehicle motion, the vehicle response without driver can be estimated. Comparing the vehicle response with and without the influence of the driver showed that the driver is able to reduce the vehicle motion up to a frequency of 0.5 Hz. Between 0.5 Hz and 2 Hz by trying to counter steer the driver actually increases the vehicle motion. Above 2 Hz the influence of the driver on the vehicle response is small. Wagner (2003) confirmed that the frequency range of 0.5 Hz - 2 Hz is critical. The findings are summarized in Table 2.1. After extensive road tests under gusty wind conditions Wagner (2003) conceived a driver model that allowed simulating the driver reaction based on input parameters describing the aerodynamic and dynamic behavior of a vehicle.

Relevant Vehicle Motion. Yawing motion is considered to be the dominating vehicle motion perceived by the driver followed by a lateral vehicle motion, compare Wallentowitz (1981), Schaible (1998), Wagner (2003), Hucho (2005). However, conclusions concerning the relevant parameters of vehicle motion vary. Wallentowitz

Frequency Range [Hz]	**Driver Influence**
0 (constant crosswind)	Driver is able to fully compensate wind excitation
0 - 0.5	Driver reduces vehicle motion
0.5 - 2	Driver amplifies vehicle motion
> 2	Driver does not influence vehicle motion

Table 2.1: Influence of the driver on vehicle motion according to Schaible (1998).

(1981) defined yaw angle, yaw rate and lateral deviation as most relevant parameters. Based on extensive road tests Wagner (2003) identified yaw rate, yaw acceleration and lateral velocity as most relevant parameters. Wagner (2003) could not detect a direct influence of rolling motion but did not exclude an indirect influence due to the coupling of rolling and yawing motion. Maeda et al. (1996) claims that a combined roll-yaw motion is most important for vehicle stability.

Relevant Aerodynamic Loads. Based on the critical parameters of vehicle motion aerodynamic yaw moment followed by aerodynamic side force are considered most relevant, compare Schaible (1998), Hucho (2005), Maeda et al. (1996). Lift forces are not considered to have a direct impact on vehicle motion. However, low lift levels are assumed to reduce steering action, thereby improving overall stability of the complete system vehicle driver, Hucho (2005). The influence of the aerodynamic roll moment has not yet been fully resolved. Similarly, little is known about the relevance of the temporal composition of the aerodynamic loads. Until now, assessments of the complete system vehicle-driver, like for example in Wagner (2003), used an approximation of the aerodynamic loads derived from steady-state results. Hence, possible unsteady aerodynamic effects were not included.

Coupling. As pointed out above, it is essential to consider the coupling between vehicle dynamics and driver. However, it is not clear how aerodynamics are influenced by the vehicle motion caused by the wind excitation and the resulting response of the driver. Aschwanden et al. (2006) investigated the influence of heave and pitching motions on the aerodynamic loads of a race car. They could prove that for a 33% scale model hysteresis effects influencing the lift balance occur for Strouhal numbers in a range of $St \sim 0.4 - 1.0$. However, little is known about the influence of typical yaw and roll motion witnessed in gusty crosswind. Vehicle motion, on the one hand, affects the angle of incidence of the oncoming flow but on the other hand may also alter the flow field around the car.

Development Tools. Traditional tools used to assess crosswind stability in the vehicle development process are road tests, tests at crosswind facilities and wind tunnel measurements under constant yaw. While road tests offer the possibility to evaluate the complete system including the driver in real-world conditions, they lack in reproducibility due to changing wind conditions and in the ability to accurately resolve small differences due to the high noise level. Furthermore, undisguised prototypes in running condition are required. This constitutes the most important drawback as such prototypes are not available until shortly before start of production when design changes are very costly or may even delay market entry. To avoid tests on public roads and to improve reproducibility crosswind facilities are used (see Fig. 2.3). These facilities consist of several large fans which are lined up at the side of a road and generate an artificial crosswind. The path deviation and yaw rate of a vehicle travelling through the crosswind are used as a measure of its crosswind stability. However, to produce acceptable signal-to-noise levels and thus reproducible results, high crosswind velocities are required which lead to unrealistic aerodynamic yaw angles of 30° and higher. Furthermore, typical crosswind facilities are not capable of modeling the stochastic variation of natural crosswinds. Since the path deviation at crosswind facilities generally correlates well with the constant aerodynamic yaw moment, sub-targets are often assigned for the aerodynamic yaw moment. Thus, wind tunnel measurements at constant yaw angle allow the verification of the steady-state aerodynamic behavior early in the development process. These constant yaw measurements, however, do not reproduce real-world wind conditions and therefore are not capable of predicting the unsteady aerodynamic behavior of the vehicle. For a more detailed comparison of development tools for crosswind stability refer to Hucho (2005) and Schaible (1998).

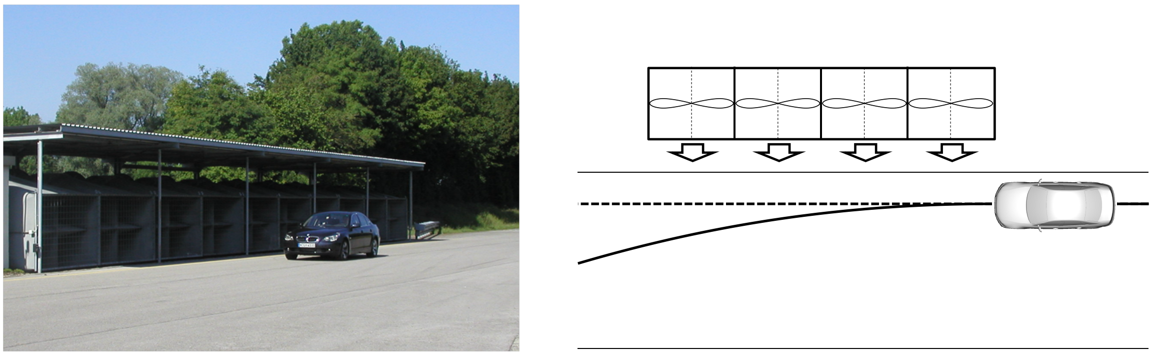

Figure 2.3: Typical development tool for vehicle crosswind stability: Crosswind facility.

In order to overcome the drawback of traditional testing methods, new approaches - numerical and experimental - are being investigated for application in the development process. This includes in particular, numerical analysis of the unsteady behavior of aerodynamics and vehicle dynamics using computational fluid dynamics and multi-body simulation. They promise to allow an evaluation of aerodynamic loads and their influence on vehicle motion very early in the conception phase when experimental hardware is not yet available. In addition, new testing methods in the wind tunnel creating time-dependent flow conditions could allow the evaluation of unsteady aerodynamic loads. Finally, driving simulators may combine models describing the vehicle behavior regarding aerodynamics and vehicle dynamics with the actual response of the driver permitting the virtual assessment of crosswind stability of the complete system.

However, for the assessment of crosswind stability in driving simulators the underlying models for aerodynamics and vehicle dynamics need to correctly predict the unsteady behavior. This requires to identify and understand occurring unsteady phenomena. As described in more detail later, this work will focus on the unsteady aerodynamic behavior. Therefore, research results and approaches regarding wind excitation and vehicle aerodynamics will be presented in more depth in Chap. 2.2.2 and Chap. 2.2.3.

The state of knowledge regarding crosswind stability of passenger cars can be summarized as follows:

- Assessing crosswind stability needs to take into account the complete system including incoming flow conditions, aerodynamics, vehicle dynamics and the driver.
- The frequency range from 0.5 Hz to 2 Hz is critical for crosswind stability. In this range the driver magnifies vehicle motion which overlaps with eigen frequencies of typical passenger vehicles.
- Yawing motion is considered to be the dominating vehicle motion perceived by the driver followed by a lateral vehicle motion.
- Aerodynamic yaw moment and side force are considered most relevant while little is known about the influence of roll moment and the time delays between the aerodynamic load components.

2.2.2 Characterization of Oncoming Flow

Aerodynamic Loads in Constant Flow. Schrefl (2008) claims that the fluctuations of aerodynamic loads that can be observed in constant flow due to flow separation are not relevant for driving stability. Recorded pressure oscillations occur at frequencies $St \sim 1$ above the critical range for driving dynamics and contain little energy compared to crosswind gusts.

Time-Dependent Flow. Therefore, a variation of the oncoming flow is required to cause a relevant change in aerodynamic loads and thus vehicle motion. In the following the oncoming flow regimes which can cause relevant variations in aerodynamic loads are characterized. Relevant changes in oncoming flow can be divided into two groups, crosswind gusts and overtaking/passing maneuvers.

Crosswind Gusts. Wojciak et al. (2010) investigated the turbulent flow characteristics for gusty crosswind conditions at Beaufort 4 to 7, which corresponds to wind speeds of approximately 6 m/s to 14 m/s at 10 m above ground. They characterize a gust as a low-frequency distortion of the axial and lateral flow velocity with respect to the vehicle coordinate system which results in a change of yaw angle. The findings of Wojciak et al. (2010) characterizing crosswind gusts are summarized below (see also Fig. 2.4):

- The turbulent length scales L_{Gust} that are relevant for driving stability are constrained to a range of 10 m to 80 m. At a vehicle speed of 40 m/s this translates into a frequency of crosswind excitation of 0.5 Hz to 4 Hz and Strouhal numbers of 0.05 to 0.4 ($L_{ref} = 4\,\mathrm{m}$).

- 2/3 of the gusts have a sinusoidal shape.
- 3/4 of the gusts feature a change of sign in lateral velocity and yaw angle.
- Maximum amplitudes of 8 m/s and mean amplitudes of 3 m/s to 5 m/s for lateral velocity.
- This translates into maximum amplitudes of 12° (e.g. $-6° \rightarrow +6° \rightarrow -6°$) and mean amplitudes of 5° to 8° for yaw angle at 140 km/h.
- The velocity profile during crosswind gusts can be assumed constant for a height between 250 mm and 750 mm above ground.

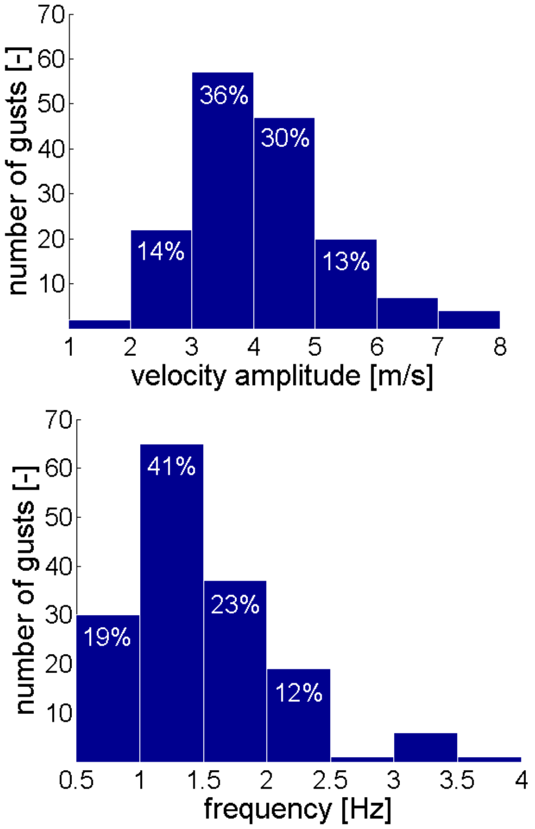

Figure 2.4: Characterization of crosswind gusts by Wojciak et al. (2010).

Similarly, Mayer et al. (2007) report mean peak yaw angles during relevant gust events of 4° at a vehicle speed of 200 km/h which translates into a lateral wind velocity of approximately 4 m/s. During these measurements at the German part of the North Sea coast maximum absolute yaw angles of 9° were observed at 200 km/h. Investigations of Cooper and Utz in Hucho (2005) prove that in general yaw angles larger than 10° rarely occur.

Fig. 2.5 summarizes the range of turbulent structures relevant for vehicle dynamics which covers length scales L_{Gust} of approximately 10 m to 80 m and frequencies of 0.5 Hz to 4 Hz at 40 m/s. Smaller turbulent structures contain less energy and lie above the eigen frequencies of typical cars. Larger turbulent structures imply time scales longer than 2 s, which can be well compensated by the driver and can be treated in a quasi-steady way. To simplify denotation in the following, the term "time-dependent flow conditions" is used for flows that are dominated by time scales of approximately $10^1 s - 10^{-1} s$. Flows which are dominated by time scales outside this range are referred to as "constant", albeit in this case of course flow properties also vary over time.

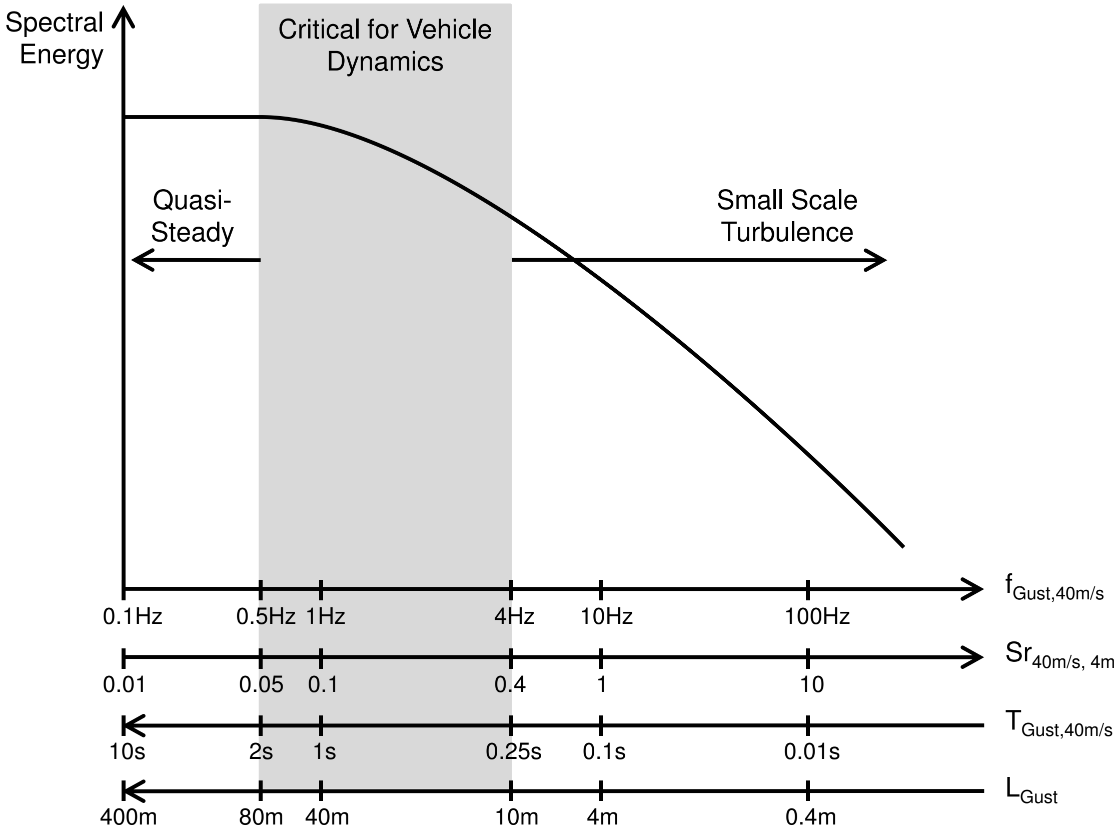

Figure 2.5: Schematic view of turbulence scales relevant for vehicle dynamics at a vehicle speed of 40 m/s and a vehicle length of 4 m(compare Theissen et al. (2011)), where f_{Gust} gust frequency, T_{Gust} gust duration and L_{Gust} gust elongation.

Passing Maneuver. Exemplarily, Schröck et al. (2007) presented the time histories of flow conditions for two car-to-car passing maneuvers. In these examples the flow angle shows a sinusoidal variation from 0° to 6° then to -6° and back to 0°. Puff (2010) numerically analyzed the variation in flow angle that is seen by a vehicle passing a single truck without additional crosswind, see Fig. 2.6. In a lateral distance of 1.6 times the width of the truck the lateral velocity V_y shows a sinusoidal shape ranging from 0.75 m/s to -1.75 m/s for a truck that travels at 80 km/h. This translates into a yaw angle of -1.2° to 2.7° for a speed of the overtaking vehicle of 140 km/h. However, flow parameters vary significantly over the width and length of the overtaking vehicle. Beyond this, statistical information on flow conditions during passing maneuvers that is based on a large database is not available at present.

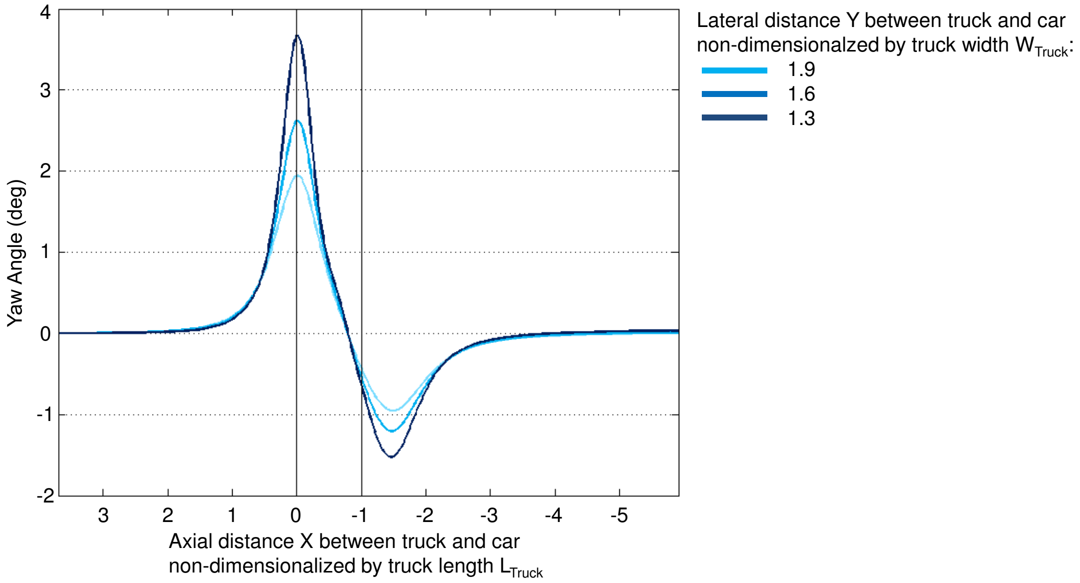

Figure 2.6: Evolution of yaw angle next to truck during imaginary passing maneuver at three lateral distances (Puff (2010)).

The characterization of the oncoming flow can be summarized as follows:

- Only time-dependent incoming flow conditions as during wind gusts or passing maneuvers can cause relevant variations in aerodynamic loads and thus vehicle motions.
- Relevant wind gusts are turbulent structures of 10 m to 80 m that cause a sinusoidal variation in yaw angle of typically 5° to 8° amplitude and include zero crossings with a probability of approximately 75%.
- Oncoming flow during passing maneuvers also shows a sinusoidal behavior in yaw angle but flow parameters vary significantly over the width and length of the vehicle.

2.2.3 Vehicle Aerodynamics

2.2.3.1 Constant Yaw

One of the most recent publications to describe the flow topology and pressure distribution for a realistic three-box geometry under constant yaw is by Lemke (2006).

Using CFD Lemke (2006) reported pressure differences between windward and leeward side, which essentially cause side force and yaw moment, to be much larger at the front and the center of the vehicle than at its rear. At the rear Lemke (2006) observes that at yaw fluid enters into the wake region mainly from the leeward and not from the windward side, which might not seem plausible at first. This wake topology including a vortex pair on the leeward side, which was witnessed in the course of this work (compare also Theissen et al. (2010) and Theissen et al. (2010)), was confirmed by Heuler (2010) using hotwire anemometry (see Fig. 2.7). The topology of the wake flow at constant crosswind including fluid entering from the leeward side and two counter-rotating vortices was similarly described by Gohlke et al. (2007) and Gohlke et al. (2008) for a very generic body.

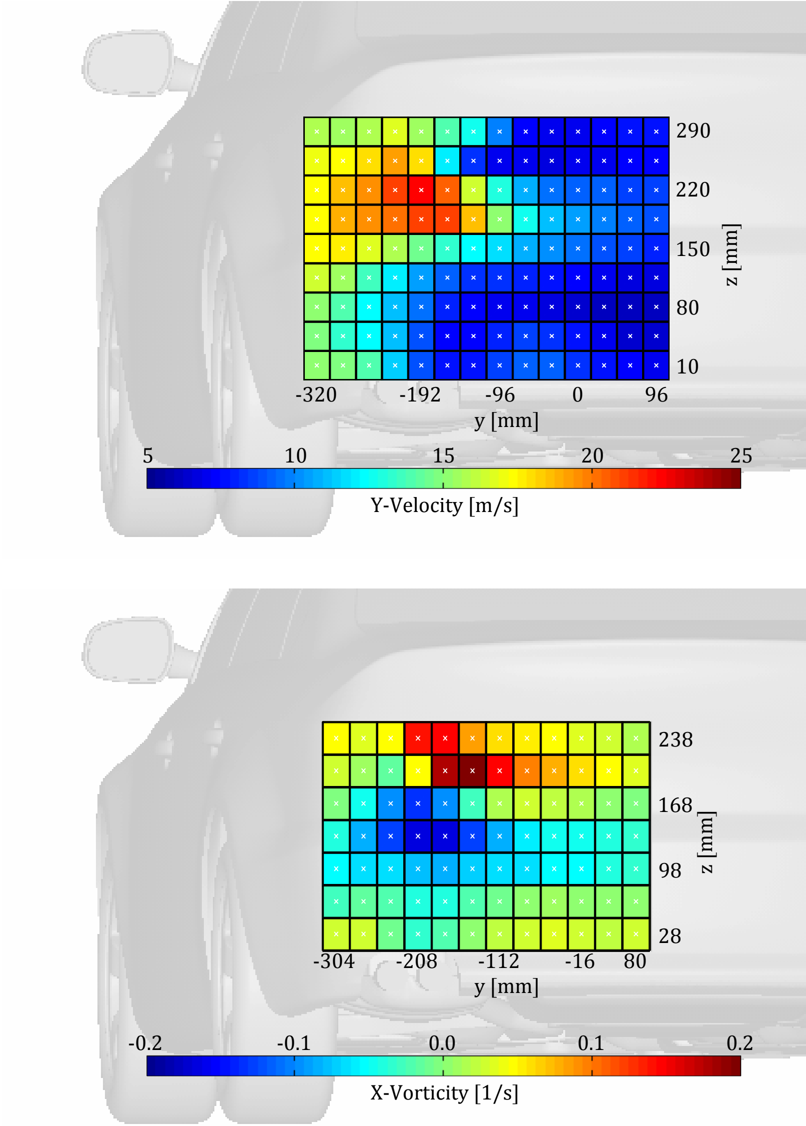

Figure 2.7: Hotwire measurements of Heuler (2010) in the leeward wake under 5° constant crosswind at 140 km/s.

In Hucho (2005) a schematic comparison between sedan, fastback und station wagon indicates that the side force is largest for station wagon and smallest for sedan. On the other hand, the yaw moment is largest for sedan and smallest for station wagon. Hucho (2005), however, notes that modern fastback geometries may exhibit even larger yaw moments than a sedan due to highly rounded rear screens.

The described aerodynamics under constant yaw can be summarized as follows:

- Under constant yaw a station wagon generally features a larger side force while sedan and fastback produce a larger yaw moment.
- For a realistic sedan flow enters into the wake from the leeward side.

2.2.3.2 Time-Dependent Flow

Various investigations have been published analyzing the aerodynamic behavior under time-dependent flow conditions. In the following, experimental results are summarized followed by numerical studies and a brief overview of vehicle aerodynamics during passing maneuvers.

Experimental Approaches. In order to generate on-flow conditions that vary over time two principal approaches have been followed: First, oscillating devices such as airfoils were used upstream of the vehicle to deflect the flow. Second, the time-dependent oncoming flow was generated by applying a rotatory or translatory motion to the test model. The major advantage of the first method is the possibility to use external as well as internal balances, since the model is stationary. Thus, in addition to vehicle models also real vehicles can be easily analyzed. Furthermore, it is easy to combine aerodynamic with aeroacoustic measurements using this setup. The challenge of the first setup is to specify the time-dependent incoming flow conditions as seen by the car. Due to the unpredictable flow development between the nozzle and the test model, the flow conditions at the position of the vehicle can only be described statistically which significantly complicates a comparison with numerical simulations. On the other hand, when working with oscillating or moving models, mechanical inaccuracies and noise often lead to poor reproducibility and big uncertainties when determining the aerodynamic loads. Depending on the generation of the model motion, it is sometimes not even possible to measure aerodynamic loads, but only surface pressures and parameters of the surrounding flow field. In order to determine aerodynamic loads for moving vehicle models inertial forces need to be considered. As opposed to the first approach, the major advantage is the precise definition of the oncoming flow as seen by the car.

Flow Deviation by Oscillating Airfoils or Flaps. To the author's knowledge the approach using oscillating airfoils was first investigated in detail by Mullarkey (1990) and Bearman and Mullarkey (1994) in a model scale wind tunnel followed by Passmore et al. (2001). It was later implemented in Pininfarina's full-scale wind tunnel (Carlino and Cogotti (2006)) and has been adopted more recently by Schröck et al. (2009). Bearman and Mullarkey (1994) carried out their experiments using the generic Davis model at a maximum Reynolds number of 4.5×10^5 based on the vehicle length of 0.3 m and varied the Strouhal number between approximately 0.05 and 0.55. The measurements led to unsteady values for side force and yaw moment that were smaller than the corresponding constant yaw values. Only for high Strouhal numbers of 0.45 to 0.55 the unsteady yaw moment showed an amplification of approximately 5%. Passmore et al. (2001) built on the setup of Mullarkey (1990) and conducted similar measurements with a 1/6 scale generic Davis model at a Reynolds number of 1×10^6 and Strouhal numbers of approximately 0.03 to 0.23. Unfortunately, forces and moments were only approximated using surface pressure measurements. Contradicting the conclusion of Bearman and Mullarkey (1994), Passmore et al. (2001) stated that the quasi-steady prediction underestimated the unsteady yaw moment by between 5% and 30% while the side force was still being overestimated. Interestingly, Passmore et al. (2001) showed that pressure measurements on the side of the model lagged the quasi-steady approximation by as much as 140°. With higher Strouhal numbers the area featuring large time delays was restricted to the rear part of the model while the front showed almost no time lag. Furthermore, the pressure at the rear side showed large amplification factors, especially at low Strouhal numbers of 0.03 to 0.06.

Schröck et al. (2009) partly confirmed the findings of Passmore et al. (2001) by investigating the unsteady behavior of a 20% SAE model at a Reynolds number of 4.5×10^6 and a Strouhal range of 0 to 0.15 based on the length of the wheelbase. While the side force was overpredicted by quasi-steady approximation throughout the whole Strouhal range, an underprediction of the yaw moment by approximately 15% was observed for the hatchback model in the Strouhal number range between 0.10 and 0.15. Interestingly, a sedan geometry showed larger absolute values for the unsteady yaw moment but smaller magnification factors than the hatchback model. Schrefl (2008) and Mayer et al. (2007) published results for a full scale production vehicle in the Pininfarina windtunnel. Thus, the measurements could be performed at a realistic Reynolds number of 1.2×10^7 but the Strouhal number of the flow excitation was limited to $St = 0.01 - 0.1$. However, due to the limited size of the wind tunnel and the deflection of the flow by simply blocking one side of the nozzle, questions arise concerning the homogeneity of the flow and, as a consequence, the comparability with realalistic flow conditions. Based on this setup, Schrefl (2008) could show that the side force was overestimated by quasi-steady approximation throughout the investigated Strouhal range while this was only the case for the yaw moment up to a Strouhal number of $St = 0.08$. Above $St = 0.08$ yaw moment admittance increases reaching a maximum of approximately 1.4 at $St = 0.1$. Contradicting the findings of Schröck et al. (2009), Schrefl (2008) reports that admittance of side force also increases towards $St = 0.1$. Schrefl (2008), however, notes that flow quality deteriorates at higher frequencies. Surprisingly, for many of the before mentioned investigations, for example Schrefl (2008), Schröck et al. (2009) and Bearman and Mullarkey (1994), admittance does not tend towards unity for frequencies approaching zero. Schröck et al. (2009) argues that for low frequencies the coherence of wind excitation and resulting aerodynamic loads is very low and therefore the resulting admittance function is not valid for frequencies approaching zero.

Rotatory Model Motion. The second approach of applying a rotatory or translatory motion to the investigated vehicle was followed by, for example, Garry and Cooper (1986), Passmore and Mansor (2006), Mansor and Passmore (2008) and Guilmineau and Chometon (2008). Garry and Cooper (1986) identified a time delay in side force and yaw moment when rotating a model around its vertical axis at a Reynolds number of 4.83×10^5. However, no further information is given regarding the accuracy and reproducibility of the determination of the aerodynamic loads. Passmore and Mansor (2006) and Mansor and Passmore (2008) estimated the aerodynamic loads of an oscillating model by calculating the aerodynamic stiffness and damping factor from the transient rotatory motion. Measurements were carried out for a 15% Davis model with different slant angles at Reynolds numbers of 4.3×10^5 to 1.7×10^6 and Strouhal numbers of approximately 0.02 to 0.23. The results showed very large fluctuations of the unsteady magnification ranging from unity to 4.0 depending on slant angle and Strouhal number which rises concern about the reproducibility and accuracy of the setup. In contrast to the before mentioned investigations Passmore and Mansor stated that both unsteady side force and yaw moment were underestimated by quasi-steady approximation. Guilmineau and Chometon (2008) performed pressure measurements on an oscillating generic body resembling the front of a high speed train at a Reynolds number of 0.9×10^6 and a Strouhal number of 0.07. They identified a hysteresis effect for pressure taps located towards the rear of the model.

Translatory Model Motion. Kobayashi and Yamada (1988) propelled generic box-type geometries of 1/10 scale along the nozzle of a wind tunnel. The setup only permitted model velocities of 7 m/s which together with the wind tunnel velocity of 4 m/s led to yaw angles of 30°. Although the Reynolds number was very low, Kobayashi and Yamada could show that on entering into the crosswind a significant overshoot in yaw moment occurred. This overshoot was caused by a delayed adjustment of the flow on the leeward side to the sudden change of the yaw angle. Kobayashi and Yamada (1988) report that approximately 4 model lengths are required for the leeward flow to reach steady state. Macklin et al. (1997) used a very similar setup to investigate the behavior of generic sedan, fastback and station wagon geometries. The results were published for a vehicle speed of 12 m/s and yaw angles of 0° to 45°, which correspond to Reynolds numbers of 3.4×10^5 to 4.7×10^5. Summarizing the results, Macklin et al. (1997) concluded that for yaw angles below 15° static data generally gave a conservative estimate of the unsteady forces and moments. However, for the sedan the unsteady yaw moment was larger than steady-state results even for lower yaw angles.

Numerical Investigations. Compared to experimental approaches, numerical studies usually investigate singular gust events instead of continuous excitations which is due to the limited computational resources. Demuth and Buck (2006) suggested using a generic sinusoidal gust as inflow boundary condition in order to study unsteady aerodynamic effects. Thus, the yaw angle was continuously varied from 0° to 6° and back to 0° over a period of 1s. Analyzing the impact on aerodynamic loads for a full scale sedan at 140 km/h and 200 km/h, they observed a significant undershoot in yaw moment at the end of the gust before reaching its initial level again. This undershoot is attributed to forces acting on the rear of the vehicle.

Tsubokura et al. (2009) investigated the impact of a stepwise change of yaw angle from 0° to 30° at a Reynolds number of 2.9×10^5 for a realistic but simplified station wagon. In particular, they reported a significant over- and undershoot for yaw and roll moment while side force converged continuously towards the steady-state level. Steady-state is reached after more than three flow passes. Similar to Kobayashi and Yamada (1988), Tsubokura et al. (2009) identify a delayed reaction of the leeward flow as main reason for the differences between unsteady and quasi-steady loads. Furthermore, Tsubokura et al. (2009) investigated aerodynamic loads during a pitching motion of the vehicle. The resulting aerodynamic pitch moment showed a time delay as well as a variation in amplitude.

Favre (2009) used a similar setup as Demuth and Buck (2006) and Tsubokura et al. (2009) but in addition to a sinusoidal function he mainly used trapezoidal functions for the variation of yaw angle over time which was inspired by the experiments done by Chadwick et al. (2001). Like in Tsubokura et al. (2009) the simulations were run at low Reynolds numbers of 2.0×10^6 and very large yaw angles of 20°. For this study, Favre (2009) used the generic squareback Windsor model which resembles a one-box design with a strongly inclined wind screen. The gradients of the baseline trapezoidal gust correspond to 1.5 model lengths or a Strouhal number of 0.33. Favre (2009) reported a significant overshoot in yaw moment and a delayed convergence of side force and roll moment towards the steady-state level. In addition, large variations were also observed for the three remaining components drag and lift force as well as pitching moment. Flow visualization identified a delayed reaction of the flow field and thus surface pressures on the leeward side. For a gust with steeper gradients corresponding to a Strouhal number of 0.5, larger overshoots occurred, in particular for the yaw moment. In contrast to the other results presented in this section, a sinusoidal gust with a Strouhal number of 0.1 did not show significant differences between unsteady and quasi-steady side force, roll and yaw moment. Drag and pitching moment, however, were still affected. In Favre and Efraimsson (2010), they compared the aerodynamic loads for three different rear screen angles of 0° (standard squareback model), 10° and 35° using a trapezoidal gust. Time histories for the yaw moment showed that the overshoot was most pronounced for the 0° squareback model while the absolute value of yaw moment peak was smaller than for the two other variants.

Guilmineau and Chometon (2008) also performed numerical simulations of the experimental setup described above which was based on a rotatory model motion. In comparison with the experiment the simulations also allowed the analysis of aerodynamic loads and the flow field. Guilmineau and Chometon (2008) reported large hysteresis effects for drag, side force and yaw moment. In the published graphs a negative time delay can be observed for the side force and a positive time delay for the yaw moment. While the unsteady amplitude of side force is only slightly larger than quasi-steady approximation, unsteady yaw moment shows an increase in amplitude of approximately 20 - 25% for a model motion ±30° at 2 Hz. For a model motion of ±10° at 2 Hz the hysteresis effects were still present while the overshoot was not as pronounced. Analyzing the wake flow Guilmineau and Chometon (2008) identified two counter-rotating vortices that react with a time delay to the change of yaw angle. As described by Gohlke et al. (2007) these two vortices form due to the flow separation at the upper and lower leeward side at high yaw angle.

Passing Maneuvers. A very thorough analysis of the aerodynamics during passing maneuvers was given by Schrefl (2008) who carried out quasi-steady wind tunnel tests with 40% scale models as well as road tests of a car overtaking a truck. Schrefl (2008) describes the typical behavior of side force and yaw moments that first pull and turn the car towards the truck which is then followed by an inversion pushing and turning the car away from the truck. During the first part of the maneuver the behavior is dominated by the contraction of the flow between the two vehicles which causes an acceleration of the flow and decreased pressures. On reaching the front of the overtaken truck the car enters the region of pressure build-up in front of the truck which increases the pressure on the side of the car facing the truck. Furthermore, Schrefl (2008) reported that quasi-steady approximations of side force and yaw moment underestimate the actual unsteady loads. These results were confirmed by Puff (2010) who investigated a similar car truck passing maneuver numerically. Puff (2010) reported that the flow phenomena described by Schrefl (2008) still dominate the aerodynamics when switching from quasi-steady to unsteady analysis.

Summarizing the important aspects it can be stated that:

- Most investigations were carried out at unrealistic Reynolds and Strouhal numbers as well as at unrealistically large yaw angles.
- Depending on model geometry and experimental or numerical setup, conclusions regarding unsteady aerodynamic loads vary largely and in most cases lack of a physical explanation for the observed aerodynamic behavior. However, most recent studies (Demuth and Buck (2006), Favre (2009), Schrefl (2008), Tsubokura et al. (2009), Chadwick et al. (2001)) agree that, among the aerodynamic loads directly influencing crosswind stability, unsteady side force is equal or smaller than quasi-steady approximation while an increase in amplitude occurs for the yaw moment. Results regarding roll moment are seldomly reported and vary largely.
- For large yaw angles above 15°, differences between unsteady and quasi-steady loads are caused by a delayed reaction of the separated flow region on the leeward side.
- The aerodynamic behavior of production cars and the underlying flow phenomena during crosswind gusts are not known.
- Aerodynamics of passing maneuvers are well described in general. Sensitivities to geometrical variations are not known.

Chapter 3

Aim of Work

As laid out in the preceding chapter, in order to optimize vehicle crosswind stability there is a need to understand the aerodynamic behavior of passenger cars under time-dependent flow conditions at realistic Reynolds and Strouhal numbers as well as realistic yaw angles. Thus, the aim of this work is:

- Determination of unsteady aerodynamic loads of realistic vehicle geometries under time-dependent flow conditions.
- Identification of unsteady aerodynamic phenomena and underlying flow mechanisms.
- Analysis of sensitivities to gust and geometrical parameters.

This investigation can be divided into two parts. The first part (Chap. 5) focuses on identifying, understanding and verifying unsteady aerodynamic phenomena. To this end, first numerical simulations are carried out with a generic gust, which allows to characterize the variations in aerodynamic loads and to identify unsteady flow phenomena (Chap. 5.1). Based on these findings a scheme of the underlying mechanism is sketched (Chap. 5.2). The identified unsteady phenomena are then verified experimentally (Chap. 5.3). In the second part (Chap. 6), the influence of gust parameters (Chap. 6.1) and the vehicle geometry (Chap. 6.2 and Chap. 6.3) on the identified unsteady phenomena is investigated. The methodology of the numerical and experimental investigation used in these two parts is described in Chap. 4.

It has to be pointed out that this work focuses on developing a broad qualitative understanding of the unsteady aerodynamic behavior rather than providing quantitative results for few selected gust events. Since little is known about occurring unsteady phenomena, a very high level of accuracy, which could for example be obtained by reducing the smallest cell size, is given less priority than the possibility to investigate a broad range of gusts and geometries.

Chapter 4

Methodology

With the focus being set on developing an understanding of the unsteady aerodynamic behavior in gusty crosswind, it was decided to primarily use CFD due to its capabilities regarding the analysis of the flow field. Instead of investigating a real-world gust that covers a broad frequency spectrum, gust events are modeled as a sinusoidal variation of the yaw angle. Using a singular frequency allows to isolate and analyze the reaction of the flow field to a change of the yaw angle. Some recent experimental setups (compare for example Schröck et al. (2009)) are capable of simulating frequency spectra in the wind tunnel that are similar to those experienced in gusty crosswind conditions. This allows assessing the overall behavior of a vehicle. However, with this approach it is difficult to identify and understand the underlying unsteady flow mechanisms. Obviously, understanding these underlying mechanisms is key to an optimization of crosswind stability.

Hence, in the first part of this investigation the aerodynamics of a BMW upper midsize sedan are analyzed numerically for a singular, generic gust event. The gust event is modeled as a sinusoidal crosswind pulse that is transported through the simulation volume and, hence, gradually passes over the vehicle. By analyzing the aerodynamic loads, surface pressures and the flow field, unsteady phenomena are identified at the rear of the vehicle and a working mechanism is proposed. The first part of this investigation is concluded by an experimental verification of the identified unsteady phenomena. The gust event is again modeled as a sinusoidal variation of the yaw angle which is obtained by rotating a 50% scale model around its vertical axis in the free stream flow of a wind tunnel. For this experimental investigation a realistic, joint research geometry, called DrivAer vehicle, is used. The numerical results are verified experimentally using the resulting unsteady aerodynamic loads as well as measurements of surface pressure and flow velocity.

In the second part, first a parameter study of the crosswind gust is carried out, again using the numerical approach. In this study the parameters ‘number of peaks’, ‘vehicle speed’, ‘gust frequency’, ‘gust amplitude’ as well as ‘initial yaw angle’ are varied and their influence on the unsteady behavior is analyzed. Then, the numerical approach is applied to different vehicle types including sedan, fastback and station wagon of the BMW and DrivAer vehicle. Finally, the influence of geometry modifications is investigated for the DrivAer sedan.

In the following, the incoming flow conditions of the considered, generic gusts are defined (Chap. 4.1), followed by a detailed description of the numerical and experimental investigations (Chap. 4.2 and Chap. 4.3).

4.1 Generic Incoming Flow Conditions

Standard Gust. Based on the results of Wojciak et al. (2010), the standard generic gust referred to in the following is defined as a sinusoidal variation of the yaw angle ranging from $-3°$ to $+3°$ at a frequency of $f = 1\,\text{Hz}$ and a vehicle speed of $U = 140\,\text{km/h}$. An amplitude of 6° and a gust frequency of 1 Hz correspond to the respective maxima in probability of occurrence as measured by Wojciak et al. (2010). A symmetric variation of the yaw angle was chosen in order to include zero-crossings. Variations in x-velocity, as observed by Wojciak et al. (2010), are disregarded for the numerical investigations. Irrespective of the numerical modeling of the wind gust it can be assumed that the small relative variations in x-velocity only have a minor impact on the flow field. For the numerical simulations the axial velocity V_x is therefore always kept at a constant value while the change in yaw angle is obtained by varying the lateral velocity V_y accordingly. Exemplarily, in Fig. 4.1a a single-peak standard gust is shown.

(a) Numerical Gust

(b) Experimental Gust

Figure 4.1: Flow conditions for (a) numerical and (b) experimental standard gust.

As described later different vehicle geometries are used for the numerical investigations which can be divided into two groups of reference lengths, i.e. vehicle lengths L and wheelbases L_{WB}. For this standard gust, the Reynolds number is $Re = 1.25 \times 10^7$ and the Strouhal number is $St = 0.125$ for the BMW vehicles. For the shorter DrivAer vehicles the Reynolds number is slightly smaller at $Re = 1.19 \times 10^7$ while the Strouhal number is $St = 0.119$.

Experimental Flow Conditions. For the experimental investigation with a 50% scale model, the excitation frequency and wind speed need to be scaled in order to satisfy the Reynolds and Strouhal similarity which would result in $U = 280\,\text{km/h}$ and $f = 4\,\text{Hz}$. However, at these velocity and frequency levels the aerodynamic and inertial loads increase significantly and hence limit the maximum amplitude of yawing motion for the selected experimental setup. Therefore, in order to improve testing procedures, a free stream velocity of $U = 210\,\mathrm{km/h}$ and a frequency of $f = 2\,\mathrm{Hz}$ is chosen. This results in a Reynolds number of $Re = 0.89 \times 10^7$ and a Strouhal number of $St = 0.08$ for the 50% DrivAer model which are only slightly smaller than the original values. Test results for $U = 280\,\mathrm{km/h}$ were published in Wojciak et al. (2011). While in the first part of the investigation a single-peak gust is used, a continuous sinusoidal function is applied for the experimental verification. Furthermore, due to the experimental setup where the model is rotated around its vertical axis the velocity magnitude, which is essentially the free stream velocity of the wind tunnel, is kept constant while both x- and y-velocity vary according to the yaw angle. However, variations in x-velocity are very small at about 1% of the free stream velocity. The experimental flow conditions are shown in Fig. 4.1b. The rotation of the model around its z-axis causes additional velocity components in x- and y-direction which are proportional to the yaw rate. However, the velocity vector points in opposite directions at the front and the rear of the model. Hence, the actual yaw angle differs depending on the position. As already shown by Watkins et al. (1992), superposing the velocities due to the yaw angle and the velocities due to the yaw rate results in a phase shift for all points that do not lie on the vertical axis of rotation. The time shift is positive for the front and negative for the rear of the vehicle which means that the vehicle enters the gust with the rear end first, compare Fig. 4.2. Therefore, the time-dependent flow conditions as seen by the model do not perfectly replicate a real-world gust and the numerical setup. However, as already pointed out before and as it will be shown later, it can be assumed that these differences between numerical and experimental setup have a minor impact on the flow field compared to the dominating effect of the change of yaw angle.

Turbulence Intensity. Free stream turbulence intensity, not including the flow variation due to the gust, is kept at very low levels of $Tu = 0.5\%$ for the numerical simulations and $Tu < 0.5\%$ for the experiment. Although, these turbulence levels do not correspond to real world measurements (compare Wojciak et al. (2010)), low turbulence intensities reduce the noise and allow for a clearer analysis of the relevant time-scales.

Boundary Layer. Based on the results of Wojciak et al. (2010), the boundary layer thickness during gust events can be assumed to be less than 250 mm. However, since a more precise definition of the boundary layer thickness or of its profile is not available, the variation of the oncoming flow above the ground is set to a simple block profile. To this end, the wind tunnel boundary layer system, consisting of a boundary layer scoop and suction system, is used in the experiment. Below 50 mm the velocity profile differs by less than 1% from a perfect block-type profile, compare Schäufele (2010). For the numerical simulations a negligible boundary layer thickness of 10 mm is observed, which is due to the applied sliding wall boundary condition at the floor, as will be described in Chap. 4.2.2.

Variation of Gust Parameters. In the last part of this work, gust parameters are varied to cover the whole range of relevant gust events. First the number of peaks is varied, ranging from half an oscillation, which is essentially a sinusoidal step, to 5

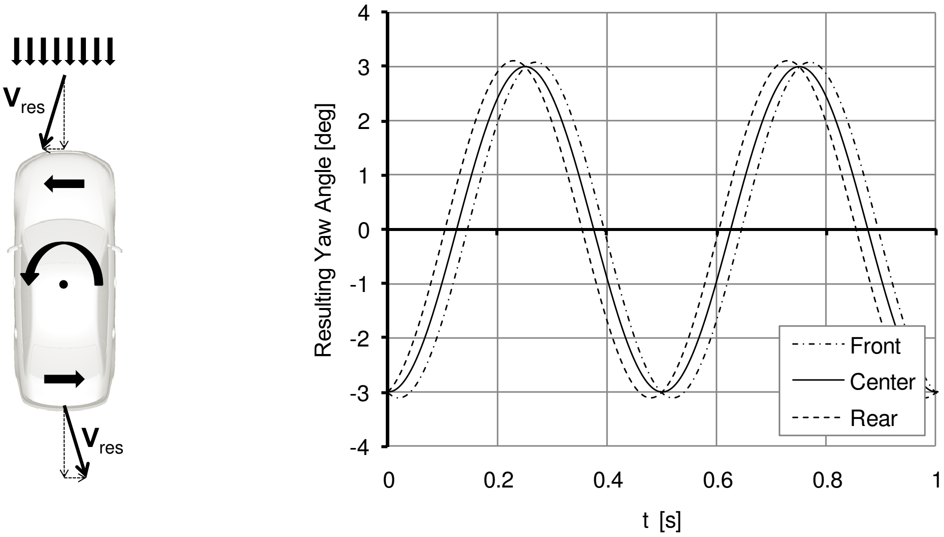

(a) (b)

Figure 4.2: (a) Schematic view of the resulting velocity vectors at the front and the rear of the vehicle due to the model rotation. (b) Comparison of the yaw angle evolution at the front, the center and the rear of the model.

consecutive oscillations. The gust frequency is varied from 0.25 Hz to 4 Hz and the vehicle speed from 70 km/h to 220 km/h. The yaw amplitude, which is measured as absolute difference between minimum and maximum yaw angles, ranges from 3° to 60° including different initial yaw angles. The corresponding Reynolds and Strouhal numbers are summarized in Table 4.1 where the reference length of the BMW sedan is used.

	Standard Gust	Variation of Frequency	Variation of Amplitude	Variation of Vehicle Speed
Frequency [Hz]	1	**0.25 - 4**	1	1
Amplitude [deg]	6	6	**3 - 60**	6
Vehicle Speed [km/h]	140	140	140	**70 - 220**
Reynolds Number [$\times 10^7$]	1.2	1.2	1.2	**0.63 - 1.96**
Strouhal Number [1]	0.12	**0.03 - 0.50**	0.12	**0.08 - 0.25**

Table 4.1: Summary of investigated gust parameters and corresponding Reynolds and Strouhal numbers.

4.2 Numerical Simulation

The numerical approach used in both parts of this study is described in detail in the following. After a brief overview of the numerical code (Chap. 4.2.1), the implementation of constant crosswind as well as of crosswind gusts is presented (Chap. 4.2.2). This is followed by a description of the vehicle geometries (Chap. 4.2.3) and the general setup (Chap. 4.2.4). Since not all of the applied post-processing methods are commonly known, they are presented thereafter (Chap. 4.2.5). Finally, the accuracy and reproducibility of the results are discussed (Chap. 4.2.6).

4.2.1 Numerical Code

For all numerical calculations the Lattice-Boltzmann code PowerFLOW 4.1 is used. The solver is based on the Lattice-Boltzmann approach as presented in Annex A.1 and uses a threedimensional lattice consisting of 19 discrete velocities. Furthermore, the code makes use of a two-equation k-ϵ-RNG turbulence model and a turbulent wall model, which are both described in Annex A.2.

The code and typical setups have been extensively validated for time-averaged results. Fares (2006), for example, compared surface pressures and velocity profiles for the Ahmed body with experimental results of Ahmed et al. (1984). Schäufele (2010) compared aerodynamic loads and surface pressures for realistic vehicle geometries.

Unsteady results have for example been compared to experimental data by Li et al. (2004) and Sims-Williams and Duncan (2003). Li et al. (2004) studied the flow past an impulsively started cylinder. Using this academic case they confirmed the time-accuracy of PowerFLOW. Sims-Williams and Duncan (2003) investigated the wake topology and total pressure fluctuations behind the Ahmed body and identified symmetrical oscillations of the rear pillar vortices at a Strouhal number of approximately $St = 0.5$. They report that the oscillations are captured in good agreement by both numerics and experiment.

Based on these investigations, it can therefore be assumed that PowerFLOW provides results with a sufficient level of accuracy. Of course, the obtained level of accuracy largely depends on the number of cells invested as well as the level of geometric detail included in the simulation. Furthermore, it can principally be assumed that PowerFLOW is capable of correctly simulating unsteady aerodynamics. Nevertheless, in this work the observed unsteady phenomena (see Chap. 5.1) are verified experimentally as described in Chap. 5.3.

4.2.2 Implementation of Crosswind

The numerical approach is based on the findings of Demuth and Buck (2006). The gust is implemented as a time-dependent velocity boundary condition at the inlet. As defined above, the x-velocity is kept constant while the y-velocity is varied according to the desired change of yaw angle. In order to ensure a homogeneous convection of the gust through the simulation volume, periodic boundary conditions are used at the side walls. The road is modeled by applying a sliding wall boundary condition to the floor which corresponds to the vehicle velocity vector. Hence, inlet and floor velocity differ in y-direction. A standard pressure boundary condition is used at the outlet of the simulation volume and a free-slip boundary condition at its roof. A schematic view of the setup is shown in Fig. 4.3a. In Fig. 4.4 the evolution of the lateral velocity is shown in a slice parallel to the ground for three instants before, at the peak and after the gust. Fluid probes placed at the inlet and in the far field above the car prove that the gust is not significantly altered before reaching the vehicle (Fig. 4.5).

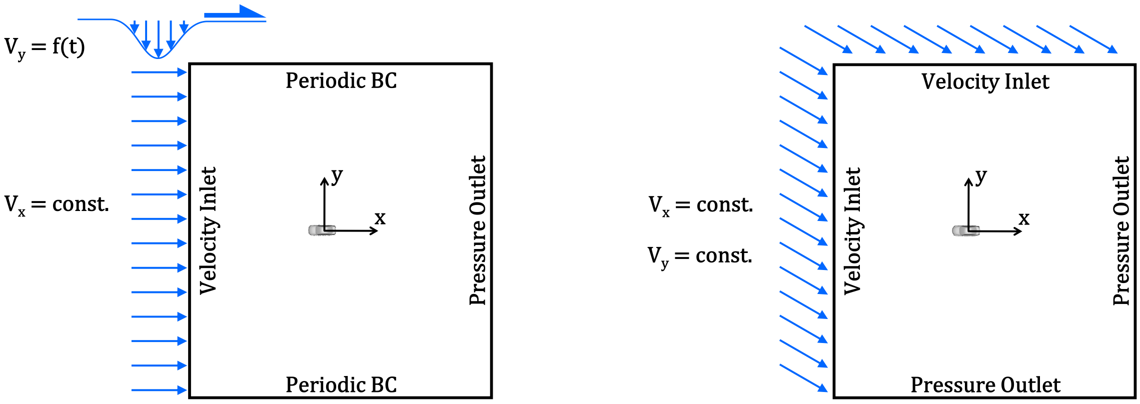

(a) Crosswind Gust (b) Constant Crosswind

Figure 4.3: Numerical Setup for (a) crosswind gust and (b) constant crosswind.

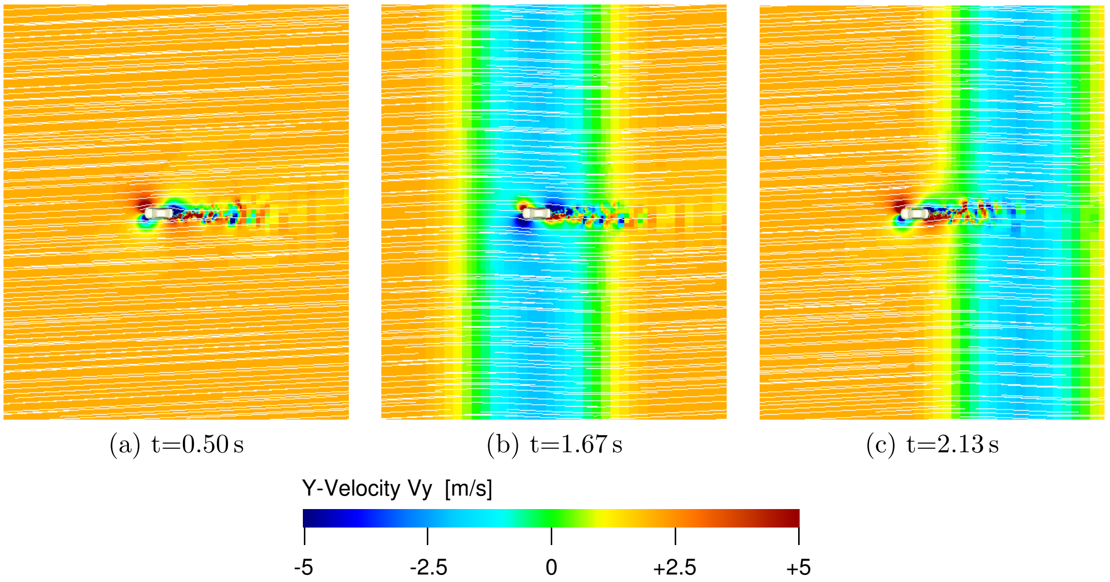
(a) t=0.50 s (b) t=1.67 s (c) t=2.13 s

Figure 4.4: Transport of the gust through the simulation volume visualized in a slice parallel to the ground at three different points in time.

Implementing the crosswind gust via a velocity variation at the inlet results in a distortion in the flow field that gradually passes over the vehicle. Early investigations showed that a gust that captures the whole vehicle instantaneously can be modeled using a coordinate transformation. Results obtained with this alternative method are presented in Theissen et al. (2010). In the following only the first method is applied as it is considered to be more realistic, compare Wojciak et al. (2010).

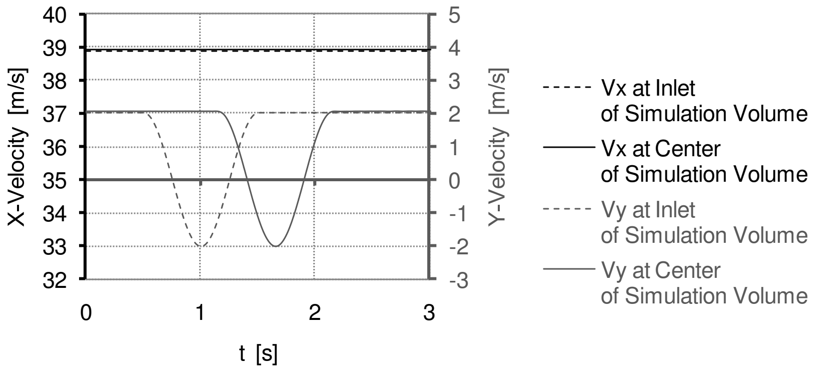

Figure 4.5: Variation of x- and y-velocity during a singular gust event captured by fluid probes placed at the inlet and at the center of the simulation volume.

In order to provide averaged steady-state results for comparison with the unsteady results, additional constant yaw simulations are carried out. Instead of rotating the vehicle in the simulation volume, the boundary conditions are modified in order to create a yawed constant flow. This permits a direct comparison of steady-state and gust results without coordinate transformations. In comparison with the gust setup, constant velocity boundary conditions are used at the inlet and the upstream side wall, while pressure boundary conditions are applied to the outlet and the downstream side wall, see Fig. 4.3b. Wherever possible, additional constant yaw simulations are avoided by extracting the steady-state data directly from the gust simulations before or after the arrival of the gust. All simulations are seeded from a coarse pre-run with a smallest cell size of 24 mm.

4.2.3 Vehicle Geometries

In the first part of this work (Chap. 5.1), the identification of possible unsteady phenomena, a detailed version of a BMW upper midsize sedan is used. The same geometry is also used for the sensitivity study of gust parameters in the second part (Chap. 6.1). The geometry features a realistic upper and under body including for example brake discs, suspension and exhaust parts (see Fig. 4.6). In favor of practical simulation runtimes underhood flows are not considered. In order to estimate the influence of cooling flows, preliminary studies with extremely detailed vehicle geometries including underhood flows were carried out, see Theissen et al. (2010). Compared to the mock-up geometries, the characteristic flow topology at the rear end and the fundamental pressure distribution on the sides of the vehicles are not altered. Furthermore, for the investigated vehicle geometries the unsteady phenomena described in Chap. 5.1 as well as the underlying unsteady mechanism described in Chap. 5.2 are not changed. Hence, this confirms that disregarding underhood flows is justified, in particular given the qualitative nature of the aim of this work. However, once the fundamental behavior is understood, the influence of underhood flows should be studied in more detail.

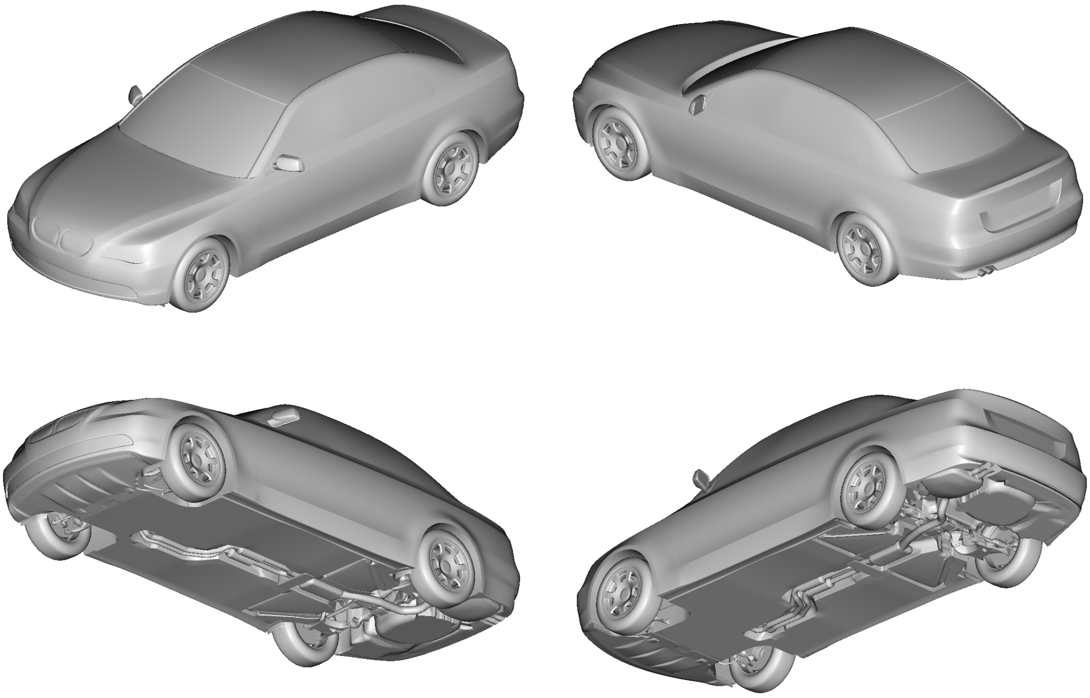

Figure 4.6: Geometry of detailed BMW upper midsize sedan.

As already described above, a comparison between the three vehicle types sedan, fastback and station wagon is presented in the second part, Chap. 6.2. For this analysis, the same vehicle geometries as in Schäufele (2010) are used, which differ from the above described BMW sedan regarding the front spoiler, a different styling of the rims, rear light tear-off edges and a modified underbody at the rear axle. Additionally, the DrivAer body[1] (see Fig. 4.7), which is a new joint-research, midsize vehicle geometry providing the three rear end types sedan, fastback and station wagon, is used (for details see Heft et al. (2011)). However, since the final geometries were not yet available, a preliminary version was employed instead, which has a more rounded rear end.

The characteristic lengths and cross sections of all vehicles are summarized in Table 4.2. The DrivAer vehicles are slightly smaller than the BMW vehicles regarding overall length, wheelbase and cross-section. For crosswind conditions the cross-section in y-direction is an important additional parameter. As expected, it is largest for the station wagon and smallest for the sedan vehicles. However, the two fastback vehicles differ regarding their y-cross-section in comparison to the corresponding sedan geometry. While the BMW fastback has a higher rear end resulting in a larger

---

[1] The DrivAer geometries can be downloaded at: http://www.aer.mw.tum.de/en/research-groups/automotive/drivaer/

y-cross-section, the DrivAer fastback has a low rear end corresponding to the sedan geometry. The side views of all vehicle types are shown in Fig 4.8.

Vehicle	Length [m]	Wheelbase [m]	Cross-Section X-Direction [m^2]	Cross-Section Y-Direction [m^2]
BMW Sedan	4.84	2.89	2.26	4.92
BMW Fastback	4.84	2.89	2.26	5.01
BMW Station Wagon	4.84	2.89	2.26	5.13
DrivAer Sedan	4.61	2.79	2.17	4.56
DrivAer Fastback	4.61	2.79	2.17	4.57
DrivAer Station Wagon	4.61	2.79	2.17	4.69

Table 4.2: Summary of characteristic lengths and cross sections of the investigated vehicles.

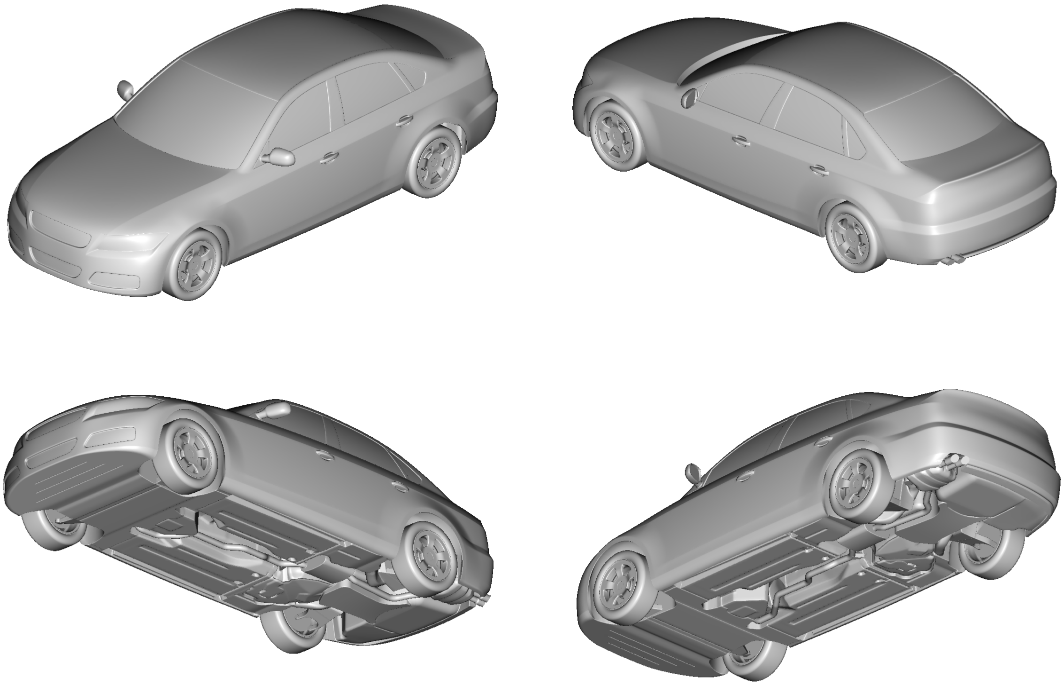

Figure 4.7: Geometry of DrivAer midsize sedan.

Finally, the DrivAer sedan is also used for analyzing the influence of geometrical modifications. The investigated variants are presented in Chap. 6.3.

4.2.4 Numerical Setup

The general layout of the numerical setup is based on best practices proposed by EXA (2008) and the configuration of Demuth and Buck (2006).

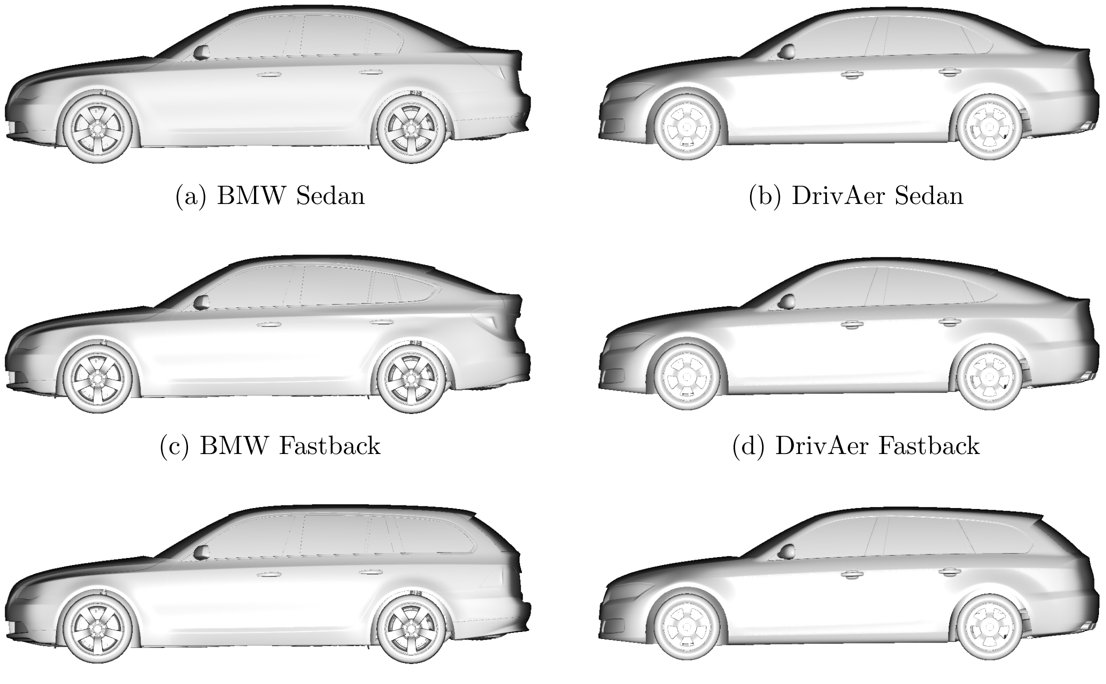
(a) BMW Sedan
(b) DrivAer Sedan
(c) BMW Fastback
(d) DrivAer Fastback
(e) BMW Station Wagon
(f) DrivAer Station Wagon

Figure 4.8: Side views of BMW and DrivAer vehicle types.

Simulation Volume. The simulation volume extends approximately 5 vehicle lengths upstream and 6 downstream. Furthermore, the cross-section of the simulation volume is chosen to provide a blockage of 0.1%. This results in a spacing of 6 vehicle lengths to each side and 8 vehicle lengths above the vehicle.

Grid Refinement. Cell refinement regions are defined around the vehicle via boxes and offset regions. The two most inner regions are created via offsets of the vehicle geometry (see Fig. 4.9), the outer 5 regions via simple boxes as shown in Fig. 4.10. Between two refinement levels the cell size is always varied by a factor of 2. A minimum cell size of 6 mm is chosen which results in a maximum cell size of 768 mm at the outer boundaries. For the BMW and the DrivAer vehicle geometries this results in a total number of cells of 36 Mio. and 39 Mio., respectively.

Grid Dependancy. The influence of the mesh resolution was investigated beforehand in order to determine the optimal tradeoff between accuracy and simulation runtimes. The cell size in the most inner refinement zone was varied between 3 mm and 12 mm in 3 mm steps. In addition, the cell size in a box enclosing the vehicle, which spans approximately 1.3 times the vehicles width, height and length, was varied between 6 mm, 9 mm and 12 mm. For all investigated grids, the characteristic pressure distribution and flow topology as well as the fundamental unsteady behavior were similar. Given the aim of this work, a mesh resolution of 6 mm was chosen, as a smaller minimum cell size would have increased simulation runtimes significantly without changing the characteristic behavior. On the other hand, a smallest cell size of 9 mm or 12 mm was considered too large to correctly capture the expected differences of the geometry variations in Chap. 6.3.

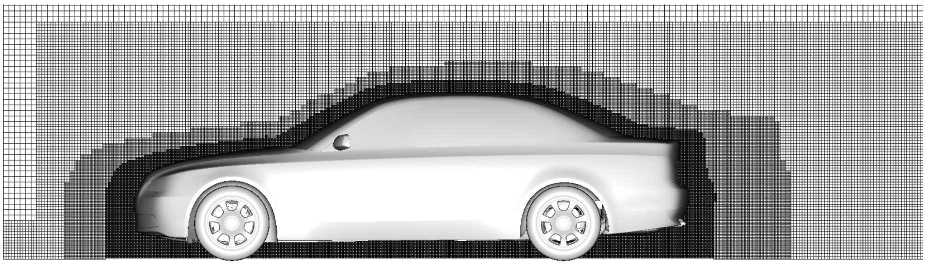

(a) Side view

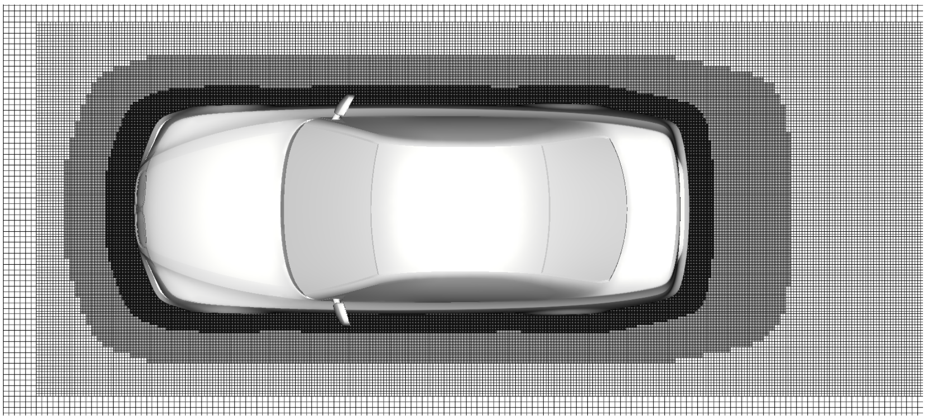

(b) Top view

Figure 4.9: Grid refinement in the proximity of the vehicle.

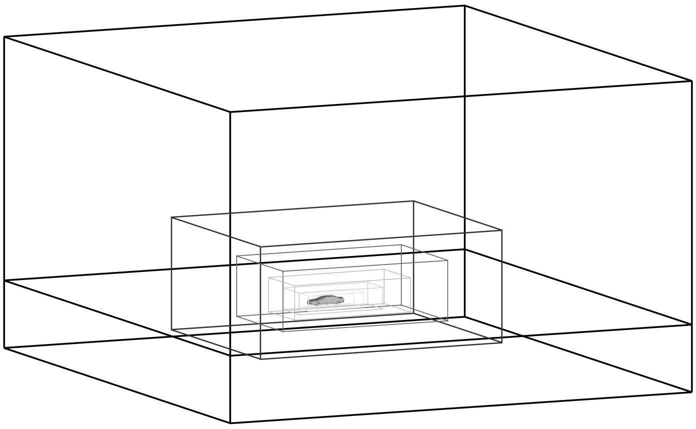

Figure 4.10: Regions of grid refinement.

Wheel Rotation. In all simulations the rotation of the rims is modeled using local rotating reference frames (LRRF) as suggested by Modlinger et al. (2007). Tires and brake discs are modeled using rotating wall boundary conditions.

Output Files. Output files of surface and fluid data are saved with an output frequency of 100 Hz for the BMW vehicles and 50 Hz for the DrivAer vehicles. However, instead of recording a snapshot every 0.01 s and 0.02 s, respectively, simulation data is averaged between two output points and written to file. Additionally, aerodynamic loads per part are saved at a frequency of 1000 Hz.

4.2.5 Post-Processing

Due to the unsteady nature of the gust simulation the post-processing needs to be modified compared to typical cases focusing on drag optimization. In the following, the standardized post-processing routines, which are applied in Chap. 5 and Chap. 6, are described.

Unsteady Aerodynamic Loads. In order to filter out high-frequency oscillations, which are not relevant for vehicle dynamics, the unsteady aerodynamic loads are filtered using a sliding average window of 0.2 s, compare Fig. 4.11. For the same reason, surface and fluid data is averaged over 0.2 s at the positive and negative gust peaks before it is used for visualization. The exact position of the averaging window is determined by the respective minimum or maximum of the filtered yaw moment. The data is not simply averaged around the prescribed gust peaks since the peaks in aerodynamic loads generally occur with a time delay, which varies depending on the vehicle geometry and the gust parameters. Since the yaw moment is considered the most important aerodynamic load, the averaging intervals are therefore defined to capture the peaks in yaw moment. As will be presented in detail later, the peaks occur at different points in time for the other aerodynamic loads. This implies that the chosen averaging interval generally does not perfectly capture the peaks of the other aerodynamic loads.

Quasi-Steady Loads. In order to obtain steady-state data, the unsteady results from constant yaw simulations are averaged as well as the results from gust simulations before and after the arrival of the gust. The averaging intervals for steady-state data have a minimum length of 0.5 s. However, whenever possible an averaging length of 1.0 s is used. In Fig. 4.11 the averaging intervals are shown exemplarily for a standard gust simulation. For a better comparison between steady-state and unsteady loads a quasi-steady approximation is calculated from the steady-state values. This quasi-steady approximation is derived by simply interpolating between minimum and maximum steady-state values according to the theoretical change of yaw angle at the reference point at mid wheelbase. This is, however, only possible for aerodynamic loads that show a linear behavior over the yaw angle. Therefore, quasi-steady curves are only presented for the side force, roll and yaw moment in the following.

Segmentation of the Vehicle Geometry. To analyze the contribution of different vehicle regions the geometry is split into multiple segments. First, the vehicle is divided into front and rear half, followed by a segmentation into six slices as shown

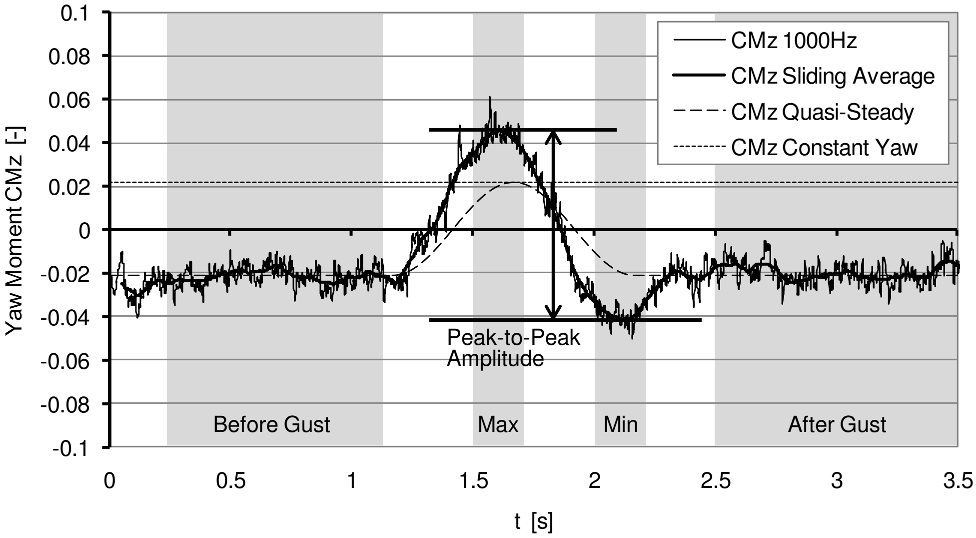

Figure 4.11: Schematic view of averaging intervals.

in Fig. 4.12a. Additionally, the rear of the vehicle is divided into eight segments, left rear door, left C-pillar, left rear wheel and left rear end as well as their counterparts on the right side (Fig. 4.12b). Quasi-steady curves are calculated for each segment using the theoretical change of yaw angle at the center of each division. Thus, the time shift of the yaw variation between the aerodynamic reference point and the center of the segments is captured. The time delay between the front end of the vehicle and the reference point amounts to $dt \approx -0.06\,\mathrm{s}$ at $U = 140\,\mathrm{km/h}$. A similar positive time delay of $dt \approx +0.07\,\mathrm{s}$ occurs between the reference point and the rear end of the vehicle. The characteristic time delays are summarized in Table 4.3. The influence of the delayed impact of the gust due to the length of the vehicle is analyzed in Chap. 5.1.1.

Magnification Factor and Time Delay. Unsteady aerodynamic loads are compared to quasi-steady loads using the magnification factor and time delay. The magnification factor is defined as the ratio of unsteady to quasi-steady peak-to-peak amplitude. As shown in Fig. 4.11, maximum and minimum peak values are derived from the filtered signal, in order to blend out fluctuating high frequency oscillations. A positive time delay is defined as the unsteady signal lagging the quasi-steady signal.

	Time Shift [s] (relative to Moment Reference Point)
Front End of Vehicle	−0.06
Center of Front Half	−0.03
Center of Rear Half	+0.03
Rear End of Vehicle	+0.07

Table 4.3: Time shifts due to delayed impact of crosswind gust.

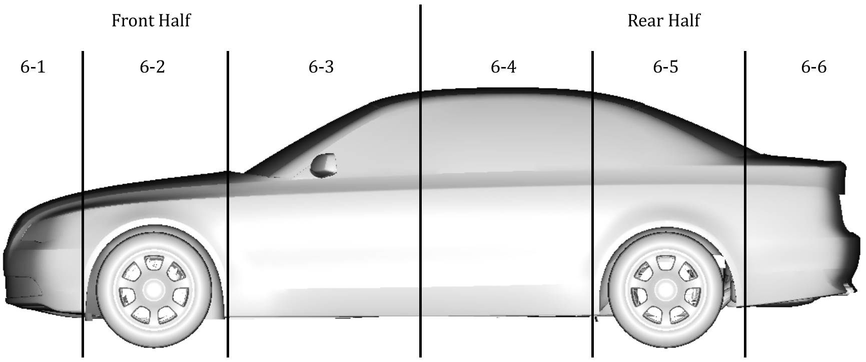

(a) Six Segments

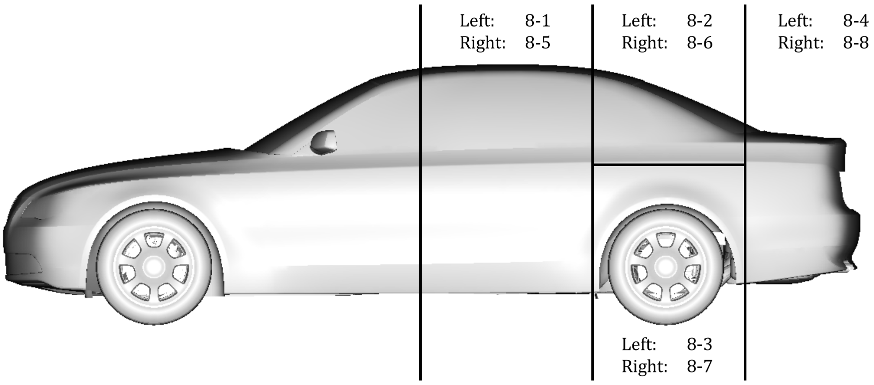

(b) Eight Segments

Figure 4.12: Segmentation of vehicle geometry.

Casediff of Surface Data. Since differences between left and right side are essential to understand the behavior under crosswind, a so-called *"Casediff Left - Right"* is calculated. As the name indicates, the data of the right vehicle side is subtracted from the data of the left side. Hence, for example a positive *"Casediff Left - Right"* pressure value indicates a pressure that is larger on the left than on the right side. Since the geometries are not completely symmetrical in y-direction, *"Casediff Left - Right"* cannot be executed everywhere. Similarly, the differences in averaged surface data between unsteady and steady-state results are calculated (*"Casediff Unsteady - Quasi-Steady"*).

Wake Analysis. In order to understand the evolution of the wake flow during a crosswind gust, the wake flow is analyzed using several control surfaces as shown in Fig. 4.13. Four lateral control surfaces on the left and right rear of the vehicle, which are aligned in x-direction, are used to record the evolution of x-velocity and total pressure. Similarly, two control surfaces in the wake, aligned in y-direction, are used to calculate the evolution of y-velocity. The latter pair of control surfaces is positioned to capture the fluid entering into the wake region. The flow properties are averaged over the control surfaces. Additionally, the evolution of the surface pressure averaged over the area enclosed by the two lateral control surfaces on each side is recorded.

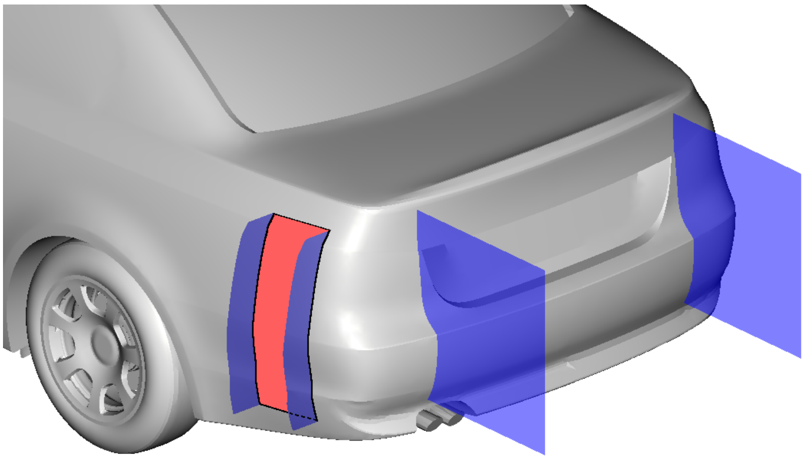

Figure 4.13: Control surfaces at the rear of the BMW sedan.

4.2.6 Reproducibility

Due to the unsteady nature of the flow field around bluff bodies like the geometries used in this study, aerodynamic loads fluctuate for both constant yaw and gust simulations. Depending on which state the flow field and especially the wake flow are in when the gust arrives at the vehicle, peak values may vary. Since PowerFlow, in contrast to typical finite volume codes, is a non-deterministic code, two identically defined simulations will yield results that differ regarding their evolution over time. Hence, while the general behavior persists, resulting peak values vary. Exemplarily, this is shown for the yaw moment in Fig. 4.14 for three identically defined simulations of the standard gust. Therefore, it is necessary to estimate the reproducibility of the numerical results.

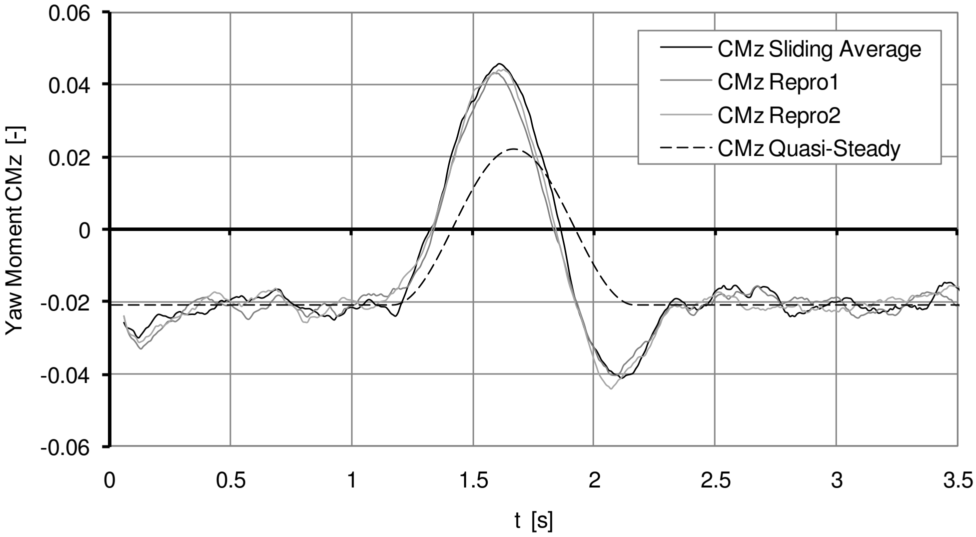

Figure 4.14: Evolution of yaw moment coefficient for three identically defined simulations indicating the level of reproducibility.

Gust Peaks. Due to the fluctuations of the unsteady loads, the amplitude is averaged over several gust peaks when comparing different geometries or gust variants. As explained below, this is necessary in order to improve the reproducibility. In the following, consecutive gust peaks are assumed to be independent events. This assumption is certainly not strictly true, however acceptable for the intended estimation of reproducibility. Simulations with multiple gust peaks show that the standard deviation amounts to 0.008 for C_y and 0.003 for C_{Mx} and C_{Mz}. For a singular peak this leads to a confidence interval of 0.006 for C_{Mx} and C_{Mz} at a confidence level of 95%. In other words, the probability that for a singular peak the resulting value lies in the interval of the actual mean value ±0.006 is 95%. For C_y the confidence interval for a singular peak is 0.016. Compared to steady-state values at a yaw angle of 3°, where $C_y \approx 0.13$ and $C_{Mz} \approx 0.02$, the confidence interval amounts to approximately ±30% of the steady-state level for single-peak gusts.

Since this clearly limits the possibility to evaluate and compare different geometries or gust parameters, gusts with $3\frac{1}{2}$ or 5 peaks are used in these cases. For a gust with $3\frac{1}{2}$ peaks 6 minima and maxima can be evaluated, leading to a confidence interval of 0.002 for C_{Mx} and C_{Mz} and of 0.006 for C_y (see Table 4.4). This corresponds to approximately ±10% of the before-mentioned steady-state values at a yaw angle of 3°. An interval of ±10% is thought to be acceptable in order to evaluate significant geometry modifications or variations of gust parameters, but at the same time has to be kept in mind when interpreting the results.

	C_y	C_{Mx}	C_{Mz}
Constant Yaw Expected Maximum Error (0.5 s Averaging Interval)	±0.003	±0.001	±0.001
Averaged Gust Peaks 95% Confidence Interval ($3\frac{1}{2}$ Peak Gust)	±0.006	±0.002	±0.002

Table 4.4: Summary of expected errors and confidence intervals of numerical results.

Constant Yaw. For constant yaw configurations, a stochastic estimation is not possible since consecutive data samples cannot be assumed to be independent. However, the analysis of data that was gathered over a longer period leads to the assumption that the reproducibility varies by ±0.003 for the side force and ±0.001 for the yaw and roll moment if the data is averaged over 0.5 s.

4.3 Experiment

The aim of the experimental investigation is to verify the identified unsteady phenomena and the proposed mechanism. Since similar unsteady effects have only been touched by few other numerical or experimental investigations, their existence shall be proved experimentally.

Hence, the objective of the experiment is to investigate the following points:

- Gain and phase shift of unsteady side force, roll and yaw moment compared to the quasi-steady approximation.
- Phase shift of the wake flow to a change of the oncoming flow, in particular of the flow entering from the leeward side.
- Unsteady behavior of surface pressures and their contributions to the unsteady side force and yaw moment.

The experiment was developed in a joint effort together with J. Wojciak, see also Wojciak et al. (2011) and Theissen et al. (2011). Extending beyond the scope of this work, the gathered data shall additionally be used for a future comparison between numerical simulation and experiment. Hence, the possibility to replicate the experimental setup and flow conditions numerically needs to be ensured. In the following, first the general approach (Chap. 4.3.1) and the setup of the experiment (Chap. 4.3.2) are explained. The motion of the vehicle model, which is used to simulate the time-dependent incoming flow conditions is described in Chap. 4.3.3. Due to the model motion inertial loads are recorded by the wind tunnel balance in addition to the desired aerodynamic loads. Chap. 4.3.4 presents the determination of inertial and aerodynamic loads. In Chap. 4.3.5 the accuracy of the results is discussed. In order to estimate the influence of the differences between numerical and experimental setup, finally both setups are analyzed numerically (Chap. 4.3.6).

4.3.1 Approach

Given the above mentioned objectives, the time-dependent flow conditions were chosen to be generated by oscillating a vehicle model around its z-axis whilst being exposed to constant flow in a wind tunnel. This provides a reproducible variation of the flow conditions that can also be modeled numerically. Due to the oscillating motion of the model, inertial loads act on the internal balance and need to be separated from the desired aerodynamic loads. As described in Chap. 4.3.4, the model motion and thus the inertial loads are captured using acceleration sensors. The sum of aerodynamic and inertial loads is recorded by a 6-component balance. The aerodynamic loads are finally acquired by subtracting the inertial loads from the total balance loads.

The measurement process first consists of a calibration of the system during the yawing motion but without wind. In this wind-off configuration the transformation of acceleration signals to inertial loads is determined for a fixed combination of oscillation frequency and amplitude. After the calibration, the same model motion is repeated in constant flow and the unsteady aerodynamic loads are determined. The results are averaged over 440 oscillations in order to increase the reproducibility. In addition to the load measurements, the surface pressure at various positions as well as the velocity vector at selected locations in the wake region are recorded. Furthermore, steady-state measurements at constant yaw are performed in order to obtain data for a comparison with the unsteady results.

4.3.2 Setup

4.3.2.1 Wind Tunnel and Hexapod

The experiments were conducted in BMW's Aerolab model wind tunnel featuring a nozzle cross section of $14\,\mathrm{m}^2$ and plenum dimensions of $20\,\mathrm{m} \times 14\,\mathrm{m} \times 11\,\mathrm{m}$. The maximum wind speed in the test section is 280 km/h for the nozzle configuration used for this experiment. The wind tunnel is equipped with a single moving belt of 9 m length and 3.5 m width. Since the rolling road system is not able to rotate at the desired frequency of 2 Hz, the model is lifted by 30 mm in order to prevent contact between the vehicle model and the moving belt. Thus, the measurements of the internal balance are not distorted. Due to the motion of the model the wheels are fixed to the vehicle body and wheel rotation is not included. The model is connected through a strut to a hexapod, which is mounted in the upper plenum above the test section. The hexapod is the central part of the model motion system which allows moving the model by all six degrees of freedom using mechanical actuators. Fig. 4.15 shows a schematic view of the setup including the internal balance, the acceleration sensors and the actuator for the oscillating motion. The overall setup is pictured in Fig. 4.16.

4.3.2.2 Model

For the experiment the same DrivAer sedan geometry is used as for the numerical investigations in Chap. 6.2 and Chap. 6.3. In order to significantly reduce the weight of the model it is designed as an aluminum-laminate construction in 50% scale. In line with the numerical investigations underhood flows are not included. The model has a total length of $L_{ref,Model} = 2.305\,\mathrm{m}$, a wheelbase of $L_{WB,Model} = 1.393\,\mathrm{m}$ and a cross section of $A_{ref,Model} = 0.542\,\mathrm{m}^2$.

4.3.2.3 Measurement Equipment

Balance. A dynamically calibrated 6-component balance is mounted between the strut and the model. The calibration ranges and the typical errors are summarized in Table 4.5 (RUAG (2009)).

Acceleration sensors. Several one-axis capacitance acceleration sensors suitable for a range $< \pm 10g$ with a frequency resolution from static up to 2.7 kHz and a

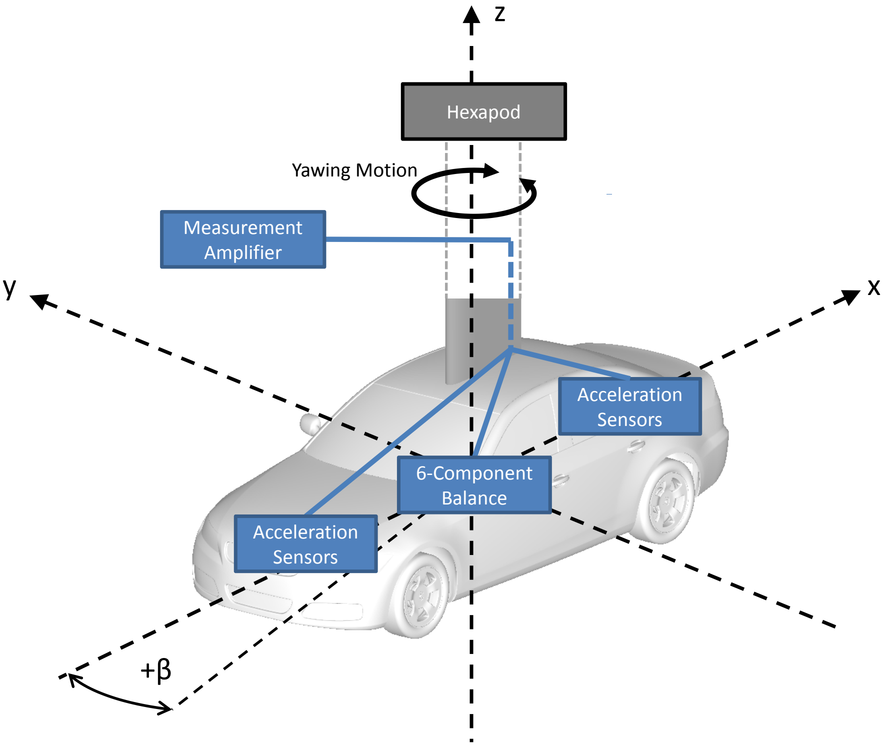

Figure 4.15: Schematic view of the experimental setup.

Figure 4.16: View of the setup in the BMW Aerolab wind tunnel.

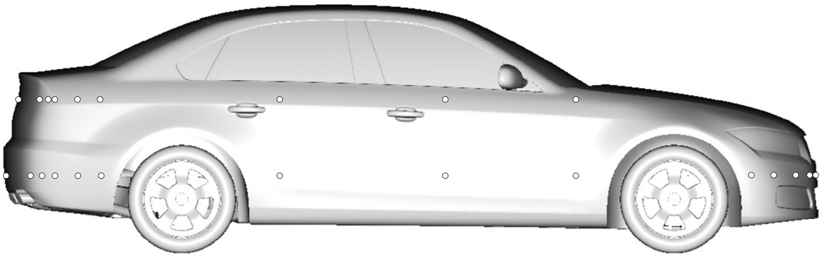

Figure 4.17: Positions of surface pressure sensors.

	Calibration Range [N, Nm]	Typical Error [% of Full Scale Output]
F_x	4000 N	1.3%
F_y	5000 N	0.6%
F_z	8000 N	0.3%
M_x	500 Nm	0.6%
M_y	1200 Nm	0.4%
M_z	700 Nm	0.7%

Table 4.5: Dynamic calibration range and typical errors for the 6-component balance.

transverse sensibility of < 3% (Kistler (2010)) are mounted at different positions of the model rig in order to record the accelerations at these positions.

Pressure sensors. Pressure measurements were taken at a total of 96 positions distributed over the vehicle surface. However, not all of the data is used in this work. The measurement positions referred to in Chap. 5.3 are located on the right side of the model covering z-slices at $z = 65$ mm and $z = 280$ mm, (see Fig. 4.17). Miniature differential pressure transducers (Kulite XT-190 (M)) with a pressure range of ±1 psi are mounted inside the vehicle featuring a typical error of ±0.1% full scale output and a maximum error of ±0.5% full scale output for combined non-linearity, hysteresis and repeatability (see Kulite (2009)). They are screwed into a connector and linked through 40 mm flexible tubing to 20 mm steel pipes (inner diameter = 0.4 mm), which are finally mounted as pressure tappings in the laminate surface. The frequency response of this setup is high enough to guarantee negligible signal damping and phase shifting for frequencies up to 15 Hz.

Hotwire probe. For the measurement of the velocity vector in the free flow field, a hot wire probe (Dantec Type 55R91) is used. The probe has been calibrated in a separate calibration facility for velocities from 3 m/s to 58 m/s and a maximum cone angle of 35°. The calibration was verified by placing the probe into the free flow of the wind tunnel at various velocities between 20 m/s and 66 m/s. 100% of the data could be evaluated by the data reduction software leading to a maximum error of 2 m/s for the mean velocity and 1° for the mean flow angles. The probe is mounted on a traverse with a probe holder, which oscillates at higher flow velocities.

The errors in flow velocity due to probe motion are limited to 1 m/s, as could be proved by initially mounting a tri-axis accelerometer to the probe holder. For a more detailed description of the setup and calibration of the hotwire probe refer to Heuler (2010).

To determine the temporal evolution and a possible time delay of the flow that enters into the wake region from the leeward side, hotwire measurements are conducted in the wake of the model. Using the setup of Heuler (2010) the probe is fixed to the wind tunnel traverse while the model is rotated. In order to obtain the data in the vehicle coordinate system as if the probe was fixed to the vehicle, flow velocities are measured at seven positions that correspond to rotations of 0°, ±1°, ±2° and ±3° (see Fig. 4.18). For the standard 2 Hz 3° yawing motion the data obtained from the seven runs are then averaged periodically and transformed into the vehicle coordinate system. To obtain the evolution of the leeward inflow, the discrete data from the seven measurement positions are interpolated according to the rotation of the model using piecewise cubic splines.

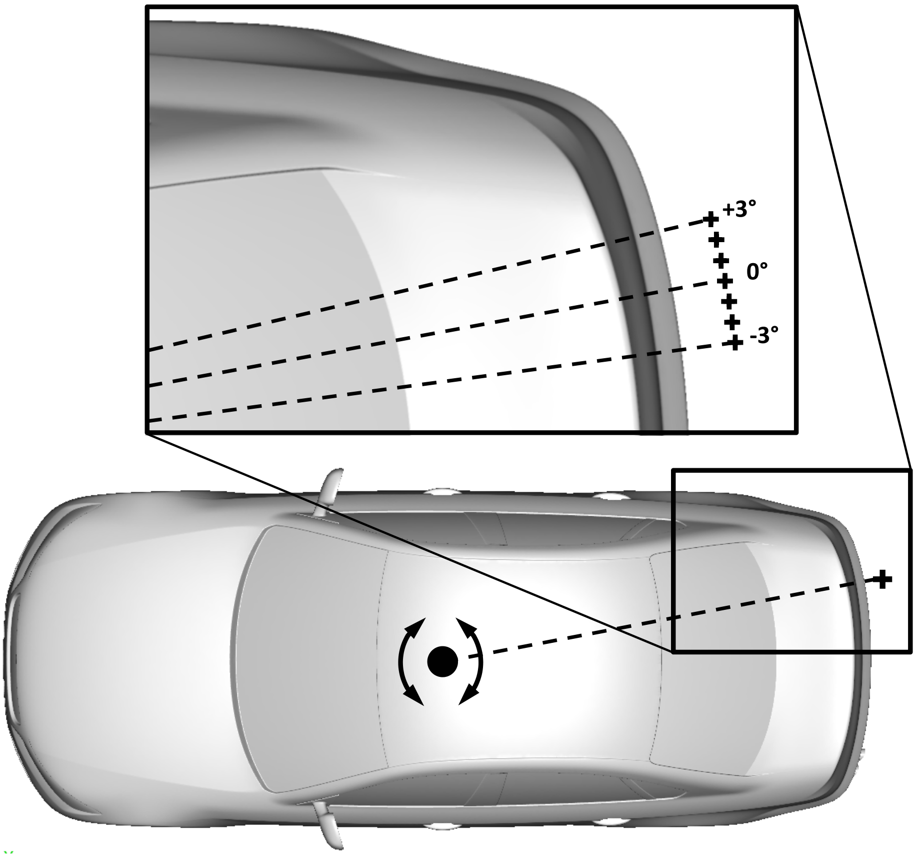

Figure 4.18: Positions of hotwire probe in the wake of the model.

Data recording. The cables of the measurement devices located inside the vehicle model are run through an extension of the strut to a 24 bit amplifier/ADC unit. The maximum cable length is 12 m. The signals are recorded simultaneously and logged at a sampling frequency of 1200 Hz in sets of 120 s for measurements without model motion and 220 s for measurements with model motion. Finally, the resulting aerodynamic loads, surface pressures and flow velocities are 11 Hz low-pass filtered and periodically averaged.

4.3.3 Model Motion

The model motion is a symmetrical sinusoidal oscillation around the vehicle's z-axis. As already defined earlier, in the frame of this work the standard oscillating motion is fixed at a frequency of 2 Hz and an amplitude of ±3°. Similar to the numerical standard gust, a symmetrical oscillation around the starting position at 0°yaw was chosen in order to include zero crossings.

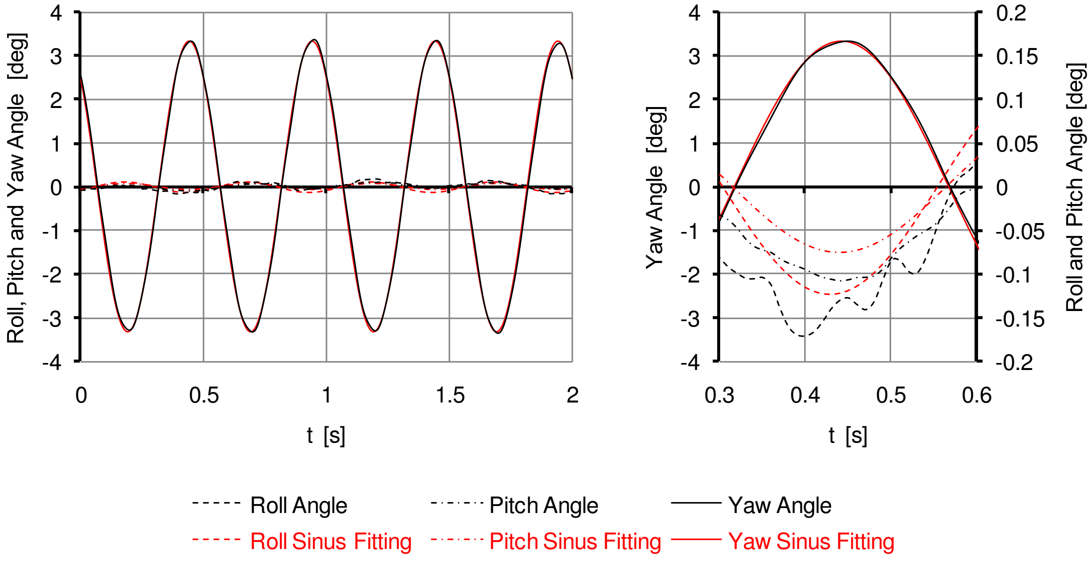

Figure 4.19: Rotatory model motion during 2 Hz 3° oscillation.

The model motion, i.e. the three translatory and three rotatory components, are calculated based on the acceleration signals. The angles of rotation around the x-, y- and z-axis are plotted in Fig. 4.19 for a short time window together with perfect sine curves. Only minor differences can be observed between the angle of z-rotation and the perfect sine curve. In order to evaluate the accuracy and thus the quality of the model motion, the average minimum and maximum as well as the absolute maximum values of the vehicle motion are summarized in Table 4.6 for the standard oscillation over 220 s.

Table 4.6 shows that for x- and y-rotations as well as for x-, y- and z-translations the maximum deviation from zero is small and can be disregarded. For the rotation around the z-axis, which is the prescribed model motion, Table 4.6 confirms the good repeatability and symmetry of the yawing motion indicating a small difference between the maximum und the average peak yaw angles. However, Table 4.6 also illustrates that the real model motion exceeds the prescribed oscillation amplitude of ±3° by 10%. This may be due to a non-ideal control of the hexapod or due to the elasticities of the strut and has to be accounted for when comparing to steady-state results.

	Average Min	Average Max	Absolute Max
Rotation Angle X	-	-	0.2°
Rotation Angle Y	-	-	0.2°
Rotation Angle Z	-3.3°	3.3°	3.5°
Translation X	-	-	1.4 mm
Translation X	-	-	3.9 mm
Translation X	-	-	1.7 mm

Table 4.6: Summary of model motion parameters.

4.3.4 Determination of Inertial Loads

As mentioned previously, the inertial loads are calculated based on the signals recorded by the acceleration sensors. Theoretically, the inertial loads can be easily calculated by multiplying the translational accelerations with the total mass and the rotational accelerations with the respective moment of inertia. Exemplarily, this is shown in Eq. 4.1 for the moment M_z, where $a_{rot,z}$ denotes the rotational acceleration around the z-axis and Θ_{zz} the corresponding moment of inertia.

$$M_z = \Theta_{zz} \cdot a_{rot,z} \tag{4.1}$$

In practice, however, non-linear effects require the use of a transfer function $H(s)$, which is frequency dependent. The transfer function is determined during constant yawing motion without wind and is calculated as the ratio of the Fourier transformations (FFT) of the balance load signal over the acceleration signal.

Strictly speaking, the aerodynamic loads that act on the vehicle model during the calibration procedure are not exactly zero since the model motion is not performed in a vacuum. The aerodynamic loads induced by the motion in still air can be estimated in the following way: By multiplying the maximum total pressure due to the yawing motion with the lateral cross section the aerodynamic side force is estimated. Similarly, the aerodynamic yaw moment is approximated by multiplying the maximum side force with the length of the vehicle divided by 2. This leads to a side force $F_y < 0.4\,\mathrm{N}$ and a yaw moment $M_z < 0.5\,\mathrm{Nm}$. Therefore, the aerodynamic loads can be neglected during the calibration procedure and the balance loads are equal to the inertial loads in wind-off configuration.

This permits the calculation of the transfer function as illustrated for M_z in Eq. 4.2.

$$H_{M_z}(s) = \left. \frac{FFT(M_{z,Balance})}{FFT(a_{rot,z})} \right|_{Wind-Off} \tag{4.2}$$

Having calibrated the system by the 6 transfer functions, the inertial loads can be determined for a wind-on yawing motion with the same frequency and amplitude. Therefore, the Fourier transformation of the acceleration signal must be multiplied by the transfer function $H(s)$ before applying an inverse Fourier transformation ($iFFT$) in order to obtain the time signal of the inertial load (compare Eq. 4.3).

$$M_{z,inertial} = iFFT[H_{M_z}(s)FFT(a_{rot,z})] \tag{4.3}$$

Despite calibrating the system using a transfer function, it is necessary to average the results over a certain number of periods in order to generate reliable and reproducible results. Hence, the aerodynamic loads as well as all other measurement data are averaged over 440 periods, which corresponds to the before mentioned measuring period of 220 s. Finally the data are 11 Hz low-pass filtered.

4.3.5 Estimation of Accuracy

In order to verify the accuracy for the determination of the inertial loads, the calibration determined during wind-off yawing motion is applied to a second set of data for the same configuration without wind. The inertial loads of this second run are predicted using the transfer function of the initial calibration run and the acceleration signals from the second run. Hence, the error is obtained by comparing the predicted inertial loads to the actual inertial loads recorded by the balance. Table 4.7 lists the maximum errors after periodic averaging.

	Error [MKS]	Error [dimless] (210 km/h)
$F_{x,inertial}$	< 0.5 N	< 0.001
$F_{y,inertial}$	< 1.6 N	< 0.002
$F_{z,inertial}$	< 1.1 N	< 0.001
$M_{x,inertial}$	< 0.5 Nm	< 0.0003
$M_{y,inertial}$	< 0.3 Nm	< 0.0002
$M_{z,inertial}$	< 0.7 Nm	< 0.0005

Table 4.7: Errors in determination of inertial loads during 2 Hz ±3° yawing motion.

According to Table 4.7 the periodically averaged inertial loads feature a maximum error of 2 N for the inertial forces and 1 Nm for the inertial moments at any time of a period, which is of the same order as the uncertainty of the balance.

For two consecutive wind-on measurements during identical yawing motions the reproducibility is also very good. At any time of the periodically averaged oscillation, differences in side force and yaw moment are less than 0.003 and 0.002, respectively. Hence, accuracy and reproducibility are exceptionally good for an oscillating model test rig and are sufficient in order to precisely measure the aerodynamic loads.

4.3.6 Comparison with Numerical Setup

As described above, numerical and experimental setup differ regarding the gap between wheels and floor, compare Fig. 4.20. As will be shown later, the wake topology - more precisely fluid that enters into the wake region from the leeward side - plays an important role in the observed unsteady effects. In order to estimate the influence of the gap on the wake topology the two setups with and without gap are compared numerically for a constant yaw angle of 6°.

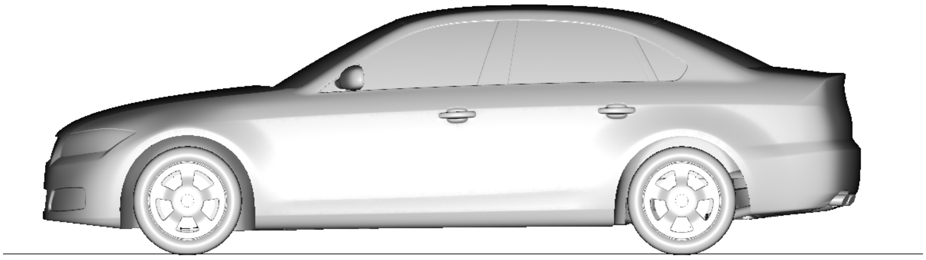

(a) Standard Setup

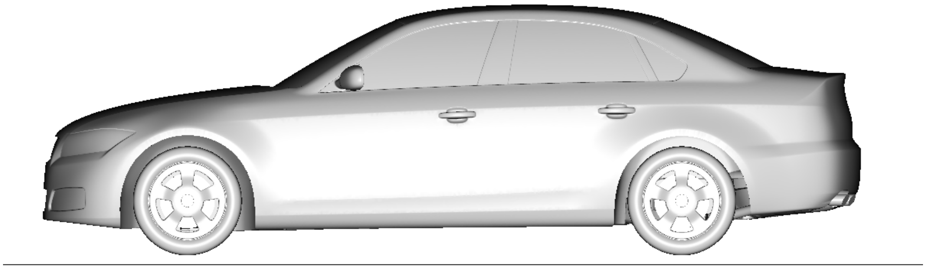

(b) Ground Clearance 60 mm

Figure 4.20: Comparison of setup used in (a) simulation and (b) experiment.

As expected, the aerodynamic drag, side force and roll moment are reduced significantly by lifting the model (see Table 4.8). The larger gap allows more fluid to pass below the vehicle which reduces the blockage effect in both x- and y-direction. The yaw moment, however, increases by almost 30%.

	C_x	C_y	C_z	C_{Mx}	C_{My}	C_{Mz}
Without Gap	0.317	-0.234	0.068	0.037	-0.114	0.052
With Gap	0.253	-0.162	-0.123	0.022	-0.149	0.066
Absolute Tendency	−	−		−		+

Table 4.8: Comparison of aerodynamic loads for setup with and without gap between wheels and floor at constant yaw 6°.

Visualizations of the flow field (Fig. 4.21) show that the characteristic flow that enters into the wake region from the leeward side is still present although its magnitude decreases. Similarly, the upper vortex structure decreases in magnitude, yet it can be

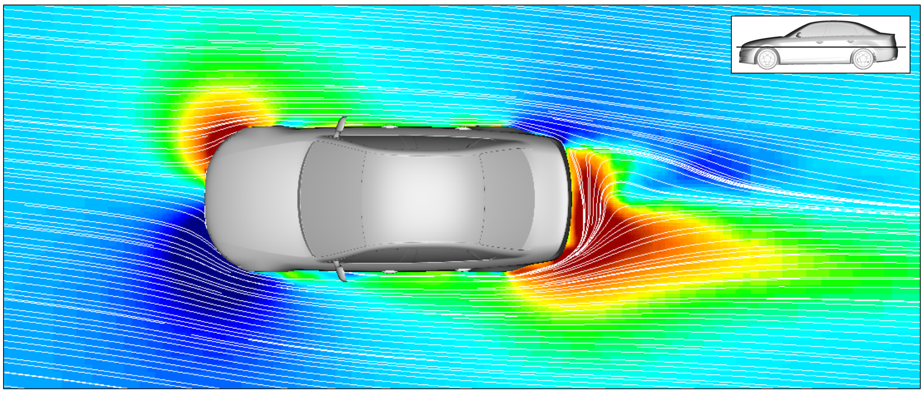

(a) Standard Setup

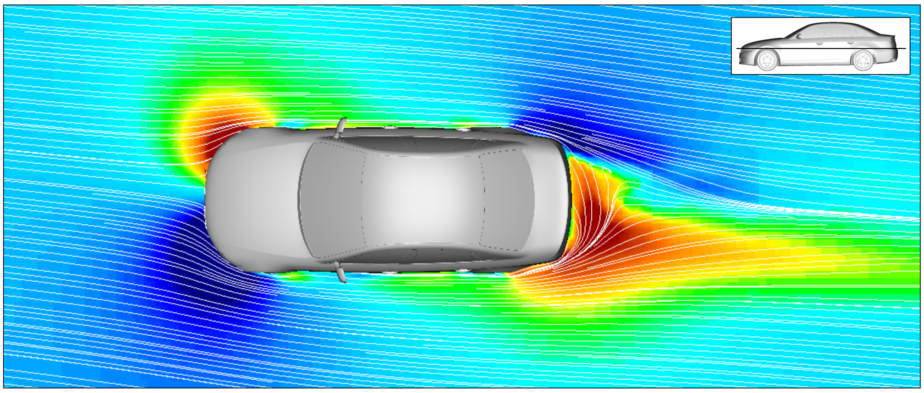

(b) Ground Clearance 60mm

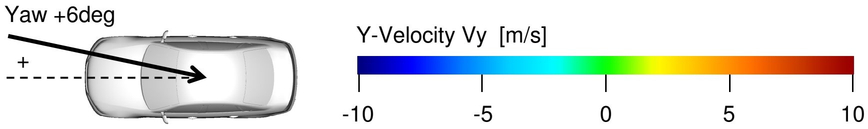

Figure 4.21: Comparison of lateral velocity V_y and velocity streamlines in z-slice for constant yaw +6°.

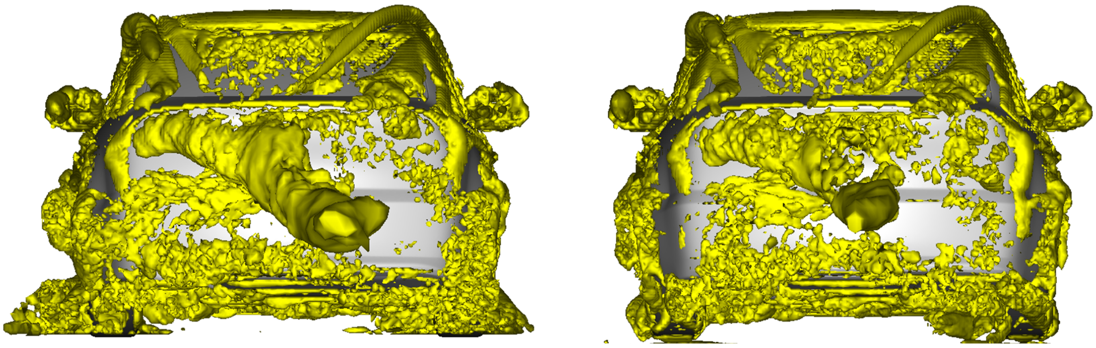

(a) Standard Setup

(b) Ground Clearance 60mm

Figure 4.22: Comparison of isosurfaces $\lambda_2 - criterion = -3000\ 1/s^2$ for constant yaw +6°.

clearly observed (Fig. 4.22). Therefore, the characteristic flow topology at the rear of the vehicle is altered slightly by lifting the vehicle, but the main characteristics are not changed.

Judging from the wake topology described above and the applied time-dependent flow conditions, similar unsteady phenomena can be expected in the experiment. However, due to the differences in setup and flow conditions, the experimental investigation cannot quantitatively validate the numerical results. Thus, the experimental investigation is only capable of proving that the numerically identified phenomena exist principally.

Chapter 5

Unsteady Aerodynamic Phenomena

As presented in Chap. 2.2, the unsteady aerodynamic behavior of realistic vehicles during typical gust events is not yet fully described and understood. Hence, first a characterization of the unsteady aerodynamic loads is required. Judging from the results of previous investigations unsteady effects need to be expected. Assuming that unsteady effects will be observed, the underlying mechanism needs to be analyzed in order to identify the cause for the differences between unsteady and quasi-steady loads. A profound understanding of the underlying mechanism is obviously key to future optimization of the unsteady aerodynamic behavior. In the following, the unsteady aerodynamic behavior during a standard gust is analyzed numerically in Chap. 5.1. Based on these results, an unsteady mechanism is derived in Chap. 5.2. In Chap. 5.3 its key aspects are verified experimentally.

5.1 Numerical Investigation of Standard Gust

Following the approach described above, in Chap. 5.1.1 the evolution of the aerodynamic loads is analyzed in detail for a single-peak gust event. To this end, the yaw angle is varied from -3° to +3° and back to -3° over a period of $T = 1s$ as shown in Fig. 4.1. In order to locate the differences between unsteady and quasi-steady results, the corresponding load distributions at characteristic points in time are presented in Chap. 5.1.2. Finally, in Chap. 5.1.3 the flow field is investigated with the aim of identifying the flow mechanism.

5.1.1 Evolution of Aerodynamic Loads

Fig. 5.1 shows the unsteady evolution of the aerodynamic load coefficients for drag C_x, side force C_y, lift force C_z, roll moment C_{Mx}, pitching moment C_{My} and yaw moment C_{Mz}. For a comparison with steady loads, the corresponding levels of constant yaw -3°, 0° and +3° are included for each component. As described in Chap. 4.2.5, the quasi-steady curves are derived from these steady loads for side force, roll and yaw moment. Vertical dotted lines indicate the arrival of the start of the gust at the front of the vehicle, of the gust peak at the vehicle reference point and of the end of the gust at the rear of the vehicle.

As expected, the variations in C_x, C_z and C_{My} are small compared to the variations in C_y, C_{Mx} and C_{Mz}. The drag coefficient C_x decreases from the initial constant-yaw level by approximately 5% and reaches the 0°-yaw level, where it remains until almost the end of the gust period. On returning to the initial constant-yaw level, the drag coefficient shows an overshoot of 0.010, which is, however, only slightly larger than typical fluctuations at constant yaw. A very similar behavior is observed for the lift coefficient C_z, which also decreases during the gust towards the level of 0°-yaw. In comparison, the pitching moment increases slightly during the gust, which corresponds to a balance shift towards the rear. All three load components C_x, C_z and C_{My} show a delayed return to the initial level. Hence, for the behavior of aerodynamic drag, lift and pitching moment it can be concluded that during the gust the unsteady loads tend towards the 0°-yaw levels and show a delayed return to the initial level. Since, typically, the 0°-yaw levels are more favorable regarding low drag, low total lift and lift balance compared to constant-yaw levels, the behavior of C_x, C_z and C_{My} during the gust event can be assumed to be uncritical.

On the other hand, large variations can be observed during the gust for the side force C_y, the roll moment C_{Mx} and the yaw moment C_{Mz}. As expected, the initial yaw angle of -3° results in a positive side force and a negative roll and yaw moment, pushing and turning the vehicle to the right away from the wind direction. At the arrival of the gust, C_y, C_{Mx} and C_{Mz} immediately react to the change of the oncoming flow and at first tend towards the corresponding +3°-yaw levels, which results in zero-crossings for each component. At the peak of the gust, however, side force and roll moment do not reach the quasi-steady +3°-yaw levels. Additionally, they show a delayed return to the initial levels at the end of the gust. In comparison, a significant over- and undershoot can be observed for the yaw moment at the peak and at the end of the gust. This pronounced deviation from the quasi-steady curve is much larger than typical constant-yaw fluctuations.

Comparing the unsteady loads to the quasi-steady approximations, unsteady effects can be identified for all three components regarding both amplitude and time delay, which are summarized in Table 5.1. The peak side force and peak roll moment reach only 55% and 44%, respectively, of the quasi-steady value. On the other hand, the unsteady yaw moment reaches 207% and 198% of the quasi-steady value during the gust peak and the following undershoot. Hence, while for the side force and the roll moment the quasi-steady curves lead to a conservative approximation, this is not the case for the yaw moment. Furthermore, for all three components a time shift can be observed. While the unsteady side force and roll moment lag the quasi-steady signal, the unsteady yaw moment precedes its quasi-steady approximation. The time shifts amount to $\Delta t = +0.04s$ for the side force, $\Delta t = +0.11s$ for the roll moment and $\Delta t = -0.08s$ for the yaw moment.

As already described in Chap. 4.2.5, the quasi-steady approximation, as used above, can be improved by taking into account the delayed impact of the crosswind gust along the x-axis of the vehicle. In this case, the vehicle is divided into six slices,

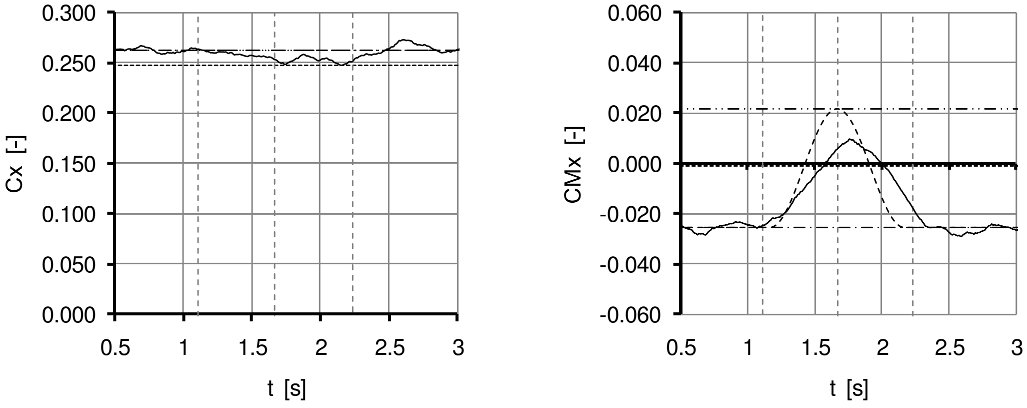

(a) Drag C_x (b) Roll Moment C_{Mx}

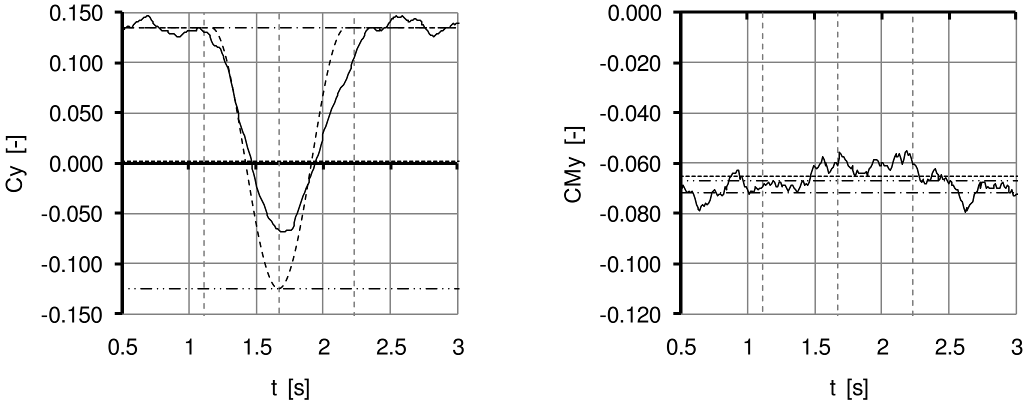

(c) Side Force C_y (d) Pitching Moment C_{My}

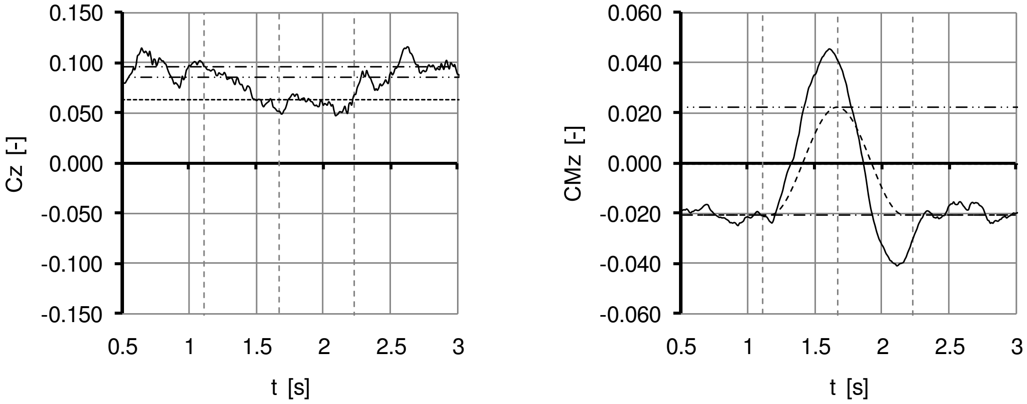

(e) Lift C_z (f) Yaw Moment C_{Mz}

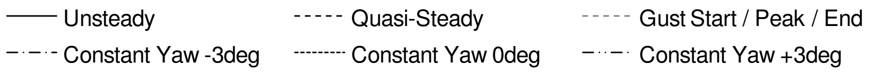

Figure 5.1: Unsteady and quasi-steady evolution of the aerodynamic loads during the gust event. For a better comparison the range of the vertical axis is kept constant for forces and moments, respectively.

	C_y	C_{Mx}	C_{Mz}
Constant Yaw -3°	0.135	-0.026	-0.021
Constant Yaw +3°	-0.126	0.021	0.022
Unsteady Peak +3°	-0.069	0.010	0.046
Unsteady Undershoot -3°	-	-	-0.041
US / QS Peak +3°	55%	44%	207%
US / QS Undershoot +3°	-	-	198%
Time Shift US vs QS	+0.04 s	+0.11 s	-0.08 s
Time Shift US vs Delayed QS	+0.05 s	+0.11 s	-0.02 s

Table 5.1: Summary of unsteady and quasi-steady results of the aerodynamic loads side force, roll and yaw moment for the investigated generic gust event.

as shown in Fig. 4.12a. The contribution of each segment is then delayed by the additional time that the gust needs to travel the distance from the aerodynamic point of reference to the center of the segment. Preliminary investigations showed that a larger number of slices does not further modify the result. In Fig. 5.2, this modified approximation of the yaw moment called “Delayed QS” is compared to the unsteady and quasi-steady curves.

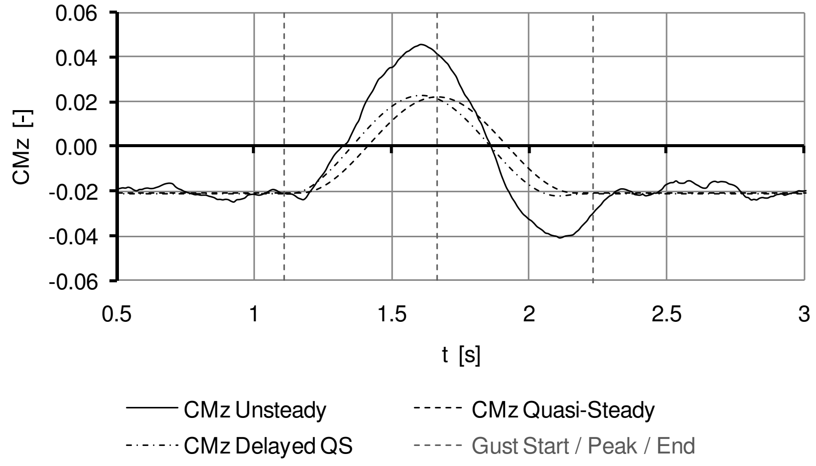

Figure 5.2: Comparison of unsteady, quasi-steady and “delayed quasi-steady” evolution of the yaw moment C_{Mz}.

For the yaw moment, the delayed QS approximation shows an increase in amplitude of only 5% over the standard quasi-steady curve, which is small compared to the unsteady overshoot in yaw moment. On the other hand, the occurrence of the yaw moment peak ahead of the gust peak is well predicted by the delayed QS approximation. For the side force and the roll moment the differences between the delayed and the standard quasi-steady approximation are much smaller than for the yaw moment and are therefore not shown. It has to be noted, however, that the differences may be larger for a vehicle that has significant load contributions of the front and the rear end, like for example a station wagon.

Hence, the delayed QS approximation principally is an improvement over its standard version as the delayed impact of the gust is taken into account. However, neither the delayed nor the standard quasi-steady approximation capture the observed unsteady effects. Furthermore, as the delayed QS curves of side force, roll and yaw moment do not reach their peak values at the same time, a comparison of time shifts is more complicated. Therefore, since the modified approximation does not provide an advantage when analyzing the unsteady loads, the standard quasi-steady approximation is used in the following.

5.1.2 Load Distribution

In Chap. 5.1.1 significant unsteady effects were identified for the side force, roll and yaw moment. In the following, it will be analyzed at which part of the vehicle the unsteady effects occur. The focus is put on the side force and the yaw moment as roll moment and side force behave very similarly.

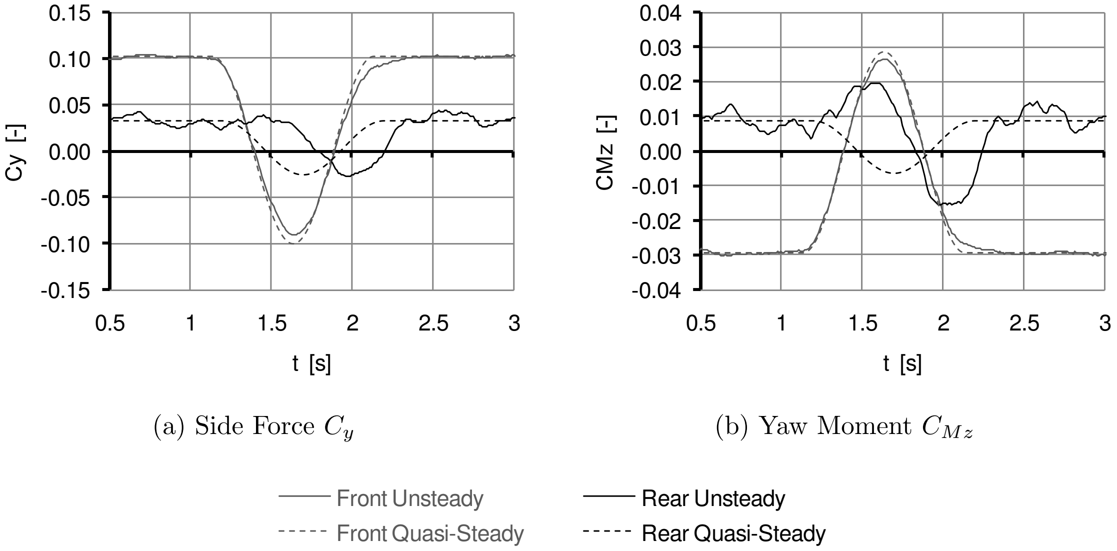

(a) Side Force C_y

(b) Yaw Moment C_{Mz}

Figure 5.3: Unsteady and quasi-steady contribution of the front and the rear half of the vehicle to (a) side force and (b) yaw moment.

In Fig. 5.3 the contributions of the front and the rear part of the vehicle to the side force and the yaw moment are shown together with the corresponding quasi-steady approximation. Due to increasing distance to the aerodynamic point of reference at mid wheelbase, forces acting at the front or the rear end have a larger impact on the yaw moment than on the side force. At the investigated yaw angle, the contributions of front and rear end are of different signs for the yaw moment, while they point in the same direction for the side force. For the investigated vehicle geometry, the steady-state values of both side force and yaw moment are dominated by the front of the vehicle. At constant yaw before and after the gust, the absolute contribution of the front half of the vehicle is approximately three times as large as the contribution of the rear half. While in both graphs the contributions of the front show only small differences between unsteady and quasi-steady curves, large differences can be observed for the rear half of the vehicle. The unsteady side force of the rear half has a time delay of $\Delta t \approx 0.26s$ compared to the quasi-steady curve. However, its unsteady amplitude is only slightly larger than the quasi-steady approximation. In comparison, the unsteady yaw moment of the rear half has a time delay of $\Delta t \approx 0.32s$ and an amplitude that is twice as large as the quasi-steady amplitude. This leads to the conclusion that the unsteady effects occur towards the rear end of the vehicle where the increasing distance to the point of reference causes a larger impact on the yaw moment.

Fig. 5.3 already explains the principally different unsteady behavior of side force and yaw moment: Due to the identical signs of front and rear C_y-contributions, the time delay of the rear side force causes a decrease in peak-to-peak amplitude and a delayed return to the initial level after the gust. In comparison, due to the opposite signs of front and rear C_{Mz}-contributions, the time delay of the rear yaw moment causes a superposition of front and rear peak values leading to the observed over- and undershoot.

In order to identify the parts of the vehicle that are relevant for side force, roll and yaw moment, the pressure differences between the left and the right side ("Casediff Left - Right") are shown in Fig. 5.4 for constant yaw and for the gust peaks. At constant yaw, pressure differences are predominantly located at the front half of the vehicle with the largest values occurring at the front corner and the A-pillar. Pressure differences are also observed at the C-pillar and the wheels. Interestingly, pressure differences can be identified stretching along the side windows, which are presumably caused by an asymmetry of the A-pillar vortices. Compared to the vehicle front and A-pillar, the pressure difference at the C-pillar is of opposite sign, thus reducing total side force but increasing total yaw moment. Small pressure differences also occur at the rear end, which have the same sign as the pressure differences at the front end and at the A-pillar.

After analyzing the steady-state surface pressures, Fig. 5.4b and d show the corresponding unsteady representation for the gust peaks. When comparing the steady-state and the unsteady pressure differences, the same general behavior can be observed for the front of the vehicle and the A- and C-pillars. The magnitude of the pressure differences is however reduced compared to the constant-yaw case. This can be attributed to the averaging period of 0.2 s around the actual peaks, which essentially reduces the effective average yaw angle. However, towards the rear end more significant differences can be observed between unsteady and steady-state pressure distributions. At the rear end of the vehicle, the unsteady pressure differences are of opposite signs and larger magnitude compared to the constant-yaw case. This corresponds to the supposition that the unsteady effects occur at the rear end of the vehicle, which was deduced from the time histories of front and rear contributions.

In order to visualize these unsteady effects in surface pressure more clearly, the delta between unsteady and quasi-steady surface pressure is shown in Fig. 5.5. The before mentioned differences in magnitude at the front of the vehicle as well as at the A- and

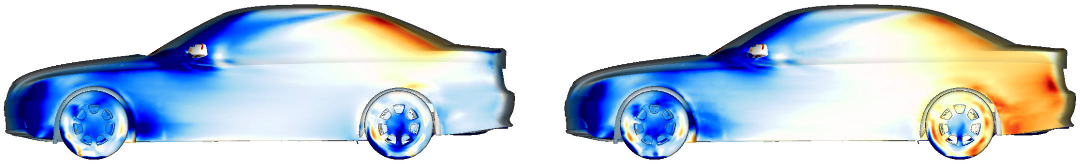

(a) Constant Yaw +3°

(b) Unsteady Yaw +3°

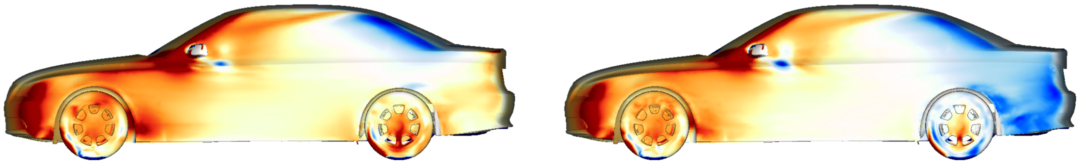

(c) Constant Yaw -3°

(d) Unsteady Yaw -3°

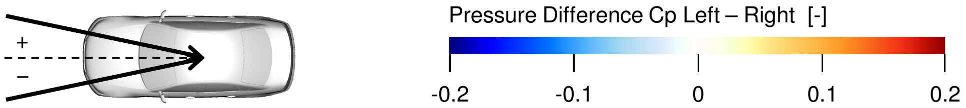

Figure 5.4: Unsteady and quasi-steady pressure differences between left and right side $C_{p,left} - C_{p,right}$ for the minimum and maximum yaw angles -3° and +3°.

C-pillars are small compared to the pressure differences at the rear end. Furthermore, the deltas between unsteady and quasi-steady surface pressure at the rear end can be observed on both sides - the windward and the leeward side. For the peak yaw angles ±3°, the unsteady surface pressure is lower on the windward side and larger on the leeward side than the quasi-steady approximation. In the unsteady case, this results in a large positive pressure difference between left and right side for +3° and a large negative pressure difference for -3°, as shown before in Fig. 5.4.

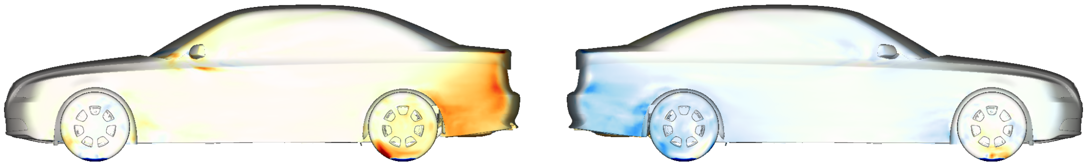

(a) Beta +3°

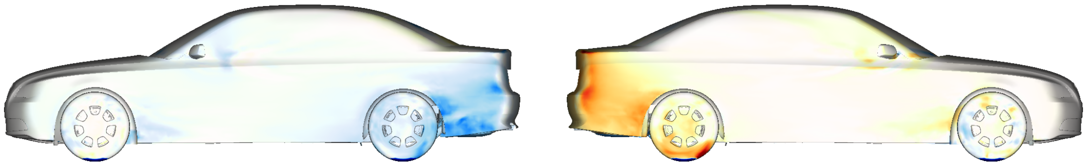

(b) Beta -3°

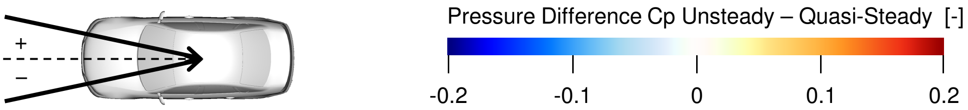

Figure 5.5: Differences between unsteady and quasi-steady surface pressures $C_{p,US} - C_{p,QS}$ for the minimum and maximum yaw angles -3° and +3°.

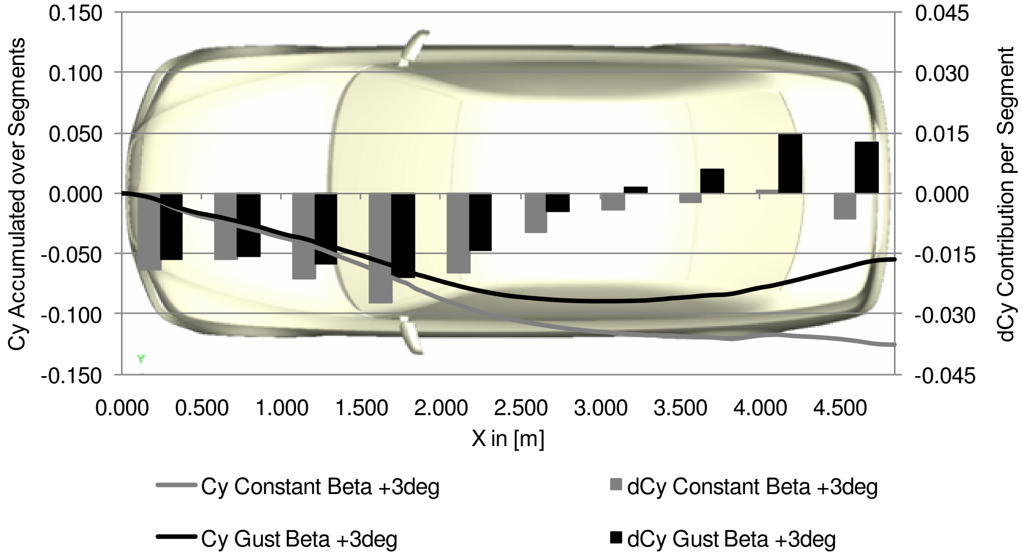

(a) Side Force C_y

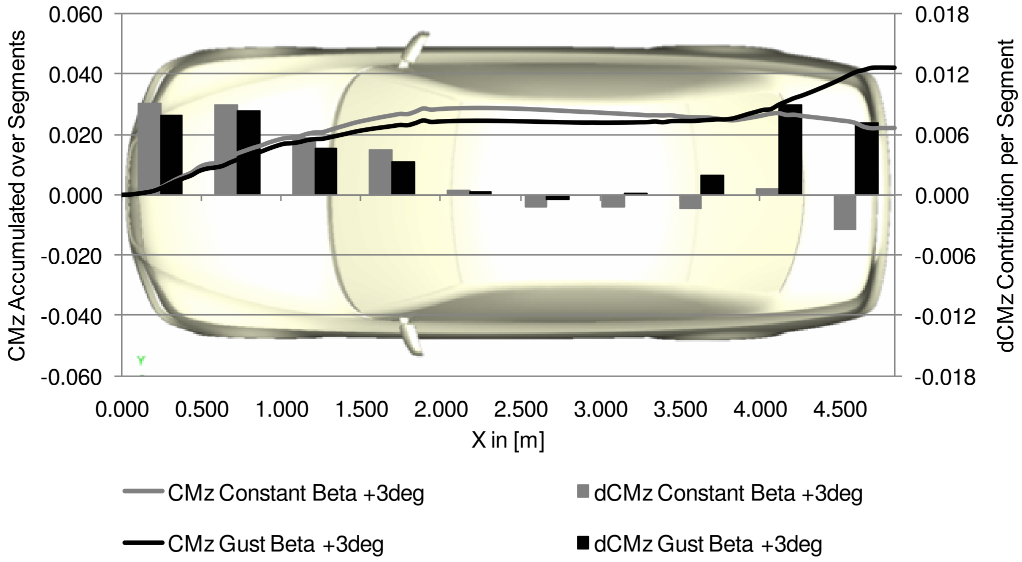

(b) Yaw Moment C_{Mz}

Figure 5.6: Unsteady and quasi-steady contribution to the (a) side force and (b) yaw moment - per segment (vertical bars) and accumulated (curves) along the vehicle axis for Beta +3°.

In order to quantify the differences between unsteady and quasi-steady load contribution along the length of the vehicle, the development of side force and yaw moment along the vehicle axis is shown in Fig. 5.6. Again, the graphs confirm the large contribution of the front of the vehicle to both side force and yaw moment. Furthermore, the differences between the unsteady and the quasi-steady curves increase linearly until mid wheelbase. As before, this can be explained by the smaller average yaw angle during the unsteady averaging period. At the rear end, the differences between unsteady and quasi-steady contributions increase dramatically and, in particular, are of different signs at the very end of the vehicle. While this leads to a decrease of the unsteady side force, the unsteady yaw moment is increased significantly.

5.1.3 Flow Field

In Chap. 5.1.2, the unsteady effects in surface pressure were identified to occur at the rear end of the vehicle. In the following, the flow field will be analyzed with the aim of understanding the cause for these unsteady effects.

Fig. 5.7 depicts a slice parallel to the ground at approximately mid vehicle height that is colored with lateral velocity V_y and additionally shows two-dimensional streamlines. The images in the left column visualize the flow field during constant yaw, while in the right column the corresponding images are shown for the unsteady case at the gust peaks. As expected, regions of high lateral velocity can be observed at the front and rear corners of the vehicle. The flow field at the rear end, however, is strongly asymmetric. Surprisingly, at constant yaw fluid enters into the wake region primarily from the leeward side and not from the windward side, as it might have been expected. This topology was already covered in Chap. 2.2.3, as a similar characteristic was identified by Lemke (2006) and Gohlke et al. (2007) and confirmed experimentally by Heuler (2010).

When comparing the unsteady flow field to the corresponding constant-yaw case, differences are not visible up to the rear axle of the vehicle. In the wake, however, a mirrored flow topology can be observed in the unsteady case with fluid entering from the windward side.

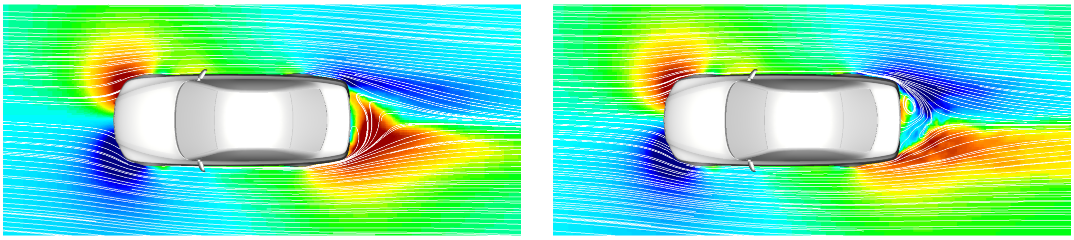

(a) Constant Yaw +3°

(b) Unsteady Yaw +3°

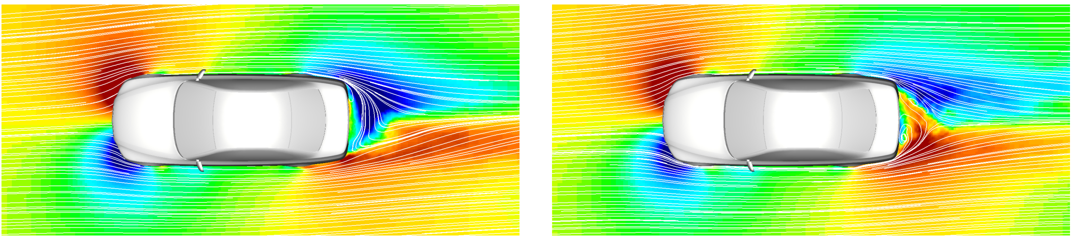

(c) Constant Yaw -3°

(d) Unsteady Yaw -3°

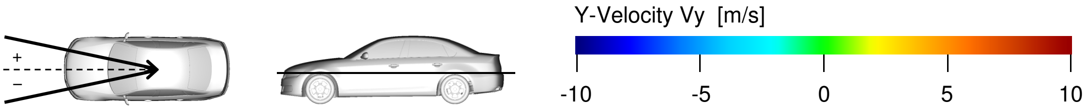

Figure 5.7: Visualization of lateral velocity V_y in z-slice for minimum and maximum constant and unsteady yaw -3° and +3°.

In order to provide a three-dimensional impression of the flow entering into the wake area, the regions of high lateral velocity are visualized in Fig. 5.8 using isosurfaces of $V_y = \pm 10\ m/s$. For the constant-yaw case, a large region of high lateral velocity can be observed on the leeward side identifying fluid that enters into the wake region. Starting at the height of the rear lights on the leeward side, it stretches inward before being directed towards the ground. As already seen in Fig. 5.7, an inversed and weakened topology is observed during the gust peaks. In this case the isosurfaces are more pronounced on the windward side but are significantly smaller compared to the constant-yaw case.

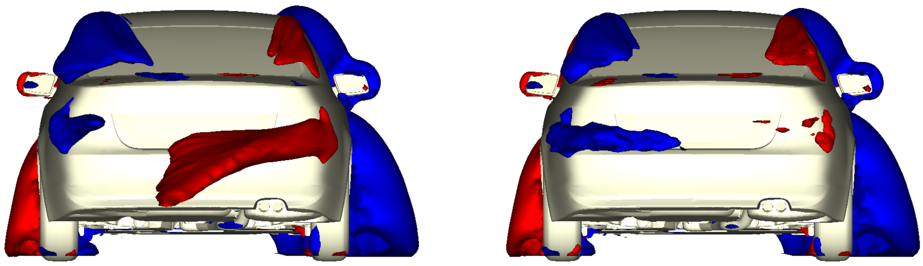

(a) Constant Yaw +3°　(b) Unsteady Yaw +3°

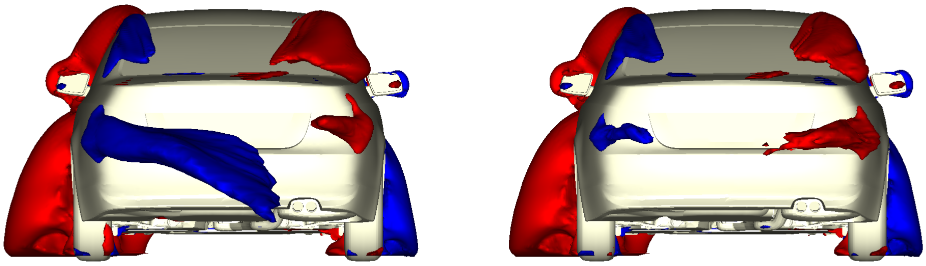

(c) Constant Yaw -3°　(d) Unsteady Yaw -3°

Figure 5.8: Isosurfaces of lateral velocity $V_y = \pm 10 m/s$ for minimum and maximum constant and unsteady yaw -3° and +3°.

Further analysis of the wake flow results in the identification of a pronounced vortex on the leeward side in the constant-yaw case. Visualizing the isosurfaces of x-vorticity $Vort_x = \pm 80\ 1/s$ (Fig. 5.9) for constant yaw, two regions of high vorticity are visible above and below the region where fluid enters into the wake region from the leeward side. The corresponding isosurfaces of the λ_2-criterion confirm that a vortex structure forms at the upper leeward corner of the wake region (Fig. 5.10). In contrast, the lower region of high x-vorticity is apparently caused by simple shear flow. In the unsteady case, the corresponding visualizations for the gust peaks show very scattered isosurfaces, which is primarily due to the shorter averaging period. Hence, a direct comparison of the vortex strength is not possible due to the different averaging lengths. However, corresponding to the inversed layout of the V_y-isosurfaces in the unsteady case, the isosurfaces of x-vorticity are also more pronounced on the wind-

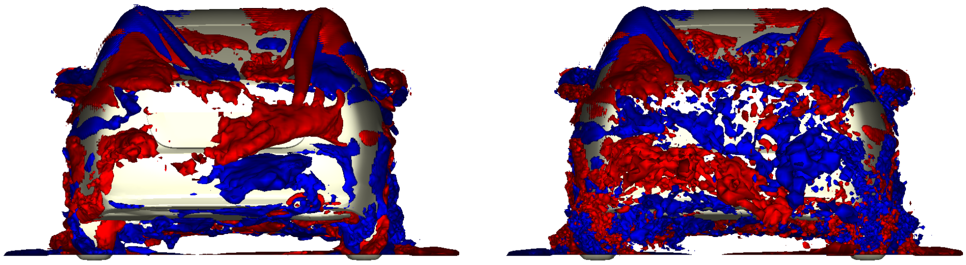

(a) Constant Yaw +3° (b) Unsteady Yaw +3°

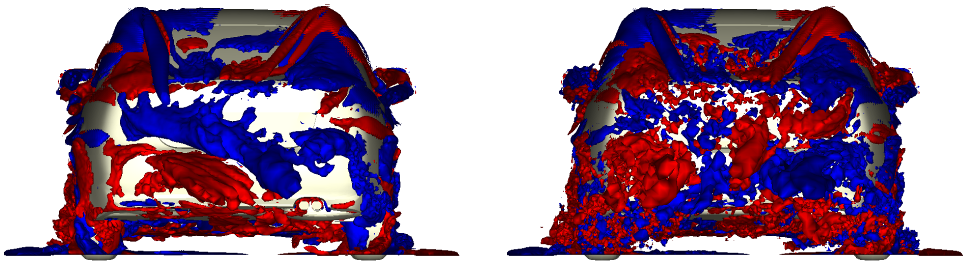

(c) Constant Yaw -3° (d) Unsteady Yaw -3°

Figure 5.9: Isosurfaces of x-vorticity $\omega_x = \pm 80\ 1/s$ for minimum and maximum constant and unsteady yaw -3° and +3°.

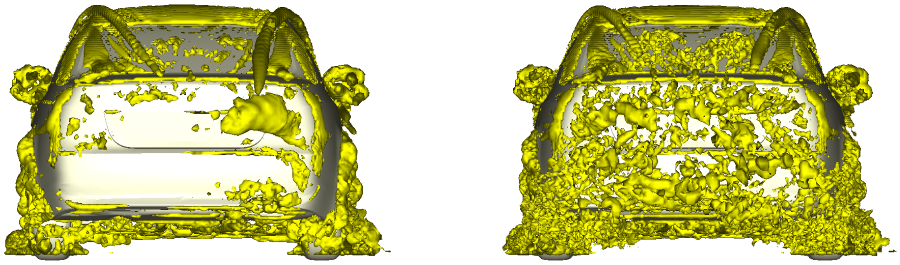

(a) Constant Yaw +3° (b) Unsteady Yaw +3°

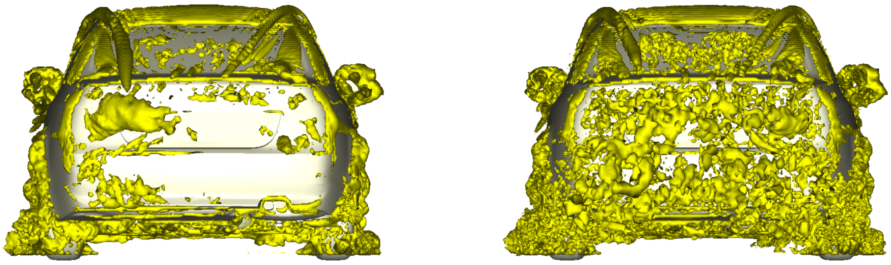

(c) Constant Yaw -3° (d) Unsteady Yaw -3°

Figure 5.10: Isosurfaces of $\lambda_2 - criterion = -3000\ 1/s^2$ for minimum and maximum constant and unsteady yaw -3° and +3°.

ward side. This underlines the observation, that at the peaks of the gust the layout of the wake flow has not yet reached the steady-state topology.

As described in Chap. 4.2.5, the temporal evolution of the wake flow is analyzed using control surfaces on the side and in the wake of the vehicle. Fig. 5.11 plots the evolution of the average lateral velocity V_y of fluid that enters into the wake region. As expected, before the arrival of the gust the average lateral velocity is low but positive on the left, windward side and high but negative on the right, leeward side. During the gust, the average lateral velocity over the right control surface decreases to the constant-yaw level of +3°. At the same time, the average lateral velocity over the left control surface increases but does not reach the level of +3°. Both curves reach their peaks with a time delay of approximately $\Delta t \approx 0.15s$ compared to the gust peak at the rear end of the vehicle.

Hence, it can be concluded that the wake reacts with a time delay to the change of the oncoming flow. Furthermore, the lateral flow entering into the wake region collapses almost completely on the right side, while the duration of the gust is too short for the lateral flow to fully establish on the left side.

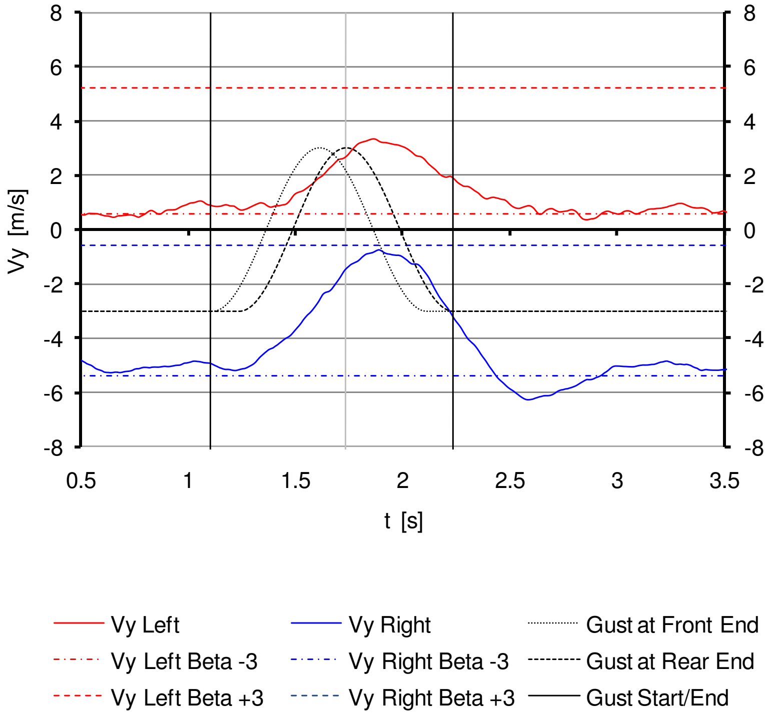

Figure 5.11: Evolution of the lateral velocity V_y averaged over two control surfaces in the left and right wake region.

Fig. 5.12 shows the behavior of total pressure $c_{p,tot}$, surface pressure c_p and dimensionless dynamic pressure in x-direction $(V_x/U)^2$. Before the arrival of the gust, total pressure and surface pressure are slightly larger on the left, windward side, while surprisingly the dynamic pressure is larger on the right, leeward side. Presumably, this is directly linked to the strong flow entering into the leeward wake region, which accelerates the flow also on the rear leeward side of the vehicle. As expected, the

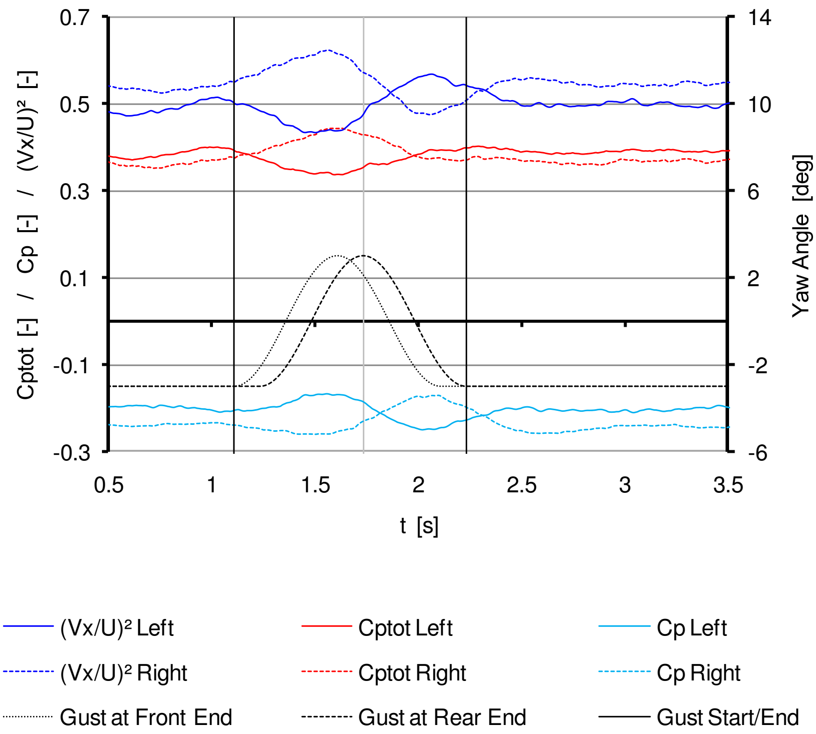

Figure 5.12: Evolution of the averaged parameters surface pressure C_p, total pressure $C_{p,tot}$ and dimensionless x-velocity $(V_x/U)^2$ on the rear side of the vehilce.

arrival of the gust causes the total pressure to increase on the right side and to decrease on the left side. Although the control surfaces recording the evolution of the total pressure are located at the rear end of the vehicle, the peaks in total pressure coincide with the gust peak at the front end of the vehicle. This suggests that the total pressure at the rear end is directly linked to the flow conditions at the front of the vehicle. Furthermore, the difference between the peak values on the left and the right side is much larger than during constant yaw. After the gust peak, the evolution of total pressure again corresponds to the variation of the yaw angle at the front of the vehicle. This implies that the curves of total pressure return to the initial levels before the gust fully passes the rear end of the vehicle.

During the gust, the rise in total pressure on the right side coincides with an increase in dynamic pressure and a decrease in surface pressure. Hence, the rise in total pressure is overcompensated by the rise in dynamic pressure, which causes the surface pressure to decrease. The inverse behavior can be observed on the left side, thus increasing the difference in surface pressure between the left and the right side. The reaction of dynamic and surface pressure at the arrival of the gust contradicts the expected quasi-steady behavior. The quasi-steady approximation would have suggested that the curves gradually converge towards the constant level of the opposite side, thus reducing the difference between the two sides until the constant levels are reached.

After the first immediate reaction of dynamic and surface pressure opposite to the quasi-steady prediction, the curves converge towards the expected steady-state levels of +3° resulting in a second pair of peaks. These second peaks occur with a time delay of $\Delta t \approx 0.3s$ compared to the gust peak at the rear end of the vehicle. Finally, all curves return to their initial levels again.

Hence, the behavior of total pressure principally agrees with the expected quasi-steady approximation, but exhibits an increased amplitude and is linked to the variation of the yaw angle at the front end of the vehicle. In comparison, dynamic and surface pressures show a different behavior including two peaks instead of only one. While the second peaks correspond to the expected but delayed quasi-steady evolution, the first peaks point into the opposite direction and thereby significantly increase the difference between left and right side.

5.2 Unsteady Mechanism

Combining the findings described above, an unsteady aerodynamic mechanism can be derived that permits a schematic explanation of the unsteady aerodynamic loads observed during a gust event. In Fig. 5.13 the schematic two-dimensional flow field around a vehicle is shown for a singular yaw change from for example -3° to +3°. At constant yaw -3°, the flow enters into the wake region from the leeward side. Consequently, the fluid is accelerated around the leeward rear corner resulting in lower pressures and a positive contribution to the side force and yaw moment. If the oncoming flow now suddenly changes to positive yaw angles, i.e. cross wind from the right, the wake flow reacts with a certain time delay while the flow around the front adjusts almost instantly. The combined effect of cross wind from the right and fluid, which still enters into the wake region from the right side results in even higher velocities and lower pressures on the right rear of the vehicle. On the left side, an inverse behavior occurs, which results in a reduction of velocity and an increase in surface pressure. Hence, the pressure difference between left and right side increases and thus the positive contribution of the rear to the side force and yaw moment. At the same time the contribution of the front of the vehicle has already changed its direction, which together with the contribution of the rear results in a smaller total side force but a larger total yaw moment. Eventually, the quasi-steady state is reached again as the wake flow adapts to the modified oncoming flow.

Assuming that the variation in pressure on the right rear side of the vehicle can be divided into an effect due to the oncoming flow and an effect due to the wake flow, a schematic development of the pressure can be sketched as shown in Fig. 5.14. The effect of the oncoming flow has almost no time shift, while the wake flow reacts with a time delay, which is set to $\Delta t/T = 0.15$. If the effect of the wake flow dominates, as shown in Fig. 5.14, the resulting pressure at the right rear exhibits a positive time delay and an increase in amplitude. If the effect of the oncoming flow dominated, the resulting pressure would exhibit a negative time delay instead. As described in Chap. 5.1.3, a positive time delay was identified for the pressure at the rear, indicating that the effect of the wake flow dominates for the investigated gust and vehicle geometry.

Furthermore, it is assumed that the contribution of the rear of the vehicle to the side

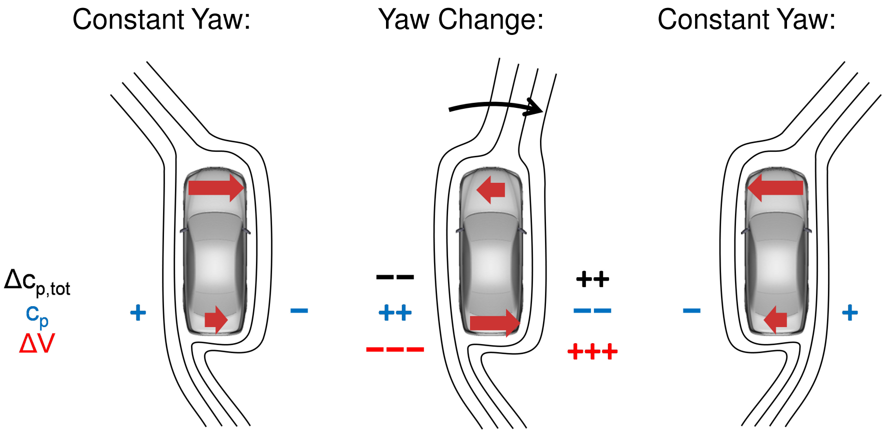

Figure 5.13: Schematic view of 2D-flow field at constant yaw (left and right) and during a gust event (center).

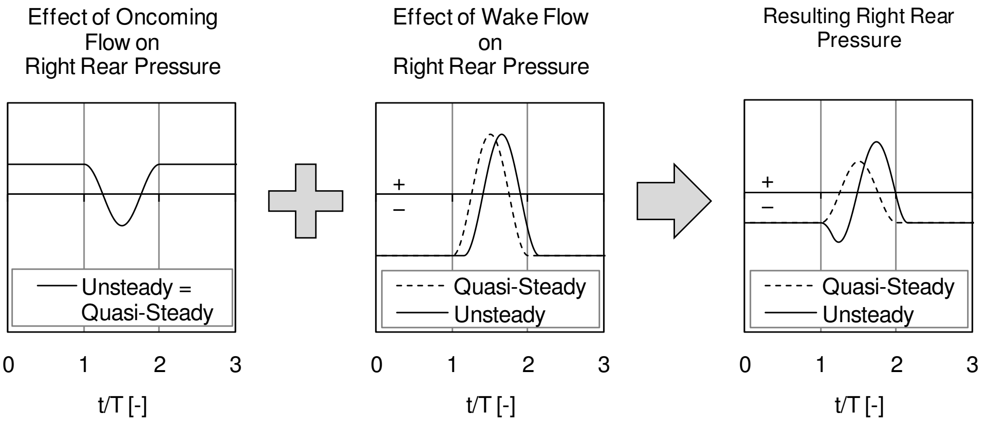

Figure 5.14: Schematic development of the surface pressure on the right rear side of the vehicle due to the oncoming flow (left), the wake flow (center) and their combination (right).

force and the yaw moment can be approximated by the evolution of the pressure at the rear, as derived above (Fig. 5.14). Superposing the schematic contributions of the front and the rear of the vehicle, the evolution of the resulting side force and yaw moment can be sketched as shown in Fig. 5.15. In both cases, the contributions of the front correspond to the quasi-steady approximation. For the side force the contribution of the front and the rear of the vehicle have the same sign, resulting in a positive time delay and a reduction in amplitude. For the yaw moment the contributions of the front and the rear are of opposite signs, which results in a negative time delay and a significant over- and undershoot. This behavior of side force and yaw moment corresponds to the observation of the preceding chapter. Hence, Figs. 5.13 - 5.15 provide a schematic mechanism that explains the cause for the time delays and the variation in amplitude.

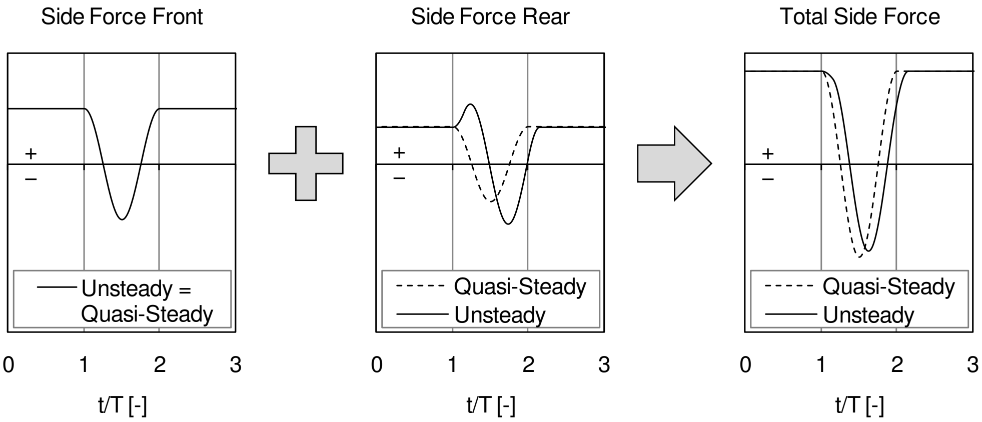

(a) Side Force

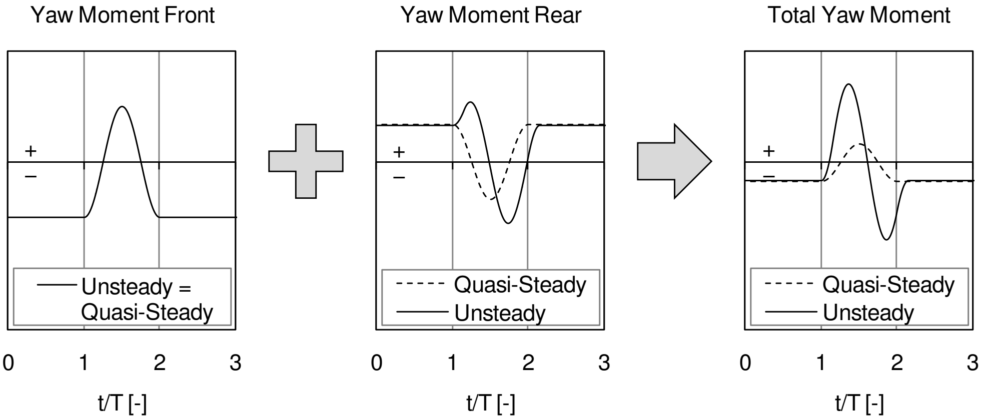

(b) Yaw Moment

Figure 5.15: Schematic development of (a) side force and (b) yaw moment at the rear of the vehicle due to the oncoming flow (left), the wake flow (center) and their combination (right).

5.3 Experimental Verification

In the following the main aspects of the unsteady mechanism described in Chap. 5.2 are verified experimentally. This includes:

Aerodynamic loads:

- Negative time delay and increase in amplitude of the unsteady yaw moment.
- Positive time delay and reduction in amplitude of the unsteady side force and roll moment.

Surface pressures:

- Quasi-steady behavior of surface pressures at the front of the vehicle.
- Increase in amplitude and positive time delay at the rear of the vehicle.

Wake flow:

- Delayed reaction of the leeward flow entering into the wake region to the change of the yaw angle.

5.3.1 Aerodynamic Loads

The unsteady aerodynamic loads, which are recorded during the 2 Hz ±3° yawing motion, are compared to the corresponding quasi-steady evolutions in Fig. 5.16. The quasi-steady curves are derived by interpolating the aerodynamic loads from constant-yaw configurations according to the measured yaw angle.

The unsteady variations in drag, lift and pitching moment are small and can be well estimated by quasi-steady approximation. Significant differences between unsteady and quasi-steady loads can be observed in the experiment for side force, roll and yaw moment. Side force and roll moment feature unsteady amplitudes that are smaller than the quasi-steady approximation, reaching only 62% and 68% of the quasi-steady values, respectively (see Table 5.2). In contrast, the unsteady amplitude of the yaw moment is increased to 183% of the quasi-steady estimation.

While the unsteady side force and roll moment lag the quasi-steady curves by $\Delta t/T = +0.12$ and $\Delta t/T = +0.22$, respectively, the unsteady yaw moment exhibits a negative time delay of $\Delta t/T = -0.04$ compared to the quasi-steady approximation. A strong asymmetry can be observed for side force, roll and yaw moment. This leads to the assumption that the flow phenomena responsible for the unsteady behavior are not symmetrical, which might be due to the asymmetric underbody or strut. Table 5.2 summarizes the experimental findings for side force, roll moment and yaw moment. The peak values are averaged between maximum and minimum.

Hence, the experiment confirms the general behavior of the aerodynamic loads proving the existence of unsteady effects for the three components side force, roll and yaw moment. Furthermore, the increase in unsteady amplitude for the yaw moment and the reduction in unsteady side force and roll moment is observed both numerically and experimentally. Despite the differences regarding the setup and the model geometry, the unsteady effects in side force, roll and yaw moment are of the same order of magnitude. Finally, also the phase shift of the unsteady loads is confirmed, with side force and roll moment lagging the quasi-steady curves, while the unsteady yaw moment precedes its quasi-steady counterpart. However, the time delays of side force and roll moment observed in the experiment are approximately twice as large as the numerical values, which may be due to the different setup and model geometry.

5.3.2 Pressure Measurements

In the following, the amplitudes and phase shifts of unsteady surface pressures are investigated with the aim of localizing the observed unsteady effects in a qualitative way. A more detailed quantitative analysis of unsteady and quasi-steady surface pressures is published by Wojciak et al. (2011). Fig. 5.17 shows the ratio of unsteady

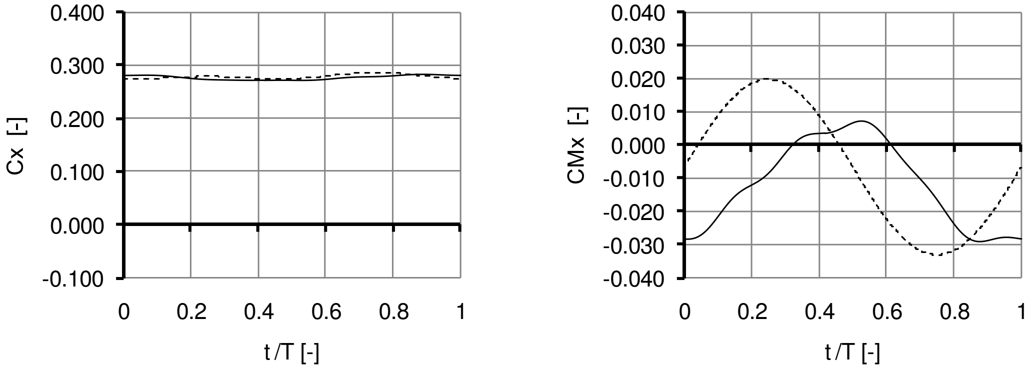

(a) Drag C_x

(b) Roll Moment C_{Mx}

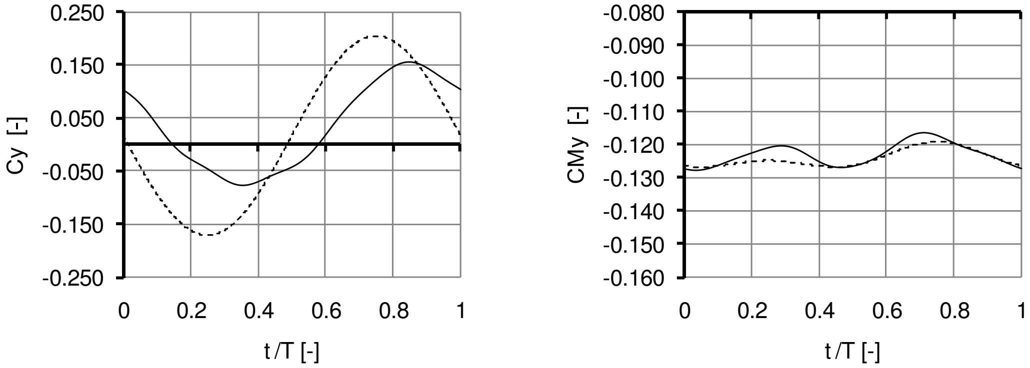

(c) Side Force C_y

(d) Pitching Moment C_{My}

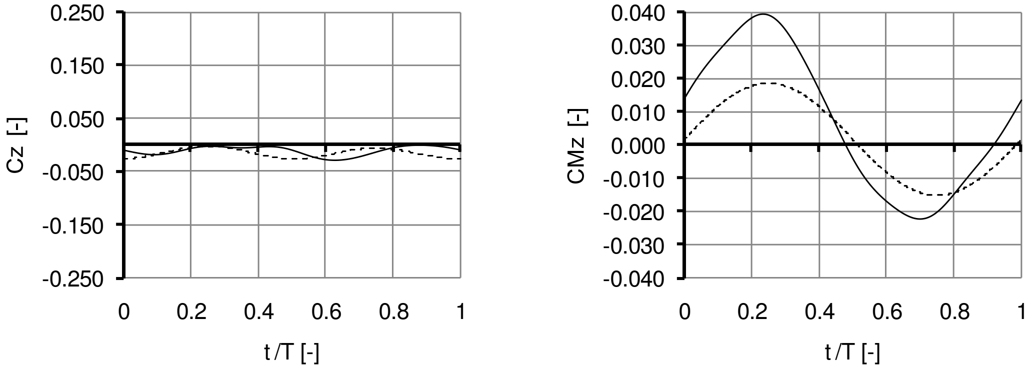

(e) Lift C_z

(f) Yaw Moment C_{Mz}

----- Quasi-Steady ——— Unsteady

Figure 5.16: Experimental unsteady and quasi-steady evolution of the aerodynamic loads for the investigated yawing motion of 2 Hz ±3°. For a better comparison the range of the vertical axis is kept constant for forces and moments, respectively.

over quasi-steady pressure amplitude for the two z-slices on the side of the vehicle. At the front half of the vehicle, the ratio is close to one, but rises significantly towards the rear of the vehicle reaching maximum values of $C_{p,US}/C_{p,QS} \approx 10$. Since the

	C_y	C_{Mx}	C_{Mz}
Unsteady Peak Amplitude	0.116	0.018	0.031
Quasi-Steady Peak Amplitude	0.188	0.026	0.017
US / QS Peak Amplitude	62%	68%	183%
US - QS Peak Amplitude	-0.072	-0.008	+0.014
Time Shift US vs QS ($\Delta t/T$)	+0.12	+0.22	-0.04

Table 5.2: Summary of experimental unsteady and quasi-steady results of the aerodynamic loads side force, roll and yaw moment for the investigated yawing motion of 2 Hz ±3°.

quasi-steady pressure amplitude may be close to zero, the ratio of unsteady over quasi-steady value can be misleading. Therefore, Fig. 5.18 additionally shows the differences between unsteady and quasi-steady pressure amplitudes, which are small at the front half of the vehicle with maximum values of $C_{p,US} - C_{p,QS} \approx 0.01$. Towards the rear end, the differences between unsteady and quasi-steady pressure amplitudes increase and peak values of $C_{p,US} - C_{p,QS} \approx 0.12$ are reached. .

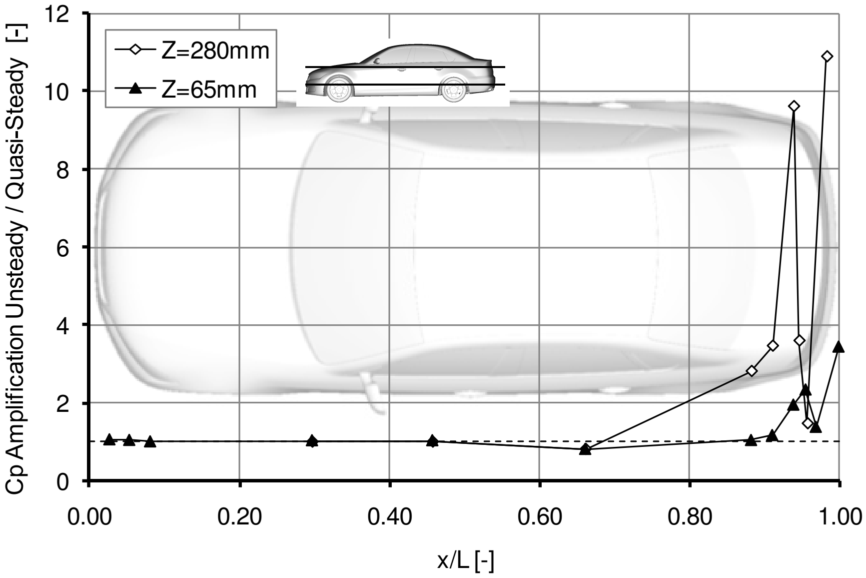

Figure 5.17: Amplification of unsteady over quasi-steady surface pressure amplitudes for two z-slices.

In Fig. 5.19 the phase shift between the unsteady pressure signal and the model motion is shown. At the front end the phase shift is very small but positive. At the height of the A-pillar, the phase shift turns negative reaching values of $\Delta t/T = -0.1$. Towards the rear of the vehicle, the phase shift turns positive again and rises significantly reaching peak values of over $\Delta t/T = 0.25$. These peak values occur directly behind the rear wheelhouse for the upper z-slice and at the rear corner for

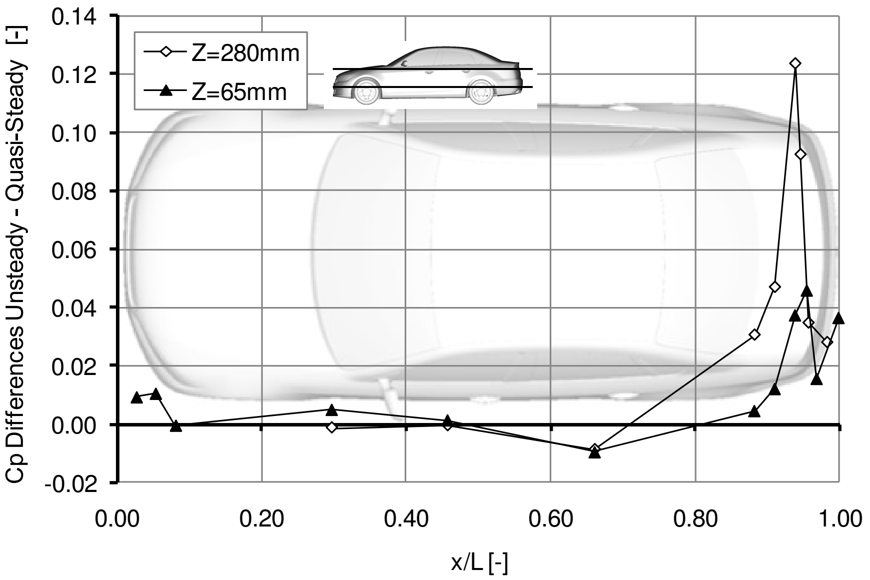

Figure 5.18: Differences between unsteady and quasi-steady surface pressure amplitudes for two z-slices.

the lower z-slice. For both z-slices the time shift decreases again for the pressure sensors positioned behind the rear corner of the vehicle.

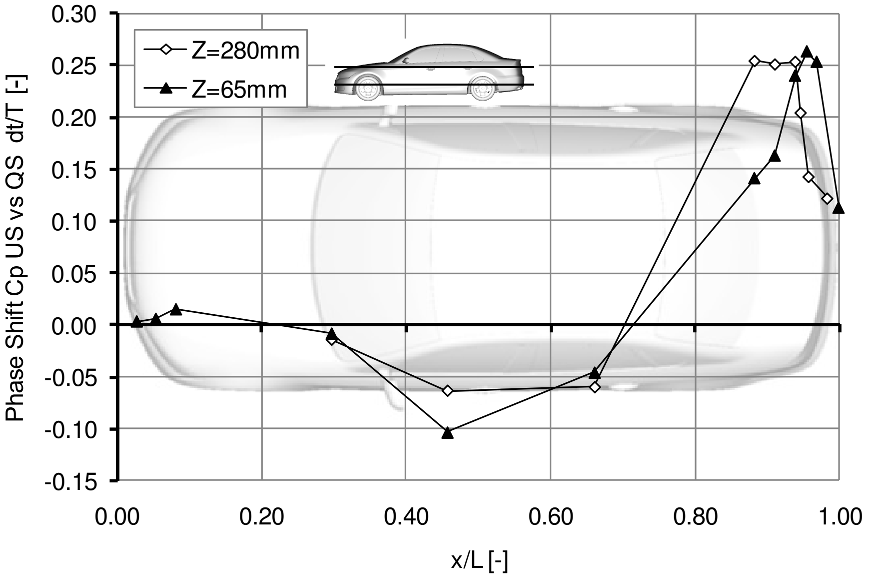

Figure 5.19: Time delay $\Delta t/T$ of unsteady to quasi-steady surface pressures for two z-slices.

Hence, the experiment confirms that unsteady effects occur at the rear end, while the front half of the vehicle shows only small differences between the unsteady and quasi-steady surface pressures. At the rear end, the unsteady increase in pressure amplitude as well as the positive time delay is also confirmed by the experiment.

5.3.3 Wake Flow

Finally, the time delay of the wake flow is investigated using the hotwire measurements described in Chap. 4.3.2. In Fig. 5.20, the evolution of the lateral velocity component is plotted for all seven measurement positions in the wake of the vehicle after applying an 11 Hz low-pass filter and periodic averaging. As described in Chap. 4.3.2, the evolution of the lateral velocity as captured by a probe fixed to the

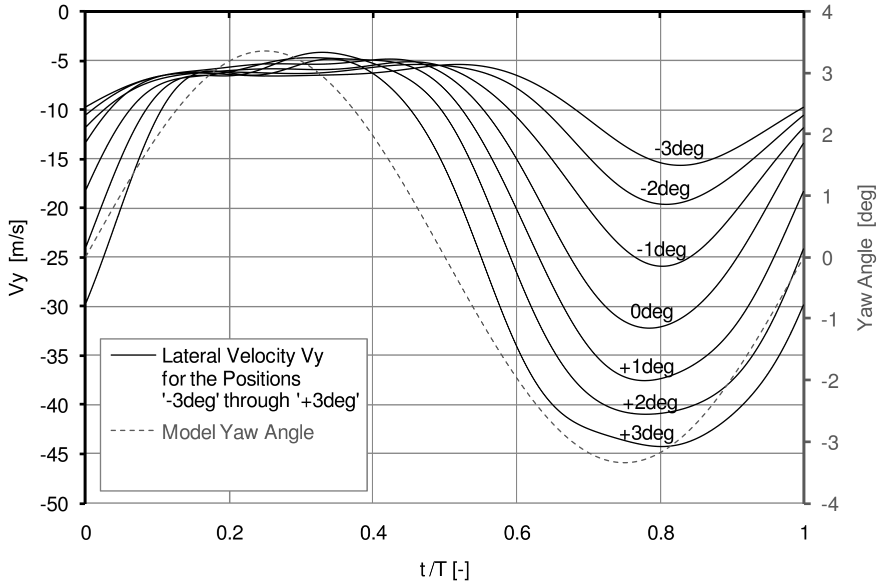

Figure 5.20: Evolution of the lateral velocity V_y at 7 positions in the region of high lateral velocity on the right rear side of the vehicle during a yawing motion of 2 Hz ±3°.

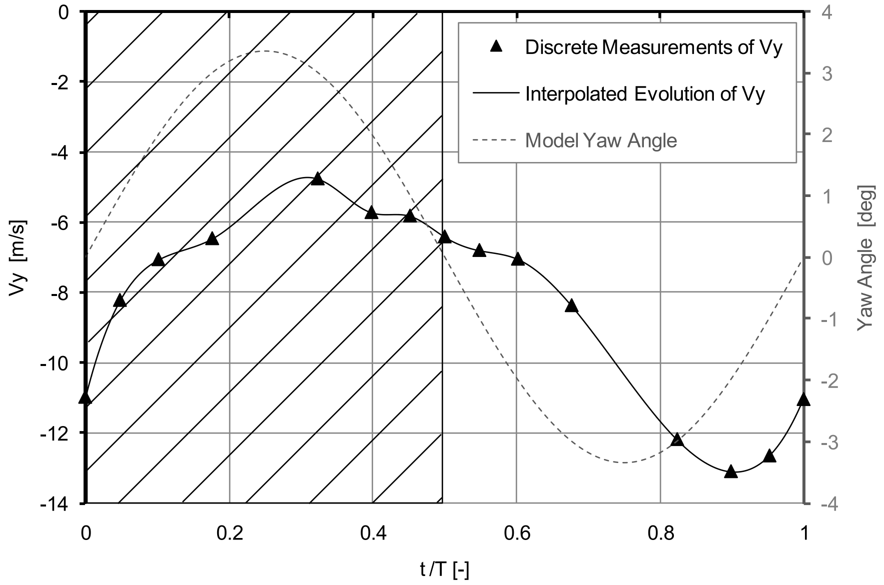

Figure 5.21: Interpolated evolution of the lateral velocity V_y measured by an imaginary probe fixed to the rear of the vehicle during yawing motion of 2 Hz ±3°.

model is derived from these seven measurement positions, Fig. 5.21. Since the validity of the hotwire measurements can only be guaranteed while the probe is located in the flow of high lateral velocity on the leeward side, the first half of the period when the probe is on the windward side of the vehicle has to be discarded (hatched area in Fig. 5.21).

When comparing the resulting evolution of lateral velocity V_y to the prescribed model motion, a normalized time delay of approximately $\Delta t/T \approx +0.15$ can be observed. Hence, the flow entering into the wake region from the leeward side, which is the main element of the wake topology, reacts to the change of the oncoming flow with a significant time delay that corresponds well with the numerical results.

Chapter 6

Sensitivities

In Chap. 5 unsteady phenomena were identified and verified for sedan vehicles underlining that the aerodynamic behavior during crosswind gusts cannot be correctly predicted by steady-state measurements or simulations. The identified unsteady phenomena and the proposed underlying mechanism were derived for a typical yet singular combination of gust parameters. In order to understand the aerodynamic behavior over the full range of relevant unsteady flow conditions, the influence of the principle gust parameters is analyzed in Chap. 6.1. Furthermore, the unsteady phenomena were so far only shown for sedan vehicles. Hence, the existence of similar effects for different vehicle types is investigated in Chap. 6.2. Finally, this leads to the essential question whether and how the unsteady behavior can be influenced by varying geometric parameters which is analyzed for a sedan vehicle in Chap. 6.3.

6.1 Gust Parameters

The generic gust event analyzed in Chap. 5 consists of a single sinusoidal peak at a frequency of 1 Hz, a vehicle speed of 140 km/h and an amplitude of 6° including two zero crossings. In order to understand the influence of these parameters but also to define the gust and the numerical setup for the geometry study, the parameters number of oscillations - or gust type - (Chap. 6.1.1), gust frequency (Chap. 6.1.2), vehicle speed (Chap. 6.1.3), gust amplitude (Chap. 6.1.4) and zero-crossing (Chap. 6.1.5) are investigated.

6.1.1 Gust Type

The single sinusoidal gust peak investigated in Chap. 5 was modeled after the public road measurements of Wojciak et al. (2010) and Mayer et al. (2007). However, looking at the gust event from a purely generic point of view, the number of oscillations can be varied from half an oscillation - resulting in a sinusoidal step gust - to several oscillations - resulting in a multiple-peak gust. In this case, five oscillations are chosen for the multiple-peak gust. The resulting functions of yaw angle over time are shown in Fig. 6.1. As the minimum and maximum yaw angles are not changed, the number of zero crossings is reduced to one for the sinusoidal step gust while the five-peak gust includes ten zero crossings.

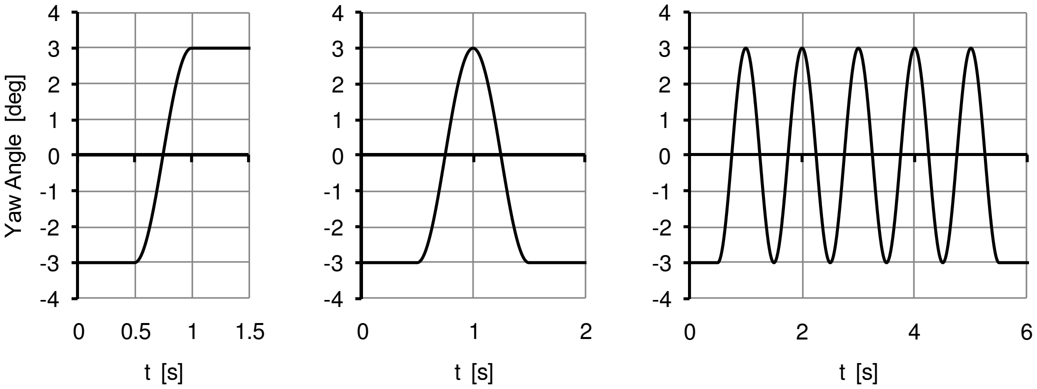

(a) Step Gust (b) Single-Peak Gust (c) 5-Peak Gust

Figure 6.1: Variation of yaw angle for (a) step gust, (b) single gust and (c) multiple-peak gust.

The results of Chap. 5 lead to the question whether unsteady phenomena can already be observed for a simple sinusoidal step change with just one zero crossing and whether their characteristics change compared to the single-peak gust. For the five-peak gust the analysis focuses on the question whether the unsteady phenomena are modified by a sequence of gust events. If this is not the case, averaging the results over several consecutive gust peaks is possible which would improve reproducibility.

Fig. 6.2 shows the resulting unsteady evolutions of side force C_y and yaw moment C_{Mz} for the two gust types and compares them to the corresponding quasi-steady approximations. For the sinusoidal step gust, the yaw moment shows a pronounced overshoot before reaching the steady-state level. In contrast, an over- or undershoot cannot be observed for the side force. However, the side force reaches the steady-state level with a time delay of approximately 0.15 s. Hence, the unsteady characteristics are very similar to the single-peak gust, although it is difficult to quantify the unsteady reduction in side force.

For the five-peak gust, the typical unsteady characteristics - identified already for the single-peak gust in Chap. 5 - can be observed in Fig. 6.2b: An overshoot and a negative time delay of the unsteady yaw moment and a reduced amplitude and a positive time delay of the side force. Furthermore, a variation of the minimum and maximum peak values can be observed over the five peaks. As expected, the peak values fluctuate due to the turbulent nature of parts of the flow. In both graphs the evolution of the roll moment is not displayed in order to improve clarity. The roll moment, however, behaves identically to the side force for both gust types.

More importantly, a modification of the aerodynamic loads over the sequence of gust oscillations cannot be observed. Therefore, averaging the peak values as described in Chap. 4.2.6 is justified.

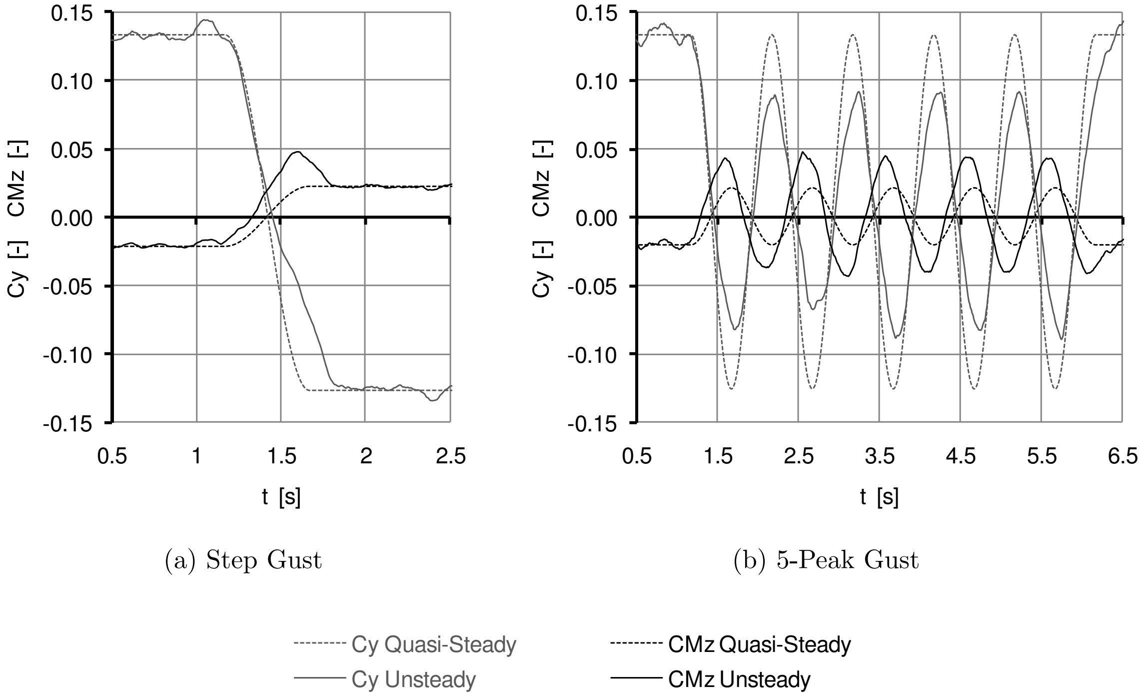

(a) Step Gust

(b) 5-Peak Gust

Figure 6.2: Aerodynamic side force C_y and yaw moment C_{Mz} for (a) step gust and (b) multiple-peak gust.

Magnification Factor Unsteady / Quasi-Steady

Cy	Step Gust	Single Gust	5-Peak Gust
Yaw Angle +3°	-	55%	65%
Yaw Angle −3°	-	-	67%

CMx	Step Gust	Single Gust	5-Peak Gust
Yaw Angle +3°	-	44%	62%
Yaw Angle −3°	-	-	66%

CMz	Step Gust	Single Gust	5-Peak Gust
Yaw Angle +3°	218%	207%	203%
Yaw Angle −3°	-	210%	205%

Table 6.1: Summary of magnification factors for the aerodynamic loads side force C_y, roll moment C_{Mx} and yaw moment C_{Mz} for the three gust types step gust, single gust and 5-peak gust.

In Table 6.1 the peak values as ratio of unsteady over quasi-steady values are summarized. As already mentioned, for the sinusoidal step gust a relative peak value can only be extracted for the yaw moment, which lies at 218%. The corresponding values of standard and five-peak gust are slightly smaller at 207% and 203%, respectively. The values for the minima in yaw moment are approximately at the same level.

The ratios of unsteady over quasi-steady side force and roll moment are slightly larger for the five-peak gust compared to the single-peak gust. This may be simply due to the improved accuracy as mentioned before but may be also due to an interaction between the consecutive gust peaks. This possible influence, however, does not prohibit the use of multiple-peak gusts and the associated averaging as long as the results are compared only among multiple-peak simulations.

Time Delay of Unsteady Loads

	Step Gust	Single Gust	5-Peak Gust
C_y	-	+0.04s	+0.04s
C_{Mx}	-	+0.11s	+0.12s
C_{Mz}	$-0.05s$	$-0.08s$	$-0.09s$

Table 6.2: Summary of the time delays of the unsteady aerodynamic loads side force C_y, roll moment C_{Mx} and yaw moment C_{Mz} for the three gust types step gust, single gust and 5-peak gust.

In Table 6.2, the time delays are summarized for the three types of gust simulations. Due to the nature of the step gust, a determination of time delays is not possible for the side force and roll moment. For the step gust the time shift of the yaw moment is smaller than for the other two gusts. Comparing the time delays between the single-peak and the five-peak gust, the results are very similar while the five-peak gust presumably provides an improvement in prediction accuracy.

Fig. 6.3 shows the unsteady and quasi-steady C_{Mz}-contributions of the front and the rear half of the vehicle. The overall behavior is identical for all three gust types. As for the single-peak gust, the differences between unsteady and quasi-steady loads are much larger at the rear than at the front for both the step gust and the five-peak gust. For the single peak, it was shown in Chap. 5.1 that the evolution of the rear yaw moment differs significantly from the quasi-steady approximation. Similarly, in the case of a single zero-crossing the unsteady rear yaw moment increases significantly at the arrival of the gust as opposed to the quasi-steady approximation which predicts a decrease in rear yaw moment. It reaches its maximum shortly after the zero-crossing just before the change in yaw angle is complete. After the peak, the unsteady rear yaw moment decreases again and converges towards the steady-state level of +3°. Hence, the characteristic behavior of the rear yaw moment, which is eventually responsible for the overshoot in total yaw moment, can already be observed for a single zero-crossing.

Compared to the single-peak and step gust, the five-peak gust provides a much more reliable quantification of the unsteady effects. At the front, the unsteady yaw moment

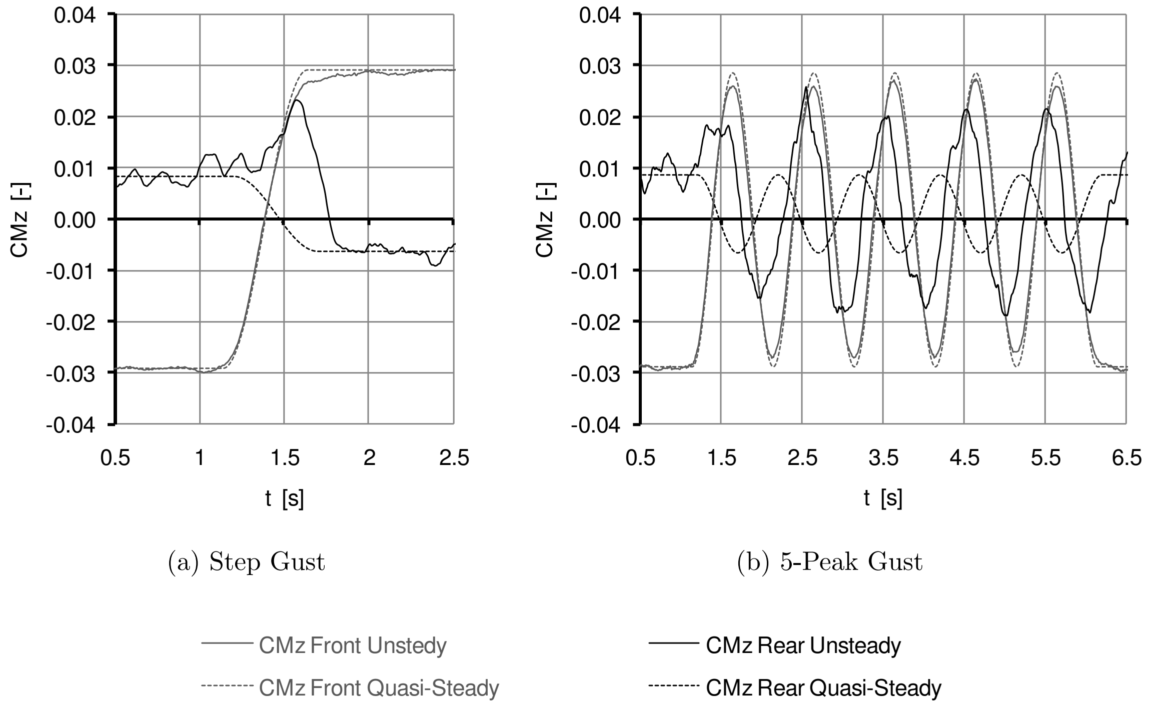

(a) Step Gust

(b) 5-Peak Gust

Figure 6.3: Front and rear contribution to the yaw moment C_{Mz} for (a) step gust and (b) multiple-peak gust.

decreases by approximately 7% while at the rear the amplitude is increased by as much as 160%. Even more importantly, a time shift of $\Delta t/T = 0.30$ occurs at the rear. Furthermore, the fluctuations at the front are very small. The variation in peak values is caused almost entirely by fluctuations at the rear which are visible before and after as well as during the gust. Obviously, these fluctuations are caused by variations of the surface pressure in the detached flow regions that occur towards the rear of the vehicle. Presumably, the detached region with the largest influence on the fluctuating peak values is the wake region at the rear of the vehicle.

Fig. 6.4 and Fig. 6.5 show the analysis of the flow at the rear of the vehicle as described in Chap. 4.2.5. Again, the overall behavior is identical for all three gust types. The flow entering into the wake area through the two control surfaces reacts with a time delay to the yaw angle change. While it is difficult to quantify this delay for the sinusoidal step gust and even for the single-peak gust (compare Fig. 4.1a), the use of multiple oscillations provides an improved accuracy leading to a time delay of $\Delta t/T = 0.14s$. The five-peak gust also shows that during a sequence of yaw changes at this Strouhal number of $Sr = 0.12$ the unsteady amplitude in average lateral flow velocity is much smaller than the quasi-steady amplitude. This means that during the sequence of yaw changes the wake flow never fully reaches the steady-state configuration.

The analysis of the parameters surface pressure C_p, total pressure $C_{p,tot}$ and dimensionless x-velocity $(V_x/U)^2$ at the rear side of the vehicle (Fig. 6.5) is particularly interesting for the sinusoidal step gust as it presents the behavior for a single zero-crossing.

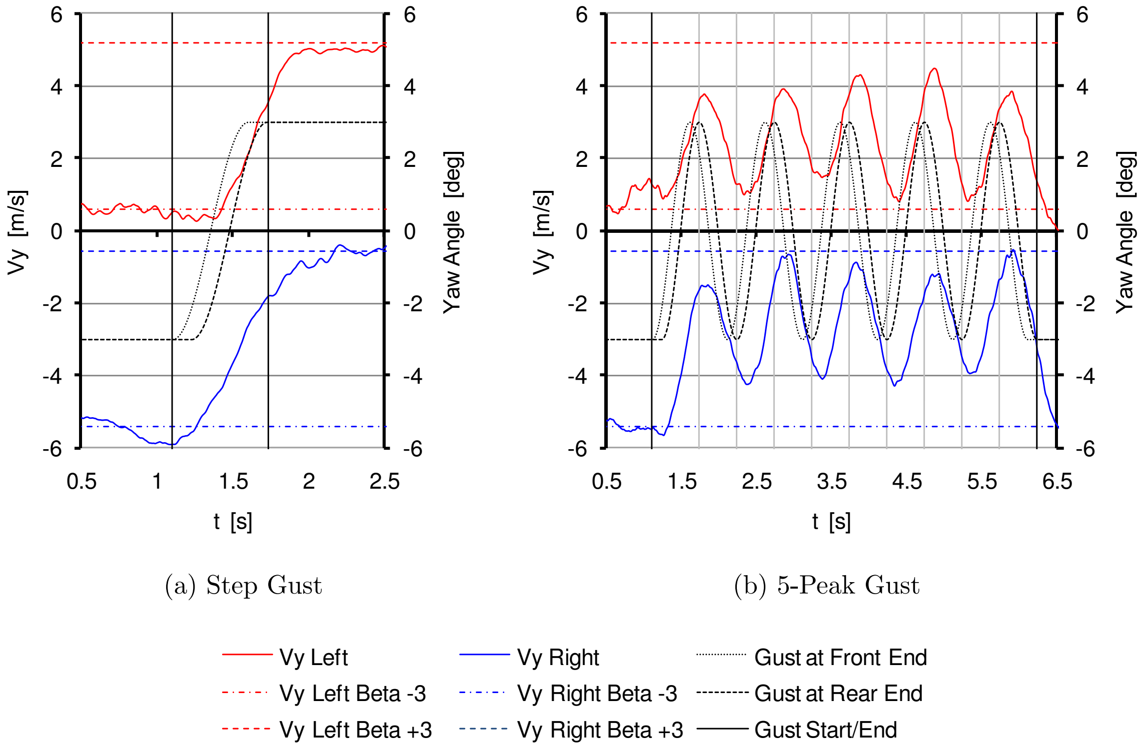

(a) Step Gust

(b) 5-Peak Gust

Figure 6.4: Evolution of the lateral velocity V_y averaged over two control surfaces in the left and right wake region for (a) step gust and (b) multiple-peak gust.

Total pressure $C_{p,tot}$ reacts to the change of yaw angle even before the gust arrives at the rear end, which corresponds approximately to the arrival of the gust at the front of the vehicle. At the same time, the velocity $(V_x/U)^2$ increases on the right (new windward) side while it decreases on the left (new leeward) side. Although this variation is very plausible due to the change of wind- and leeward sides, it does not correspond to the quasi-steady behavior. As can be seen in Fig. 6.5a, after this immediate reaction of $(V_x/U)^2$ the curves converge towards a common level which corresponds to the steady-state values. The first reaction in $(V_x/U)^2$ overcompensates the change in total pressure resulting in an increase of surface pressure C_p on the left (new leeward) side and a decrease on the right (new windward) side. Again, this does not correspond to the quasi-steady behavior. Similarly to the evolution of velocity, surface pressure reaches the steady-state values with a time delay of approximately $\Delta t = 0.25s$.

Hence, for the sinusoidal step gust the analysis of the flow at the rear of the vehicle perfectly confirms the unsteady mechanism presented in Chap. 5.2. When the cross-wind changes its direction the total pressure and the velocity obviously increase on the new windward side while they decrease on the new leeward side. However, since the topology of the wake flow reacts with a time delay, fluid still enters into the wake region primarily from the right, now the windward side further increasing the velocity at the right rear of the vehicle. This results in very low surface pressures on the right rear side and higher surface pressures on the left rear side explaining the increase in

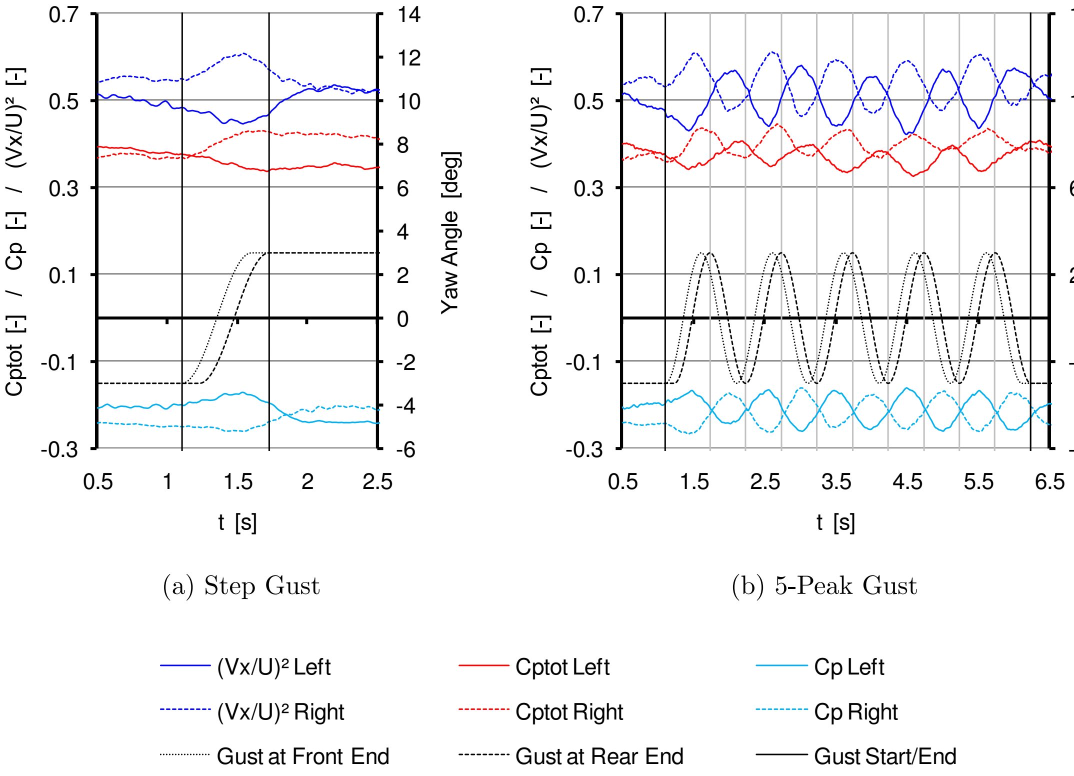

(a) Step Gust

(b) 5-Peak Gust

Figure 6.5: Evolution of the averaged parameters surface pressure C_p, total pressure $C_{p,tot}$ and dimensionless x-velocity $(V_x/U)^2$ on the rear side of the vehicle for (a) step gust and (b) multiple-peak gust.

rear contribution to the yaw moment shortly after the zero-crossing. Eventually, all parameters converge to the steady-state level.

For a sequence of zero-crossings the basic form of the unsteady mechanism described above is repeated for alternating wind directions. Again, the five-peak gust permits a more accurate quantification of the time shifts leading to $\Delta t(C_p)/T = +0.28$, $\Delta t(C_{p,tot})/T = -0.12$ and $\Delta t(V_x)/T = +0.29$.

It can be concluded that the unsteady phenomena described in Chap. 5.1 occur already during a sinusoidal step gust with a single zero-crossing. Furthermore, the analysis of the five-peak gust shows that at a gust frequency of 1 Hz these phenomena are not significantly modified by the succession of several generic gust oscillations. The sinusoidal step gust, representing the most basic element of a crosswind gust event, is ideal for investigating the underlying unsteady effects and confirms the unsteady mechanism as presented in Chap. 5.2. On the other hand, the five-peak gust permits a significant improvement in prediction accuracy of time delays and magnification factors by averaging over multiple oscillations. Hence, in order to allow for a quantitative comparison between different simulations and thus a more detailed investigation of the sensitivities of parameters, only multiple-peak gusts are used in the following.

The influence of the number of gust oscillations can be summarized as follows:

- The characteristic unsteady effects already occur for a sinusoidal step gust and are not significantly altered for a sequence of gust oscillations.
- The sinusoidal step gust, representing the most basic element of a yaw change, confirms the proposed unsteady mechanism (Chap. 5.2).
- Multiple-peak gusts provide a significant improvement in reproducibility by averaging over multiple peaks.

6.1.2 Gust Frequency

Since in real-world vehicles are exposed to gust events featuring a broad spectrum of excitation frequencies, it is important to understand the behavior of the identified unsteady phenomena over the range of relevant frequencies. Hence, it is necessary to analyze the dependency of magnification factors and time delays on gust frequency and to understand the reasons for possible variations. This investigation automatically leads to the identification of frequencies, where the unsteady effects reach a maximum or minimum, which may serve as critical testing cases in a vehicle development process.

Fig. 6.6a shows the variation of the magnification factor over the frequency range of 0.25 Hz to 4 Hz for the side force, roll and yaw moment. For all three components the magnification factors start at slightly above 1 at 0.25 Hz. With increasing frequencies the magnification factors of side force and roll moment decrease while they increase for the yaw moment. At $1.25 - 1.5$ Hz a maximum magnification of 220% is reached for the yaw moment. Afterwards it decreases continuously crossing the 100%-level between 3 Hz and 4 Hz. The magnification factors of side force and roll moment reach a local minimum at a slightly larger frequency of 1.75 Hz. The minimum ratio of unsteady over quasi-steady amplitude reaches approximately 40% for the side force while it decreases almost to zero for the roll moment. Beyond the local minima, the magnification factors of side force and roll moment increase again to approximately 50% at 3 Hz to 4 Hz.

When analyzing the magnification factors it has to be taken into account that the unsteady amplitude is determined as the difference between filtered minimum to maximum peak value. As the filter cut-off frequency is not varied, an increase in amplitude due to fluctuations around the average value has to be taken into account at low frequencies. This may explain the unexpected magnification factors of > 1 for all three components at 0.25 Hz.

As described in Chap. 2.1.3, the magnification factors are expected to tend towards 1 for frequencies approaching zero and towards 0 for infinitely large frequencies. Corresponding to the theoretical behavior, the unsteady amplitudes of side force, roll and yaw moment are close to the quasi-steady values for small gust frequencies and decrease in value for the largest investigated gust frequencies. Although the observed

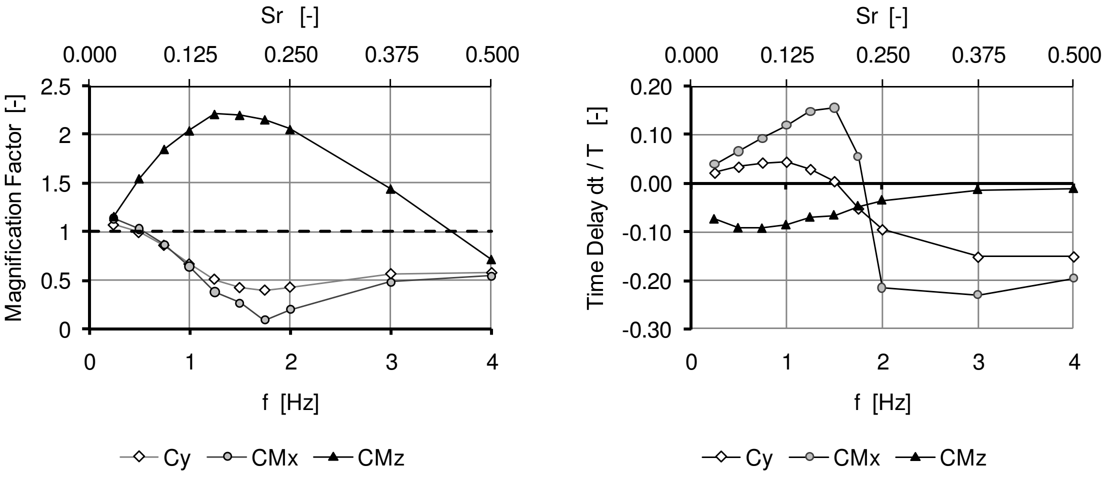

(a) Amplitude

(b) Time Delay

Figure 6.6: Variation of (a) amplitude and (b) time delay of the aerodynamic loads side force C_y, roll moment C_{Mx} and yaw moment C_{Mz} over gust frequency.

behavior does not contradict the expected theoretical behavior, the investigated range of gust frequencies is too small to permit a further comparison.

Fig. 6.6b shows the time delays $\Delta t/T$ for the side force, roll and yaw moment. Similar to the time delays described in Chap. 5 the yaw moment has a negative time shift at 0.25 Hz while the side force and roll moment feature positive time shifts. For all three components the absolute time delays first increase with increasing frequencies. The time delay in yaw moment reaches a minimum at $0.5 - 0.75$ Hz, followed by the maxima in side force at $0.75 - 1$ Hz and in roll moment at $1.25 - 1.5$ Hz. After the minimum, the time delay of the yaw moment slowly increases towards zero with increasing frequencies. In comparison, the time shift of side force and roll moment feature zero-crossings between $1.5 - 2$ Hz, thereby significantly changing the temporal composition of the three load components. Whether the time delays of side force and roll moment also tend towards zero for large frequencies cannot be concluded from the chosen range of frequencies. However, the expected tendency of the time delays towards zero for very low frequencies can be confirmed.

Fig. 6.7 shows the variation in amplitude of the lateral velocity at the rear of the vehicle and the corresponding time delays. While the relative time delay $\Delta t/T$ of the wake flow increases significantly with increasing frequencies, the amplitude decreases at the same time which reduces the effect of the time delay. The result of these opposite trends can be seen in Fig. 6.8b where a peak in the unsteady amplitude of the rear yaw moment occurs between $1.25 - 1.75$ Hz. For lower frequencies the amplitude is reduced due to the smaller relative time delay of the wake flow. For higher frequencies it is reduced due to the smaller amplitude of the leeward flow velocities, which basically means that the inertial behavior of the wake flow prevents a complete adaptation to the peak yaw angle.

At the front half of the vehicle, the contribution to the yaw moment decreases with

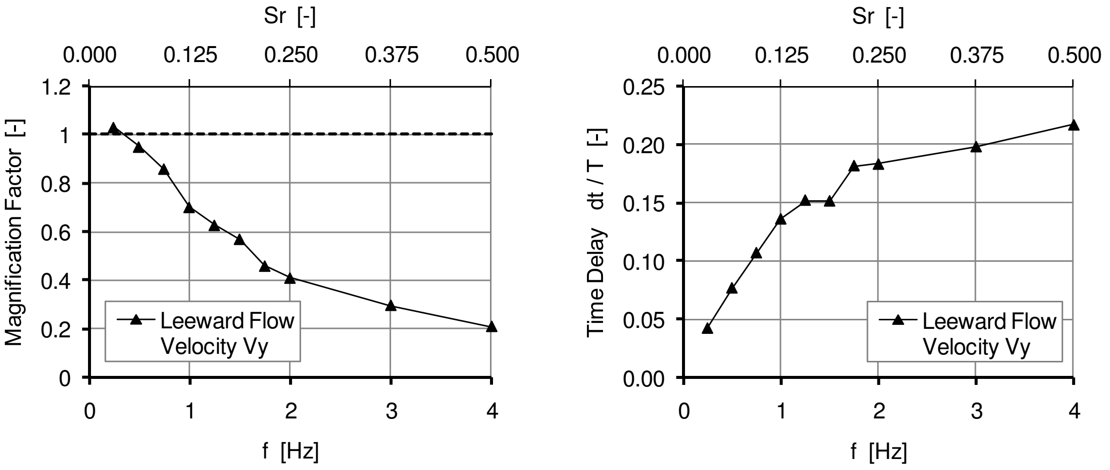

(a) Amplitude (b) Time Delay

Figure 6.7: Variation of (a) amplitude and (b) time delay of the leeward flow velocity V_y over gust frequency.

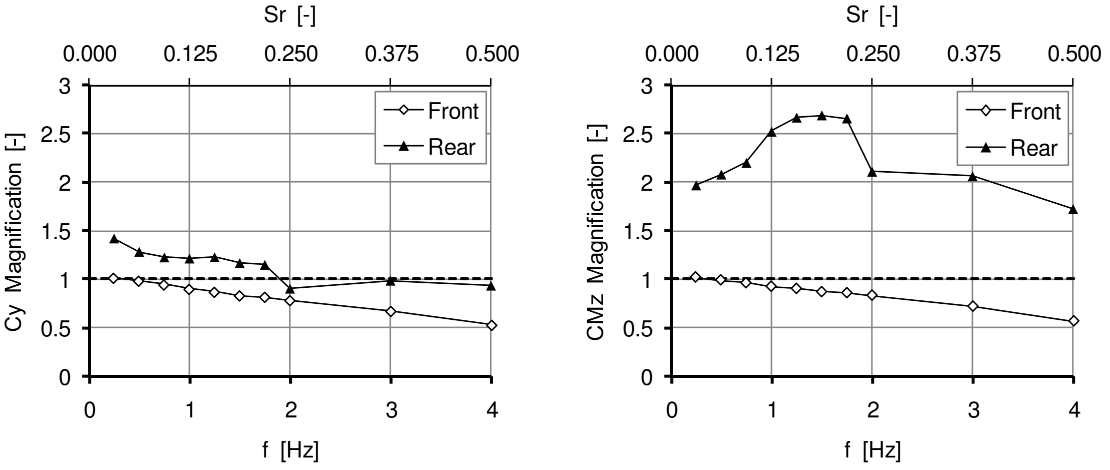

(a) Side Force C_y (b) Yaw Moment C_{Mz}

Figure 6.8: Variation of the amplitude of (a) side force C_y and (b) yaw moment C_{Mz} at the front and the rear of the vehicle over gust frequency.

increasing gust frequency. It can be assumed that a similar effect also occurs at the rear of the vehicle, which is however concealed by the dominating influence of the wake region over the investigated frequency range. For the contribution of the front, the reduction in unsteady amplitude becomes relevant even at frequencies as low as 1 Hz. At 4 Hz the magnification factor is reduced to approximately 0.5. For the side force C_y the unsteady effects at the rear end have a smaller impact. Thus, a peak in the rear contribution - such as for the yaw moment - does not occur for the side force. Instead, the magnification factor of the rear half of the vehicle is reduced with increasing frequency. Apart from the strong dependency on the gust frequency, it is remarkable that even at the lowest investigated frequency of 0.25 Hz a significant magnification of the rear contribution is apparent for the side force and in particular for the yaw moment.

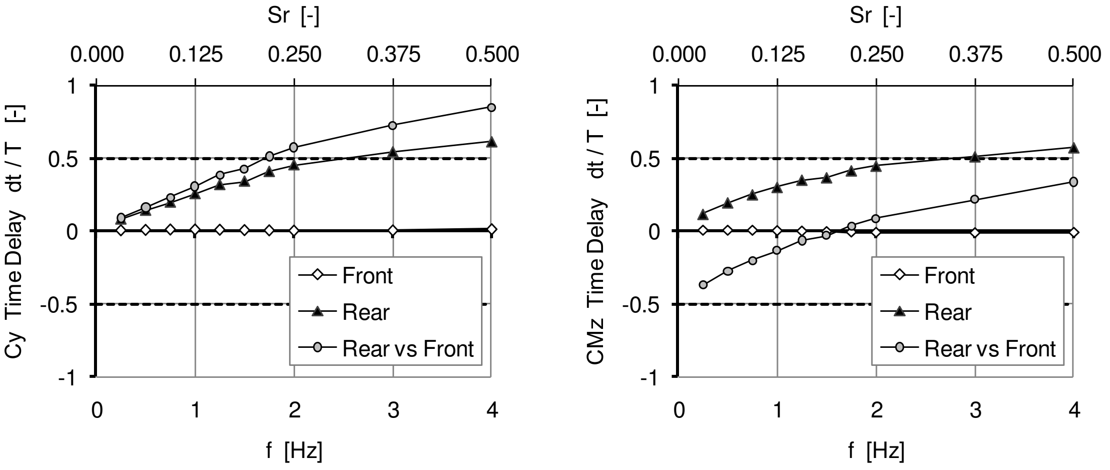

(a) Side Force C_y

(b) Yaw Moment C_{Mz}

Figure 6.9: Variation of the time delay of (a) side force C_y and (b) yaw moment C_{Mz} at the front and the rear of the vehicle over gust frequency.

Fig. 6.9 shows the variation of the time delays of the front and rear contributions over the investigated frequency range. For both side force and yaw moment, the time shift of the front contribution remains zero for all investigated frequencies. In comparison, the relative time delay of the rear contribution also starts at approximately zero but increases with increasing frequency. However, differences become apparent when plotting the relative time delay between front and rear. For the side force the constant-yaw contribution of the front and the rear point in the same direction. Therefore, the relative time delay between front and rear side force starts at approximately zero and reaches $\Delta t/T = 0.5$ at approximately 1.75 Hz. At this frequency, which corresponds to the local minimum of overall side force, front and rear peaks are exactly inversed. In comparison, for the yaw moment the constant-yaw contributions of front and rear are of opposite signs. The time delay between front and rear starts at $\Delta t/T = -0.4$ at 0.25 Hz and reaches zero between 1.5 Hz and 1.75 Hz. In this case, the peaks of front and rear contribution coincide and are of the same sign. However, the zero-crossing in relative time delay between front and rear contribution does not correspond to the overall maximum of the unsteady yaw moment which lies at $1.25 - 1.5$ Hz. This is presumably caused by the reduction in unsteady front and rear amplitude which is more pronounced at 1.75 Hz than at the lower frequencies.

Fig. 6.9 also shows the influence of the distance between the front and the rear of the vehicle. Since the vehicle speed remains constant at $U = 140$ km/h, the time for the gust to travel from the front to the rear is also constant at $\Delta t = 0.12$ s. However, as the duration of a gust oscillation decreases with increasing gust frequency the relative time delay $\Delta t/T$ increases. Hence, the length of the vehicle gains in importance with increasing gust frequency.

It can be concluded that the overall characteristics of the magnification factors correspond to the theoretical behavior. Differences to the theoretical behavior, however, occur in the frequency range at around $1-2\,\mathrm{Hz}$ where magnification factors > 1 occur for the yaw moment. The magnification factors in this frequency range are determined by two factors: The variation of the relative time delay between front and rear contribution as well as the variation of front and rear amplitudes. In addition to the magnification factors, the time delays of the aerodynamic loads exhibit a strong dependency on the gust frequency which may be crucial for vehicle dynamics. Furthermore, it is remarkable that even at the lowest frequency of $0.25\,\mathrm{Hz}$ the unsteady effects at the rear cause a significant magnification of the rear yaw moment. However, due to the time delay between front and rear they do not cause an increase in overall yaw moment.

The influence of the gust frequency can be summarized as follows:

- Corresponding to the theoretical behavior (compare Davenport (1961)), the unsteady amplitudes of side force, roll and yaw moment are close to the quasi-steady values for small gust frequencies and decrease in value for the largest investigated gust frequencies.
- At around $1-2\,\mathrm{Hz}$ the described unsteady effects result in magnification factors >1 for the yaw moment with a maximum at $1.25\,\mathrm{Hz}$ and local minima for the magnification of side force and roll moment.
- The intensity of the magnification is determined by:
  - The time delay between the front and rear contributions.
  - The unsteady amplitudes of the front and rear contributions.
- Both amplitude and time delay of the rear contribution are again influenced by the strength and the time delay of the unsteady leeward flow.
- The time delays of side force, roll and yaw moment strongly depend on the gust frequency.

6.1.3 Vehicle Speed

Similar to the gust frequency, vehicles are exposed to crosswind gusts at a wide range of driving speeds. Hence, in the following the occurrence and variation of the unsteady phenomena is investigated over a range of vehicle speeds from $70\,\mathrm{km/h}$ to $220\,\mathrm{km/h}$. Again, the aim is to understand the influence of the vehicle speed on the unsteady effects. In order to keep the minimum and maximum yaw angles constant over the range of vehicle speeds, the lateral crosswind velocity is adjusted accordingly.

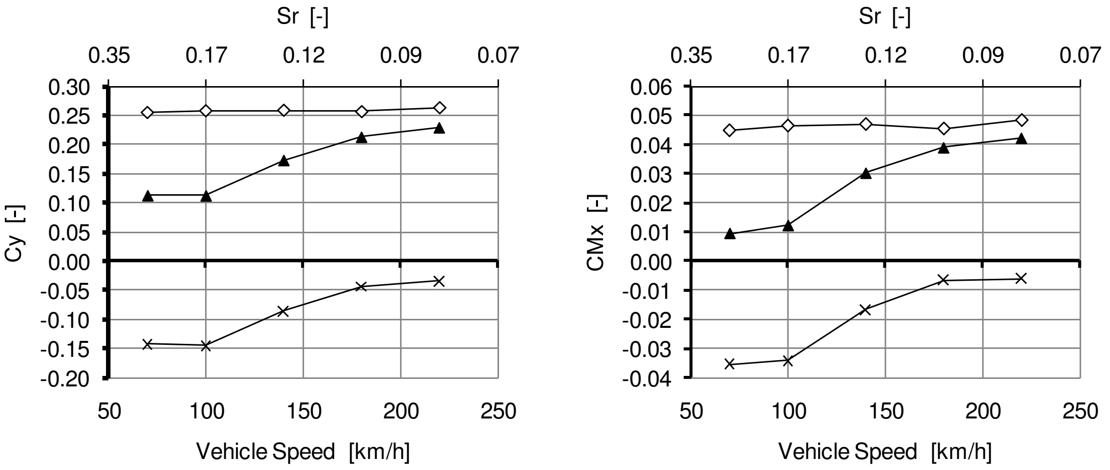

(a) Side Force C_y (b) Roll Moment C_{Mx}

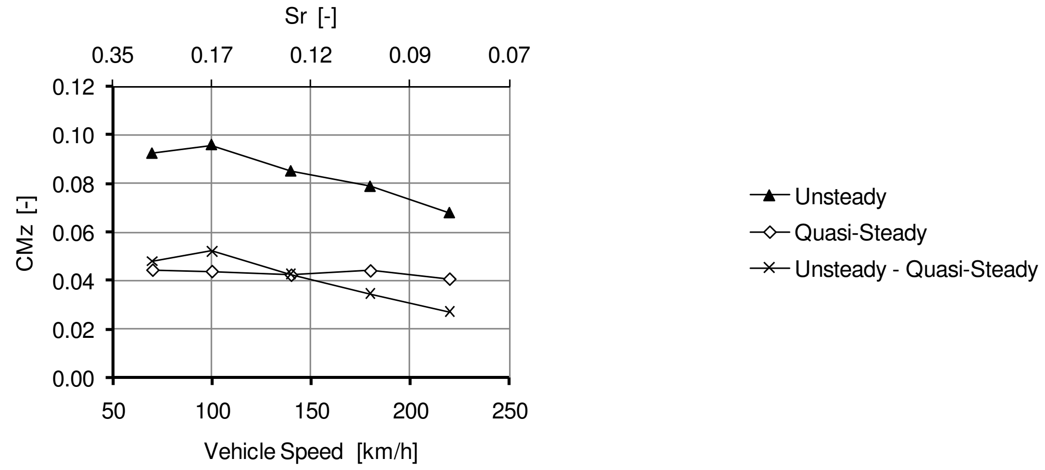

(c) Yaw Moment C_{Mz}

Figure 6.10: Variation of the amplitude of (a) side force C_y, (b) roll moment C_{Mx} and (c) yaw moment C_{Mz} over vehicle speed.

Fig. 6.10 shows the unsteady and quasi-steady amplitudes of side force, roll and yaw moment. For all three components the variation of the quasi-steady amplitudes over the range of investigated vehicle speeds is small compared to the corresponding unsteady variations. Similar to the behavior observed for the standard gust, the unsteady values of side force and roll moment are always smaller and the unsteady yaw moment is always larger than the corresponding quasi-steady values. The differences between unsteady and quasi-steady amplitudes are largest at 100 km/h for the side force and the yaw moment while for the roll moment the maximum is observed at 70 km/h. With increasing vehicle speed the differences between unsteady and quasi-steady amplitudes are reduced significantly.

In order to demonstrate the absolute magnitude of the unsteady aerodynamic loads,

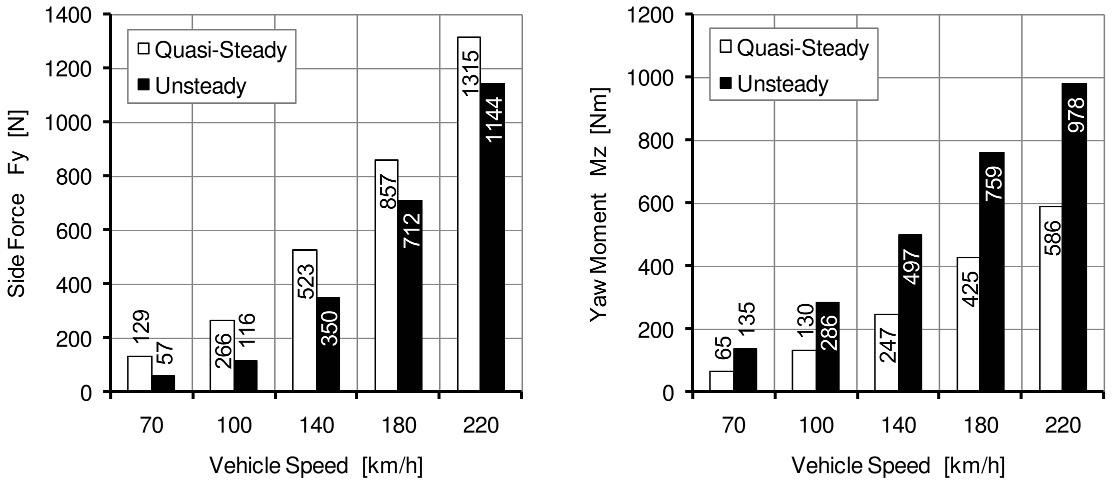

(a) Side Force F_y

(b) Yaw Moment M_z

Figure 6.11: Variation of the absolute amplitude of (a) side force F_y and (b) yaw moment M_z over vehicle speed.

Fig. 6.11 plots the side force and yaw moment before non-dimensionalization. At 220 km/h the amplitude of the unsteady side force corresponds to the equivalent weight of more than 100 kg. At the same vehicle speed the amplitude of the unsteady yaw moment corresponds to the equivalent weight of approximately 50 kg that is attached at the rear end - at a distance of about 2 m from the center of gravity. While the side force decreases by approximately 70% when the vehicle speed is reduced to 140 km/h, the yaw moment still amounts to almost 500 Nm, which corresponds to a reduction of less than 50%.

Building on the results of the preceding chapter, first the time delay between the contributions of the front and the rear of the vehicle is analyzed with the aim of explaining the variation of the unsteady effects over the range of vehicle speeds. Fig. 6.12 shows the variation of the time delay of front and rear contributions to the side force C_y and the yaw moment C_{Mz}. Again, the time delay at the front remains zero over the whole range of vehicle speeds. For both side force and yaw moment the time shift of the rear contribution remains positive for all vehicle speeds but is reduced from approximately $\Delta t/T = 0.4$ at 70 km/h to $\Delta t/T = 0.2$ at 220 km/h. Similar to the investigation of the gust frequency, the differences between side force and yaw moment are explained by the time shift between the front and the rear contributions. At 100 km/h, which corresponds to the maximum of the unsteady effects, the contributions of the front and the rear are approximately in phase for the yaw moment while they are in antiphase for the side force.

In addition to the phase shift between front and rear contributions, the differences in the integral aerodynamic loads may also be caused by variations of the local unsteady amplitudes. Fig. 6.13 indicates the differences between unsteady and quasi-steady yaw moment contributions $C_{Mz,US} - C_{Mz,QS}$. In order to analyze the local contributions, the vehicle geometry is split up into six regions along the length of the

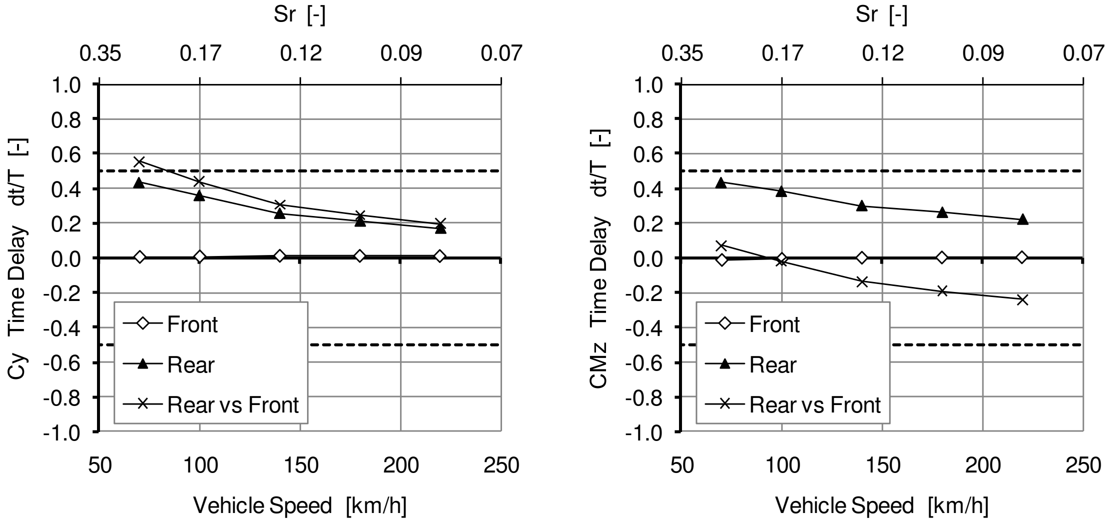

(a) Side Force C_y (b) Yaw Moment C_{Mz}

Figure 6.12: Variation of the time delay of (a) side force C_y and (b) yaw moment C_{Mz} at the front and the rear of the vehicle over vehicle speed.

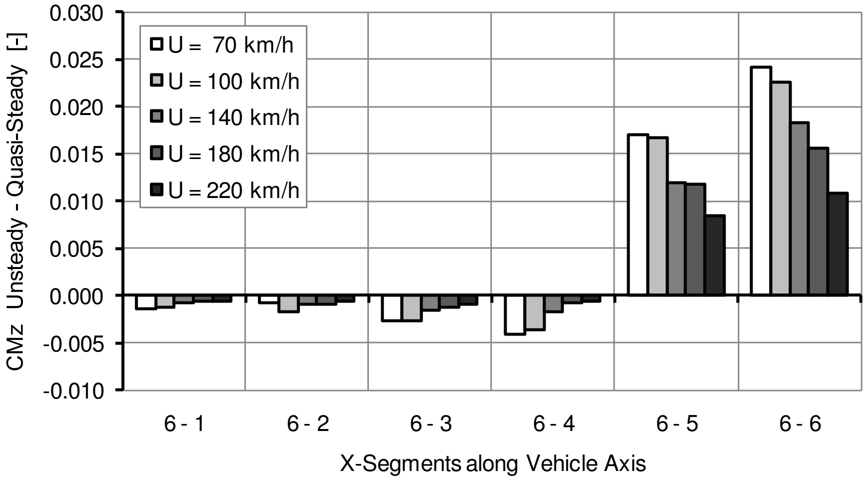

Figure 6.13: Variation of the differences between unsteady and quasi-steady yaw moment amplitudes in the x-segments of the vehicle over vehicle speed.

vehicle. In the first four regions 6-1 through 6-4 the differences between unsteady and quasi-steady yaw moment are negative for all investigated vehicle speeds, i.e. the local amplitudes are reduced in the unsteady case as already shown in Chap. 5.1. In comparison, at the rear end (regions 6-5 and 6-6) the difference $C_{Mz,US} - C_{Mz,QS}$ is positive for all vehicle speeds. However, more importantly, the differences between unsteady and quasi-steady amplitudes are reduced for all six regions with increasing vehicle speed.

The reduction of the differences between unsteady and quasi-steady local amplitudes

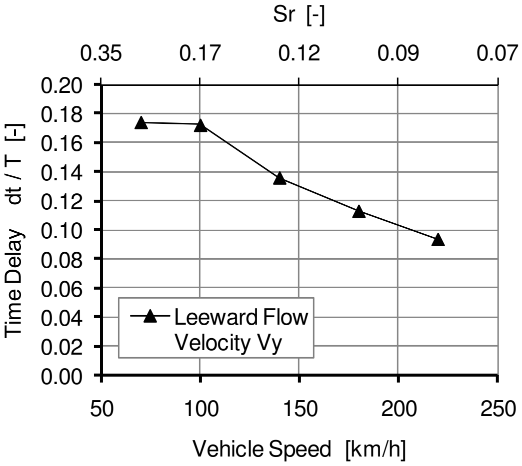

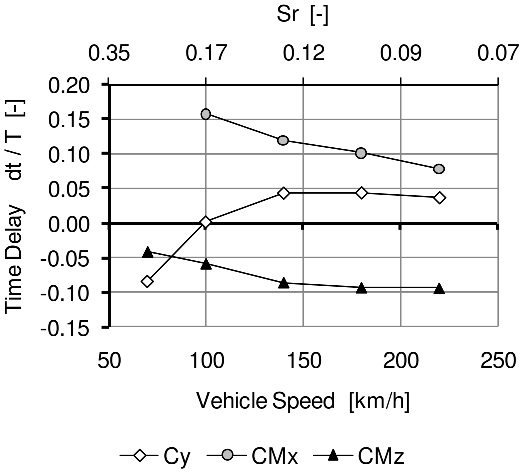

Figure 6.14: Variation of the time delay of the leeward flow velocity V_y over vehicle speed.

Figure 6.15: Variation of the time delay of the aerodynamic loads over vehicle speed.

can be explained by the time delay of the wake flow. As shown in Fig. 6.14, the time delay of the wake flow reaches a maximum of $\Delta t/T \approx 0.17$ at 70 km/h and 100 km/h. For increasing velocities the time delay is reduced and reaches $\Delta t/T \approx 0.09$ at 220 km/h. Hence, the reduction of the time delay of the wake flow results in a reduction of the local unsteady effects.

Therefore, it can be concluded that the reduction in unsteady effects at high vehicle speeds is caused by the variation of the time delay between front and rear on the one side and by the reduction of the local unsteady effects on the other side. Similar to the investigation of the gust frequency, the unsteady effects in the integral aerodynamic loads are hence influenced by two factors: The local unsteady amplitudes and the time shift between front and rear contribution.

Fig. 6.15 presents the variation of the time delays of side force, roll and yaw moment over the investigated range of relevant vehicle speeds. The characteristics of the time delays are very different for the three components: The time delays of the roll and yaw moments decrease while the time delay of the side force first increases before it also decreases again. However, if the time delays are plotted against the Strouhal number and are compared to the results of Chap. 6.1.2, the results of the two investigations complement each other almost perfectly (Fig. 6.16b). The same is true for the magnification factor (Fig. 6.16a) and the time delay of the wake flow (Fig. 6.17), where the variation of vehicle speed and gust frequency produce almost identical curves for all three components. Hence, in the investigated range of Strouhal and Reynolds numbers the unsteady phenomena are dominated by the Strouhal number while the influence of the Reynolds number is small.

Concluding the investigation of different vehicle speeds, the results can be summarized as follows:

- The unsteady effects in the integral aerodynamic loads are largest at 100 km/h

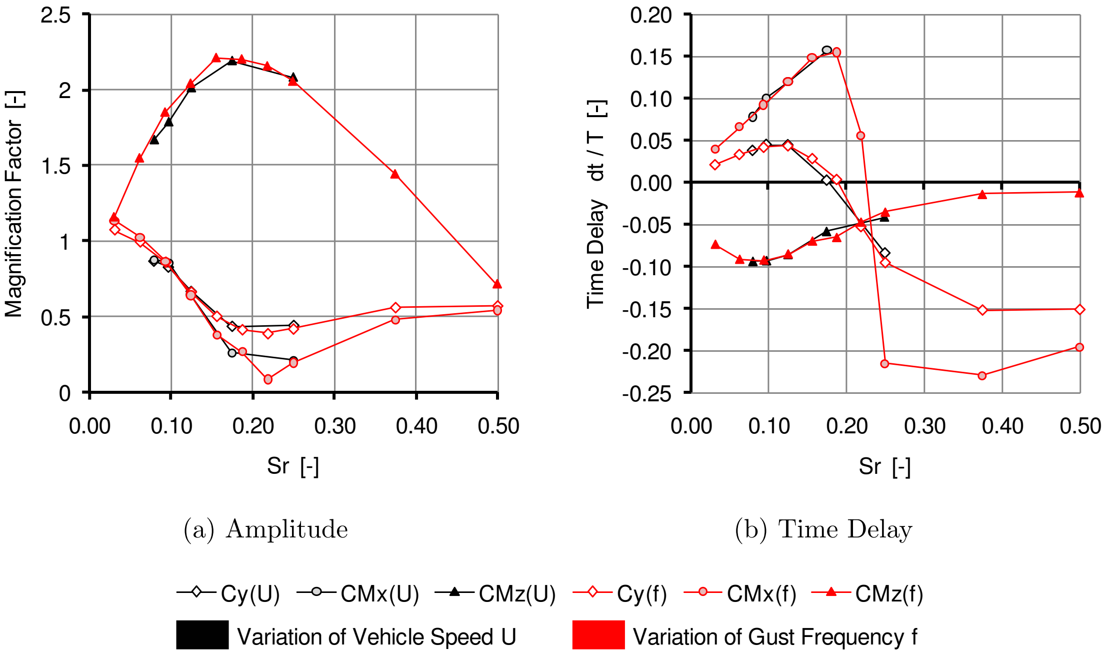

(a) Amplitude

(b) Time Delay

Figure 6.16: Variation of (a) amplitude and (b) time delay of side force C_y, roll moment C_{Mx} and yaw moment C_{Mz} with the Strouhal number Sr.

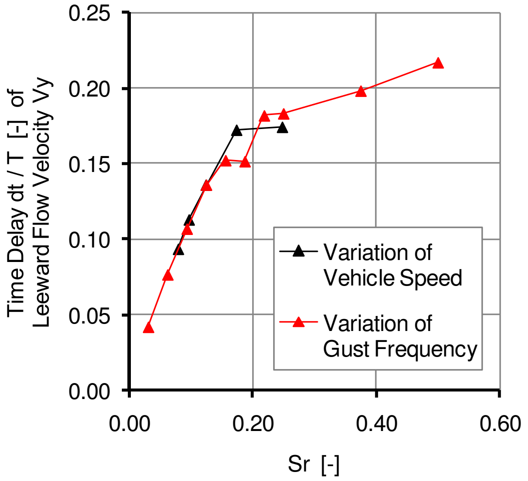

Figure 6.17: Variation of the time delay of the leeward flow velocity V_y with the Strouhal number Sr.

and are reduced significantly for larger vehicle speeds.

- For the investigated range of vehicle speeds, the influence of the Reynolds number is small. The unsteady phenomena predominantly depend on the Strouhal number.

- Similar to Chap. 6.1.2, the variation of the unsteady effects over the range of vehicle speeds depends on the two factors: Time delay and magnification of the rear contribution, which is mainly influenced by the unsteady behavior of the wake flow.

6.1.4 Gust Amplitude

After analyzing the gust type, gust frequency and vehicle speed, the influence of the gust amplitude is investigated in the following. Similar to the gust frequency, Wojciak et al. (2010) showed that a range of gust amplitudes occurs in real world. Hence in the following, the amplitude of a standard 1 Hz 5-peak gust is varied from 3° to 60°, which corresponds to symmetrical gusts of -1.5°/+1.5° and -30°/+30°, respectively. Although Wojciak et al. (2010) did not record gust events with amplitudes larger than 12°, simulations with amplitudes of 18°, 30° and 60° are included since such large variations in yaw angle typically occur at crosswind testing facilities.

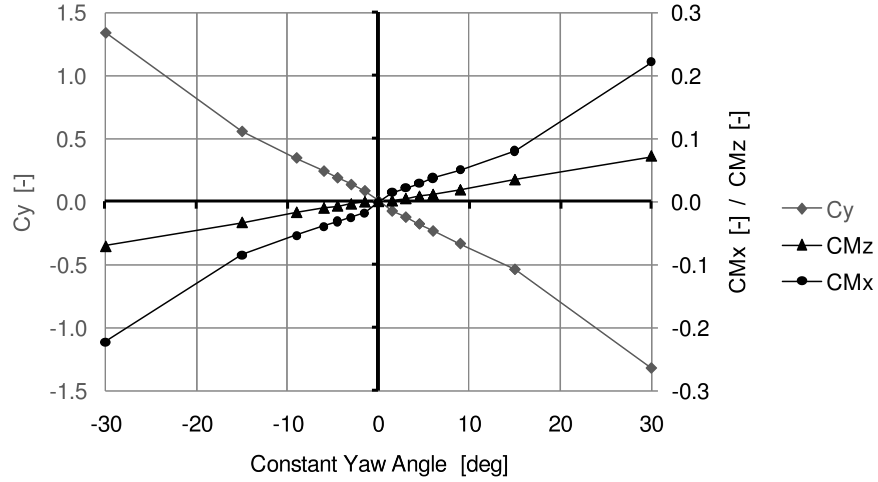

Figure 6.18: Variation of side force C_y, roll moment C_{Mx} and yaw moment C_{Mz} under constant yaw.

However, before looking into the unsteady behavior during the gust events, the aerodynamics of constant yaw are analyzed. Fig. 6.18 shows the variation of side force, roll and yaw moment over the range of yaw angles from -30° to +30°. Between 0° and ±15° the three components behave in an almost perfectly linear way. Only at ±30° in particular the values of side force and roll moment do not correspond to the linear dependency. However, more importantly, the linear curves show a discontinuity at 0° yaw. As shown in Fig. 6.19 for the side force and yaw moment, the linear functions exhibit an offset compared to a line through the origin. This offset is of opposite signs for positive and negative yaw angles but has approximately the same absolute value.

In order to identify the reason for this discontinuity at 0° yaw, Fig. 6.20 plots the C_{Mz} contributions of the divisions 6-1 through 6-6 over the yaw angle. While the regions 6-1 through 6-4 show an approximately linear behavior without discontinuities, this is

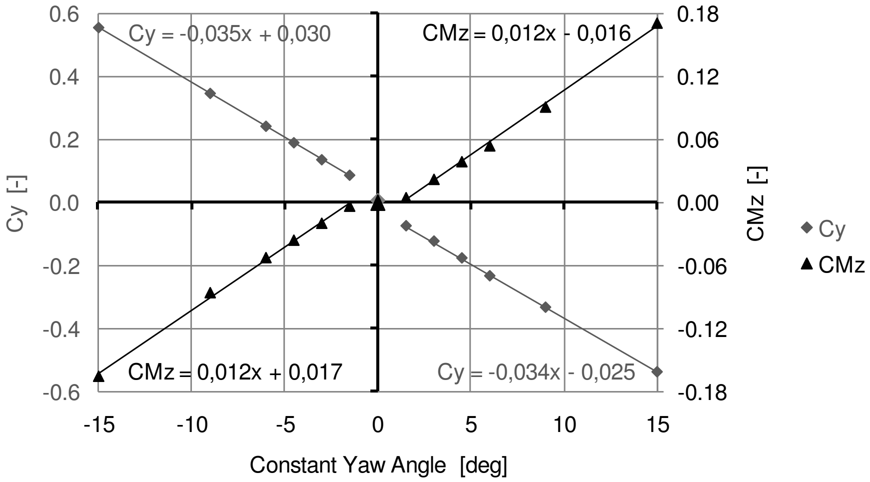

Figure 6.19: Linear interpolation of positive and negative side force C_y and yaw moment C_{Mz} under constant yaw.

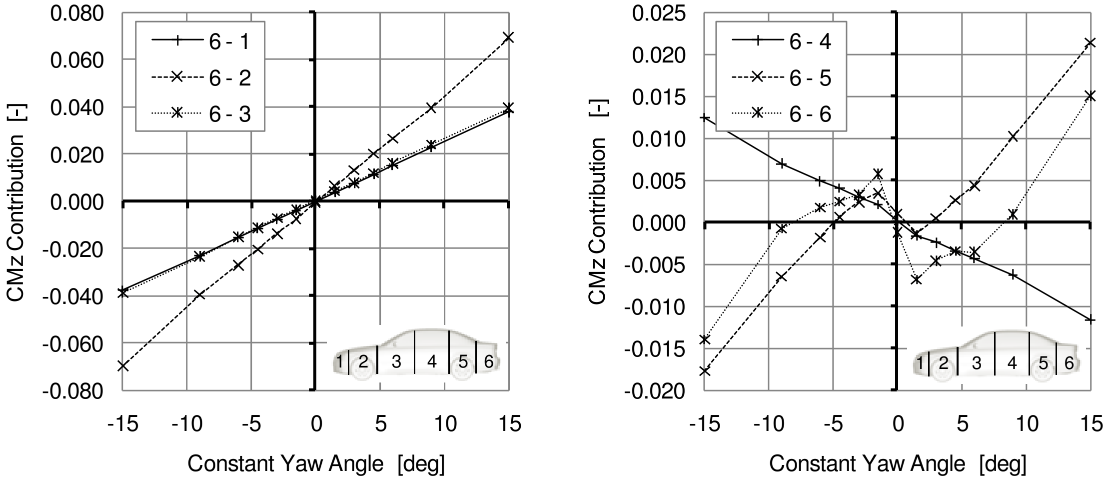

(a) Front

(b) Rear

Figure 6.20: Contribution of the x-segments of the vehicle 6-1 through 6-6 to the yaw moment C_{Mz} under constant yaw.

not the case for the regions 6-5 and 6-6. These two regions at the rear end feature an offset compared to a linear curve through the origin. The offset is more pronounced for the last division 6-6. Hence, the discontinuity in side force, roll and yaw moment results from the rear of the vehicle.

Due to the described offset at the rear, the C_{Mz} contributions of 6-5 and 6-6 exhibit zero-crossings at approximately ±3° and ±9°, respectively. For large yaw angles, the contributions of 6-5 and 6-6 are of the same sign as the contribution of the front. For small yaw angles, however, the C_{Mz} contributions of 6-5 and 6-6 are of opposite signs compared to the yaw moment of the front and hence also compared to the overall yaw moment. The offset also leads to the paradoxical effect that the absolute contribution of the rear end increases as the yaw angle tends towards 0°. For both side force and roll moment similar characteristics can be identified at the rear of the vehicle. However, due to the reduced weighting the impact of the rear end on the overall side force is significantly smaller.

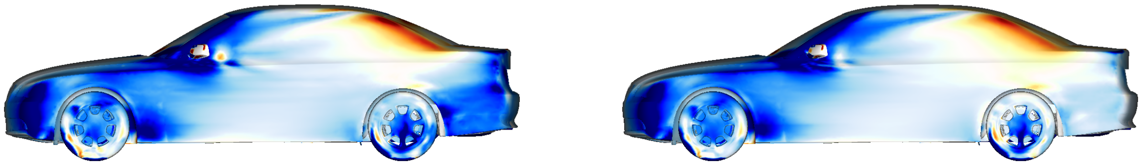

(a) +1.5° Constant Yaw

(b) +3° Constant Yaw

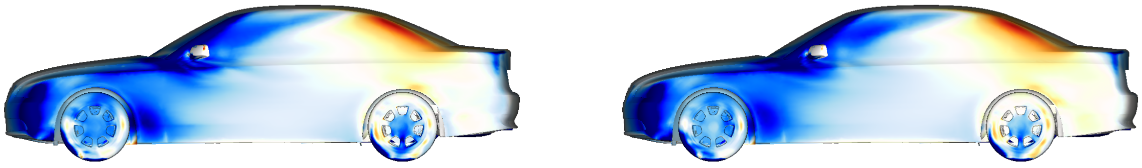

(c) +6° Constant Yaw

(d) +9° Constant Yaw

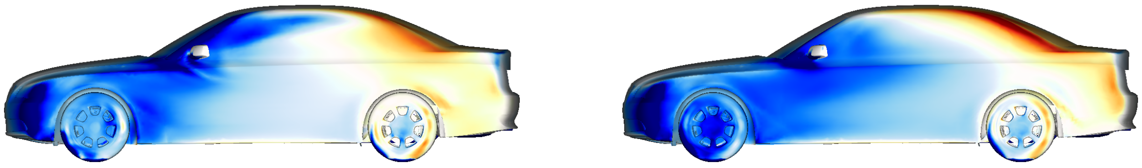

(e) +15° Constant Yaw

(f) +30° Constant Yaw

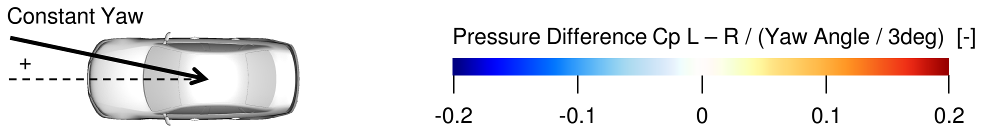

Figure 6.21: Pressure difference between left and right side $C_{p,left} - C_{p,right}$ under constant yaw. The scale is normalized with the yaw angle.

In order to obtain a more detailed impression of the load distribution, the pressure differences between left and right side are plotted for the investigated yaw angles in Fig. 6.21. In order to compare the visualizations of different yaw configurations, the scales are normalized with the yaw angle. The fundamental characteristics of the pressure distribution at the front and at the A- and C-pillar are very similar for yaw angles up to 15°. At the largest yaw angle of 30°, the leeward flow separates at the front which significantly changes the pressure differences between left and right side. It can be assumed that the large separation on the leeward side is the reason for the kink in the curves of side force and roll moment between 15° and 30° (Fig. 6.18). Since the pressure changes are primarily located at mid wheelbase close to the aerodynamic reference point, the impact on the yaw moment is small. Although the principal pressure distribution at the front and at the A- and C-pillar remain constant over a wide range of yaw angles, the details of the pressure differences vary. In particular, the imprint of the A-pillar vortex becomes broader with increasing yaw angles and finally disappears at a yaw angle of 30°.

More unusual, however, is the variation in pressure difference that occurs at the

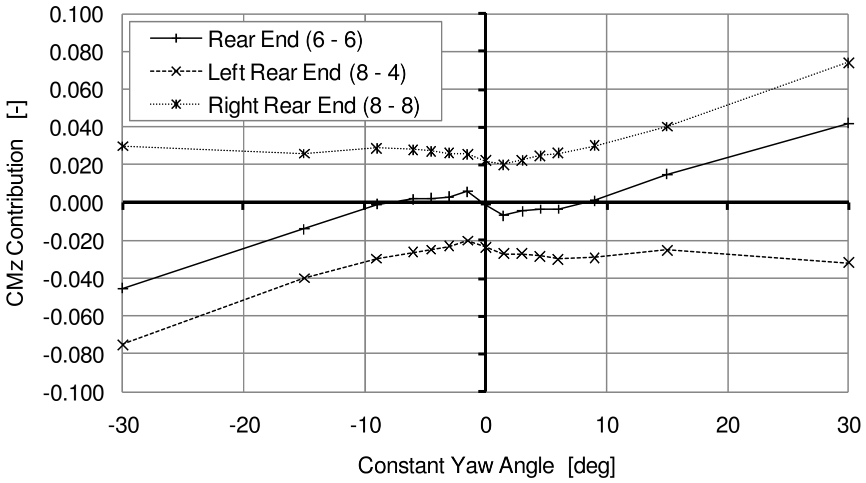

Figure 6.22: Contribution of the left and right rear end to the yaw moment C_{Mz} under constant yaw.

rear of the vehicle. Corresponding to the described offset of the rear yaw moment (Fig. 6.20b), the pressure difference at the rear end is strongly negative at +1.5° resulting in a negative contribution to the yaw moment. With increasing yaw angles the negative pressure difference is reduced and turns positive at approximately +9°. For yaw angles >9° the pressure difference increases again.

Fig. 6.22 confirms the significant change of pressure levels at the rear end plotting the C_{Mz}-contributions of the left and right side of region 6-6. For small yaw angles below ±9° the absolute contribution to the yaw moment is larger on the leeward than on the windward side. Hence, the surface pressures are lower on the leeward side, which may be explained by the flow that enters into the wake region from this side. For yaw angles above ±9° the absolute contribution of the windward side increases significantly, which corresponds to a decrease of the surface pressures obviously caused by an acceleration of the windward flow around the rear corner of the vehicle. On the leeward side, the reduction in surface pressures and thus the increase in yaw moment are much less pronounced. Therefore, it can be concluded that the influence of the leeward flow dominates at small yaw angles, while at larger yaw angles the acceleration of the flow on the windward side is more important.

In order to analyze the impact of the yaw angle on the flow topology, the flow field around the vehicle is visualized for different constant yaw angles using streamlines and the lateral velocity component V_y in Fig. 6.23. The characteristic topology of the leeward flow entering into the wake region, as described in Chap. 5.1.3, is visible for all yaw angles - even for 30° where the flow detaches at the leeward front of the vehicle. The strength of the leeward flow, however, varies over the investigated yaw angle range. In Fig. 6.24, the strength of the leeward flow is quantified by integrating the lateral velocity V_y over the isosurfaces of $V_y > \pm 5 m/s$ and $V_y > \pm 8 m/s$. The strength of the leeward flow increases with increasing absolute yaw angles and reaches a maximum at ±9°. For yaw angles above ±9° its strength is reduced again.

After analyzing the aerodynamics under constant yaw, the behavior during the gust

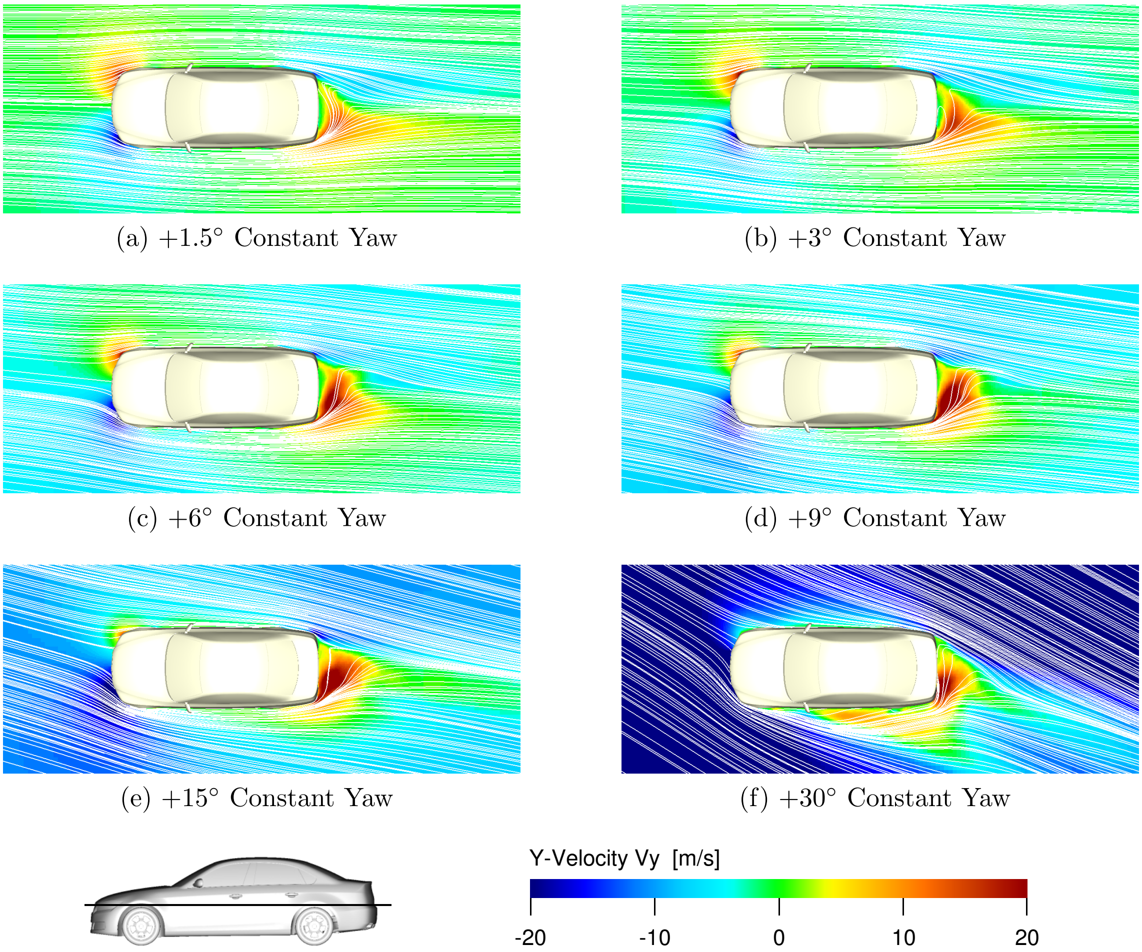
(a) +1.5° Constant Yaw

(b) +3° Constant Yaw

(c) +6° Constant Yaw

(d) +9° Constant Yaw

(e) +15° Constant Yaw

(f) +30° Constant Yaw

Figure 6.23: Visualization of lateral velocity V_y in z-slice for different constant yaw configurations.

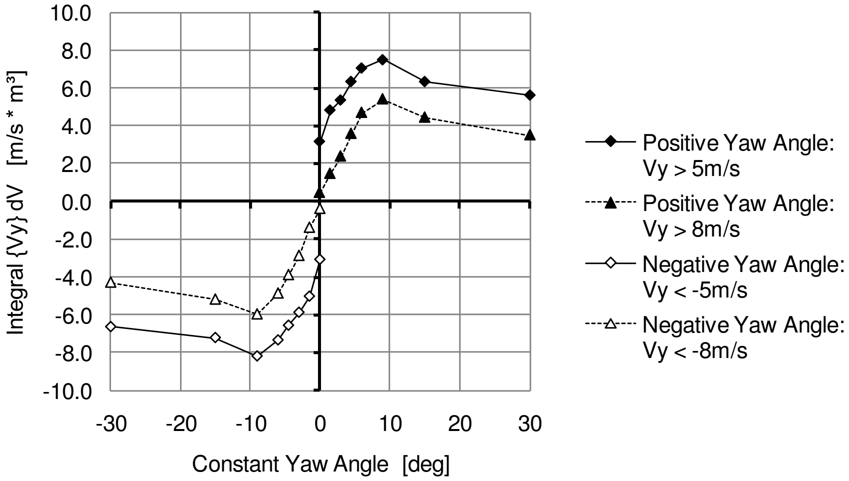

Figure 6.24: Strength of the leeward flow under constant yaw calculated by integrating over the isosurfaces of $V_y > 5m/s$ and $V_y > 8m/s$, respectively.

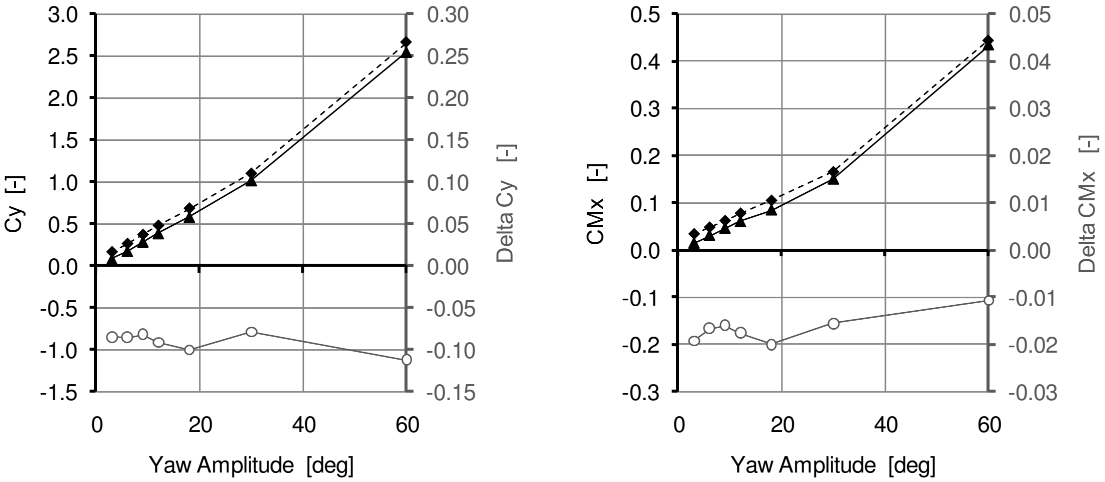

(a) Side Force C_y

(b) Roll Moment C_{Mx}

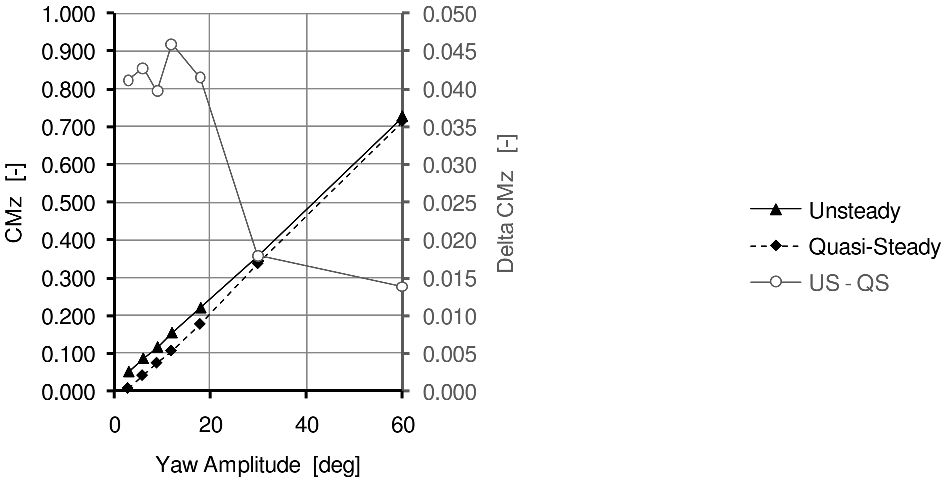

(c) Yaw Moment C_{Mz}

Figure 6.25: Variation of unsteady and quasi-steady (a) side force C_y, (b) roll moment C_{Mx} and (c) yaw moment C_{Mz} with gust amplitude.

is investigated in the following. Fig. 6.25 shows the unsteady and quasi-steady amplitudes of side force, roll and yaw moment over the investigated range of yaw amplitudes. As expected, the unsteady and quasi-steady amplitudes increase with increasing yaw angles. For the side force and the roll moment the differences between unsteady and quasi-steady amplitudes vary over the range of investigated gust amplitudes but do not exhibit a clear trend. For the yaw moment, the differences $C_{Mz,US} - C_{Mz,QS}$ remain approximately constant up to a gust amplitude of 18°. For the larger amplitudes of 30° and 60°, the differences unsteady to quasi-steady are reduced significantly. As the differences between unsteady and quasi-steady amplitudes stay constant or even decrease with increasing gust amplitudes, the magnification factors converge towards 1 for all three components (Fig. 6.26). Hence, the impact of the unsteady effects is reduced significantly for large gust amplitudes.

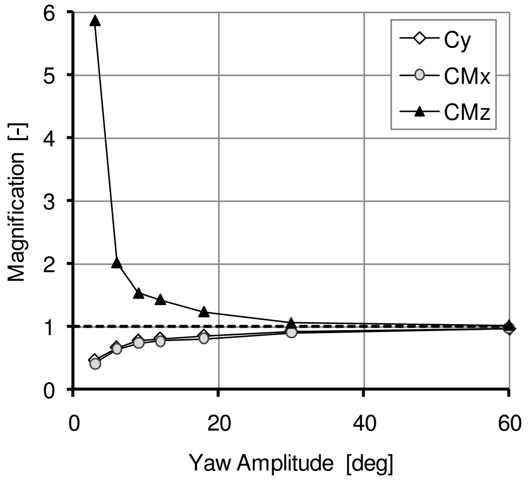

Figure 6.26: Variation of the magnification factors of side force C_y, roll moment C_{Mx} and yaw moment C_{Mz} with the gust amplitude.

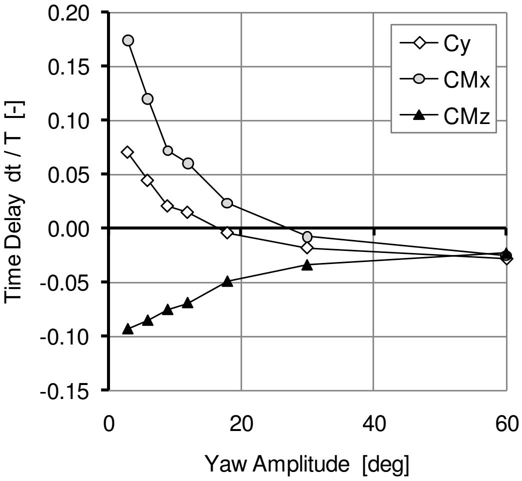

Figure 6.27: Variation of the time delays of side force C_y, roll moment C_{Mx} and yaw moment C_{Mz} with the gust amplitude.

Similarly, the time delays of side force, roll and yaw moment are reduced with increasing gust amplitudes as the influence of the unsteady effects decreases, see Fig. 6.27. However, they do not converge towards $\Delta t/T = 0$ but towards $\Delta t/T = -0.03$, which can be explained by the larger influence of the front compared to the rear of the vehicle.

Fig. 6.28 shows the time delay of the wake flow. The time delay is largest for the smallest gust amplitude of 3° and decreases up to a gust amplitude of 9° where it reaches a minimum of $\Delta t/T = 0.11$. However, for gust amplitudes larger than 9° the time delay increases again and almost reaches the same level as for the smallest gust amplitude. Interestingly, the largest time delay of the wake flow does not correspond to the maximum in strength of the leeward flow (Fig. 6.24).

Although it is not reflected in the integral unsteady amplitudes of side force, roll and yaw moment, Fig. 6.28 proves that also for large gust amplitudes unsteady effects occur in the wake flow. Consequently, significant differences between unsteady and quasi-steady amplitudes would be expected at the rear of the vehicle. This is confirmed by Fig. 6.29, which shows that at the rear of the vehicle the difference between unsteady and quasi-steady yaw moment reaches its maximum for the largest investigated gust amplitude of 60°. Therefore, the reduction of the unsteady effects in yaw moment cannot be explained by the inexistence of the unsteady flow phenomena at the rear of the vehicle. Furthermore, Fig. 6.29 shows that at the front of the vehicle the differences between unsteady and quasi-steady yaw moment are small up to a gust amplitude of 30° but increases for a gust amplitude of 60°. This shows that for very large yaw angles unsteady effects may also occur at the front of the vehicle, which is presumably due to the large flow separation. However, the reduction of the unsteady C_{Mz}-amplitude at the front is small compared to the C_{Mz}-increase at the rear end. Therefore, it does not completely explain the reduction of the unsteady

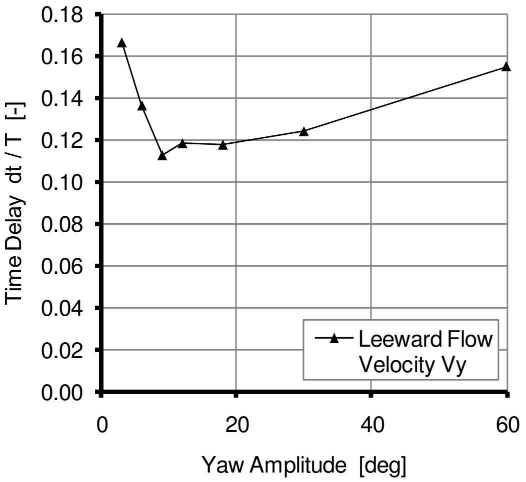

Figure 6.28: Variation of the time delay of the leeward flow velocity V_y with gust amplitude.

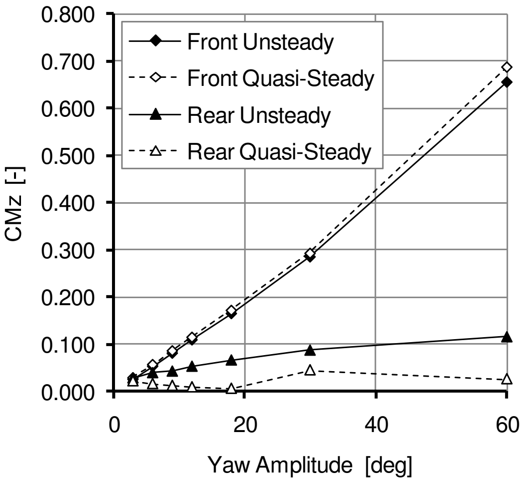

Figure 6.29: Variation of the amplitudes of front and rear yaw moment C_{Mz} with gust amplitude.

yaw moment at large gust amplitudes.

Instead, the answer is provided by the inversion of the pressure difference at the rear of the vehicle that occurs at approximately ±9° in constant yaw. As explained above, the steady-state contribution of the rear end reduces the integral yaw moment for small yaw angles, while it increases the overall yaw moment for large yaw angles. Hence, for large gust amplitudes the quasi-steady contribution of the rear end is in phase with the overall yaw moment while it is in antiphase for small amplitudes. In other words, at small gust amplitudes the increase in unsteady yaw moment is caused by the superposition of front and rear contribution. At small gust amplitudes, this superposition of front and rear contribution is already included in the quasi-steady approximation. Therefore, the reduction of the unsteady effects in yaw moment at large gust amplitudes does not result from smaller unsteady values but primarily from a relative increase of the quasi-steady values. The reason why - in contrast to side force and roll moment - the unsteady yaw moment is still larger than the corresponding quasi-steady value is the larger impact of the increased unsteady amplitudes at the rear end that over-compensates a small time delay between front and rear contribution. On the other hand, it has to be noted again that at large gust amplitudes of >18° the differences between unsteady and quasi-steady loads are small compared to the absolute aerodynamic loads. It can be concluded that at small yaw angles the unsteady aerodynamic loads are strongly influenced by the unsteady effect of the wake flow while at large yaw angles the effect of the oncoming flow dominates.

The aerodynamic characteristics in constant yaw can be summarized as follows:

- Over the investigated yaw angle range, side force, roll and yaw moment exhibit a linear dependency up to yaw angles of ±15°. For larger yaw angles, large flow separations occur on the leeward side causing deviations from the linear dependency.

- The linear dependencies of side force, roll and yaw moment exhibit a discontinuity at 0° yaw which is caused by the influence of the leeward flow at the rear of the vehicle.
- Due to the varying influence of the leeward and of the oncoming flow, the pressure difference at the rear end exhibits a change of sign over the yaw angle range (at ±9° for this vehicle). At small yaw angles the influence of the leeward flow dominates, while at larger yaw angles the acceleration of the flow on the windward side is more important.
- At small yaw angles the yaw moment of the rear end reduces the overall yaw moment, while at large yaw angles it causes a further increase of the overall yaw moment.
- Fluid that enters into the wake region from the leeward side can be identified for all investigated yaw angles. The strength of the leeward flow reaches a maximum at ±9°.

Regarding the influence of the gust amplitude it can be concluded that:

- The influence of the unsteady effects is reduced significantly with increasing gust amplitudes: Magnification factors converge towards 1 and time delays towards $\Delta t/T = -0.03$.
- Even for large gust amplitudes unsteady effects, however, occur at the rear end and in the wake flow.
- The influence of the unsteady effects at the rear end is reduced for large yaw angles due to:
  - The inversion of the pressure difference at the rear end in constant yaw.
  - The dominating influence of the front of the vehicle.

6.1.5 Zero-Crossing

Following the investigation of the gust amplitude, the influence of zero-crossings and hence of the initial yaw angle is analyzed using four standard 5-peak gusts with a frequency of 1 Hz and an amplitude of 6°. The minimum and maximum yaw angles are varied between -4.5°/+1.5°, -3°/+3°, -1.5°/+4.5° and +3°/+9°. Hence, the first three generic gusts include zero-crossings while the latter does not.

Fig. 6.30 shows the magnification of unsteady over quasi-steady aerodynamic loads. The three gusts featuring a zero-crossing all exhibit the same characteristic unsteady behavior including an magnification factor > 1 for the yaw moment and magnification factors < 1 for the side force and roll moment. Although the gust without

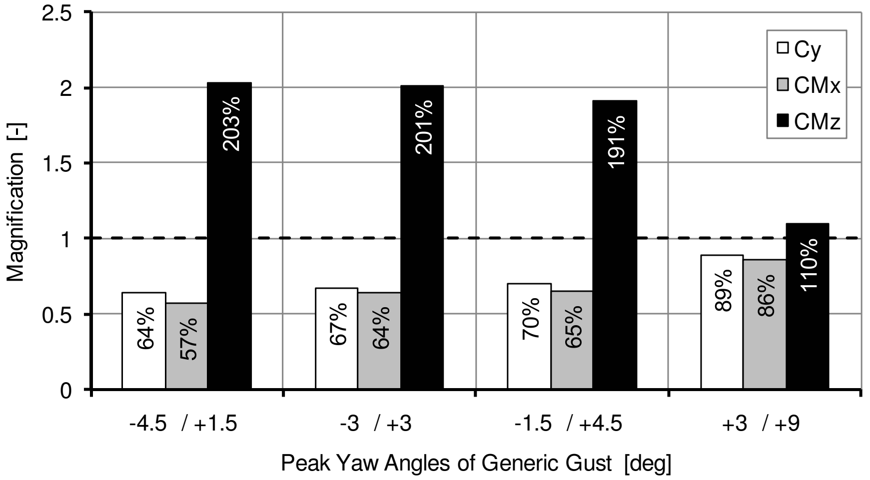

Figure 6.30: Magnification of side force C_y, roll moment C_{Mx} and yaw moment C_{Mz} for four gusts with different initial yaw angles.

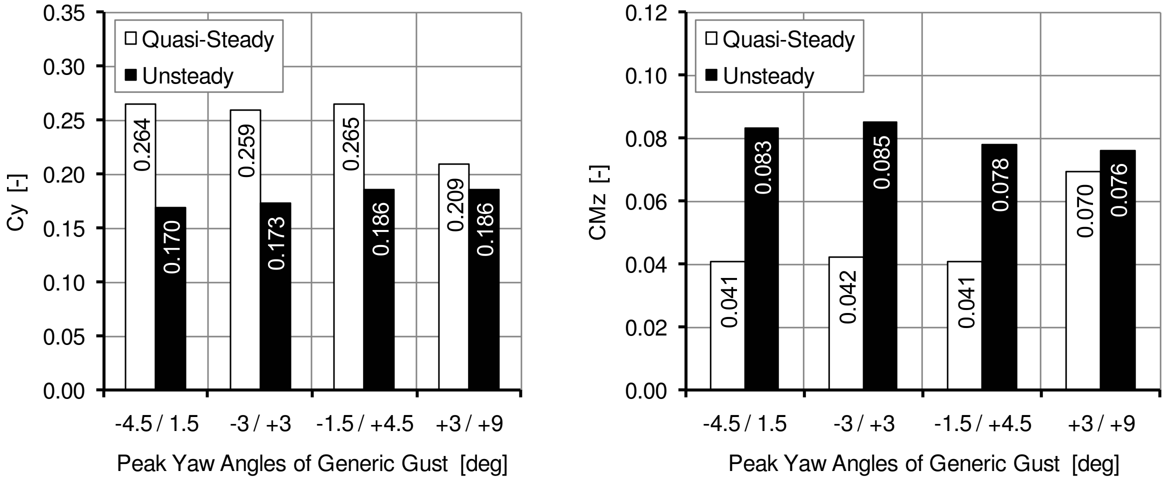

(a) Side Force C_y

(b) Yaw Moment C_{Mz}

Figure 6.31: Variation of the amplitudes of (a) side force C_y and (b) yaw moment C_{Mz} with the initial yaw angle.

zero-crossings principally also shows the same characteristics, the unsteady effects are significantly reduced with the magnification factors being close to one.

In Fig. 6.31 the absolute values of the unsteady and quasi-steady amplitudes are plotted. For both side force and yaw moment the unsteady amplitudes are very similar for all gusts - with and without zero-crossings. The reduction of the unsteady effects is caused by a significant change of the quasi-steady amplitude for the gust without zero-crossings. As explained above, the aerodynamic loads side force, roll and yaw moment principally show a linear dependency over the yaw angle which would result in an approximately constant quasi-steady amplitude for the four gusts regardless of the initial yaw angle. The discontinuity of the linear dependency around 0° yaw, however, significantly changes the quasi-steady amplitude for gusts with versus without zero-crossings. While this explains the quasi-steady differences between the four investigated gusts, it does not provide an answer, why the unsteady amplitude does not increase accordingly, too.

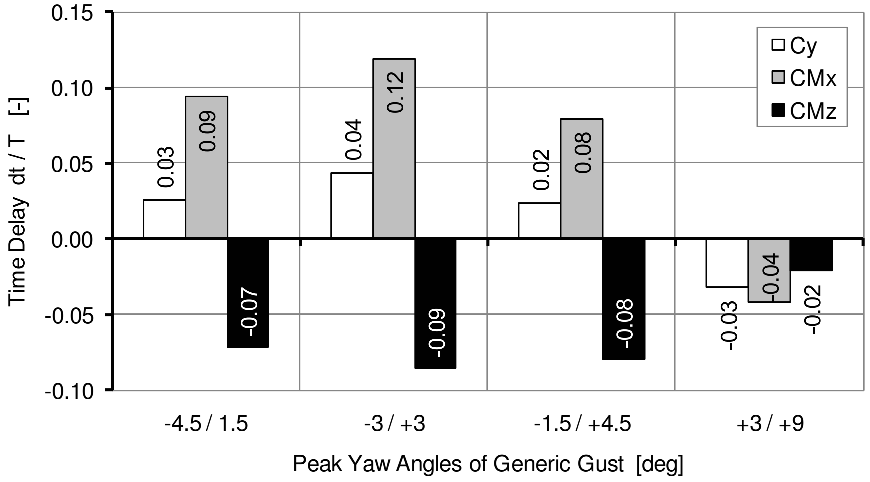

Figure 6.32: Variation of the time delays of side force C_y, roll moment C_{Mx} and yaw moment C_{Mz} with the initial yaw angle.

Looking at the time delays in Fig. 6.32 for side force, roll and yaw moment, they are largest for the symmetrical gust and slightly reduced for the two gusts -4.5°/+1.5° and -1.5°/+4.5°. For the +3°/+9° gust the characteristics are very different as the time delays are negative for all three components side force, roll and yaw moment.

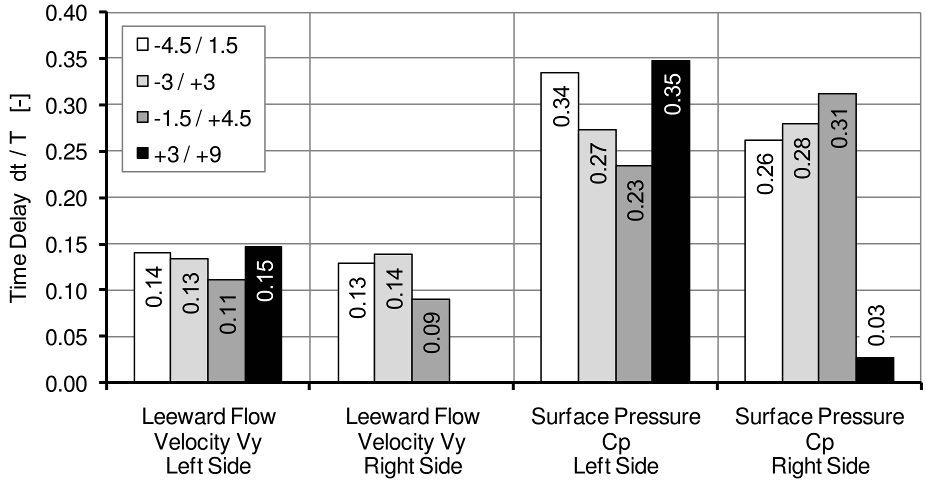

Figure 6.33: Variation of the time delays of lateral flow velocity V_y and surface pressure C_p at the rear end of the vehilce with the initial yaw angle.

In Fig. 6.33 the time delays of the wake flow are shown. Since the majority of the gusts is asymmetric, the time delays are presented separately for the left and the right side. For the +3°/+9° gust the time delay is only available for the left side as leeward and windward side do not alternate in this case. Analyzing the results, the time delays are very similar for the two gusts -4.5°/+1.5° and -3°/+3°. For the gust -1.5°/+4.5° the time delays are reduced, which would explain the reduction in unsteady effects regarding the overall aerodynamic loads. The different time delays of the wake flow for the three gusts may be caused by an asymmetry of the leeward flow which differs in strength for positive and negative yaw angles due to the asymmetry of the vehicle, in particular of its underbody (compare Fig. 6.24). Furthermore, the asymmetric start of the wind gust may have an influence on the time delays and the resulting unsteady effects. The largest time delay of the wake flow, however, occurs for the +3°/+9° gust. Hence, the absence of a zero-crossing in yaw angle and thus the absence of the change of windward and leeward sides does not prevent a delayed reaction of the wake flow to the change of the oncoming flow.

Fig. 6.33 also shows the resulting time delays for the surface pressure on the left and right rear end of the vehicle. The time delays of the symmetric gust -3°/+3° are almost identical for the left and the right side. For the asymmetric gusts with zero-crossings the time delays differ significantly for the left and the right side. For the -4.5°/+1.5° gust the time delay is larger on the left side and smaller on the right side than for the symmetric gust. The -1.5°/+4.5° gust shows exactly the inverse behavior, which is presumably due to the asymmetric maximum and minimum yaw angles. The largest differences between left and right side, however, occur for the gust without zero-crossings. In this case the time delay of the surface pressure on the left (leeward) side is larger than for the three other gusts, while on the right (windward) side the time delay is almost zero. Hence, the surface pressures on the leeward side are strongly influenced by the delayed reaction of the wake flow. On the other hand, the behavior of the surface pressures on the windward side is dominated by the variation of the oncoming flow.

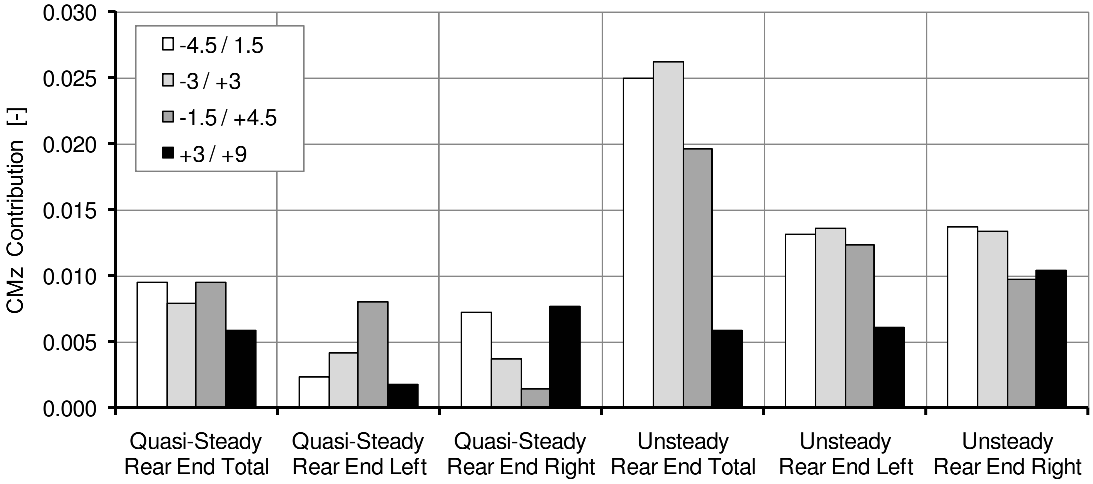

Figure 6.34: Variation of the yaw moment contributions of the left and the right rear end with the initial yaw angle.

Following the analysis of the time delays of the wake flow and the surface pressures at the rear, Fig. 6.34 plots the quasi-steady and unsteady amplitudes at the rear end (6-

6) and on the left (8-4) and the right (8-8) rear side of the vehicle. The quasi-steady amplitudes in region 6-6 are very similar for the three gusts with zero-crossings as the differences on the left and right sides compensate each other. However, more important are the unsteady amplitudes for the +3°/+9° gust. The unsteady contributions of left and right side are smaller than the corresponding values of the standard -3°/+3° gust. Yet, they are nevertheless significantly larger than the quasi-steady contribution of each side. The combination of left and right side, however, results in an unsteady contribution of the rear end (6-6) that is only slightly larger than the quasi-steady contribution. Hence, the increased amplitudes on either rear side of the vehicle are canceled out since the signals are not in phase.

It can be concluded that the absence of a zero-crossing significantly reduces the differences between unsteady and quasi-steady amplitudes of side force, roll and yaw moment. Nevertheless, the leeward flow as well as the leeward surface pressures exhibit significant time delays. However, the unsteady effects on the leeward side of the vehicle do not have a relevant influence on the overall aerodynamic loads due to the following two factors: First, the amplitudes are reduced due to the absence of an alternating transition between windward and leeward side. Second, the peaks of windward and leeward side are out of phase which results in a smaller maximum contribution of the rear end. Hence, unsteady effects occur in the wake flow regardless of the initial yaw angle. However, only for changes of the yaw angle including zero-crossings these unsteady effects have a significant impact on the overall aerodynamic loads side force, roll and yaw moment.

The influence of zero-crossings can be summarized as follows:

- For gusts without zero-crossings, the differences between unsteady and quasi-steady amplitudes are reduced significantly for side force, roll and yaw moment.
- A delayed reaction of the wake flow and thus also of the leeward surface pressures occurs regardless of the inclusion of zero-crossings.
- For gusts without zero-crossings, the unsteady effects at the rear of the vehicle are not reflected in the integral aerodynamic loads since the peaks of the left and the right rear contributions are out of phase.

6.2 Vehicle Types

As summarized briefly in Chap. 2.2.3, sedan, fastback and station wagon exhibit very different maxima in yaw moment and side force for steady-state measurements. In the following, the unsteady behavior of the three vehicle types is compared using the presented numerical approach of a multiple-peak gust with a yaw angle varying between -3° and +3°. For both the BMW and the DrivAer vehicle family the influence of the rear end type on the unsteady effects is investigated. This eventually leads to the conclusion whether the proposed unsteady mechanism of Chap. 5.2, which was originally derived for sedan vehicles, also applies to fastback and station wagon.

Fig. 6.35 presents the quasi-steady and unsteady peak-to-peak amplitudes of side force, roll and yaw moment for the six vehicles. The quasi-steady results exhibit the expected behavior of sedan and station wagon with the sedan vehicle featuring a lower side force but a larger yaw moment. However, the differences between sedan and station wagon are much more pronounced for the BMW than for the DrivAer vehicles. In contrast, the results of the two fastback geometries differ very significantly. While the BMW fastback shows a quasi-steady side force and yaw moment, which are almost identical to the BMW station wagon, the DrivAer fastback features the smallest side force and the largest yaw moment of the DrivAer family. Hence, regarding the steady-state results the BMW fastback is very similar to the station wagon, whereas the DrivAer fastback resembles the sedan. Regarding the quasi-steady roll moment, the amplitudes of sedan and station wagon are approximately the same within each vehicle family. Again, the two fastbacks do not show the same behavior: The BMW fastback marks the highest roll moment while the DrivAer fastback features the lowest roll moment of their respective family. Hence, the quasi-steady behavior of the six vehicles principally corresponds to the expected characteristics, except for the BMW fastback which is closer to a station wagon than to a sedan.

However, looking at the unsteady results a different picture evolves. All vehicles show the same principle unsteady behavior consisting of a reduction of side force and roll moment and an magnification of the yaw moment. Furthermore, the typical differences in side force and yaw moment persist between sedan and station wagon. The absolute values, however, differ significantly spanning a range of variation which is approximately twice as large as for the quasi-steady results. While in the DrivAer family at least the ranking does not change, in the BMW vehicle family the fastback shows a very interesting behavior. In contrast to its quasi-steady results, the BMW fastback features unsteady amplitudes of side force and roll moment which are now similar to the sedan vehicle and even exceed the sedan in case of the unsteady yaw moment. Hence, the largest amplitudes in unsteady yaw moment within each vehicle family are identified for the two fastback geometries followed by the sedan vehicles.

In Fig. 6.36 the differences between unsteady and quasi-steady amplitudes are summarized. As mentioned before, for all vehicles the differences are always negative for side force and roll moment and remain always positive for the yaw moment. For the BMW vehicles the differences between unsteady and quasi-steady amplitudes are largest for the fastback and smallest for the station wagon. Within the DrivAer family, however, the differences are largest for the sedan and smallest for the station

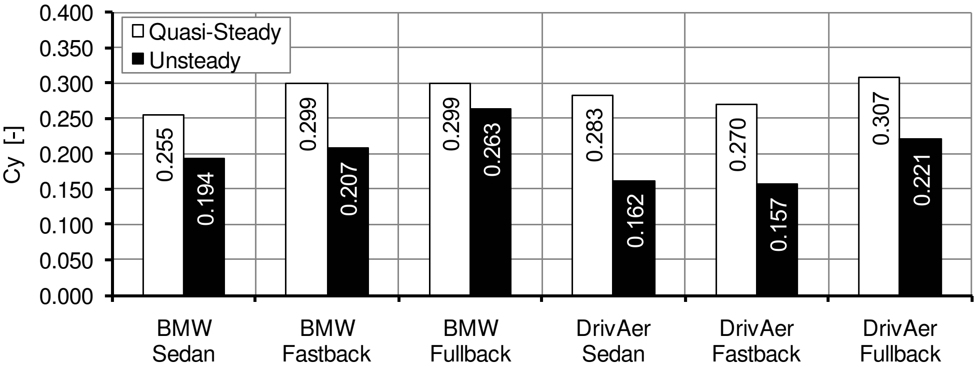

(a) Side Force C_y

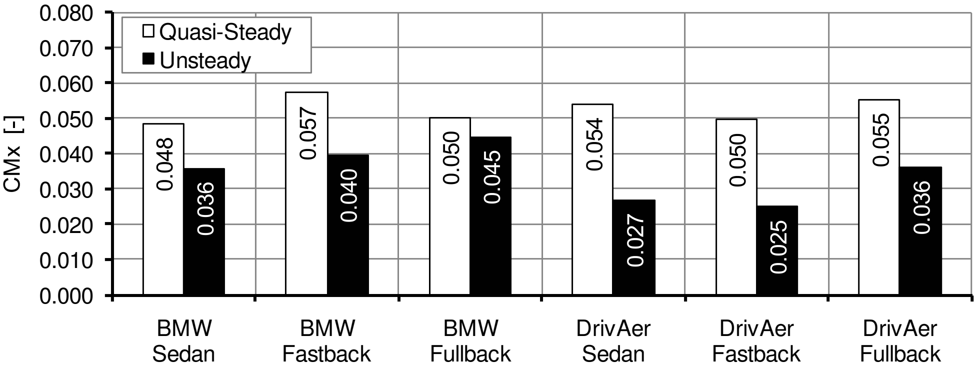

(b) Roll Moment C_{Mx}

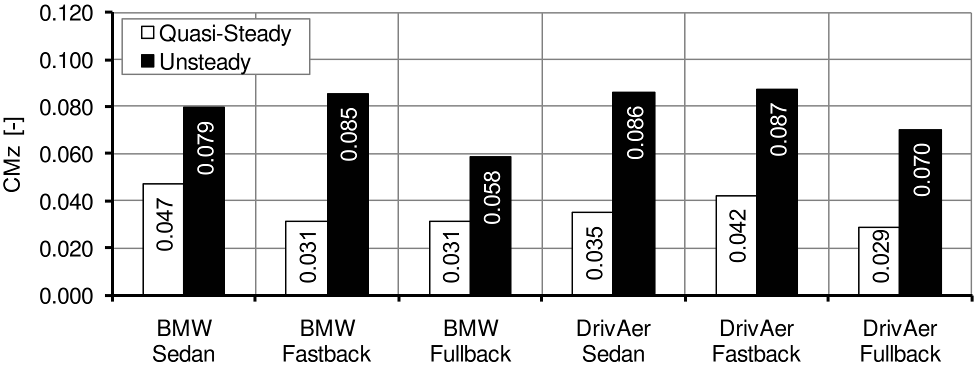

(c) Roll Moment C_{Mz}

Figure 6.35: Unsteady and quasi-steady amplitudes of (a) side force C_y, (b) roll moment C_{Mx} and (c) yaw moment C_{Mz} for six different vehicle geometries.

wagon. Interestingly, the unsteady effects are still very pronounced for the DrivAer station wagon while they are significantly smaller for the BMW station wagon.

Fig. 6.37 lists the magnification factors for the three load components with values smaller than one for the side force and roll moment and values larger than one for the yaw moment. Compared to Fig. 6.36, the bar sizes differ significantly due to the variations in quasi-steady reference amplitudes and do not allow for a consistent

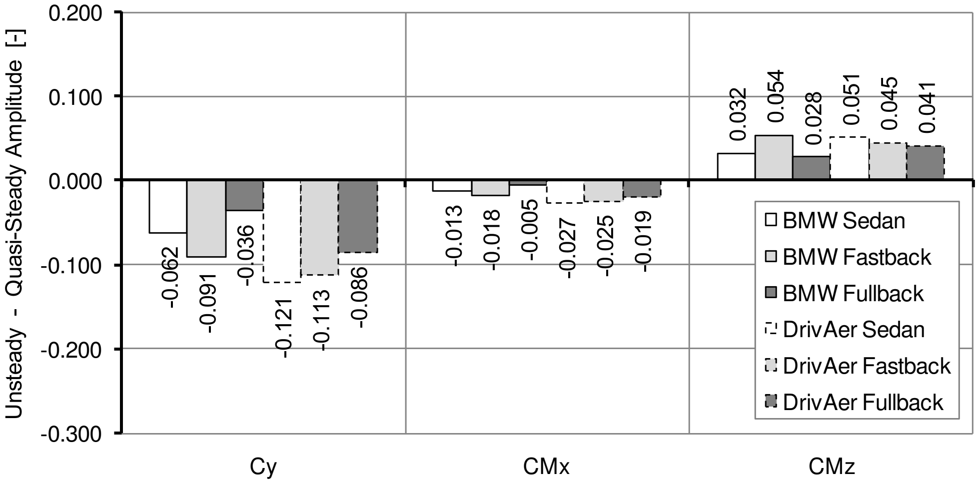

Figure 6.36: Differences between unsteady and quasi-steady amplitudes of side force C_y, roll moment C_{Mx} and yaw moment C_{Mz} for six different vehicle geometries.

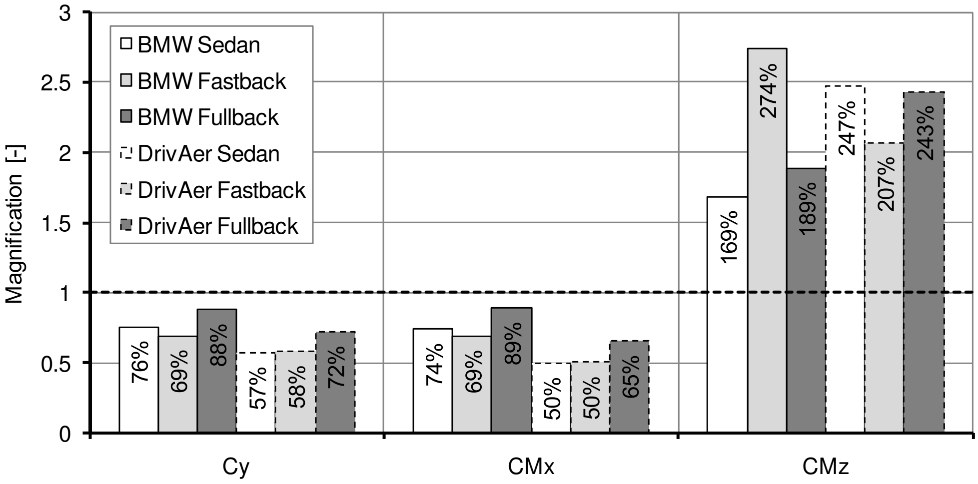

Figure 6.37: Magnification of unsteady side force C_y, roll moment C_{Mx} and yaw moment C_{Mz} compared to the corresponding quasi-steady amplitudes for six different vehicle geometries.

interpretation. The largest magnification factor in yaw moment occurs for the BMW fastback reaching an magnification of close to three. Due to its large quasi-steady yaw moment the BMW sedan features a much smaller magnification of only 169%. For the side force and roll moment, the magnification factors vary between 50% for the DrivAer sedan and fastback and 89% for the BMW station wagon.

The resulting time delays between unsteady and quasi-steady loads are presented in Fig. 6.38. Again, the fundamental characteristics do not change over the range of vehicles. The time delay of side force and roll moment are both positive with the roll moment featuring a larger time delay than the side force. In comparison, the time delay of the yaw moment remains negative for all vehicles. In general, all vehicles show very similar time delays, except for the BMW station wagon, which features

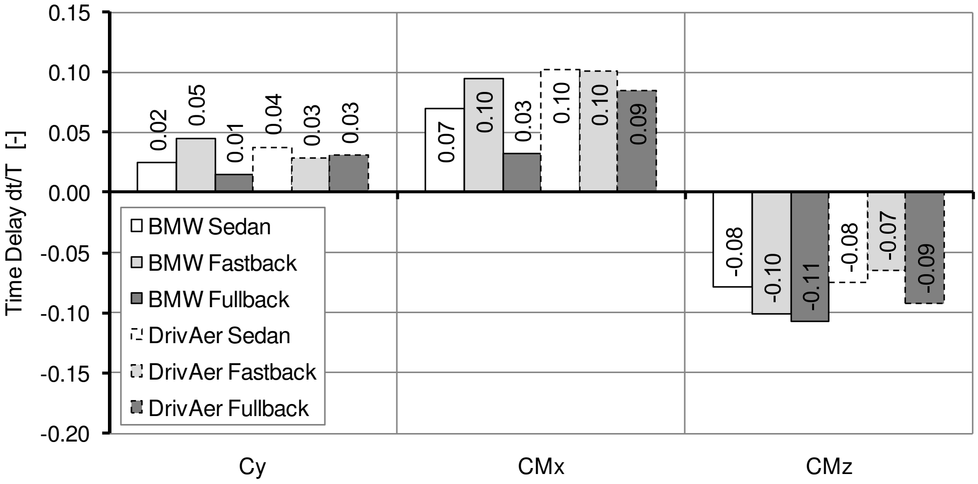

Figure 6.38: Time delays between unsteady and quasi-steady amplitudes of side force C_y, roll moment C_{Mx} and yaw moment C_{Mz} for six different vehicle geometries.

very small time delays in side force and roll moment but the largest time delay in yaw moment.

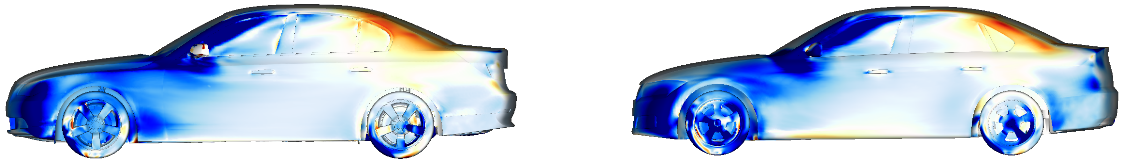

(a) BMW Sedan (b) DrivAer Sedan

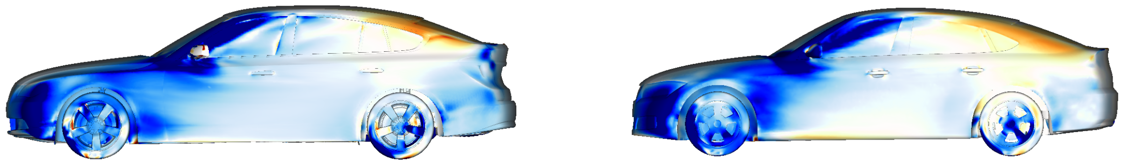

(c) BMW Fastback (d) DrivAer Fastback

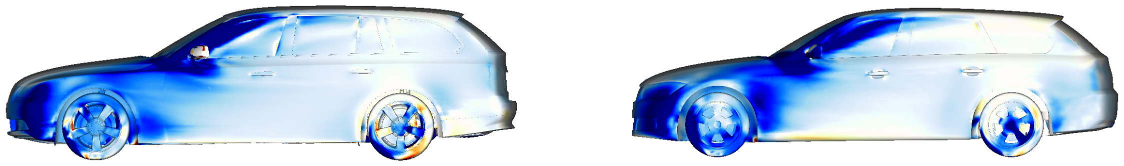

(e) BMW Station Wagon (f) DrivAer Station Wagon

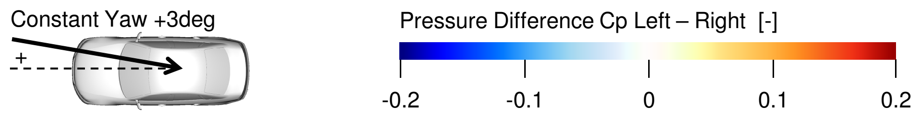

Figure 6.39: Quasi-steady pressure differences between left and right side $C_{p,left} - C_{p,right}$ for six different vehicle geometries for a constant yaw angle of +3°.

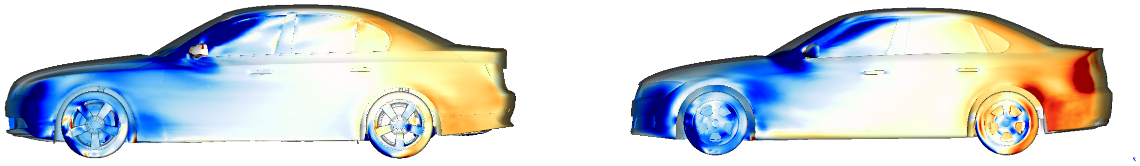

(a) BMW Sedan

(b) DrivAer Sedan

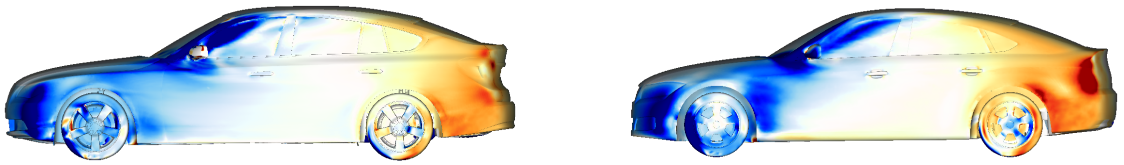

(c) BMW Fastback

(d) DrivAer Fastback

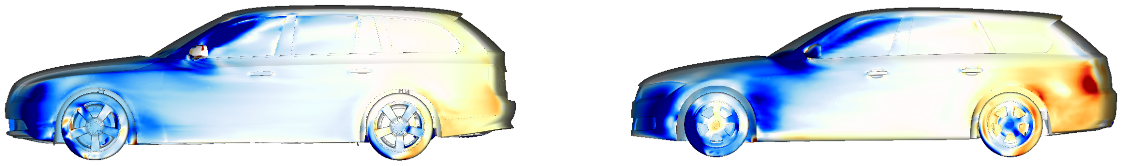

(e) BMW Station Wagon

(f) DrivAer Station Wagon

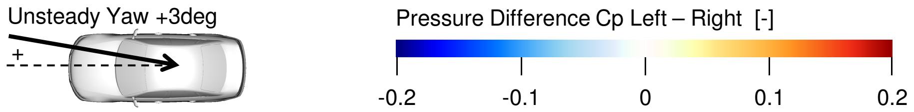

Figure 6.40: Unsteady pressure differences between left and right side $C_{p,left} - C_{p,right}$ for six different vehicle geometries for the peak yaw angle of +3°.

In order to understand the different behavior of the vehicles the surface pressures and the wake flow are investigated in the following. In Fig. 6.39 and Fig. 6.40 the distribution of the pressure differences between left and right side is plotted for a constant yaw angle of +3° and for the corresponding maximum gust peak. Sedan and fastback geometries all feature a similar quasi-steady distribution consisting of a negative pressure difference at the front and the A-pillar and a positive pressure difference at the C-pillar. At the rear end, both vehicle types exhibit a negative pressure difference. For the DrivAer sedan this negative pressure difference at the rear end is more pronounced than for the BMW sedan providing an explanation why the DrivAer sedan has a larger quasi-steady side force but a smaller quasi-steady yaw moment. The DrivAer fastback features a less pronounced pressure difference at the rear end in Fig. 6.39. As will be shown later, for the DrivAer fastback the wake flow and thus the pressure differences at the rear behave asymmetrically for positive and negative yaw angles. At a yaw angle of -3° the fastback geometries feature pressure differences at the rear end that are as pronounced as for the sedan.

Although the BMW fastback principally shows the same distribution of pressure differences as the other sedan and fastback vehicles, it features a higher trunk lid and therefore a larger lateral area. This larger lateral area increases the quasi-steady side force and reduces the quasi-steady yaw moment, which may explain the similarities between BMW fastback and station wagon. Finally, the station wagons do not feature a positive pressure difference at the C-pillar but show a negative pressure difference over the whole side area.

Comparing the unsteady and the quasi-steady plots, the initially negative pressure difference at the rear end is inversed and amplified for all vehicles. The differences between the unsteady and the quasi-steady plots occur mainly at the rear ends and to a lesser extent at the A-pillar and the wheels. The differences in surface pressure are most pronounced for the DrivAer vehicles and the BMW fastback while they are much less significant for the BMW sedan and station wagon.

In Chap. 5.1, the time delay of the wake flow was identified as the main cause for the differences between unsteady and quasi-steady pressure distribution at the rear of the vehicle. Therefore, the wake topologies of the six vehicles are compared in the following. Fig. 6.41 and Fig. 6.42 present the isosurfaces of lateral velocity $V_y = \pm 10 m/s$ for constant yaw angles of +3° and -3°, respectively. First, it has to be pointed out that for the DrivAer vehicles, in particular the fastback, the lateral rear flow behaves highly asymmetrically for positive and negative yaw angles. The leeward isosurfaces are much larger for -3° than for +3°. Since the DrivAer vehicles are symmetric except for the underbody, the asymmetric behavior is inevitably caused by the underbody. Hence, the vehicle underbody can be assumed to have a relevant influence on the leeward flow. In comparison, the BMW vehicles show equally strong isosurfaces for positive and negative yaw angles.

Irrespective of the asymmetric yaw dependency, the leeward isosurfaces exhibit the same shape for all vehicles except for the BMW station wagon. The flow always enters into the wake slightly above the rear wheels from the leeward side and is then directed downwards. The isosurfaces are largest for the BMW fastback as well as for the DrivAer sedan and fastback. In Fig. 6.41 and Fig. 6.42, isosurfaces of the lateral velocity ±10 m/s are not visible for the BMW station wagon since in this case the lateral velocities that occur in the wake region are smaller. However, in a more detailed analysis of the wake topology fluid of lower lateral velocity was identified to enter into the wake region from the leeward rear bumper which is then directed upwards. Hence, even for this relatively square rear end the characteristic wake topology persists to some extent. Comparing the wake flow of the BMW sedan with the results of Chap. 5.1, the leeward isosurfaces are significantly larger for the previously investigated sedan geometry. The two versions feature different wheels, tear-off edges and a slightly different underbody. Hence, at least one of these factors reduces the strength of the leeward flow.

In Chap. 5.1, the fluid entering into the wake region goes in line with the formation of two vortices - a stronger one above and a weaker one below the region of high lateral velocity. Fig. 6.43 shows the isosurfaces of x-vorticity $\omega_x = \pm 80\ 1/s$. All vehicles, except for the BMW station wagon, exhibit the same characteristics, while the strength of the vortices seems to vary with the strength of the leeward flow. In line with its very weak leeward flow, vortices are not visible in the wake of the BMW station wagon.

The strength of the leeward flow was again measured by integrating over isosurfaces of $V_y > \pm 5m/s$, which is summarized in Fig. 6.44. The plot confirms the asymmetrical behavior of the DrivAer vehicles, which is most pronounced for the fastback.

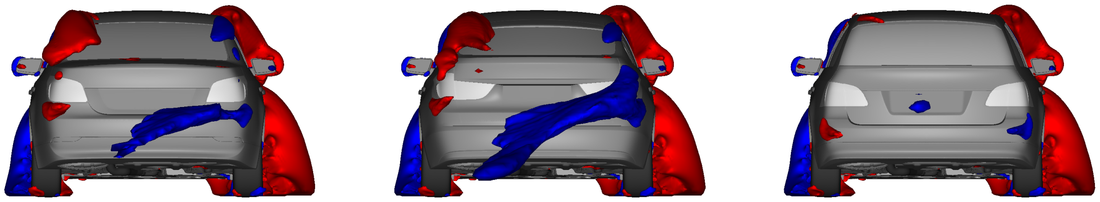

(a) BMW Sedan (b) BMW Fastback (c) BMW Station Wagon

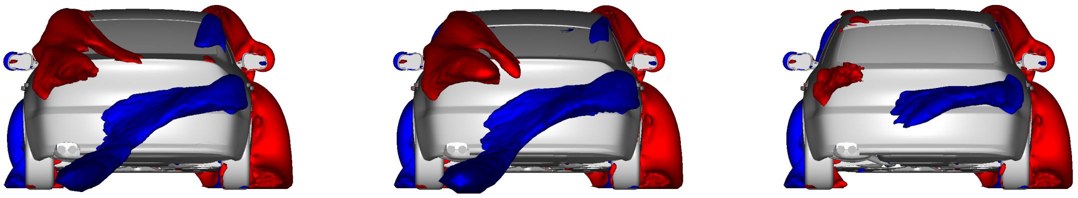

(d) DrivAer Sedan (e) DrivAer Fastback (f) DrivAer Station Wagon

Figure 6.41: Isosurfaces of lateral velocity $V_y < 10m/s$ and $V_y > 10m/s$ for six different vehicle geometries at a constant yaw angle of -3°.

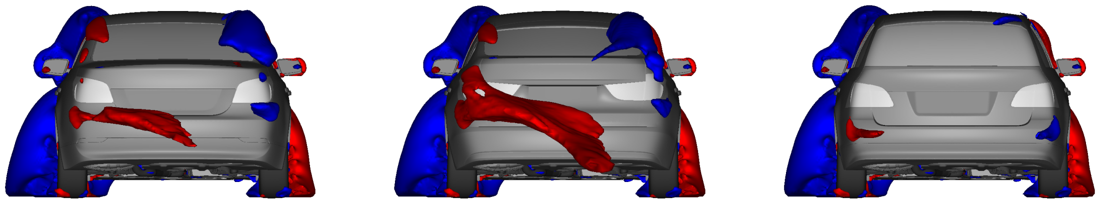

(a) BMW Sedan (b) BMW Fastback (c) BMW Station Wagon

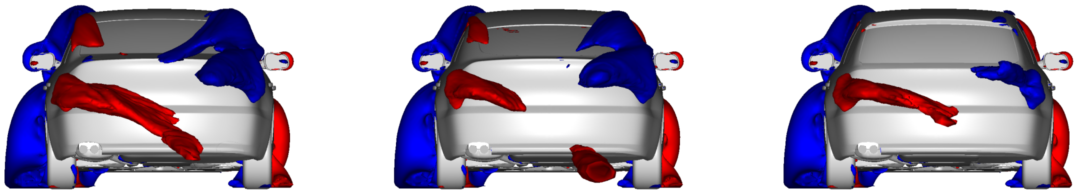

(d) DrivAer Sedan (e) DrivAer Fastback (f) DrivAer Station Wagon

Figure 6.42: Isosurfaces of lateral velocity $V_y < 10m/s$ and $V_y > 10m/s$ for six different vehicle geometries at a constant yaw angle of +3°.

Furthermore, the graph confirms that the leeward flow is strongest for the BMW fastback as well as the DrivAer sedan and DrivAer fastback. However, the DrivAer station wagon also shows a well pronounced leeward flow, which is even stronger than

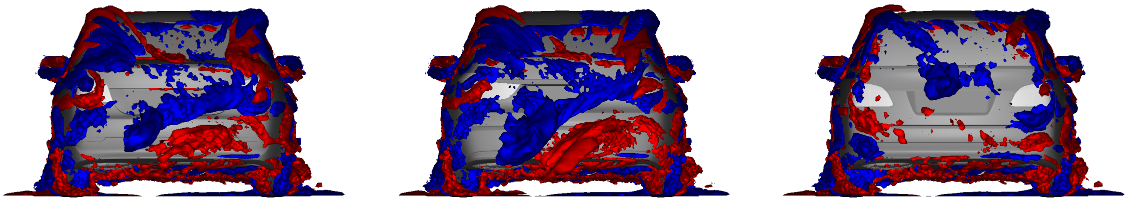

(a) BMW Sedan (b) BMW Fastback (c) BMW Station Wagon

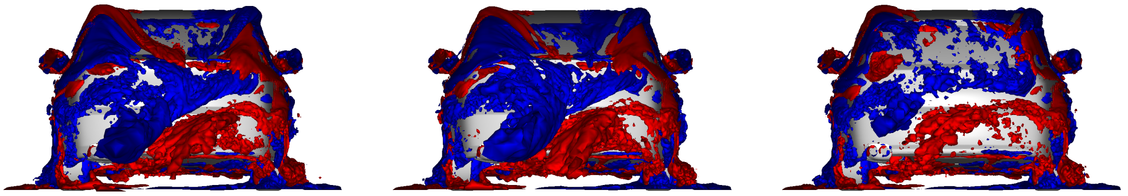

(d) DrivAer Sedan (e) DrivAer Fastback (f) DrivAer Station Wagon

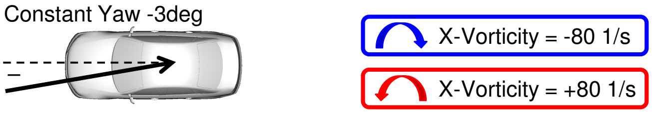

Figure 6.43: Isosurfaces of x-vorticity $\omega_x = \pm 80\ 1/s$ for six different vehicle geometries at a constant yaw angle of -3°.

for the BMW sedan and station wagon.

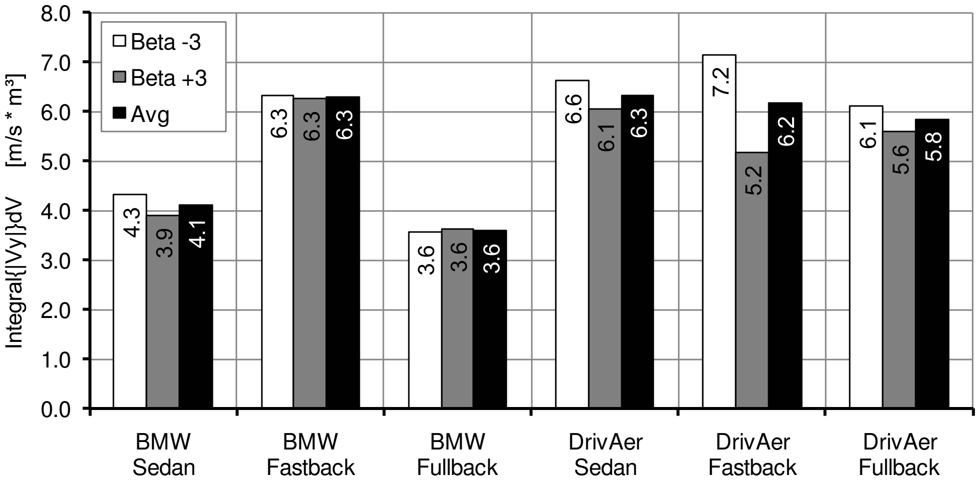

Figure 6.44: Strength of the leeward flow for six different vehicle geometries under constant yaw calculated by integrating over the isosurfaces of $V_y > \pm 5m/s$.

Fig. 6.45 plots the time delay of the wake flow for the six vehicles. The largest time delays occur for the DrivAer vehicles, in particular the station wagon. Compared to the DrivAer family, the BMW vehicles all feature a smaller time delay of the wake flow. In particular the sedan and the station wagon exhibit very small time delays.

In general, vehicles with a pronounced leeward flow also feature a large time delay of the wake flow. Although this holds true in a general way, it cannot explain why

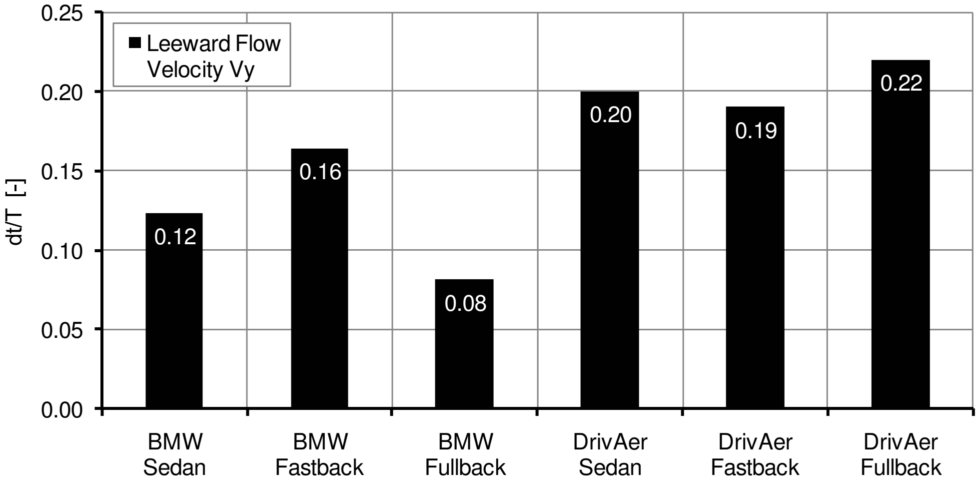

Figure 6.45: Time delay of the leeward flow for six different vehicle geometries.

for the BMW fastback the leeward flow is as pronounced as for the DrivAer vehicles and yet it features a significantly smaller time delay of the wake flow. Furthermore, the time delays of the wake flow within the DrivAer family do not correspond to the strength of the leeward flow. One possible explanation is an influence of the size of the wake region. A larger recirculation region may result in larger characteristic length scales, and thus larger time scales of the wake region. This would explain the large time delay of the wake flow in the case of the DrivAer station wagon. Furthermore, the strength of the leeward vortices may also increase the time delay of the wake flow, as the vortices can be assumed to exhibit a certain inertial effect. This again would explain the relatively large differences in time delay of the wake flow of BMW sedan and station wagon although the strength of the leeward flow is very similar. A more detailed investigation of these presumptions however exceeds the frame of this work and should be analyzed separately.

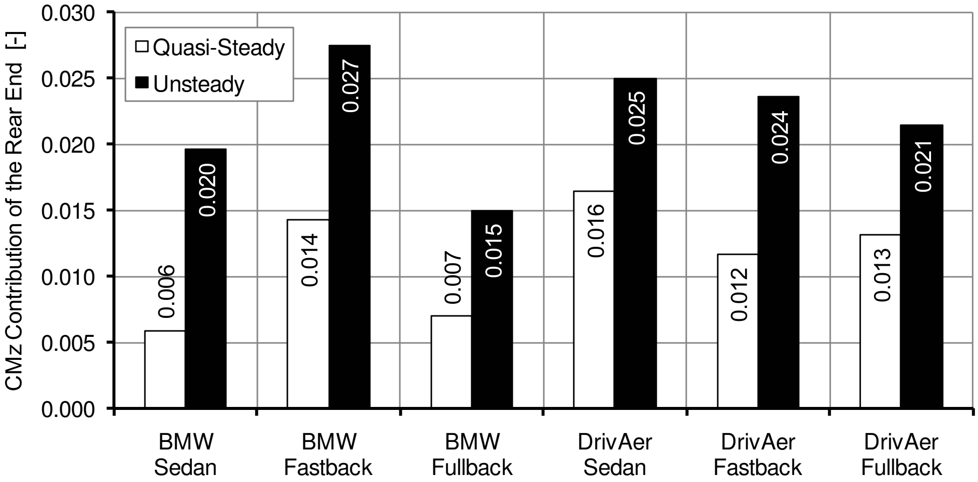

Figure 6.46: Unsteady and quasi-steady contribution of the rear end to the yaw moment C_{Mz} for six vehicle geometries.

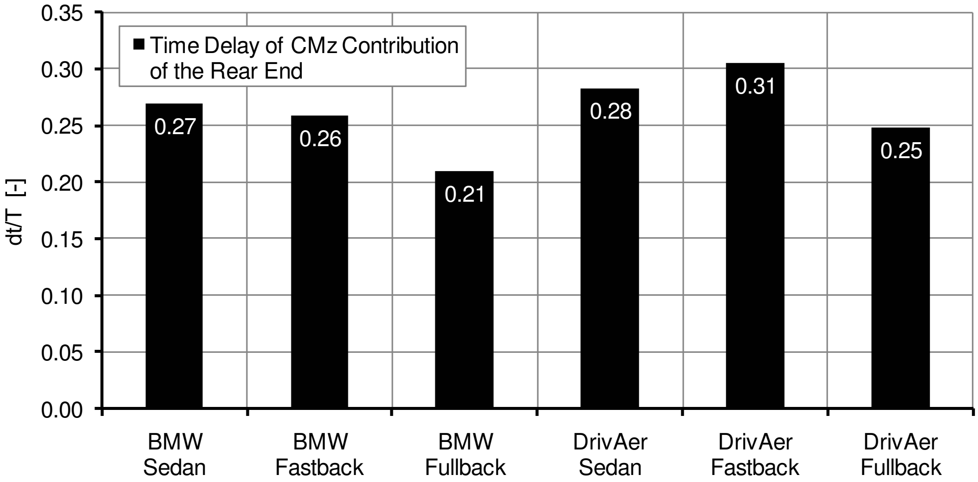

Figure 6.47: Time delay of the yaw moment C_{Mz} at the rear end for six vehicle geometries.

Given the variations in intensity of the characteristic wake topology, the unsteady effects at the rear end - which are essentially responsible for the integral differences - are expected to vary accordingly, too. Fig. 6.46 and Fig. 6.47 quantify the contribution of the rear end (region 6-6) to the yaw moment and its corresponding time delay. As expected, the unsteady and quasi-steady contributions to the yaw moment differ significantly. Focusing on the unsteady contribution, the amplitudes are largest for the fastbacks and the DrivAer sedan and smallest for the BMW station wagon. This corresponds very well with the strength of the leeward flow. For the corresponding time delays a direct correlation with the strength of the leeward flow cannot be identified. The time delay is largest for the DrivAer fastback and smallest for the BMW station wagon. Presumably, the time delay of the rear contribution to the yaw moment depends not only on the strength and time delay of the leeward flow but also on the direct influence of the oncoming flow. As shown schematically in Chap. 5.2, the time delay at the rear end is influenced by both the wake flow as well as the oncoming flow.

Finally, the contribution of the rear end of course also depends on the size of the lateral area that is influenced by the leeward flow. Fig. 6.48 plots the lateral area behind the rear wheels for all six vehicles. Unsurprisingly, the station wagons feature the largest rear area followed by the fastback vehicles. Furthermore, the lateral size of the rear end is larger for the BMW vehicles as they are longer than the DrivAer vehicles.

Summarizing the presented results, it can be concluded that the six vehicles generally show the same unsteady characteristics described in Chap. 5.1 but to very different extents. Measuring the unsteady effects using the differences between unsteady and quasi-steady amplitudes, they are largest for the BMW fastback and the DrivAer sedan and smallest for the BMW station wagon. The unsteady mechanism proposed in Chap. 5.2 for sedan vehicles also applies to fastback and station wagon vehicles. Building on the detailed investigation, the intensity of the unsteady effects may be assumed to depend on the following three factors:

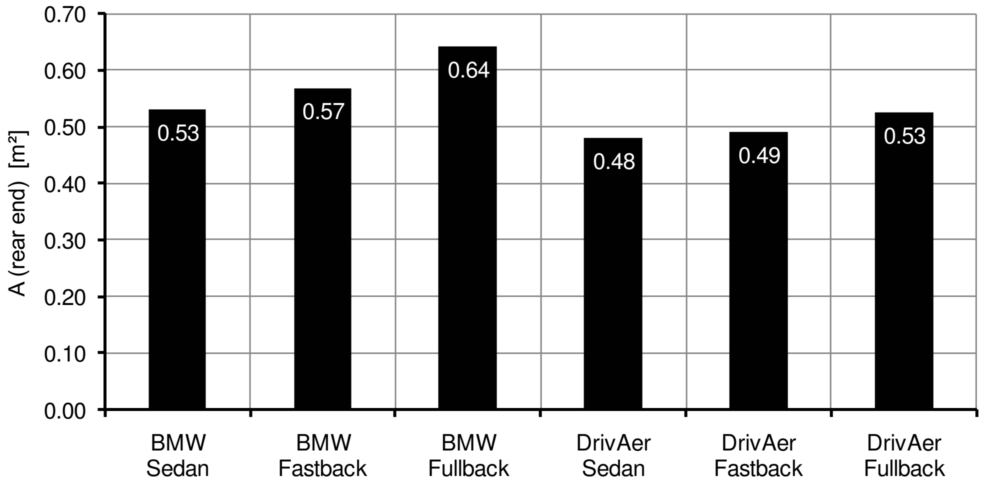

Figure 6.48: Comparison of the lateral area behind the rear wheel for the six investigated vehicles.

- The strength of the leeward flow,
- The time delay of the wake flow and
- The size of the lateral impact area.

Hence, if any of the three parameters is increased the unsteady effects are also expected to increase. However, due to the complexity of the system, a prediction of the unsteady effects based on these three factors can only provide a rough estimate. In particular, it was not always possible to consequently explain smaller differences between the investigated vehicle types. Irrespective of the intensity of the unsteady effects, it has to be kept in mind that for vehicle dynamics the absolute unsteady aerodynamic loads are relevant and not the differences between unsteady and quasi-steady values. Hence, a vehicle with small unsteady effects but large quasi-steady loads may still be less desirable than a vehicle with large unsteady effects but small quasi-steady loads. In addition, the effect of the time delays of side force, roll and yaw moment on the vehicle motion and on the driver is yet unclear.

Concluding the analysis of the three different vehicle types, the results can be summarized as follows:

- Sedan, fastback and station wagon feature the same characteristic unsteady behavior featuring a decrease of side force and roll moment and an unsteady overshoot of the yaw moment.
- The unsteady mechanism as described in Chap. 5.2 also applies to fastbacks and station wagons. Hence, the unsteady effects are caused by a time delay of the wake flow for all three vehicle types.
- The characteristic wake topology is similar for sedan, fastback and station wagon consisting of fluid entering with high lateral velocities into the wake

region from the leeward side forming two x-aligned vortices above and below the leeward flow.

- The unsteady effects are generally more pronounced for sedan and fastback than for the station wagon. However, the DrivAer station wagon proves that unsteady effects during gust events may be significant also for station wagons.
- The unsteady effects are assumed to be influenced by the strength of the leeward flow, the time delay of the wake flow and the size of the lateral impact area.

6.3 Geometrical Parameters

After investigating the unsteady phenomena for a range of different gust parameters and for different vehicle types in the preceding chapters, the influence of geometrical parameters is studied for the DrivAer sedan in the following. In order to analyze possibilities to influence the unsteady aerodynamic behavior during gust events three different types of geometric variations are studied: First, large flaps are attached to the rear end with the aim of preventing flow to enter into the wake region (Chap. 6.3.1). Second, the influence of the vehicle length on the unsteady effects is analyzed (Chap. 6.3.2) and finally, the shape of the rear end is varied (Chap. 6.3.3). As opposed to the preceding chapter, a generic three-peak gust with peak yaw angles of ±6° is used.

6.3.1 Rear End Flaps

In order to confirm that the flow entering into the wake region from the leeward side or, more precisely, its delayed reaction to the change of yaw angle is the source of the unsteady effects at the rear end, unrealistically large flaps are attached to the rear end with the aim of disturbing the leeward flow. As shown in Fig. 6.49, two versions of the flaps are investigated: One version with lateral flaps and one with flaps in the wake of the vehicle, called rearward flaps. According to the unsteady mechanism of Chap. 5.2, the unsteady effects are expected to disappear or to decrease if the flaps prevent or at least reduce the leeward flow.

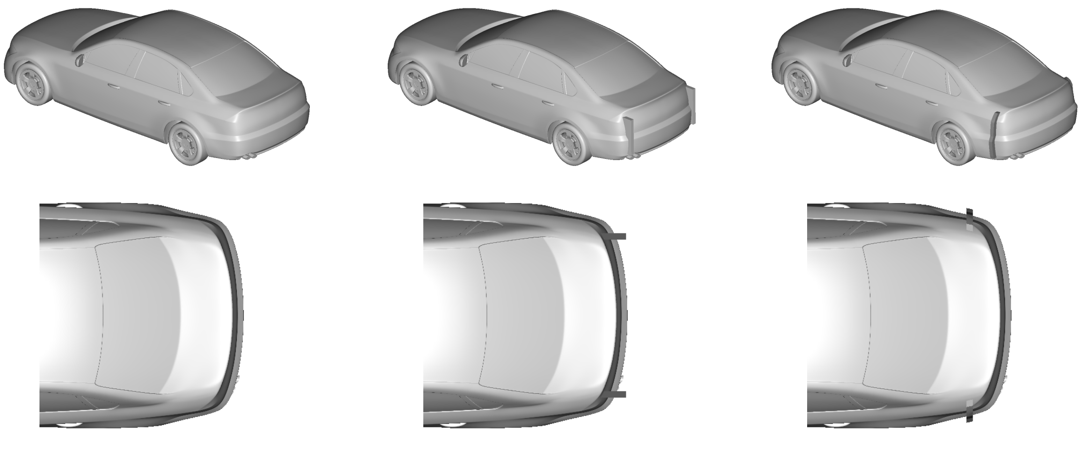

(a) Baseline (b) Rearward Flaps (c) Lateral Flaps

Figure 6.49: Vehicle geometries for (a) baseline, (b) rearward flaps and (c) lateral flaps.

In Fig. 6.50 the lateral velocity V_y is plotted together with streamlines in a z-slice at mid vehicle height for a constant yaw angle of +6°. As described before, the fluid is accelerated around the leeward rear corner and enters into the wake region from the leeward side for the baseline geometry. In comparison, the rearward flaps prevent the fluid from following the geometry of the leeward corner and from entering directly into

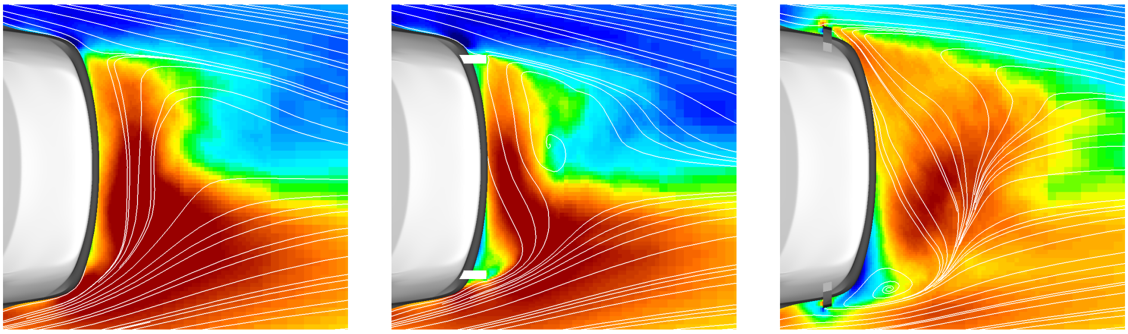

(a) Baseline (b) Rearward Flaps (c) Lateral Flaps

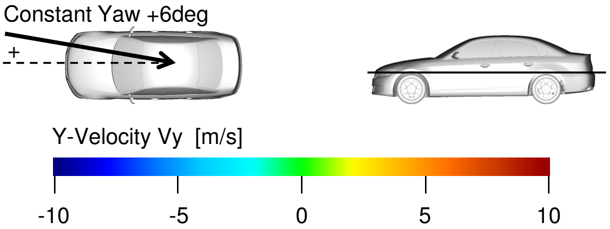

Figure 6.50: Visualization of the lateral velocity V_y in a z-slice for the baseline and rear end flaps geometries at constant yaw +6°.

the wake region. The fluid is forced to continue further downstream. Furthermore, the rearward flaps define a sharp edge of separation. However, since the flaps are symmetric the same applies to the flow on the windward side which is therefore also prevented from entering into the wake region. As a result, the leeward and windward flow separate at the end of the rearward flaps and it is again the leeward flow which is then pulled into the wake region.

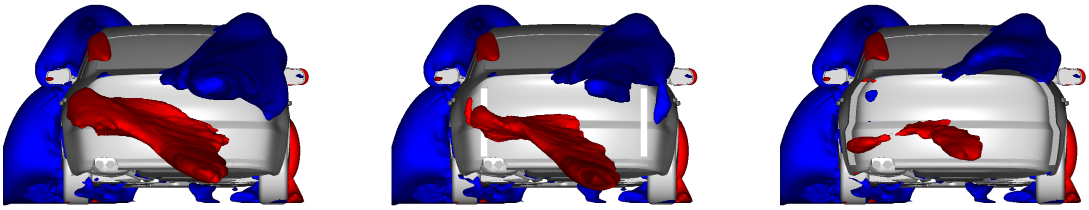

(a) Baseline (b) Rearward Flaps (c) Lateral Flaps

Figure 6.51: Isosurfaces of of lateral velocity $V_y = \pm 10 m/s$ for the baseline and rear end flaps geometries at constant yaw +6°.

In comparison, the lateral flaps disturb the flow much earlier before it starts to be accelerated around the leeward corner. The impact of the lateral flaps is much larger causing a considerable change of the wake flow and a significant increase of the recirculation zone. Nevertheless, fluid still enters into the wake region primarily from the leeward side, although with a reduced lateral velocity. Hence, even very obtrusive modifications like the flaps at the rear end do not completely prevent the leeward

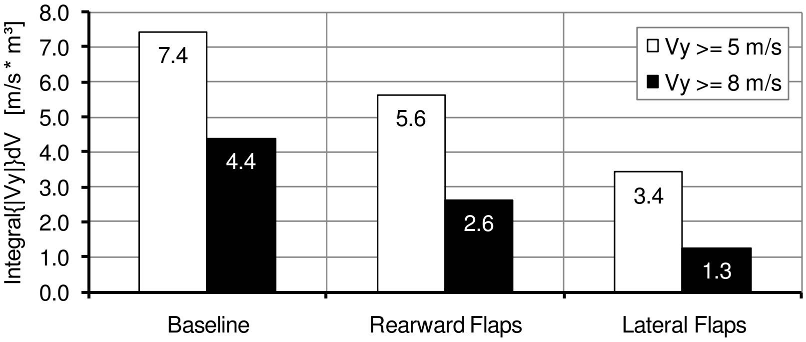

Figure 6.52: Strength of the leeward flow for the baseline and rear end flaps geometries under constant yaw calculated by integrating over the isosurfaces of $V_y > \pm 5m/s$ and $V_y > \pm 8m/s$.

flow from entering into the wake region. The typical isosurfaces of $V_y = \pm 10m/s$ are shown in Fig. 6.51 confirming this conclusion. The strength of the leeward flow is again calculated by integrating over the isosurfaces of $V_y > \pm 5m/s$ and $V_y > \pm 8m/s$ (Fig. 6.52). The results confirm that the rearward and in particular the lateral flap versions significantly reduce the strength of the leeward flow.

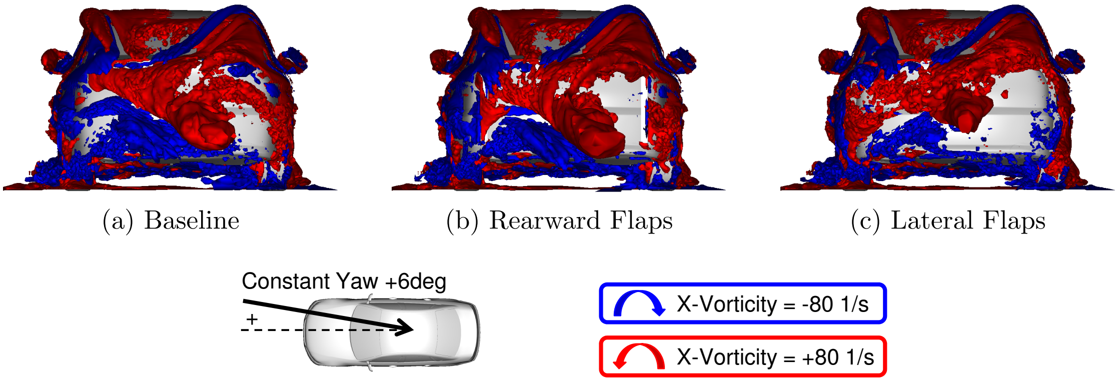
(a) Baseline (b) Rearward Flaps (c) Lateral Flaps

Figure 6.53: Isosurfaces of x-vorticity $\omega_x = \pm 80\ 1/s$ for the baseline and rear end flaps geometries at constant yaw $+6°$.

Fig. 6.53 and Fig. 6.54 show the isosurfaces of $Vort_x = \pm 80\ 1/s$ and of the $\lambda_2 - criterion = -3000\ 1/s^2$. While for the rearward flaps the leeward wake vortices are only slightly less pronounced, they are significantly weaker for the lateral flaps. The isosurfaces of x-vorticity and the $\lambda_2 - criterion$ indicate that the flow structures are broken up by the lateral flaps, which also results in smaller characteristic time scales.

Based on the reduced strength of the leeward flow, the unsteady effects are expected to decrease for both flap versions. Fig. 6.55 plots the quasi-steady and unsteady amplitudes of the side force, roll and yaw moment. Surprisingly, the impact of the relatively large modifications on the quasi-steady amplitudes is comparatively small confirming that the quasi-steady amplitudes are dominated by the contributions of the front and the greenhouse. The quasi-steady side force is reduced by the rearward flaps

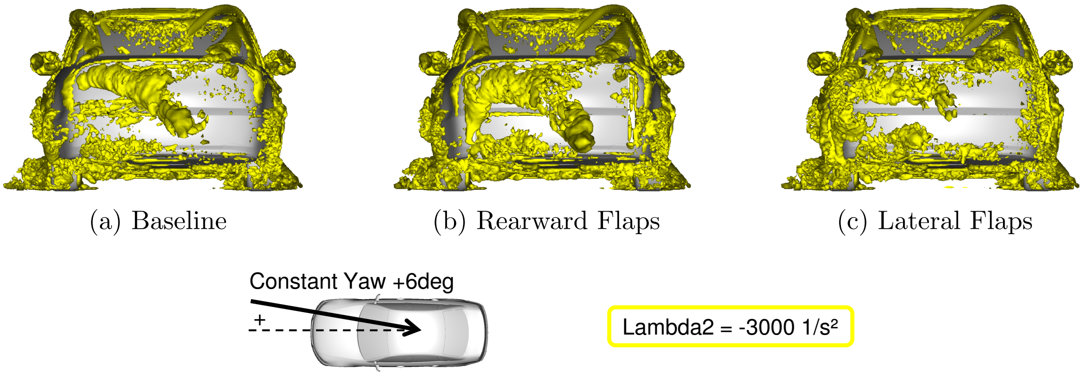
(a) Baseline (b) Rearward Flaps (c) Lateral Flaps

Figure 6.54: Isosurfaces of $\lambda_2 - criterion = -3000\ 1/s^2$ for the baseline and rear end flaps geometries at constant yaw +6°.

by approximately 4%, while the lateral flaps do not have an effect on the quasi-steady side force. The variations in quasi-steady roll moment are limited to 0.003. Only the quasi-steady yaw moment exhibits a larger range of variation. The rearward flaps increase the yaw moment by approximately 10%, while the lateral flaps cause a reduction of approximately 5%.

In comparison, the unsteady variations are much larger, spanning approximately 0.1 in side force, 0.03 in roll moment and 0.05 in yaw moment. The unsteady side force as well as the unsteady roll moment are significantly increased by the rearward and in particular by the lateral flaps. For the yaw moment, the order is inversed with the baseline geometry featuring the maximum and the lateral flaps the minimum unsteady yaw moment. Hence, the flaps increase the unsteady side force and roll moment while they decrease the unsteady yaw moment.

In Fig. 6.56 the differences between unsteady and quasi-steady amplitudes are summarized. As for the baseline geometry, the flaps feature positive differences for the yaw moment and negative differences for the side force and roll moment. For all three load components the absolute differences between unsteady and quasi-steady amplitudes are reduced significantly by the flaps. Again, the lateral flaps are more effective in reducing the unsteady effects than the rearward flaps. Regarding the time delays of the aerodynamic loads, the flaps do not exhibit the same large influence as for the amplitudes (Fig. 6.57). Only the time delay of the roll moment is reduced, while the time delays of side force and yaw moment remain approximately constant.

Given the strong impact on the unsteady behavior, the contribution of the rear end (segment 6-6) is of particular interest. Fig. 6.58 plots the quasi-steady and unsteady amplitudes of the yaw moment at the rear end. While the quasi-steady amplitudes do not exhibit a continuous trend, the unsteady amplitudes are reduced by the flaps. Again, the smallest amplitudes occur for the lateral flaps. Additionally, the lateral flaps significantly reduce the time delay of the unsteady yaw moment compared to the baseline geometry. This corresponds to the assumption, mentioned above, that the flow structures and thus the timescales of the wake flow are reduced by the lateral flaps. However, for the rearward flaps this is not the case (Fig. 6.59), resulting in similar time delays for the rearward flaps and the baseline geometry.

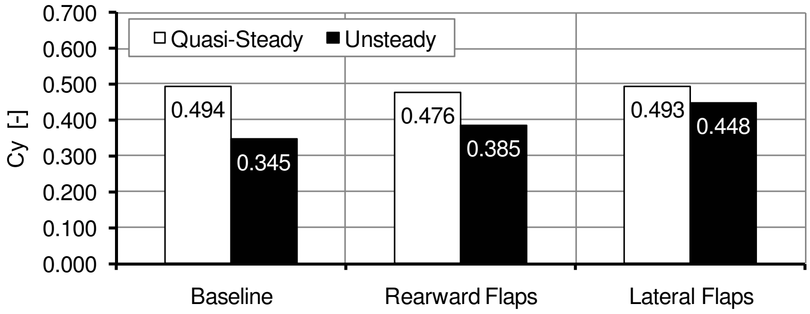

(a) Side Force C_y

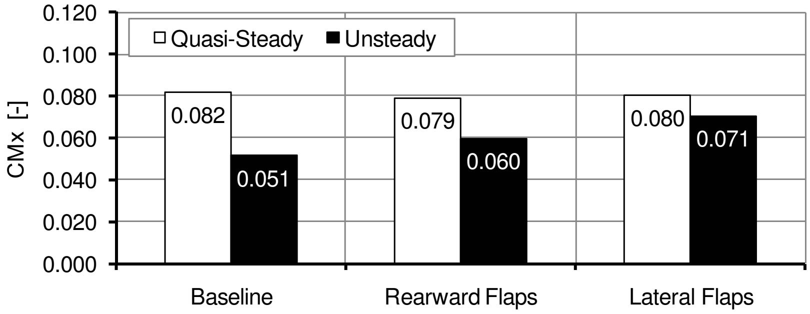

(b) Roll Moment C_{Mx}

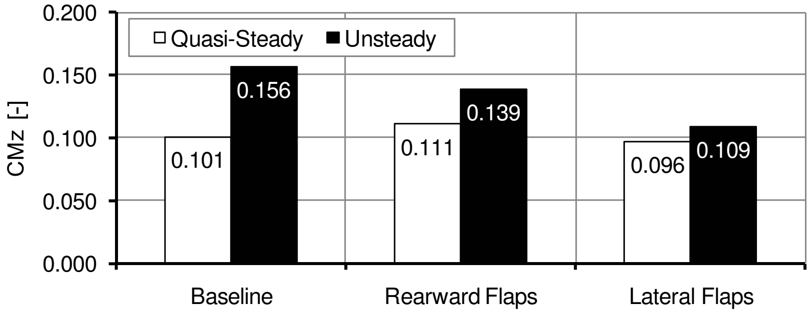

(c) Yaw Moment C_{Mz}

Figure 6.55: Unsteady and quasi-steady amplitudes for (a) side force, (b) roll moment and (c) yaw moment.

In order to explain the variations in quasi-steady and unsteady aerodynamic loads, Fig. 6.60 shows the distribution of the pressure differences between left and right side for the three geometries. As expected, the quasi-steady and unsteady pressure differences at the front and the greenhouse are not affected by the flaps. At the rear end the rearward flaps reduce the quasi-steady pressure differences. In contrast, the quasi-steady pressure differences are increased in front of the lateral flaps. Thus, the counter-rotating contribution of the rear yaw moment is reduced by the rearward flaps and increased by the lateral flaps, which explains the inverse behavior of the two flap versions regarding the quasi-steady yaw moment. In the unsteady case, the rearward flaps again simply reduce the pressure differences at the rear. For the lateral flaps,

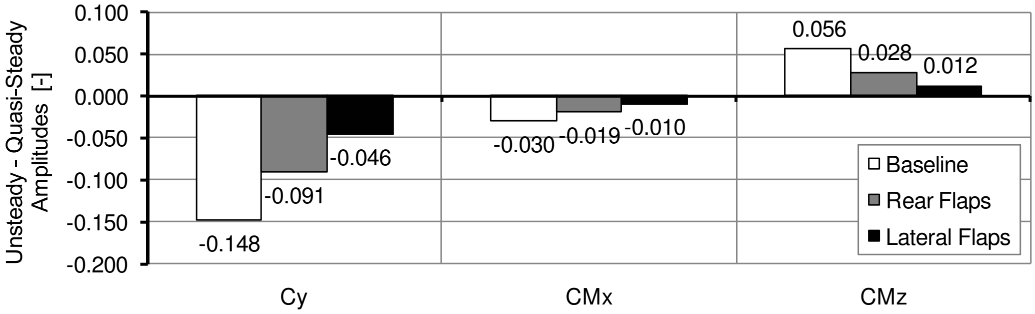

Figure 6.56: Differences between unsteady and quasi-steady amplitudes for side force, roll moment and yaw moment.

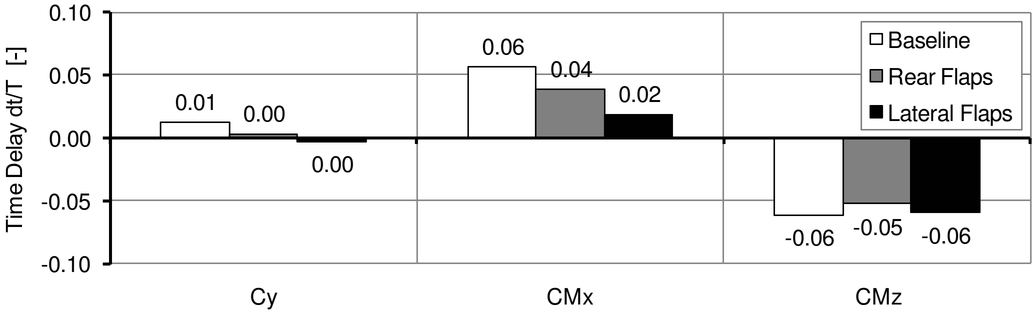

Figure 6.57: Time delays between unsteady and quasi-steady side force, roll moment and yaw moment.

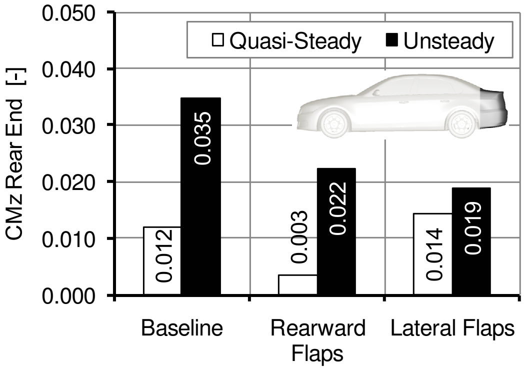

Figure 6.58: Contribution of the rear end to the yaw moment amplitude.

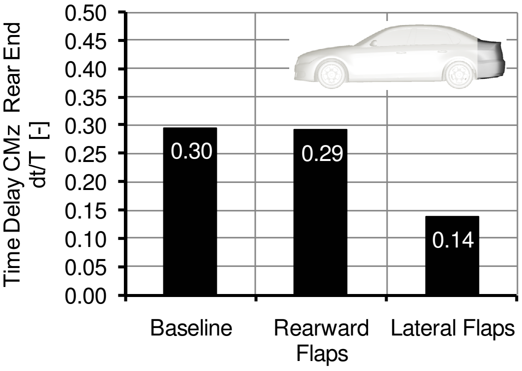

Figure 6.59: Time delays of the yaw moment at the rear end.

however, the pressure difference is inverted compared to the baseline geometry and is similar to the quasi-steady distribution. Hence, the differences between unsteady and quasi-steady pressure distribution are largest for the baseline geometry and smallest for the lateral flaps.

It can be concluded, that the flaps, in particular the lateral flaps, effectively reduce the unsteady effects. This leads to a reduction of the unsteady yaw moment on the

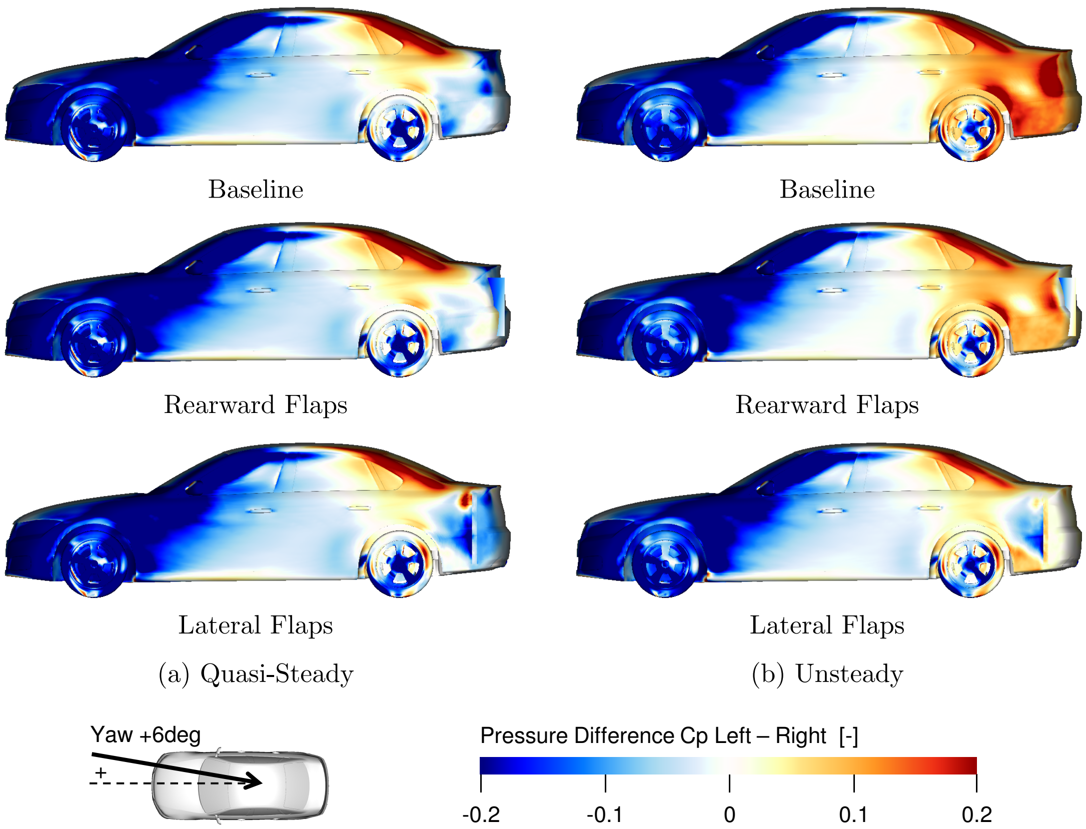

Baseline

Baseline

Rearward Flaps

Rearward Flaps

Lateral Flaps

Lateral Flaps

(a) Quasi-Steady

(b) Unsteady

Figure 6.60: Unsteady and quasi-steady pressure differences between left and right side $C_{p,left} - C_{p,right}$ for the baseline and the rear end flaps geometries for the peak yaw angle of +6°.

one hand, but also to an increase of the unsteady side force and roll moment on the other hand. In contrast to the unsteady variations, the quasi-steady influence of the modifications is relatively small, which may be explained by the dominating effect of the front and the greenhouse in the quasi-steady case. Key to the reduction of the unsteady effects is the reduced strength of the leeward flow. For the lateral flaps this leads to smaller amplitudes and also to smaller time delays of the contribution of the rear end. Therefore, this investigation confirms that the intensity of the identified unsteady effects is primarily influenced by the strength and the time delay of the characteristic leeward flow. Furthermore, the flow topology behind the lateral flaps suggests that a reduction of the unsteady phenomena may be achieved by preventing the formation of large flow structures in the wake region. Such large flow structures are likely to exhibit an increased inertial resistance to adapt to changes of the oncoming flow.

The investigation of the rear end flaps can be summarized as follows:

- Rearward and in particular lateral flaps significantly reduce the unsteady effects in side force, roll and yaw moment.
- Compared to the baseline geometry, flaps reduce the unsteady yaw moment but

increase the unsteady side force and roll moment.

- The reduction of the unsteady effects is directly linked to a reduction in strength and time delay of the leeward flow.
- The unsteady differences between the three geometry variants are much larger than the corresponding quasi-steady differences.

6.3.2 Vehicle Length

In the preceding chapter, it was shown how the leeward flow and thereby the unsteady aerodynamic behavior can be influenced by unrealistically large add-on parts. In this chapter, it is investigated how this can instead be achieved by varying the proportions of the vehicle, namely the wheelbase, the front and the rear overhang. In order to increase the differences between the variants the modifications are exaggerated. Starting from the baseline geometry the three parameters wheelbase, front and rear overhang are each varied by ±150 mm, see Fig. 6.61. Of particular interest is how the geometry modifications influence the unsteady loads in comparison to the quasi-steady loads as the latter correspond to the data typically used in the development process today.

(a) Front Overhang −150 mm

(b) Front Overhang +150 mm

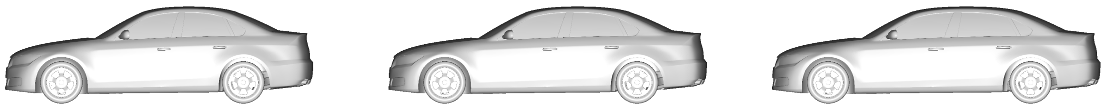

(c) Wheelbase −150 mm

(d) Baseline

(e) Wheelbase +150 mm

(f) Rear Overhang −150 mm

(g) Rear Overhang +150 mm

Figure 6.61: Vehicle geometries for the variation front overhang, wheelbase and rear overhang.

Fig. 6.62 plots the unsteady and quasi-steady side force, roll and yaw moment for the three types of geometry modifications. Except for the yaw moment, the variations of the quasi-steady loads are again very small and in most cases do not show a clear trend. This is particularly surprising for the side force as the quasi-steady results do not reflect the variation of the lateral area of the vehicle. This suggests that at small yaw angles the side force is not primarily influenced by the lateral projection surface but by the pressure peaks at the front and rear corners and at the A- and C-pillar. Similar to the side force, the quasi-steady roll moment shows

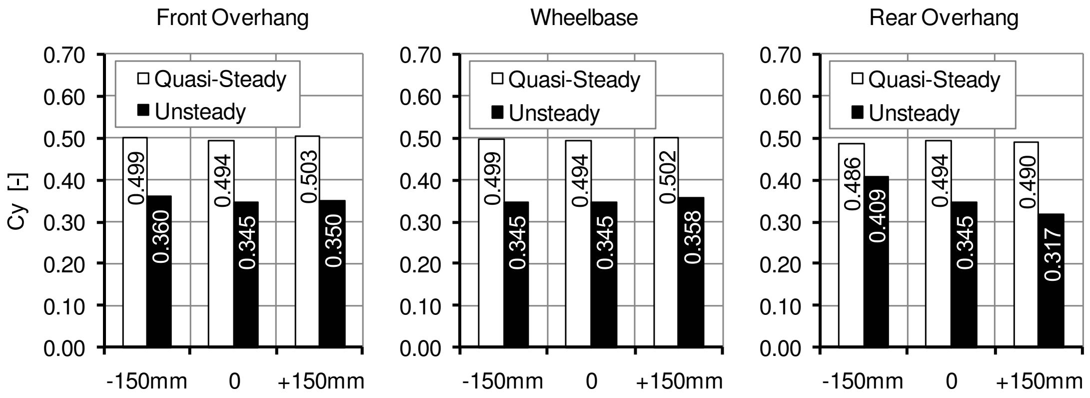

(a) Side Force C_y

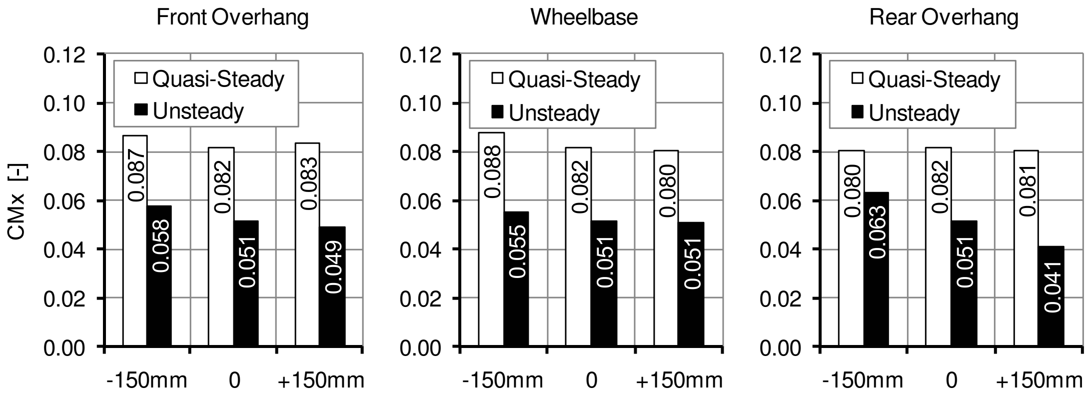

(b) Roll Moment C_{Mx}

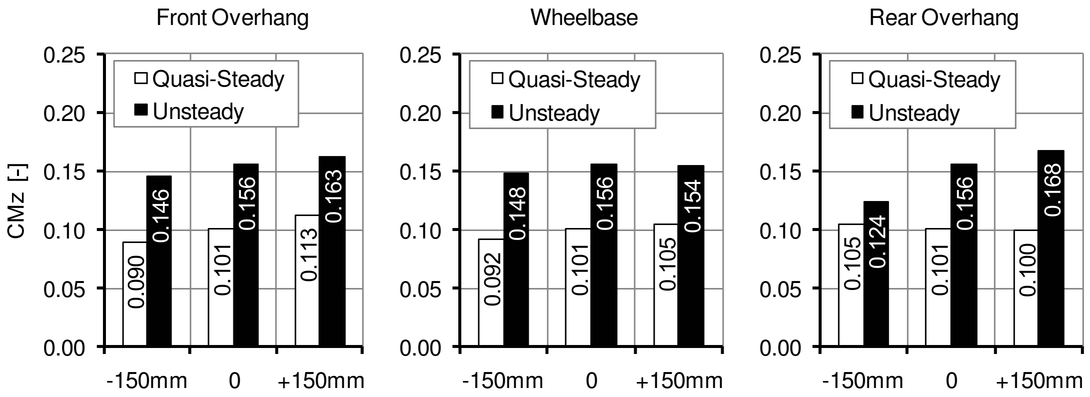

(c) Yaw Moment C_{Mz}

Figure 6.62: Unsteady and quasi-steady amplitudes for (a) side force, (b) roll moment and (c) yaw moment.

only small variations. A clear trend can only be identified for the modification of the wheelbase, which can however be explained by the associated variation of the reference length. In comparison, the quasi-steady yaw moment is more sensitive to the geometrical modifications. The increase of the front overhang and of the wheelbase results in a 10% respectively 5% increase of the quasi-steady yaw moment. On the other hand an increase of the rear overhang reduces the quasi-steady yaw moment slightly. Generally, the variations of the aerodynamic moments may be due to changes in the surface pressure distributions but also due to a variation of the distances to the aerodynamic point of reference.

As already seen for the different vehicle types in Chap. 6.2 or for the rear end flaps in Chap. 6.3.1, the range of unsteady variations is generally larger than the corresponding quasi-steady range. In particular the modification of the rear overhang has a pronounced effect on the unsteady loads. Increasing the rear overhang from −150 mm to +150 mm, the unsteady side force and roll moment are reduced by 0.092 and 0.022, which corresponds to a variation of 27% and 43% relative to the baseline amplitudes. At the same time, the unsteady yaw moment is increased by 0.044, which corresponds to a variation of 28% relative to the baseline amplitude.

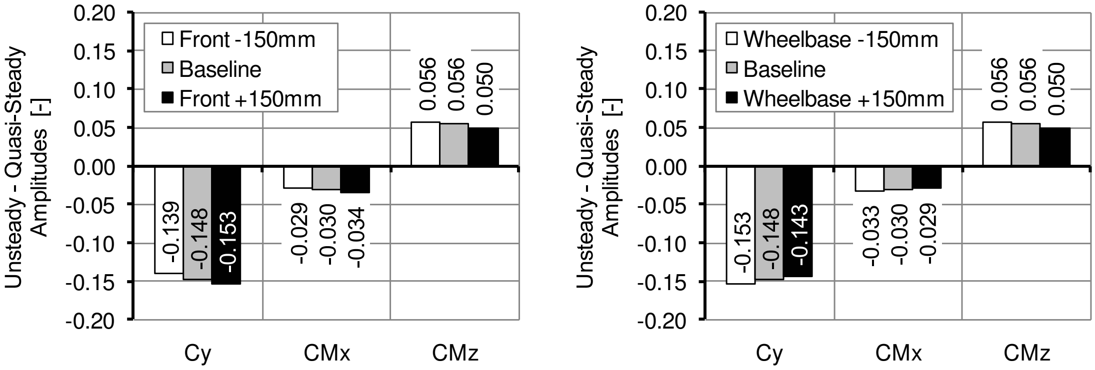

(a) Front Overhang

(b) Wheelbase

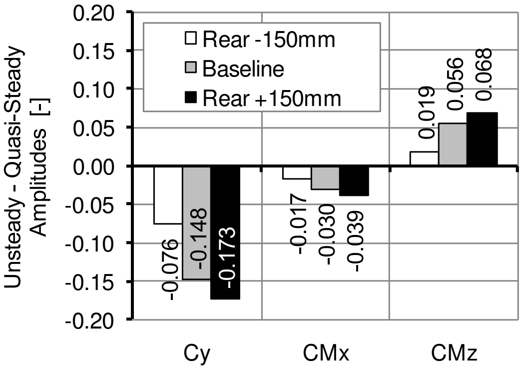

(c) Rear Overhang

Figure 6.63: Differences between unsteady and quasi-steady amplitudes for the variation of the (a) front overhang, (b) wheelbase and (c) rear overhang.

In comparison, the variation of the unsteady loads due to the modification of the wheelbase and the front overhang are relatively small. In particular for the variation of the wheelbase, the unsteady aerodynamic loads do not exhibit a clear trend.

Extending the front overhang slightly reduces the unsteady roll moment, while the unsteady yaw moment is increased. Interestingly, the unsteady side force does not show a corresponding trend.

Fig. 6.63 summarizes the differences between unsteady and quasi-steady amplitudes. With increasing length of the front overhang the unsteady effects increase slightly for the side force and the roll moment, while they decrease for the yaw moment. For the wheelbase, the unsteady effects are reduced for all three load components as the length increases. The most significant variations occur for the modification of the rear overhang where the absolute differences between unsteady and quasi-steady amplitudes significantly increase with the length of the rear overhang.

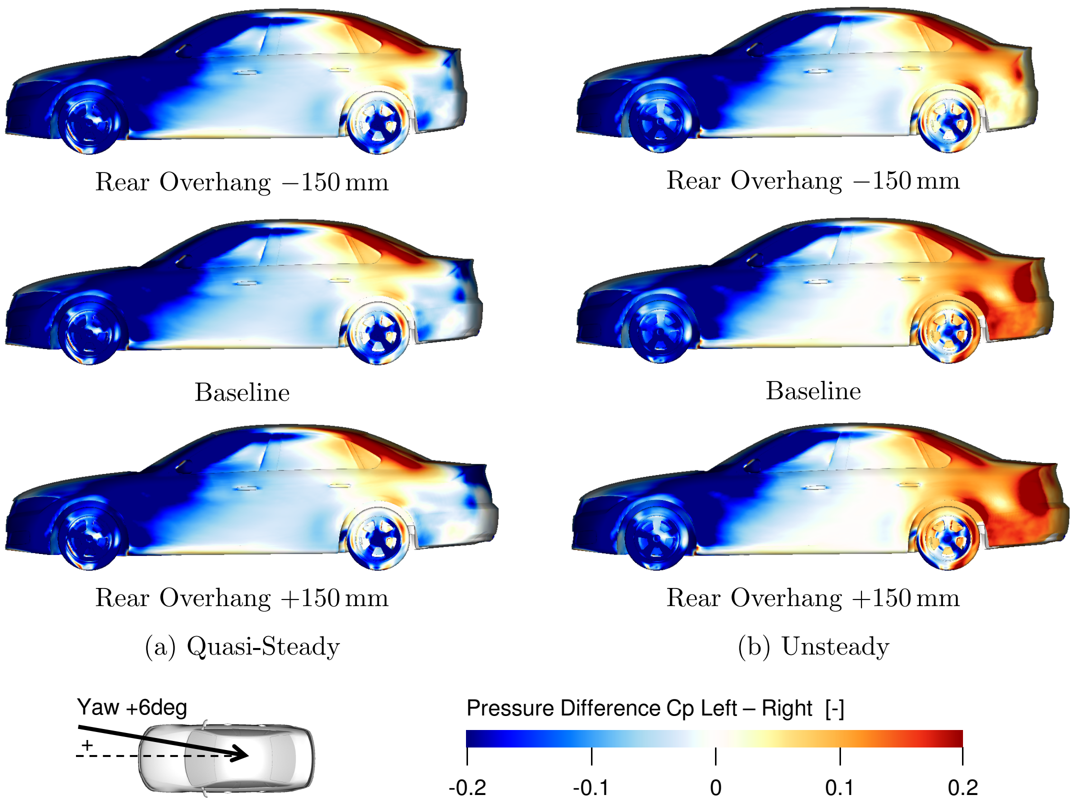

(a) Quasi-Steady (b) Unsteady

Figure 6.64: Unsteady and quasi-steady pressure differences between left and right side $C_{p,left} - C_{p,right}$ for the baseline and the variation of the rear overhang for the peak yaw angle of +6°.

As the modification of the rear overhang exhibits the largest impact on the aerodynamic loads, the pressure differences between left and right side are shown for this modification in Fig. 6.64 for the quasi-steady as well as the unsteady case. The quasi-steady pressure distribution varies only very little for the three variants. However, in the unsteady case the pressure differences at the rear end change significantly depending on the length of the rear overhang. All three variants show inverted pressure differences at the rear end compared to the quasi-steady case. However, for the variant with the shortened rear overhang the intensity of the pressure differences is much smaller than for the extended rear overhang.

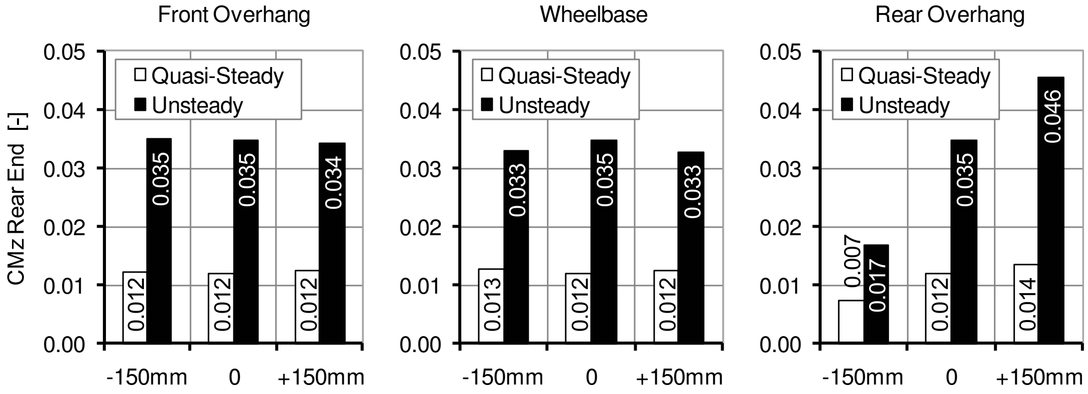

Figure 6.65: Unsteady and quasi-steady yaw moment amplitudes at the rear end of the vehicle for the variation of front overhang, wheelbase and rear overhang.

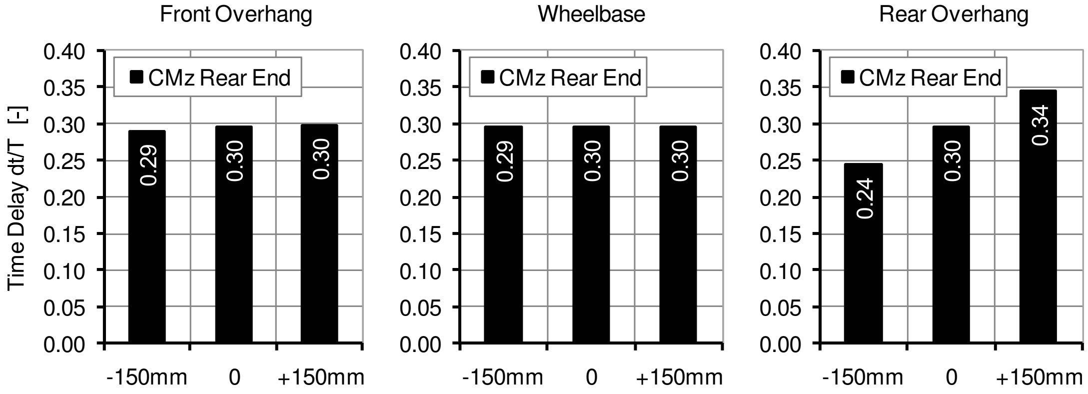

Figure 6.66: Time delay of the unsteady yaw moment at the rear end of the vehicle for the variation of front overhang, wheelbase and rear overhang.

To quantify these differences at the rear of the vehicle, the contributions of the rear end (segment 6-6) to the yaw moment are plotted in Fig. 6.65. The modifications of the front overhang and the wheelbase do not affect the quasi-steady nor the unsteady yaw moment at the rear end. Large variations are, however, visible for the modification of the rear overhang. The quasi-steady amplitude increases from 0.007 to 0.014. The increase in unsteady amplitude is even more pronounced featuring an increase from 0.017 to 0.046. Hence, for the extended rear overhang the unsteady amplitude in the rear segment reaches more than three times the quasi-steady amplitude. At the same time, the corresponding time delay increases significantly from $\Delta t/T = 0.24$ to $\Delta t/T = 0.34$, compare Fig. 6.66. In comparison, for the modification of the front overhang and the wheelbase the time delays vary by only $\Delta t/T \leq 0.01$.

Finally, in Fig. 6.67 the strength of the leeward flow is compared for all geometry modifications. As expected, the strength of the leeward flow varies only very little for the modifications of front overhang and wheelbase. In contrast, it increases with the length of the rear overhang which correlates with the intensity of the unsteady effects at the rear end seen above. In addition to the variation of the leeward flow,

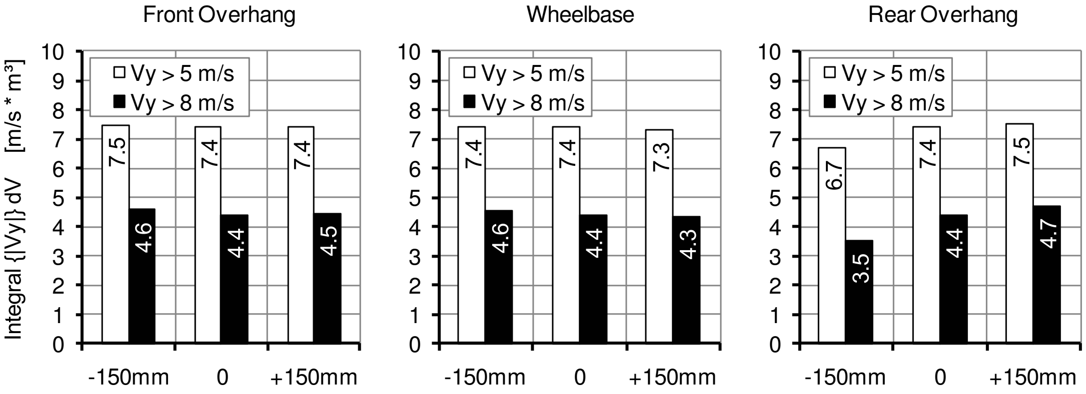

Figure 6.67: Strength of the leeward flow for the variation of front overhang, wheelbase and rear overhang under constant yaw calculated by integrating over the isosurfaces of $V_y > \pm 5m/s$ and $V_y > \pm 8m/s$.

also the lateral projection area at the rear end is increased. This may explain why the extended rear overhang features much larger unsteady effects at the rear end compared to the baseline geometry, although the strength of the leeward flow does not increase to the same extent.

It can be concluded that the largest sensitivities occur for the variation of the rear overhang and for the yaw moment. While the parameters front overhang and wheelbase only have a small influence on the side force and the roll moment, they cause an increase of the unsteady and quasi-steady yaw moment. This variation mainly results from an increase of the lever arms of the load contributions. Since unsteady and quasi-steady amplitudes are equally affected, the differences between the two change only very little. The third geometry modification, the extension of the rear overhang, does not have a large influence on the quasi-steady amplitudes. However, the unsteady amplitudes are strongly dependent on the length of the rear end. Extending the rear overhang leads to a reduction of unsteady side force and roll moment and an increase of the unsteady yaw moment. Hence, extending the rear overhang reduces the quasi-steady yaw moment but increases the unsteady yaw moment. Therefore, an optimization using the quasi-steady data would lead to a result which significantly increases the unsteady effects and thus the peak yaw moments that occur in real world. The increase in unsteady yaw moment is caused by an increase of the amplitude as well as the time delay of the rear-end contribution, which correlates very well with the increased strength of the leeward flow.

The influence of the wheelbase, front and rear overhang can be summarized as follows:

- The parameters front overhang and wheelbase have a small influence on the quasi-steady aerodynamic loads and on the unsteady results. However, the differences between unsteady and quasi-steady amplitudes remain constant.
- The parameter rear overhang strongly influences the unsteady effects at the rear end and thus the unsteady aerodynamic loads.

- An extension of the rear overhang results in a reduction of the unsteady side force and roll moment but in an increase of the unsteady yaw moment.
- The unsteady effects at the rear correlate well with the strength of the leeward flow and the affected lateral rear area.
- A quasi-steady optimization would lead to an increase in unsteady yaw moment, which is assumed to have a negative effect on the vehicle dynamics during crosswind gusts.

6.3.3 Rear End Shape

As seen for the rear end flaps and the rear overhang, the unsteady effects can be reduced by decreasing the intensity of the leeward flow. Therefore, in the following investigation the shape of the rear end corners is varied with the aim of influencing the leeward flow and thereby the unsteady effects. In addition to the baseline geometry, three rear end shapes are studied: A rounded version, a version with a clearly defined line of separation, called "edged", and a widened, cut-off rear end, called "angular", see Fig. 6.68.

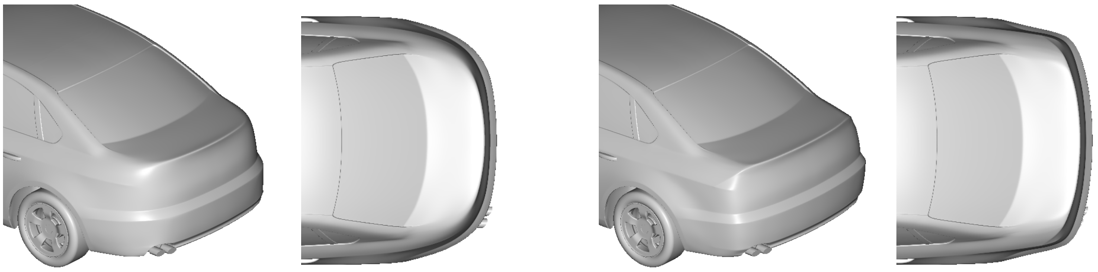

(a) Round Rear End

(b) Baseline

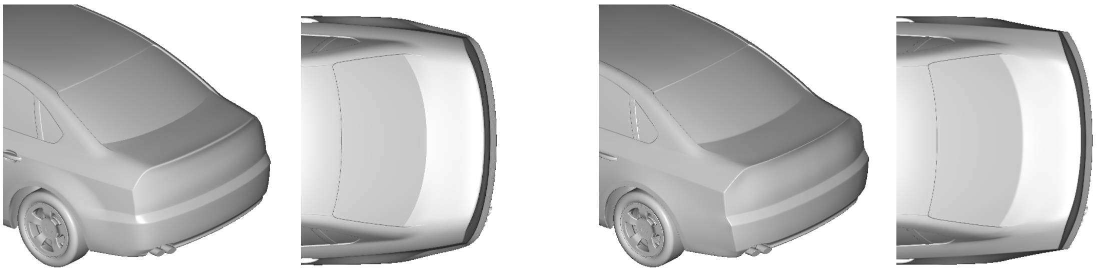

(c) Edged Rear End

(d) Angular Rear End

Figure 6.68: Vehicle geometries for the (a) round rear end, (b) baseline, (c) edged rear end and (d) angular rear end.

In Fig. 6.69, the unsteady and quasi-steady side force, roll and yaw moment are plotted for the four variants. The quasi-steady side force and roll moment are largest for the baseline and the edged rear end. In comparison, the variation of the quasi-steady yaw moment is exactly inversed. In this case the quasi-steady yaw moment for the baseline and edged rear end is smaller than for the rounded and angular rear ends.

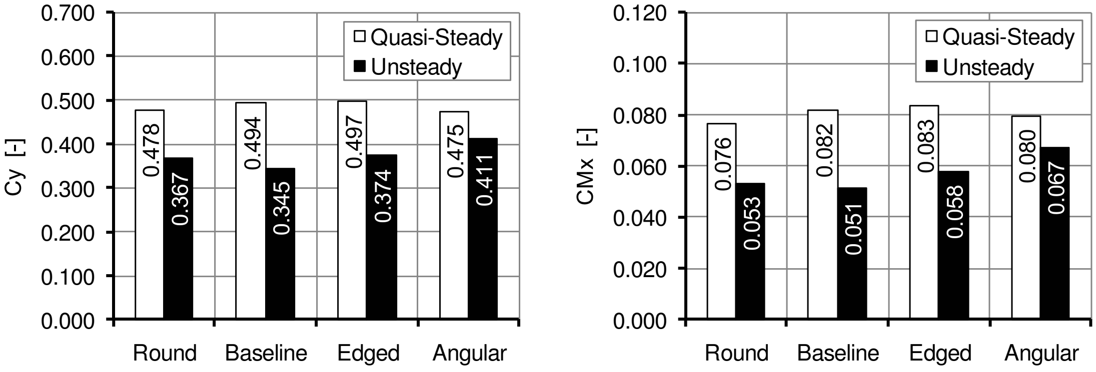

(a) Side Force C_y

(b) Roll Moment C_{Mx}

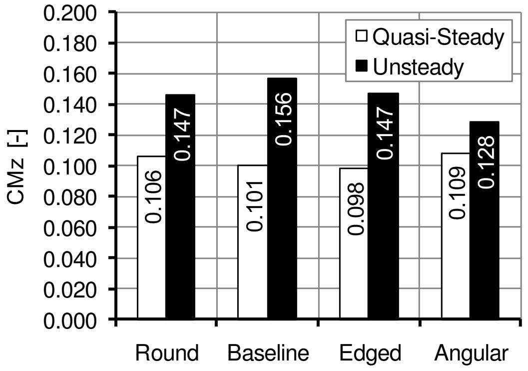

(c) Yaw Moment C_{Mz}

Figure 6.69: Unsteady and quasi-steady amplitudes for (a) side force, (b) roll moment and (c) yaw moment.

Hence, in the quasi-steady case both a more rounded as well as an angular rear end reduce the side force and roll moment but increase the yaw moment.

Looking at the unsteady results, the quasi-steady behavior is exactly inversed. The minimum unsteady side force and roll moment as well as the maximum unsteady yaw moment now occur for the baseline geometry. A change towards a rounded rear end as well as towards an angular rear end decreases the unsteady yaw moment but increases the unsteady side force and roll moment. Again, the range of unsteady variations is much larger than the quasi-steady range. For example for the yaw moment, the variation between minimum and maximum quasi-steady amplitudes amounts to 0.011 but reaches 0.028 in the unsteady case. However, most importantly, unsteady and quasi-steady trends are exactly inverted and would therefore lead to opposite decisions in the optimization process.

Calculating the differences between unsteady and quasi-steady amplitudes, the unsteady effects are largest for the baseline geometry and are reduced for both the rounded and the angular rear end (see Fig. 6.70). For the yaw moment this corresponds to an magnification factor of 1.55 for the baseline geometry and only 1.18 for the angular rear end. In Fig. 6.71, the resulting time delays of side force, roll and

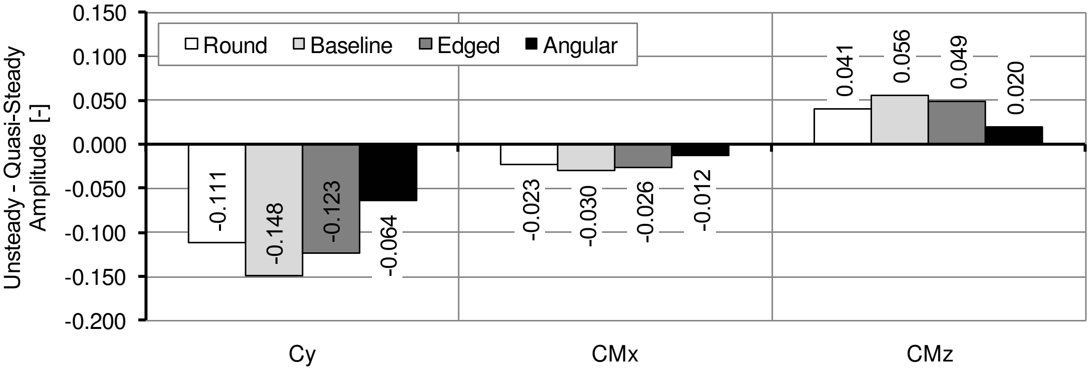

Figure 6.70: Differences between unsteady and quasi-steady amplitudes for the baseline and the round, edged and angular rear end variants.

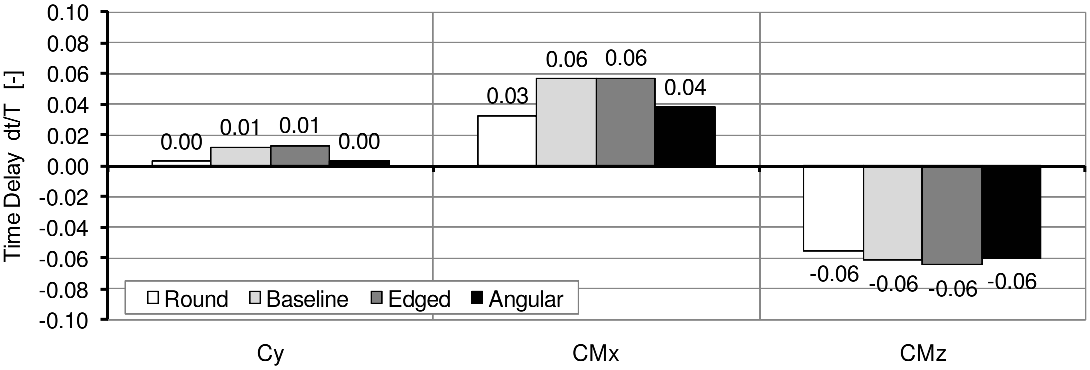

Figure 6.71: Time delay of unsteady side force, roll and yaw moment for the baseline and the round, edged and angular rear end variants.

yaw moment are plotted for the four variants. The time delays are largest in absolute value for the baseline geometry and the edged rear end and are reduced for both the rounded as well as the angular rear end. However, the general characteristics of a negative time delay in yaw moment and positive time delays in side force and roll moment do not change. Furthermore, the variations are very small for the side force and the yaw moment. Only the time delay of the roll moment varies by $\Delta t/T = 0.03$.

Fig. 6.72 shows the distribution of the pressure differences between left and right side for the quasi-steady as well as the unsteady case at the peak yaw angle of $+6°$. As expected, the differences are limited to the rear of the geometries. In the quasi-steady case the negative pressure differences at the rear corner vary in intensity, reaching a maximum for the edged version. Surprisingly, the intensity of the pressure differences is reduced for both the rounded and the angular rear. In the unsteady case, the pressure differences are inverted at the rear end for all variants, as it was described in detail in Chap. 5.1 and are most pronounced for the baseline geometry. For the edged and the angular rear, the intensity is reduced significantly. In particular, for the angular rear the differences between left and right rear end are very small. In comparison, the rounded geometry exhibits large pressure differences behind the rear

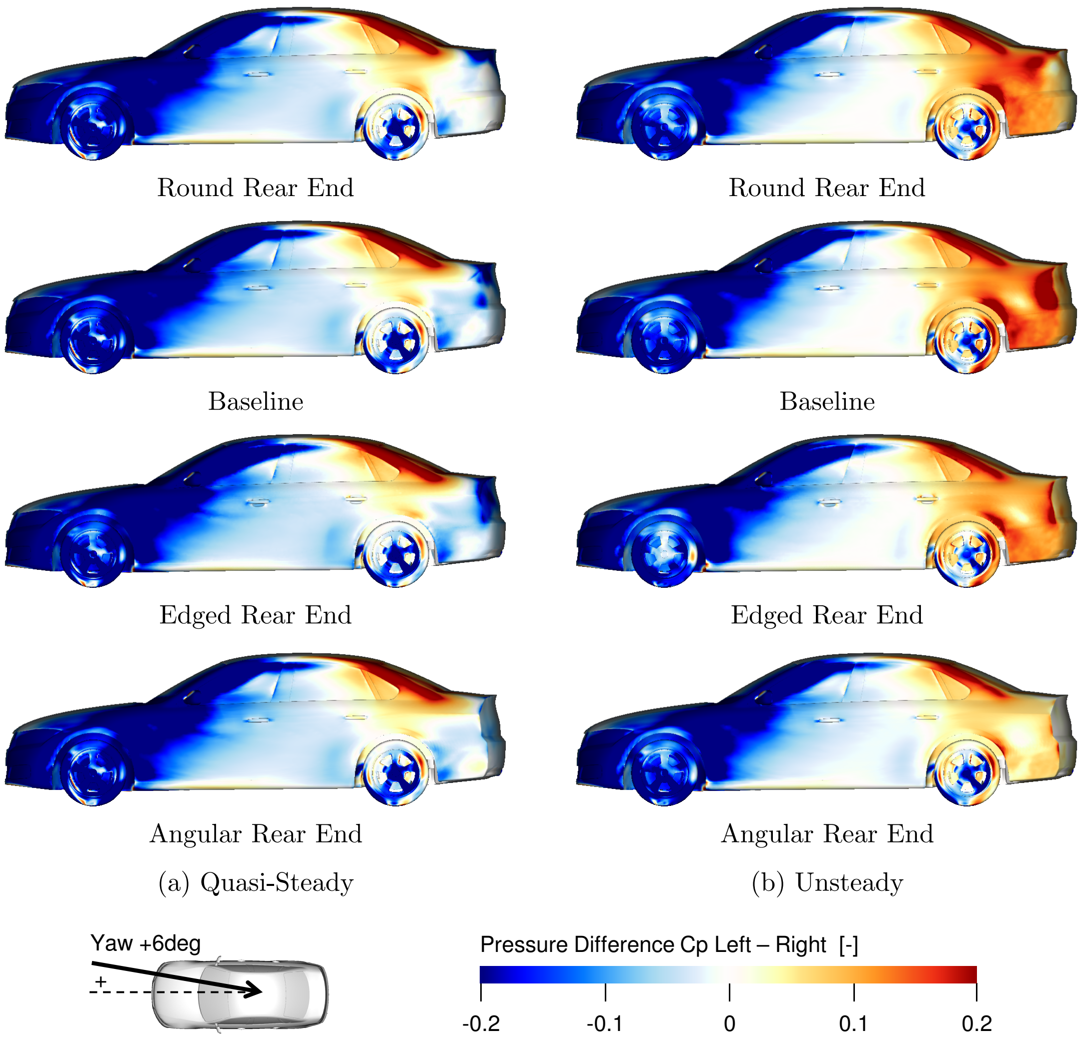

Figure 6.72: Unsteady and quasi-steady pressure differences between left and right side $C_{p,left} - C_{p,right}$ for the baseline and the round, edged and angular rear end variants.

wheel but their intensity is reduced significantly towards the rear end.

The corresponding amplitude and time delay of the rear end contributions are plotted in Fig. 6.73 and Fig. 6.74. As expected, the quasi-steady amplitude is largest for the edged rear end followed by the baseline geometry. The smallest quasi-steady amplitude occurs for the angular rear end. As the contribution of the rear end reduces the overall yaw moment in the quasi-steady case, Fig. 6.73 explains the differences described above. In the unsteady case, the baseline geometry shows the largest amplitude followed by the edged rear end. Again, the angular rear end exhibits the smallest amplitude. Due to the time delay the rear C_{Mz}-contribution is now in phase with the contribution of the front and therefore increases the integral yaw moment. Hence, the amplitudes of the rear end explain the increase in unsteady yaw moment seen in Fig. 6.69. The variation of the time delays, shown in Fig. 6.74, corresponds roughly to the variation of the unsteady amplitudes. The baseline geometry exhibits

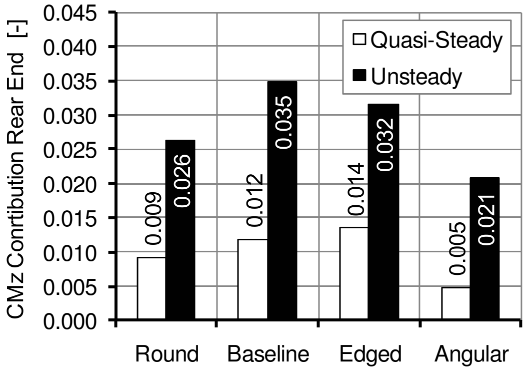

Figure 6.73: Contribution of the rear end to the yaw moment amplitude.

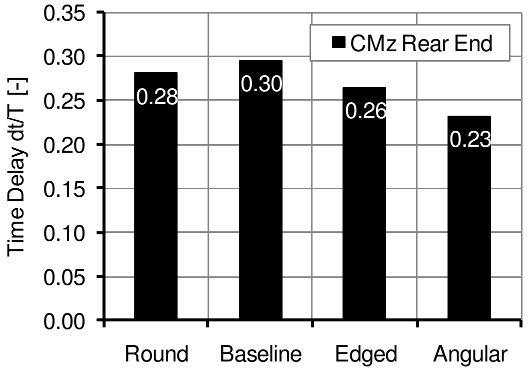

Figure 6.74: Time delays of the yaw moment at the rear end.

the largest time delay, while the angular rear end features the smallest time delay. However, the time delays of the rounded and the edged rear end do not perfectly correspond to the gradation of the unsteady amplitudes.

Given the differences in the pressure distributions at the rear end, significant variations of the flow phenomena, namely of the leeward flow, are to be expected. Fig. 6.75 visualizes the lateral velocity V_y in a z-slice together with streamlines. For all variants the fluid enters into the wake region from the leeward side. In particular for the baseline geometry, the fluid is accelerated around the leeward corner causing low pressures. For the angular rear end, the flow separates at the sharp-edged corners, both on the leeward and on the windward side. Very interestingly, the rounded rear end differs from the baseline geometry in that the fluid is not accelerated but rather decelerated at the leeward rear corner. Fig. 6.76 plots the strength of the leeward flow. As expected, the leeward flow is the least pronounced for the angular rear end and increases for the edged and the baseline geometry. However, for the rounded rear end the strength of the leeward flow is similar to the baseline geometry, which does not correspond to the reduced unsteady effects at the rear end.

In order to obtain a spatial impression of the leeward flow entering into the wake region, Fig. 6.77 shows the isosurfaces of $V_y = \pm 10\ m/s$ for the peak yaw angle of $+6°$. As seen before, the positive isosurface begins at the leeward rear light and stretches inward. For the angular rear end the size of the leeward isosurface is reduced significantly but its shape is very similar. For the rounded rear end, however, the leeward isosurface starts higher and enters into the wake region diagonally from the top of the trunk. This change of flow topology is confirmed by the isosurfaces of x-vorticity $\omega_x = \pm 80\ 1/s$ shown in Fig. 6.78. For the baseline geometry, the edged and the angular rear end the two vortices are aligned vertically on the leeward side and only vary in strength for the angular rear end. The rounded geometry variant, however, features two regions of high positive and negative x-vorticity at the upper leeward corner of the rear end.

Hence, the reduction of the unsteady effects for the rounded rear end can be explained by the fact that the leeward flow enters into the wake region diagonally from the top and not from the side of the rear end. Thus, the fluid is not significantly accelerated

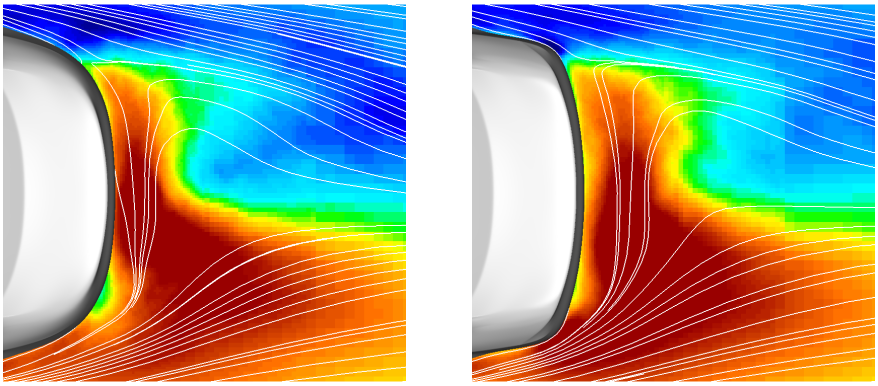

(a) Round Rear End (b) Baseline

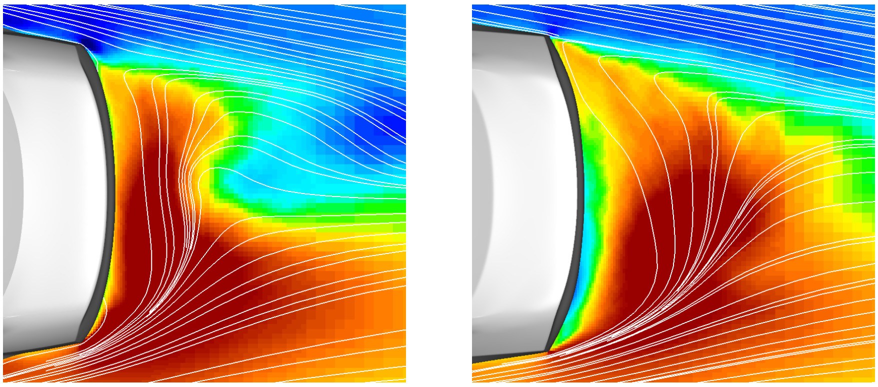

(c) Edged Rear End (d) Angular Rear End

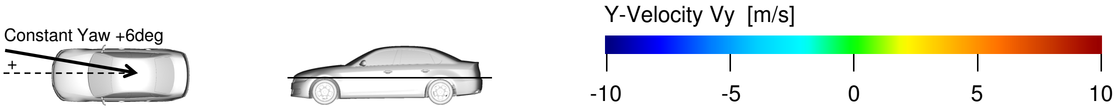

Figure 6.75: Visualization of lateral velocity V_y in z-slice for the baseline and rear end variants at constant yaw +6°.

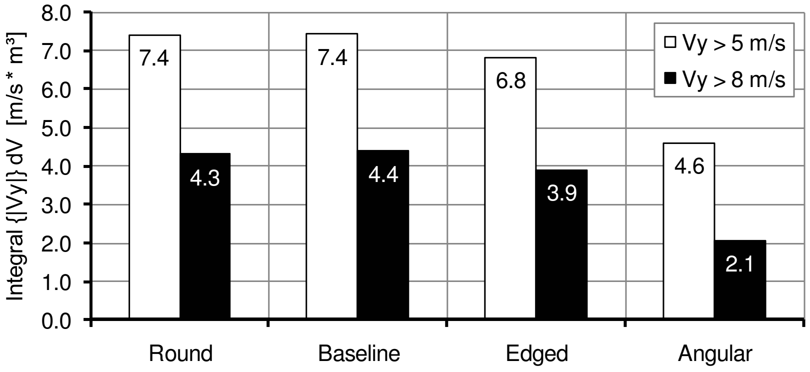

Figure 6.76: Strength of the leeward flow for the baseline as well as for the round, edged and angular rear end under constant yaw calculated by integrating over the isosurfaces of $V_y > \pm 8\ m/s$ and $V_y > \pm 8\ m/s$.

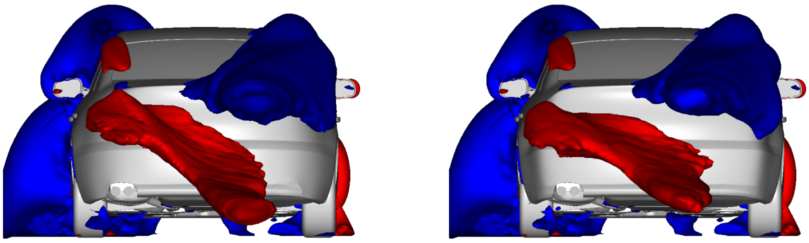

(a) Round Rear End (b) Baseline

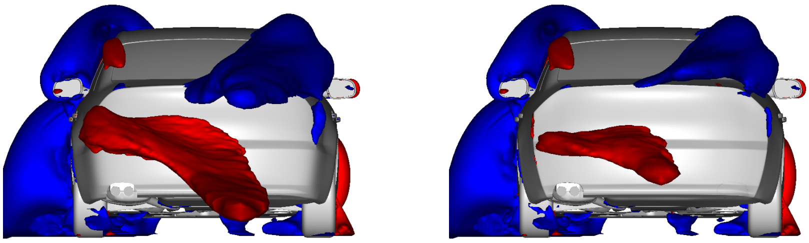

(c) Edged Rear End (d) Angular Rear End

Figure 6.77: Isosurfaces of of lateral velocity $V_y = \pm 10\ m/s$ for the baseline and the round, edged and angular rear end variants at constant yaw $+6°$.

around the leeward corner and the influence of the leeward flow on the lateral surface pressures is reduced. Apart from this particular effect for the rounded rear end, it can be concluded that a sharp-edged rear end reduces the intensity of the leeward flow and thus the unsteady effects in the overall aerodynamic loads.

The results of the investigation of the rear end shape can be summarized as follows:

- The rear end shape has a significant influence on both unsteady and quasi-steady side force, roll and yaw moment. Again, the sensitivity is much larger in the case of the unsteady loads.
- For the investigated rear ends, the quasi-steady and unsteady behavior of side force, roll and yaw moment is exactly inverted.
  - Quasi-steady: A sharp-edged rear end increases $C_{Mz,QS}$ but reduces $C_{y,QS}$ and $C_{Mx,QS}$.
  - Unsteady: A sharp-edged rear end reduces $C_{Mz,US}$ but increases $C_{y,US}$ and $C_{Mx,US}$.
- Generally, the intensity of the leeward flow and thus the unsteady effects in the aerodynamic loads can be reduced by a sharp-edged rear end.
- For the round rear end, the unsteady effects in the aerodynamic loads are reduced due to an upward shift of the leeward flow to the top of the trunk. Thus,

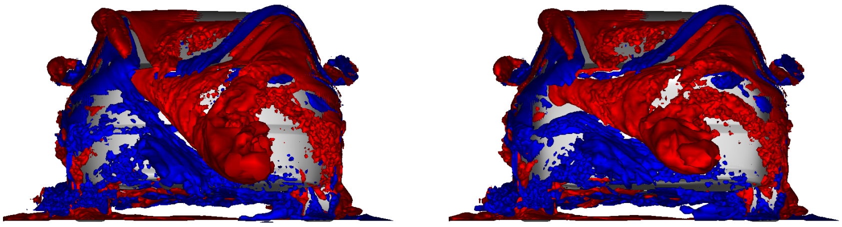

(a) Round Rear End (b) Baseline

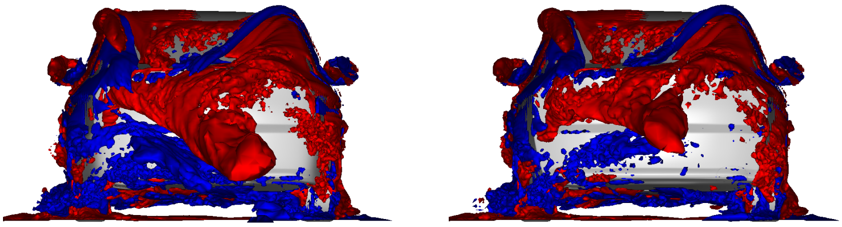

(c) Edged Rear End (d) Angular Rear End

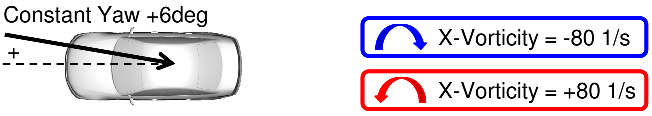

Figure 6.78: Isosurfaces of of x-vorticity $\omega_x = \pm 80\ 1/s$ for the baseline and the round, edged and angular rear end variants at constant yaw +6°.

the lateral surface pressure is less affected by the unsteady flow phenomena in the wake region.

Chapter 7

Summary and Outlook

The aim of this work was to investigate the unsteady aerodynamic behavior in gusty crosswind. Using both numerical simulation and wind tunnel experiments, it was possible to characterize the unsteady aerodynamic loads during generic gust events, which can be divided into two groups: The aerodynamic drag C_x, lift C_z and pitching moment C_{My} exhibit only small variations and in addition tend towards the 0°-yaw levels, which are generally less critical for vehicle dynamics than the corresponding values in yawed configuration. On the other hand, the side force C_y, roll moment C_{Mx} and yaw moment C_{Mz}, which are assumed to be relevant for vehicle dynamics during gust events, exhibit very large variations. Compared to the quasi-steady approximation side force and roll moment show smaller unsteady amplitudes while the unsteady amplitude of the yaw moment is significantly larger than its quasi-steady counterpart. This corresponds to the findings of Demuth and Buck (2006), Favre (2009), Schrefl (2008), Tsubokura et al. (2009), Chadwick et al. (2001), some of which have however been performed at unrealistic yaw angles, Strouhal or Reynolds numbers. For the investigated sedan vehicle and the standard test case at 140 km/h and 1 Hz the reduction of unsteady side force and roll moment amounts to -34% and -36%, respectively. The unsteady yaw moment is increased by +104%.

Furthermore, the unsteady aerodynamic loads exhibit significant time delays compared to the quasi-steady approximation. For the standard test case mentioned above, the unsteady side force and roll moment show positive time delays of $\Delta t/T = +0.04$ and $\Delta t/T = +0.12$, respectively. In comparison, the unsteady yaw moment exhibits a negative time delay of $\Delta t/T = -0.09$.

Following the characterization of the unsteady loads the underlying flow mechanism was identified. The unsteady effects described above are caused by a delayed reaction of the wake flow to the change of the oncoming flow. This results in a time delay and an amplification of the load contribution of the rear end. Due to the inversed sign, the superposition of the delayed and amplified rear contribution with the load contributions of the remaining vehicle explains the opposite results for side force and yaw moment. The time delay of the wake flow is strongly influenced by its characteristic topology, which consists of fluid entering into the wake region from the leeward side flanked by two counter-rotating vortices above and below. Starting from the time delay of the wake flow the proposed unsteady mechanism provides an understanding for the unsteady flow mechanism at the rear end as well as an explanation for the differences between unsteady and quasi-steady aerodynamic loads.

Together with Johannes Wojciak a novel wind tunnel experiment was conceived which allows investigating unsteady vehicle aerodynamics during time-dependent flow conditions at realistic Reynolds and Strouhal numbers. In the frame of this work, the existence and the fundamental characteristics of the unsteady phenomena as well as the proposed unsteady mechanism could thereby be verified experimentally.

Following the identification, characterization and verification of the unsteady phenomena, the influence of the parameters number of oscillations, gust frequency, vehicle speed, gust amplitude and initial yaw angle were investigated numerically. Varying the number of oscillations showed that the unsteady phenomena already occur for a single sinusoidal yaw change. However, in order to improve reproducibility, the use of multiple-peak gusts with at least 3 to 5 oscillations is recommended. In addition, the variation of the initial yaw angle showed that the existence of a zero-crossing in the yaw angle change is key to the occurrence of unsteady effects in side force, roll and yaw moment. In the case of a yaw change without zero-crossing the unsteady effects disappear almost completely.

Varying the gust amplitude lead to the conclusion that the identified flow phenomena at the rear end occur for small as well as large amplitudes. However, only for small amplitudes - which dominate in real world - these flow phenomena are of relevance. At yaw angles below approximately 9° the surface pressures at the rear end and thus its aerodynamic loads are dominated by the wake flow. At large yaw angles above approximately 9° the direct influence of the oncoming flow increases and the influence of the wake flow is reduced considerably.

Furthermore, it was shown that gust frequency and vehicle speed have a significant impact on the unsteady effects. Plotting the amplification factor over the Strouhal number (Fig. 6.16) led to the observation that the unsteady behavior of side force, roll and yaw moment does not fully comply with the theoretical behavior, which describes a monotonic decrease of the amplification factor starting at 1 for $St = 0$ and tends towards 0 for $St \to \infty$. In contrast to the theoretical behavior, a maximum of the amplification factor occurs for the yaw moment and a local minimum for the side force and the roll moment at around $St = 0.2$ for the investigated vehicle geometry. In addition to the effects in unsteady amplitude, the time delays of the aerodynamic loads exhibit a strong dependency on the Strouhal number which may have a crucial impact on vehicle dynamics. In the investigated range of Strouhal and Reynolds numbers the unsteady phenomena are dominated by the Strouhal number while the effect of the Reynolds number is small.

In a very generic way, it can be concluded that the unsteady effects are obviously influenced by the two factors “unsteady amplitude” and “time delay of the local contribution of each surface element”. Applying this generic statement to the investigated gust events, the local contributions can be roughly divided into the contribution of the front and the rear of the vehicle. Hence, the unsteady phenomena are influenced by the unsteady amplitudes of front and rear and by the time delay between front and rear contribution. These two factors are again influenced by three time scales of the flow:

- The time scale of gust excitation,
- The time delay of the wake flow compared to the quasi-steady behavior, and
- The time delay between front and rear quasi-steady contributions due to the length of the vehicle.

The first is simply proportional to $1/f_{gust}$. The second time scale is determined by the vehicle speed U, by a characteristic geometric length and of course by the geometric shape of the vehicle. The third time scale is proportional to the vehicle length L and the vehicle speed U. Hence, if the shape of the vehicle is not changed, the Strouhal number $St = fL/U$ includes all relevant parameters.

In the frame of this work, the wheelbase of the vehicle L_{WB} was chosen as characteristic length scale. However, judging from the presented findings, the time delay of the wake flow may be better described using a length scale that is proportional to the size of the recirculation zone like for example the square root of the rear end projection area.

Following the investigation of gust parameters, the influence of different vehicle types was analyzed. It was shown that unsteady effects also occur for fastbacks and station wagons and that the proposed unsteady mechanism also applies for these vehicle types. However, depending on the type of the rear end the intensity of the unsteady effects in aerodynamic loads varies significantly. The differences between unsteady and quasi-steady aerodynamic loads are generally very pronounced for sedan and fastback geometries, while they are not as pronounced for station wagons. However, it is very important to remark that the quasi-steady and the unsteady ranking of side force, roll and yaw moment do not coincide. Furthermore, the differences between the two investigated vehicle families suggest that in addition to the rear end type, its design is also of great importance.

Comparing the results for the three vehicle types lead to the suggestion that the intensity of the unsteady effects depends on the three factors

- Strength of the leeward flow,
- Time delay of the wake flow, and
- Size of the influenced lateral area.

Although the investigated station wagons generally exhibit a less pronounced leeward flow, this is compensated for by a larger influenced lateral area and a larger time delay of the wake flow, which is presumably caused by a larger recirculation zone.

Finally, the impact of geometry variations on the unsteady effects was analyzed. By adding large flaps to the rear end, it was proved that reducing the strength of the leeward flow also reduces the intensity of the unsteady effects. Furthermore, it can be assumed that by breaking up the characteristic flow structures in the wake region, its time delay can be reduced.

The variation of the vehicle length showed that the length of the rear overhang has a significant influence on the unsteady phenomena. By increasing the rear overhang, the intensity of the unsteady effects is increased. Again, it is important to remark that the variations of unsteady and quasi-steady aerodynamic loads with the length of the rear overhang are of opposite directions. The same is true for the variation of the rear end shape, where a more angular geometry reduces the unsteady effects and thereby the unsteady yaw moment but increases the corresponding quasi-steady amplitude.

Although the investigated geometry variations are exaggerated, it can generally be concluded that the variation of the proportions and of the shape of the rear end provides measures to influence the unsteady aerodynamic loads in a relevant way. Interestingly, the range of investigated geometries showed that for geometrical variations at the rear of the vehicle the impact on the unsteady aerodynamic loads is much larger than on the corresponding quasi-steady values. As already remarked, an optimization based on unsteady aerodynamic loads at realistic yaw angles leads to a different optimum compared to today's steady-state optimization at large yaw angles. For most of the investigated rear end modifications unsteady and quasi-steady data even indicated completely inverted trends. Similarly, the impact of geometry variations may lead to different results for small and for large yaw angles, due to the influence of the wake flow at small yaw angles.

Given the deficiencies of today's steady-state measurements, the simulation of a multiple-peak gust as used in this work provides a tool to determine the unsteady aerodynamic behavior during a generic gust event and thus allows identifying critical vehicle geometries early in the development process. As described in the beginning, the aim of this work is to provide a broad understanding of the unsteady aerodynamic behavior in gusty crosswind. Extending the presented experimental verification of the unsteady phenomena, now a quantitative validation of the numerical results is required for a reliable application in the development process.

On the other hand, it has to be kept in mind that although reducing the unsteady effects results in a smaller unsteady yaw moment, the amplitudes of unsteady side force and roll moment are increased at the same time. Furthermore, the influence on the time delays is even much more complex. Therefore, without more detailed information regarding the impact of aerodynamic amplitudes and time delays on vehicle dynamics and eventually on the perception of the driver, an unsteady aerodynamic optimization is not possible. It is also very important to remark, that this work intentionally focuses on the aerodynamic aspects of crosswind sensitivity. In the development process of a vehicle, however, the combined system of aerodynamics, vehicle dynamics and driver reaction has to be analyzed with the aim of creating a customer benefit, i.e. an improved crosswind stability and hence a greater perceived passenger safety. Making use of today's simulation capabilities - CFD, multi-body simulations and driving simulators - ultimately a method is required that allows assessing the crosswind stability as perceived by the driver from an integral point of view.

Annex A

Fundamentals of Fluid Dynamics

The numerical investigations in this work are carried out using a Lattice Boltzmann solver. Compared to popular finite volume solvers, which are typically based on the macroscopic Navier-Stokes equations, the Lattice Boltzmann method is based on the Boltzmann equation, which describes the behavior of particles on a molecular level. In the following, a brief introduction to the Lattice Boltzmann method and the corresponding governing equations is given, which follows the very comprehensible formulations of Hänel (2004). For a more detailed discourse into molecular kinetic theory, the author recommends the books of Succi (2001) and Hänel (2004).

A.1 Governing Equations

Macroscopic Approach. Most commonly, fluid dynamics are described on a macroscopic level where the fluid is regarded as a continuum. The conservation laws of mass, momentum and energy can be written in the Einstein notation where repeated indexes i, j imply a summation over $i, j = 1, 2, 3$:

$$\begin{aligned} \frac{\partial \rho}{\partial t} + \frac{\partial}{\partial x_i}(\rho v_i) &= 0 \\ \frac{\partial}{\partial t}(\rho v_i) + \frac{\partial}{\partial x_j}(\rho v_i v_j + p\delta_{ij} - \sigma_{ij}) &= 0 \\ \frac{\partial}{\partial t}(\rho(e + v^2/2)) + \frac{\partial}{\partial x_i}(\rho v_i(e + v^2/2) + v_i p - v_j \sigma_{ij} - q_i) &= 0. \end{aligned} \tag{A.1}$$

where ρ represents the macroscopic density, v_i the velocity in direction i, e internal energy, p static pressure and δ_{ij} the Kronecker delta, which is equal 1 for $i = j$ and equal 0 for $i \neq j$. The transport terms viscous stress tensor σ_{ij} and heat flux q_i are not specified, yet. Hence, additional information on σ_{ij} and q_i is necessary to solve the system of equations.

Navier-Stokes Equations. Using the empirical formulations of Newton and Fourier, the viscous stresses σ_{ij} and the heat flux q_i can be written as:

$$\sigma_{ij} = \mu(\frac{\partial v_i}{\partial x_j} + \frac{\partial v_j}{\partial x_i} - \frac{2}{3}\frac{\partial v_k}{\partial x_k}\delta_{ij}) \tag{A.2a}$$

$$q_i = \lambda\frac{\partial T}{\partial x_i}, \tag{A.2b}$$

where μ is the dynamic viscosity and λ the thermal conductivity. Inserting (A.2) into (A.1) leads to the formulation of the Navier-Stokes equations as given in (A.3). Although, the term "Navier-Stokes Equations" is often only used for the momentum equation, it refers to the whole system of equations (A.3) in the following.

$$\begin{aligned}
\frac{\partial \rho}{\partial t} + \frac{\partial}{\partial x_i}(\rho v_i) &= 0 \\
\frac{\partial}{\partial t}(\rho v_i) + \frac{\partial}{\partial x_j}(\rho v_i v_j) + \frac{\partial p}{\partial x_i} &= \frac{\partial}{\partial x_j}\mu\left(\frac{\partial v_i}{\partial x_j} + \frac{\partial v_j}{\partial x_i} - \frac{2}{3}\frac{\partial v_k}{\partial x_k}\delta_{ij}\right) \\
\frac{\partial}{\partial t}(\rho E) + \frac{\partial}{\partial x_i}(\rho v_i E + v_i p) &= \frac{\partial}{\partial x_i} v_j \mu\left(\frac{\partial v_i}{\partial x_j} + \frac{\partial v_j}{\partial x_i} - \frac{2}{3}\frac{\partial v_k}{\partial x_k}\delta_{ij}\right) \\
&\quad + \frac{\partial}{\partial x_i}\left(\lambda\frac{\partial T}{\partial x_i}\right),
\end{aligned} \tag{A.3}$$

where the total energy $E = e + v^2/2$ is the sum of internal and kinetic energy.

Molecular Approach. Alternatively to the macroscopic approach, fluid dynamics can be described on a molecular level, which eventually leads to the formulation of the Boltzmann equation. In this case, the fluid is not represented as a continuum but consists of a very large number of particles. The particles travel at a speed of $\boldsymbol{\xi}$ and collide with each other. The particle velocity $\boldsymbol{\xi}$ can be divided into a thermal velocity $\boldsymbol{c}$ and a macroscopic flow velocity $\boldsymbol{v}$.

$$\boldsymbol{\xi} = \boldsymbol{c} + \boldsymbol{v} \tag{A.4}$$

The mean free path without collision is labeled l_f. Thus, the flow regime can be characterized using the Knudsen number Kn, which is defined as the mean free path without collision l_f over a characteristic macroscopic length scale L that corresponds to a variation of the macroscopic flow properties.

$$Kn = \frac{l_f}{L} \tag{A.5}$$

For continuum flow the mean free path is much smaller than the macroscopic length scale, hence $Kn << 1$. On the other end, for free molecular flow $Kn >> 1$.

Boltzmann Equation. Due to the extremely large number of particles in practical flow problems, the particles cannot be treated individually but are instead described statistically. To this end, the velocity distribution function $f(\boldsymbol{r}, \boldsymbol{\xi}, t)$ is defined, which describes the number of particles at a certain place $\boldsymbol{r}$ with a certain velocity $\boldsymbol{\xi}$ at a given point in time t. The evolution of the distribution function f is described by the Boltzmann equation:

$$\frac{\partial f}{\partial t}+\xi_i\frac{\partial f}{\partial x_i}+\frac{F_i}{m}\frac{\partial f}{\partial \xi_i}=\int\limits_{\xi_1}\int\limits_{A_C}(f'f_1'-ff_1)(\boldsymbol{\xi_1}-\boldsymbol{\xi})\,dA_C d\boldsymbol{\xi_1}. \tag{A.6}$$

The terms on the left side describe the temporal and spatial evolution of the distribution function as well as the variation due to external forces F_i. The term on the right side is called collision operator and describes the number of particles that - due to collisions - enter or exit the velocity space $d\boldsymbol{\xi}$ around $\boldsymbol{\xi}$. f_1 represents the distribution function of a collision partner before the collision and f' and f_1' the distribution functions after the collision. A_C represents the collision cross section. The inner integral $\int dA_C$ describes the probability of collisions, where the collision partners feature the velocities $\boldsymbol{\xi}$ and $\boldsymbol{\xi_1}$ before the collision and $\boldsymbol{\xi'}$ and $\boldsymbol{\xi_1'}$ after the collision. The outer integral $\int d\boldsymbol{\xi_1}$ finally integrates over all possible velocities $\boldsymbol{\xi_1}$ of collision partners. The Boltzmann equation is valid in rarefied gas where the mean free path without collision l_f is much larger than the size of the particles. Furthermore, intermolecular interactions are limited to binary collisions and the duration of the collisions is assumed to be very short so that the velocity distribution function f does not change during the collision.

Macroscopic Flow Properties. Using the velocity distribution function f, the macroscopic flow properties mass, momentum and energy can be derived as follows:

$$\begin{aligned}\rho(\boldsymbol{r},t)&=m\int f(\boldsymbol{r},t,\boldsymbol{\xi})d\boldsymbol{\xi}\\ \rho(\boldsymbol{r},t)\cdot\boldsymbol{v}(\boldsymbol{r},t)&=m\int \boldsymbol{\xi}f(\boldsymbol{r},t,\boldsymbol{\xi})d\boldsymbol{\xi}\\ \rho(\boldsymbol{r},t)\cdot E(\boldsymbol{r},t)&=\rho\left(e+\frac{\boldsymbol{v}^2}{2}\right)=m\int\frac{\boldsymbol{\xi}^2}{2}f(\boldsymbol{r},t,\boldsymbol{\xi})d\boldsymbol{\xi}.\end{aligned} \tag{A.7}$$

From Boltzmann to the Macroscopic Laws of Conservation. Starting from the Boltzmann equation, the basic laws of conservation of mass, momentum and energy can be derived via the Maxwell-Boltzmann moment equations. Multiplying the Boltzmann equation by a function $\Phi(\boldsymbol{\xi})$ followed by an integration over $d\boldsymbol{\xi}$ leads to:

$$\begin{aligned}\frac{\partial}{\partial t}\int\Phi f d\boldsymbol{\xi}+&\frac{\partial}{\partial x_i}\int\Phi\xi_i f d\boldsymbol{\xi}\\ &=\int\limits_{\xi}\int\limits_{\xi_1}\int\limits_{A_C}\Phi(f'f_1'-ff_1)(\boldsymbol{\xi_1}-\boldsymbol{\xi})\,dA_C d\boldsymbol{\xi_1}d\boldsymbol{\xi},\end{aligned} \tag{A.8}$$

where external forces are discarded.

The integral of the collision term on the right side can be rewritten as shown in Hänel (2004), which leads to:

$$\begin{aligned}\frac{\partial}{\partial t}\int \Phi f d\boldsymbol{\xi}+&\frac{\partial}{\partial x_i}\int \Phi \xi_i f d\boldsymbol{\xi}\\ &=\frac{1}{2}\int\limits_{\xi}\int\limits_{\xi_1}\int\limits_{A_C}(\Phi'+\Phi_1'-\Phi-\Phi_1)ff_1(\boldsymbol{\xi_1}-\boldsymbol{\xi})dA_C d\boldsymbol{\xi_1}d\boldsymbol{\xi}.\end{aligned} \tag{A.9}$$

The system of equations (A.9) cannot be solved without additional information since for each function $\Phi_n(\boldsymbol{\xi})$ of order n, the second term in (A.9) is of order $n+1$ regarding $\boldsymbol{\xi}$. The moment equations of mass, momentum and energy are obtained by choosing:

$$\begin{aligned}\Phi_0 &= m\\ \Phi_1 &= m\boldsymbol{\xi}\\ \Phi_2 &= m\boldsymbol{\xi}^2/2.\end{aligned} \tag{A.10}$$

Assuming the particle collisions to be elastic, the properties mass, momentum and energy are conserved throughout the collision.

$$\Phi_i(\boldsymbol{\xi'})+\Phi_i(\boldsymbol{\xi_1'})=\Phi_i(\boldsymbol{\xi})+\Phi_i(\boldsymbol{\xi_1}),\qquad i=0,1,2 \tag{A.11}$$

Exemplarily, the conservation of mass is written as:

$$m'+m_1'=m+m_1,$$

where m and m_1 represent the mass before the collision and m' and m_1' after the collision.

Therfore, the right side of (A.9) becomes zero for Φ_0, Φ_1 and Φ_2, which leads to:

$$\begin{aligned}&n=0 \qquad \frac{\partial}{\partial t}\int mfd\boldsymbol{\xi}+\frac{\partial}{\partial x_i}\int m\xi_i fd\boldsymbol{\xi}=0\\ &n=1 \qquad \frac{\partial}{\partial t}\int m\xi_j fd\boldsymbol{\xi}+\frac{\partial}{\partial x_i}\int m\xi_j\xi_i fd\boldsymbol{\xi}=0\\ &n=2 \qquad \frac{\partial}{\partial t}\int \frac{m}{2}|\xi|^2 fd\boldsymbol{\xi}+\frac{\partial}{\partial x_i}\int \frac{m}{2}|\xi|^2\xi_i fd\boldsymbol{\xi}=0.\end{aligned} \tag{A.12}$$

Using the relation between the molecular distribution function and the macroscopic properties (A.7), (A.12) finally leads to the laws of conservation (A.1):

$$\begin{aligned}\frac{\partial\rho}{\partial t}+\frac{\partial}{\partial x_i}(\rho v_i)&=0\\ \frac{\partial}{\partial t}(\rho v_i)+\frac{\partial}{\partial x_j}(\rho v_i v_j+p\delta_{ij}-\sigma_{ij})&=0\\ \frac{\partial}{\partial t}(\rho(e+v^2/2))+\frac{\partial}{\partial x_i}(\rho v_i(e+v^2/2)+v_i p-v_j\sigma_{ij}-q_i)&=0,\end{aligned}$$

where σ_{ij} is the viscous stress tensor and q_i the heat flux. σ_{ij} can be derived from the general stress tensor p_{ij} with the definition of the static pressure p:

$$p_{ij} = p\delta_{ij} - \sigma_{ij} = m\int c_i c_j f d\boldsymbol{c} \tag{A.13a}$$

$$p = \frac{m}{3}\int c^2 f d\boldsymbol{c} \tag{A.13b}$$

$$\sigma_{ij} = \frac{m}{3}\int c^2 f d\boldsymbol{c}\delta_{ij} - m\int c_i c_j f d\boldsymbol{c}. \tag{A.13c}$$

The heat flux q_i is given by:

$$q_i = -\frac{m}{2}\int c_i c^2 f d\boldsymbol{c}. \tag{A.14}$$

BGK-Model. An important simplification of the complex collision term of the Boltzmann equation was proposed by Bhatnagar, Gross and Krook. The so-called BGK-model replaces the collision term by an approach that describes the relaxation of the distribution function towards local equilibrium.

$$\left.\frac{Df}{dt}\right|_{Coll,BGK} = \omega(F - f) \tag{A.15}$$

$$\frac{\partial f}{\partial t} + \xi_i \frac{\partial f}{\partial x_i} + \frac{F_i}{m}\frac{\partial f}{\partial \xi_i} = \omega(F - f), \tag{A.16}$$

where ω is the molecular collision frequency, which corresponds to the inverse of the time scale τ of the relaxation process $\omega = 1/\tau$. ω can be derived from the dynamic fluid viscosity $\nu = \mu/\rho$ and the molecular velocity $c_S^2 = RT$:

$$\omega = \frac{c_S^2}{\nu} = \frac{c_S^2}{\mu/\rho}. \tag{A.17}$$

F is the Maxwell-Boltzmann distribution function of local thermodynamic equilibrium:

$$F = \frac{n}{(2\pi RT)^{3/2}}\exp\left(-\frac{\boldsymbol{c}^2}{2RT}\right) = \frac{n}{(2\pi RT)^{3/2}}\exp\left(-\frac{(\boldsymbol{\xi} - \boldsymbol{v})^2}{2RT}\right). \tag{A.18}$$

At local thermodynamic equilibrium, the number of particles that exit the velocity space $d\boldsymbol{\xi}$ around $\boldsymbol{\xi}$ equals the number of particles that enter the velocity space. This corresponds to $Kn \to 0$, which means that the mean free path l_f is very small compared to the macroscopic length scale, which again signifies that local equilibrium is reached almost instantaneously due to the high frequency of collisions.

For the BGK-approach the moment equations are obtained analogously to the Maxwell-Boltzmann moment equations (A.9):

$$\frac{\partial}{\partial t}\int \Phi f d\boldsymbol{\xi} + \frac{\partial}{\partial x_i}\int \Phi \xi_i f d\boldsymbol{\xi} = \omega \left(\int \Phi F d\boldsymbol{\xi} - \int \Phi f d\boldsymbol{\xi} \right). \tag{A.19}$$

Thermodynamic Equilibrium - Euler Equations. For thermodynamic equilibrium the Euler equations can be derived from the moment equations of the BGK-approach (A.19) - or also from the Maxwell-Boltzmann moment equations (A.9). At equilibrium $f(\boldsymbol{\xi}) = F(\boldsymbol{\xi})$, hence the collision term becomes zero, which gives:

$$\frac{\partial}{\partial t}\int \Phi F d\boldsymbol{\xi} + \frac{\partial}{\partial x_i}\int \Phi \xi_i F d\boldsymbol{\xi} = 0. \tag{A.20}$$

Inserting equations (A.10) and following the derivation of the general equations of conservation leads to the Euler equations.

$$\begin{aligned} \frac{\partial \rho}{\partial t} + \frac{\partial}{\partial x_i}(\rho v_i) &= 0 \\ \frac{\partial}{\partial t}(\rho v_i) + \frac{\partial}{\partial x_j}(\rho v_i v_j) + \frac{\partial p}{\partial x_i} &= 0 \\ \frac{\partial}{\partial t}(\rho E) + \frac{\partial}{\partial x_i}(\rho v_i E + v_i p) &= 0 \end{aligned} \tag{A.21}$$

By definition of local equilibrium the viscous stress tensor σ_{ij} and the heat flux q_i are zero.

Non-Equilibrium - Navier-Stokes Equations. Thermodynamic equilibrium and the corresponding Euler equations represent an idealized flow regime, which allows solving the Boltzmann equation since the collision term becomes zero. For general non-equilibrium this is not possible. However, for small deviations from thermodynamic equilibrium the Chapman-Enskog procedure provides an approximate solution and enables the calculation of the stress tensor σ_{ij} and the heat flux q_i. Since the Lattice-Boltzmann code used in this work is based on the BGK-model of the Boltzmann equation, the Chapman-Enskog procedure is derived for this approach. First, a non-dimensionalized formulation of the BKG-model is obtained using the definitions below.

$$\epsilon \frac{D\bar{f}}{d\bar{t}} = \bar{\omega}(\bar{F} - \bar{f}), \tag{A.22}$$

where $\epsilon = Kn$, $\bar{x}_i = \frac{x_i}{L}$, $\bar{t} = \frac{t}{L/c_0}$, $\bar{\xi} = \frac{\xi}{c_0}$, $\bar{f} = \frac{f}{n/c_0^3}$, $\bar{\omega} = \frac{\omega}{c_0/l_f}$.

For small deviations from local equilibrium $\epsilon << 1$ the distribution function $\bar{f}$ can be written as:

$$\bar{f} = \bar{f}^{(0)} + \epsilon \bar{f}^{(1)} + \epsilon^2 \bar{f}^{(2)} + \ldots + \epsilon^n \bar{f}^{(n)}, \tag{A.23}$$

with the distribution functions $\bar{f}_i$ being of the order of one. Inserting (A.23) into (A.22) leads to:

$$\begin{aligned}\epsilon\frac{D}{dt}(\bar{f}^{(0)}+\epsilon\bar{f}^{(1)}+\epsilon^2\bar{f}^{(2)}+\ldots+\epsilon^n\bar{f}^{(n)}) \\ =\omega(\bar{F}-\bar{f}^{(0)}-\epsilon\bar{f}^{(1)}-\epsilon^2\bar{f}^{(2)}-\ldots-\epsilon^n.\bar{f}^{(n)})\end{aligned} \tag{A.24}$$

For an approximation of order zero and $\epsilon \to 0$ one obtains:

$$\bar{f}=\bar{f}^{(0)}=\bar{F}, \tag{A.25}$$

which corresponds to the Maxwell-Boltzmann equilibrium distribution and leads to the Euler equation (A.21), as already shown above. Using (A.25), the first order approximation leads to (A.26).

$$\bar{f}=\bar{F}+\epsilon\bar{f}^{(1)} \tag{A.26}$$

Inserting (A.26) into the first order approximation of (A.24) gives (A.27) in dimensional form again.

$$\frac{\partial F}{\partial t}+\xi_i\frac{\partial F}{\partial x_i}=-\omega\epsilon f^{(1)} \tag{A.27}$$

As described in Hänel (2004) $f^{(1)}$ can be determined from (A.27).

$$f^{(1)}=-\frac{F}{\epsilon\omega}\left[\left(\frac{\boldsymbol{c}^2}{2RT}-\frac{5}{2}\right)\frac{c_i}{T}\frac{\partial T}{\partial x_i}+\frac{1}{RT}c_ic_j:S_{ij}\right], \tag{A.28}$$

where S_{ij} is the strain tensor $S_{ij}=\frac{1}{2}\left(\frac{\partial v_i}{\partial x_j}+\frac{\partial v_j}{\partial x_i}-\frac{2}{3}\frac{\partial v_k}{\partial x_k}\delta_{ij}\right)$. Inserting (A.28) into (A.26) finally gives the first order non-equilibrium distribution function:

$$f=F\left(1-\frac{1}{\omega}\left[\left(\frac{\boldsymbol{c}^2}{2RT}-\frac{5}{2}\right)\frac{c_i}{T}\frac{\partial T}{\partial x_i}+\frac{1}{RT}c_ic_j:S_{ij}\right]\right). \tag{A.29}$$

Now, that the distribution function for non-equilibrium is known, the viscous stresses σ_{ij} and the heat flux q_i can be determined using (A.13) and (A.14).

$$\begin{aligned}\sigma_{ij}&=m\int c^2fd\boldsymbol{c}\delta_{ij}-m\int c_ic_jfd\boldsymbol{c}\\&=2\frac{nkT}{\omega}\cdot S_{ij}\\&=\frac{nkT}{\omega}\left(\frac{\partial v_i}{\partial x_j}+\frac{\partial v_j}{\partial x_i}-\frac{2}{3}\frac{\partial v_k}{\partial x_k}\delta_{ij}\right)\end{aligned} \tag{A.30}$$

$$\begin{aligned}q_i&=-m\int c_ic^2fd\boldsymbol{c}\\&=\frac{5}{2}\frac{k}{m}\frac{nkT}{\omega}\frac{\partial T}{\partial x_i}\end{aligned} \tag{A.31}$$

Comparing (A.30) with the empirical formulations (A.2) used in the Navier-Stokes equations leads to a description of the dynamic viscosity μ and the thermal conductivity λ derived from kinetic molecular theory.

$$\mu = \frac{nkT}{\omega} \sim \sqrt{T} \tag{A.32}$$

$$\lambda = \frac{5}{2}\frac{k}{m}\frac{nkT}{\omega} \sim \sqrt{T} \tag{A.33}$$

(A.32) and (A.33) correspond to the behavior of molecules described by the elastic, rigid sphere model. A general formulation of μ and λ can be derived by applying the Chapman-Enskog expansion to the Boltzmann equation itself instead of the simplified BGK-model.

A.2 Lattice Boltzmann Method

The Lattice Boltzmann method represents a discrete approximation of the Boltzmann equation. Its name is derived from the phase space of discrete velocities called “lattice”. In Fig. A.1 two typical Cartesian lattices are shown for two and three dimensions, respectively. The lattice restricts the movement of particles within one time step to a discrete number of neighboring grid points. In two dimensions, commonly an equidistant Cartesian grid of nine discrete velocities is used, which point along the four Cartesian and the four diagonal directions. The ninth discrete velocity represents the zero vector. Alternatively, also a hexagonal grid can be used. In three dimensions, a lattice consisting of 15 discrete velocities is widely used, as shown in Fig. A.1b. The time step δt, the distances δx, δy and δz and the discrete velocities ξ_i are related by (A.34) so that particles travelling at speed ξ_i arrive at the neighboring grid points after exactly one time step δt.

$$\delta x = \delta y = \delta z = \xi_0 \delta t, \tag{A.34}$$

where ξ_0 is the common velocity along each axis.

Discretization of the Boltzmann-BGK equation leads to:

$$f_i(\boldsymbol{r} + \boldsymbol{\xi_i}\delta t, t + \delta t) = f_i(\boldsymbol{r}, t) + \omega \delta t \left(f_i^{eq}(\boldsymbol{r}, t) - f_i(\boldsymbol{r}, t) \right), \tag{A.35}$$

where $f_i = f(\boldsymbol{\xi_i})$ is the velocity distribution function for the discrete velocity $\boldsymbol{\xi_i}$. It is, however, also possible to divide (A.35) into a transport and a collision step that are solved consecutively. In order to solve (A.35) the equilibrium distribution function f_i^{eq} is required for the discrete velocities $\boldsymbol{\xi_i}$. Based on the assumption of small Mach numbers the equilibrium distribution function f_p^{eq} of the Lattice-BGK method is given for the normalized absolute velocity $p = \left(\frac{\xi_i}{\xi_0}\right)^2$ by

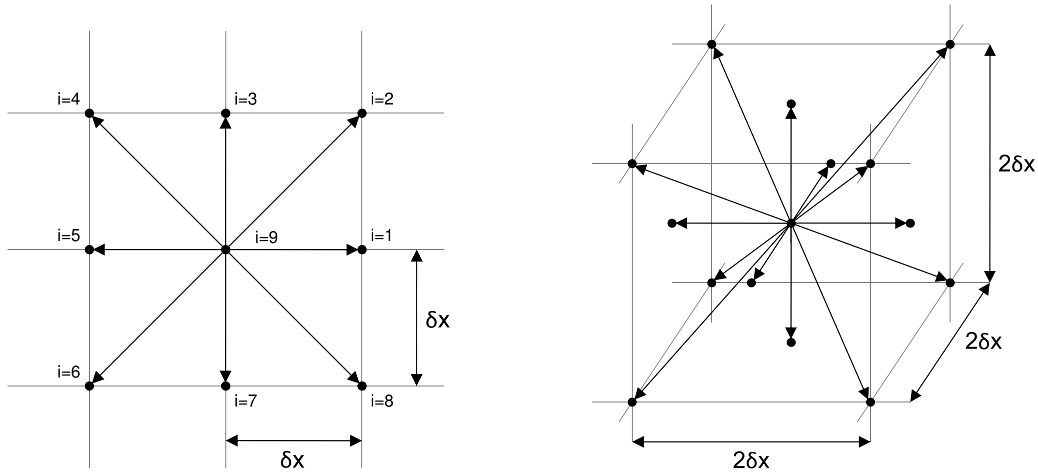

(a) 2D (b) 3D

Figure A.1: Examples for a discrete velocity space defined by two- and three-dimensional lattices as sketched in Hänel (2004).

$$f_p^{eq}(x_\alpha, t, \xi_\alpha) = \rho t_p \left[1 + \frac{v_\alpha \xi_\alpha}{c_S^2} + \frac{v_\alpha v_\beta}{2c_S^2}\left(\frac{\xi_\alpha \xi_\beta}{c_S^2} - \delta_{\alpha\beta}\right)\right], \tag{A.36}$$

where $\alpha, \beta = 1, 2, 3$, $c_S = \sqrt{RT}$ and t_p is a weighting factor which depends on the normalized absolute velocity $p(\boldsymbol{\xi_i})$. In the discretized case the collision frequency ω is defined by:

$$\omega = \frac{c_S^2}{\nu + \delta t c_S^2/2} = \frac{RT}{\nu + \delta t RT/2}. \tag{A.37}$$

Finally, the macroscopic flow parameters density, momentum and energy are obtained by summing over the discrete velocity distributions

$$\begin{aligned} \rho(\boldsymbol{r}, t) &= \sum_{i=1}^{n_{states}} f_i(\boldsymbol{r}, t) = \sum_{i=1}^{n_{states}} f_i^{eq}(\boldsymbol{r}, t) \\ \rho v_\alpha(\boldsymbol{r}, t) &= \sum_{i=1}^{n_{states}} \xi_{i,\alpha} f_i(\boldsymbol{r}, t) = \sum_{i=1}^{n_{states}} \xi_{i,\alpha} f_i^{eq}(\boldsymbol{r}, t) \\ \rho E(\boldsymbol{r}, t) &= \frac{1}{2}\sum_{i=1}^{n_{states}} \xi_{i,\alpha}^2 f_i(\boldsymbol{r}, t) = \frac{1}{2}\sum_{i=1}^{n_{states}} \xi_{i,\alpha}^2 f_i^{eq}(\boldsymbol{r}, t). \end{aligned} \tag{A.38}$$

Turbulence Modeling. The Lattice Boltzmann method is capable of time-accurately calculating turbulent flows if the grid resolution is fine enough to resolve all turbulent scales. As this is generally not possible for industrial applications due to the extreme computational requirements, only large eddies are resolved by the grid directly while the influence of unresolved small scale turbulence is taken into account by turbulence modeling. The implementation of a two-equation k-ϵ-RNG-model (**Re**Normalization **G**roup), as it is used in the numerical code applied in the frame of this work, is described by Teixeira (1998) and Pervaiz and Teixeira (1999).

To this end, the relaxation frequency ω is modified to include an additional term called the eddy viscosity $\nu_t = \mu_t/\rho$ which describes the influence of unresolved flow scales. $\nu_0 = \mu_0/\rho$ represents the molecular viscosity as derived in (A.30).

$$\nu = \nu_0 + \nu_t \tag{A.39}$$

$$\omega = \frac{RT}{\nu + \nu_t + \delta t RT/2} \tag{A.40}$$

In the k-ϵ-RNG-model, the eddy-viscosity ν_t is calculated from the turbulent kinetic energy k and the dissipation rate ϵ.

$$\nu_t = \frac{\mu_t}{\rho} = \frac{C_\mu k^2}{\epsilon} \tag{A.41}$$

Where C_μ is a constant parameter, which is set to $C_\mu = 0.085$ for the RNG model.

The turbulence properties k and ϵ are determined by a system of two transport equations that have to be solved separately from the Lattice Boltzmann equations.

$$\frac{\partial k}{\partial t} + \boldsymbol{v} \cdot \nabla k = \frac{\partial}{\partial x_j}\left[\left(\frac{\nu_0}{\sigma_{k0}} + \frac{\nu_t}{\sigma_{kt}}\right)\frac{\partial k}{\partial x_j}\right] + \nu_t \left|S_{ij}\right|^2 - \epsilon \tag{A.42}$$

$$\begin{aligned}\frac{\partial \epsilon}{\partial t} + \boldsymbol{v} \cdot \nabla \epsilon = {}& \frac{\partial}{\partial x_j}\left[\left(\frac{\nu_0}{\sigma_{\epsilon 0}} + \frac{\nu_t}{\sigma_{\epsilon t}}\right)\frac{\partial \epsilon}{\partial x_j}\right] + C_{\epsilon 1}\frac{\epsilon}{k}\left|S_{ij}\right|^2 \\ & - \left[C_{\epsilon 2} + C_\mu \frac{\eta^3(1-\eta/\eta_0)}{1+\beta\eta^3}\right]\frac{\epsilon^3}{k},\end{aligned} \tag{A.43}$$

where $\eta = |S|\, k/\epsilon$ is a dimensionless shear rate and the closure coefficients are $C_\mu = 0.085$, $C_{\epsilon 1} = 1.42$, $C_{\epsilon 2} = 1.68$, $\sigma_{k0} = \sigma_{\epsilon 0} = \sigma_{kt} = \sigma_{\epsilon t} = 0.719$, $\eta_0 = 4.38$, $\beta = 0.719$.

Wall Model. Similar to the small scale turbulence, it is computationally very expensive to completely resolve the boundary layer profile. However, taking advantage of the universal form of the boundary layer close to the wall, the shear stress at the first grid point above the wall can be determined using the so-called law-of-the-wall. Assuming that the law-of-the-wall applies at the first grid point, the local shear stress equals the wall shear stress τ_W, which can be defined as follows:

$$\tau_W \equiv \rho u_\tau^2 = \frac{1}{2} c_f \rho u^2, \tag{A.44}$$

with the friction velocity $u_\tau = \sqrt{\tau_W/\rho}$ and a local skin friction coefficient c_f.

The boundary layer can be divided into three regions using the non-dimensional wall-normal distance $y^+ = y u_\tau/\nu$ and the non-dimensional velocity $u^+ = u/u_\tau$. As shown in Fig. A.2, directly at the wall the viscous sublayer features a linear variation of u^+ with y^+, while in the outer region the velocity increases logarithmically. The transition layer connects the two regions. Eqs. (A.45) and (A.46) describe the variation of u^+ and hence the relation between u and u_τ in the viscous sublayer and in the logarithmic region. For the transition layer, the constants κ and B are adjusted in order to obtain a continuous curve linking the sublayer and the logarithmic region.

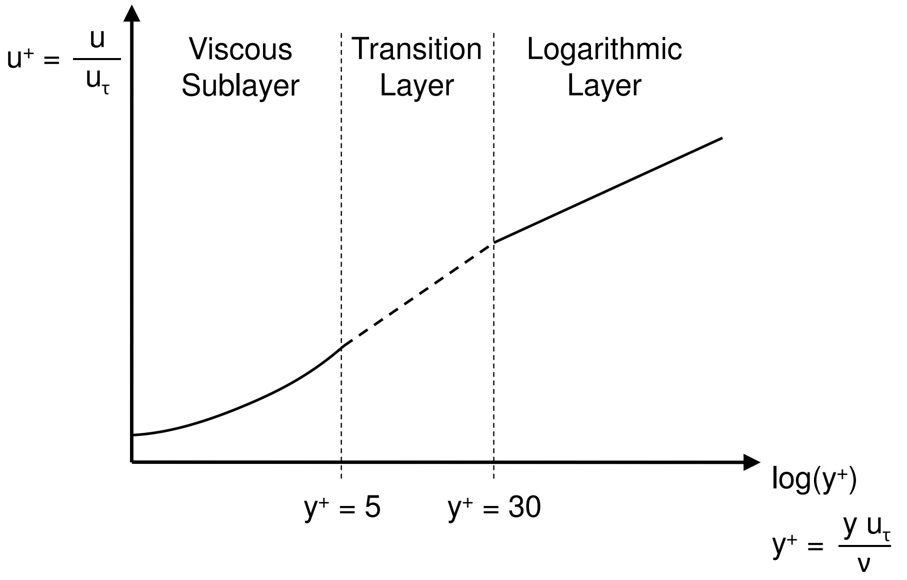

Figure A.2: Schematic view of the law-of-the-wall describing the velocity profile in the boundary layer.

$$y^+ \leq 5: \quad u^+ = y^+ \tag{A.45}$$

$$y^+ \geq 30: \quad u^+ = \frac{1}{\kappa} \ln y^+ + B \quad \kappa = 0.41, B = 5.0 \tag{A.46}$$

Hence, (A.44) in combination with the wall model provide two equations for the determination of the two unknowns u_τ and c_f. In order to capture the influence of a streamwise pressure gradient $\partial p/\partial s$ the wall-normal distance y^+ is scaled by a factor $1/\zeta_p$.

$$y_p^+ = \frac{y^+}{\zeta_p}, \tag{A.47}$$

where $\zeta_p = 1 + f(\partial p/\partial s)$.

Bibliography

Ahmed, S., G. Ramm, and G. Faltin (1984). Some salient features of the time-averaged ground vehicle wake. *SAE Paper 840 300*.

Aschwanden, P., J. Müller, and R. Müller (2006). Assessment of the aerodynamic load distribution of a race car under the influence of model motion by use of non-static wind tunnel tests. In *Proceedings of 6th MIRA International Vehicle Aerodynamics Conference, UK.*

Bearman, P. (1971). An investigation of the forces on flat plates normal to a turbulent flow. *Journal of Fluid Mechanics 46*, 177–198.

Bearman, P. and S. Mullarkey (1994). Aerodynamic forces on road vehicles due to steady side winds and gusts. In *RAeS Conference on Vehicle Aerodynamics, UK.*

Carlino, G. and A. Cogotti (2006). Simulation of transient phenomena with the turbulence generation system in the pininfarina wind tunnel. *SAE Technical Paper Series 2006-01-1031*.

Chadwick, A., K. Garry, and J. Howell (2001). Transient aerodynamic characteristics of simple vehicle shapes by the measurement of surface pressures. *SAE Technical Paper Series 2001-01-0876*.

Davenport, A. G. (1961). The application of statistical concepts to the wind loading of structures. *Proceedings of the Institution of Civil Engineers 19*, 449–472.

Demuth, R. and P. Buck (2006). Numerical investigations on the unsteady aerodynamics of road vehicles under gusty weather conditions. In *Proceedings of 6th MIRA International Vehicle Aerodynamics Conference, UK.*

EXA (2008). *PowerFlow Best Practices Guide 1.1 Revision 2.*

Fares, E. (2006). Unsteady flow simulation of the ahmed reference body using a lattice boltzmann approach. *Computers & Fluids 35*, 940–950.

Favre, T. (2009). *Numerical Investigation of Unsteady Crosswind Aerodynamics for Ground Vehicles.* Ph. D. thesis, KTH Stockholm (Licentiate Thesis).

Favre, T. and G. Efraimsson (2010). Numerical study of design alterations affecting the crosswind characteristics of a generic road vehicle model. In *Proceedings of 8th MIRA International Vehicle Aerodynamics Conference, UK.*

Garry, K. P. and K. R. Cooper (1986). Comparison of quasi-steatic and dynamic wind tunnel measurements on simplified tractor-trailor models. *Journal of Wind Engineering and Industrial Aerodynamics 22*, 185–194.

Gohlke, M., J. Beaudoin, M. Amielh, and F. Anselmet (2007). Experimental analysis of flow structures and forces on a 3d-bluff-body in constant cross-wind. *Experiments in Fluids 43*, 579–594.

Gohlke, M., J. Beaudoin, M. Amielh, and F. Anselmet (2008). Thorough analysis of vortical structures in the flow around a yawed bluff body. *Journal of Turbulence 9(15)*, 1–28.

Guilmineau, E. and F. Chometon (2008). Numerical and experimental analysis of unsteady seperated flow behind an oscillating car model. *SAE Technical Paper Series 2008-01-0738*.

Heft, A., T. Indinger, and N. A. Adams (2011). Investigation of unsteady flow structures in the wake of a realistic generic car model. *29th AIAA Applied Aerodynamics Conference, USA*.

Heuler, K. S. (2010). Untersuchung der strömungstopologie am heck einer limousine bei schräganströmung. Master's thesis, TU Munich.

Hänel, D. (2004). *Molekulare Gasdynamik.* Springer-Verlag, Berlin Heidelberg.

Hucho, W. H. (2005). *Aerodynamik des Automobils.* Vieweg Verlag, Wiesbaden.

Jeong, J. and F. Hussain (1995). On the identification of a vortex. *Journal of Fluid Mechanics 285*, 69–94.

Kistler (2010). *Kistler Instruments Manual K-Beam Capacitance Acceleration Sensor.*

Kobayashi, N. and M. Yamada (1988). Stability of a one box type vehicle in a crosswind - an analysis of transient aerodynamic forces and moments. *SAE Technical Paper Series 881878*.

Kulite (2009). *Kulite Miniature Ruggedized IS Pressure Transducers XT-190 (M) Series.*

Lemke, T. (2006). *Untersuchung der Fahrzeugumströmung bei Seitenwind für die Frühphase der PKW-Entwicklung.* Ph. D. thesis, University Siegen.

Li, Y., R. Shock, R. Zhang, and H. Chen (2004). Numerical study of flow past an impulsively started cylinder by the lattice-boltzmann method. *Journal of Fluid Mechanics 519*, 273–300.

Macklin, R., K. Garry, and J. Howell (1997). Assessing the effects of shear and turbulence during the dynamics testing of the crosswind sensitivity of road vehicles. *SAE Technical Paper Series 970135*.

Maeda, K., H. Sakai, and M. Tomiyama (1996). Analysis of aerodynamic effects on the vehicle stability in high speed running. In *International Symposium on the Advanced Vehicle Control (AVEC), Aachen.*

Mansor, S. and M. Passmore (2008). Estimation of bluff body transient aerodynamics using an oscillating model rig. *Journal of Wind Engineering and Industrial Aerodynamics 96*, 1218–1231.

Mayer, J., M. Schrefl, and R. Demuth (2007). On various aspects of the unsteady aerodynamic effects on cars under crosswind conditions. *SAE Technical Paper Series 2007-01-1548*.

Modlinger, F., R. Demuth, and N. A. Adams (2007). Investigations on the realistic modeling of the flow around wheels and wheel arches by cfd. *JSAE Paper No. 20075195*.

Mullarkey, S. (1990). *Aerodynamic Stability of Road Vehicles in Side Winds and Gusts.* Ph. D. thesis, University of London.

Passmore, M. and S. Mansor (2006). The measurement of transient aerodynamics using an oscillating model fascility. *SAE Technical Paper Series 2006-01-0338*.

Passmore, M., S. Richardson, and A. Imam (2001). An experimental study of unsteady vehicle aerodynamics. *Journal of Automobile Engineering 215(7)*, 779–788.

Pervaiz, M. M. and C. M. Teixeira (1999). Two equation turbulence modeling wit the lattice-boltzmann method. *Proceeding of ASME PVP Division Conference: 2nd International Symposium on Computational Technologies for Fluid/Thermal/Chemical Systems with Industrial Applications, Boston, USA.*

Puff, A. (2010). Numerical simulation of unsteady vehicle aerodynamics during an overtaking manoeuvre. Master's thesis, University Erlangen-Nürnberg.

RUAG (2009). *RUAG Calibration Report DMS Balance 788-6B.*

Schaible, S. (1998). *Fahrzeugseitenwindempfindlichkeit unter natürlichen Bedingungen.* Ph. D. thesis, RWTH Aachen.

Schröck, D., N. Widdecke, and J. Wiedemann (2007). On-road wind conditions experienced by a moving vehicle. In *6th FKFS Conference Progress in Vehicle Aerodynamics and Thermal Management.*

Schröck, D., N. Widdecke, and J. Wiedemann (2009). Aerodynamic response of a vehicle model to turbulent wind. In *7th FKFS Conference Progress in Vehicle Aerodynamics and Thermal Management.*

Schrefl, M. (2008). *Instationäre Aerodynamik von Kraftfahrzeugen: Aerodynamik bei Überholvorgang und böigem Seitenwind.* Ph. D. thesis, TU Darmstadt.

Schäufele, S. (2010). *Validierung der neuen Windkanäle im Aerodynamischen Versuchszentrum der BMW Group und Analyse der Übertragbarkeit der Ergebnisse.* Ph. D. thesis, Karlsruhe Institute of Technology (KIT).

Sims-Williams, D. B. and B. D. Duncan (2003). The ahmed model unsteady wake: Experimental and computational analysis. *SAE Technical Paper Series 2003-01-1315*.

Succi, S. (2001). *The Lattice Boltzmann Equation for Fluid Dynamics and Beyond.* University Press, Oxford.

Teixeira, C. M. (1998). Incorporating turbulence models into the lattice-boltzmann method. *International Journal of Modern Physics C*.

Theissen, P., R. Demuth, and N. A. Adams (2010). Unsteady phenomena in vehicle aerodynamics under time-dependent flow conditions. In *10th Stuttgart International Symposium "Automotive and Engine Technology", GER.*

Theissen, P., J. Wojciak, R. Demuth, N. A. Adams, and T. Indinger (2010). Unsteady aerodynamic phenomena under time-dependent flow conditions for different vehicle shapes. In *Proceedings of 8th MIRA International Vehicle Aerodynamics Conference, UK.*

Theissen, P., J. Wojciak, K. Heuler, R. Demuth, N. A. Adams, and T. Indinger (2011). Experimental investigation of unsteady vehicle aerodynamics under time-dependent flow conditions – part1. *SAE Technical Paper Series 2011-01-0177*.

Tsubokura, M., T. Nakashima, K. Kitoh, and Y. Sasaki (2009). Development of unsteady aerodynamic simulator using laerge-eddy simulation. In *7th FKFS Conference Progress in Vehicle Aerodynamics and Thermal Management.*

Wagner, A. (2003). *Ein Verfahren zur Vorhersage und Bewertung der Fahrerreaktion bei Seitenwind.* Ph. D. thesis, University Stuttgart.

Wallentowitz, H. (1981). Fahren bei seitenwind. *Automobil-Industrie 2*, 163–171.

Watkins, S., S. Toksoy, and J. Saunders (1992). On the generation of tunnel turbulence for road vehicles. In *11th Australasian Fluid Mechanics Conference.*

Wojciak, J., T. Indinger, N. A. Adams, P. Theissen, and R. Demuth (2010). Experimental study of on-road aerodynamics during crosswind gusts. In *Proceedings of 8th MIRA International Vehicle Aerodynamics Conference, UK.*

Wojciak, J., P. Theissen, K. Heuler, T. Indinger, N. A. Adams, and R. Demuth (2011). Experimental investigation of unsteady vehicle aerodynamics under time-dependent flow conditions - part2. *SAE Technical Paper Series 2011-01-0164*.

List of Figures

List of Tables